

AEDC-TR-01-5



**Free-Piston Shock Tunnel
Test Technique Development:
An AEDC/DLR Cooperative Program**

D. W. Stallings, W. D. Williams, and E. J. Felderman
Jacobs Sverdrup AEDC Group
W. H. Beck and K. Hannemann
DLR

February 2003

Final Report for Period October 1997 — September 2001

Approved for public release; distribution unlimited.

**ARNOLD ENGINEERING DEVELOPMENT CENTER
ARNOLD AIR FORCE BASE, TENNESSEE
AIR FORCE MATERIEL COMMAND
UNITED STATES AIR FORCE**

NOTICES

When U. S. Government drawings, specifications, or other data are used for any purpose other than a definitely related Government procurement operation, the Government thereby incurs no responsibility nor any obligation whatsoever, and the fact that the Government may have formulated, furnished, or in any way supplied the said drawings, specifications, or other data, is not to be regarded by implication or otherwise, or in any manner licensing the holder or any other person or corporation, or conveying any rights or permission to manufacture, use, or sell any patented invention that may in any way be related thereto.

Qualified users may obtain copies of this report from the Defense Technical Information Center.

References to named commercial products in this report are not to be considered in any sense as an endorsement of the product by the United States Air Force or the Government.

APPROVAL STATEMENT

This report has been reviewed and approved.



RONALD T. BISHEL
Applied Technology Division
Test Operations Directorate

Approved for publication:

FOR THE COMMANDER



ROBERT T. CROOK
Deputy Chief, Applied Technology Division
Test Operations Directorate

REPORT DOCUMENTATION PAGE

*Form Approved
OMB No. 0704-0188*

The public reporting burden for this collection of information is estimated to average 1 hour per response, including the time for reviewing instructions, searching existing data sources, gathering and maintaining the data needed, and completing and reviewing the collection of information. Send comments regarding this burden estimate or any other aspect of this collection of information, including suggestions for reducing the burden, to Department of Defense, Washington Headquarters Services, Directorate for Information Operations and Reports (0704-0188), 1215 Jefferson Davis Highway, Suite 1204, Arlington, VA 22202-4302. Respondents should be aware that notwithstanding any other provision of law, no person shall be subject to any penalty for failing to comply with a collection of information if it does not display a currently valid OMB control number.
PLEASE DO NOT RETURN YOUR FORM TO THE ABOVE ADDRESS.

1. REPORT DATE (DD-MM-YYYY) February 2003			2. REPORT TYPE Final AEDC Technical Report (TR)		3. DATES COVERED (From - To) October 1997-September 2001	
4. TITLE AND SUBTITLE Free-Piston Shock Tunnel Test Technique Development: An AEDC/DLR Cooperative Program					5a. CONTRACT NUMBER	
					5b. GRANT NUMBER	
					5c. PROGRAM ELEMENT NUMBER	
6. AUTHOR(S) D. W. Stallings, W. D. Williams, and E. J. Felderman, Jacobs Sverdrup AEDC Group W. H. Beck and K. Hannemann, DLR					5d. PROJECT NUMBER 4159/9179	
					5e. TASK NUMBER	
					5f. WORK UNIT NUMBER	
7. PERFORMING ORGANIZATION NAME(S) AND ADDRESS(ES) Jacobs Sverdrup AEDC Group Arnold Air Force Base, Tennessee 37389-5051					8. PERFORMING ORGANIZATION REPORT NUMBER AEDC-TR-01-5	
9. SPONSORING/MONITORING AGENCY NAME(S) AND ADDRESS(ES) SAF/IAQ Attn: Maj. Keller 1080 Air Force Pentagon Washington, DC 20330-1080					10. SPONSOR/MONITOR'S ACRONYM(S)	
					11. SPONSOR/MONITOR'S REPORT NUMBER(S)	
12. DISTRIBUTION/AVAILABILITY STATEMENT Approved for public release; distribution is unlimited.						
13. SUPPLEMENTARY NOTES Available in Defense Technical Information Center (DTIC).						
14. ABSTRACT Arnold Engineering Development Center (AEDC) and the German Aerospace Institute (DLR) have conducted a cooperative program on operation and test technique development for high enthalpy shock tunnels. The AEDC Free-Piston Shock Tunnel (FPST) and the DLR High Enthalpy Göttingen (HEG) facility were used for complementary test programs. The two organizations individually and jointly analyzed data from these tests to assess and advance the state of their computational fluid dynamics capabilities. Several nonintrusive diagnostic techniques were employed at each facility, resulting in new and improved diagnostic capabilities for each partner. This report explains the organization of the joint program, reviews the operation of free-piston shock tunnels, and presents the results of data acquisition and analysis from the test programs.						
15. SUBJECT TERMS high enthalpy facilities; free-piston shock tunnels; nonintrusive diagnostics; high enthalpy flows						
16. SECURITY CLASSIFICATION OF:			17. LIMITATION OF ABSTRACT U	18. NUMBER OF PAGES 242	19a. NAMES OF RESPONSIBLE PERSON Ronald T. Bishel	
a. REPORT	b. ABSTRACT	c. THIS PAGE			19b. TELEPHONE NUMBER (Include area code) 931-454-7734	
Unclassified	Unclassified	Unclassified				

PREFACE

This project was carried out under a Memorandum of Understanding (MoU) for Research and Technology Projects concluded between the U.S. Secretary of Defense and the German Ministry of Defense in March of 1995. Funding for this project was provided under the NATO ICR&D Program with matching funds from AEDC and DLR. This project furthers one of the stated objectives of the NATO ICR&D program which is to reduce defense RDT&E costs through technology and facility sharing between the US and its NATO allies.

The work reported herein was conducted by the Arnold Engineering Development Center (AEDC), Air Force Materiel Command (AFMC) in cooperation with the German Aerospace Center, DLR.. The AEDC test results were obtained by Jacobs Sverdrup AEDC Group, contractor for support testing at AEDC, AFMC, Arnold Air Force Base, Tennessee, under Job Numbers 4159 and 9719. The Air Force Project Manager was Mr. Ron Bishel, AEDC/DOT. The data analysis was completed on September 30, 2001, and the manuscript was submitted for publication in November 2001.

L. L. Price, M. S. Smith, C. W. Brasier, F. L. Heltsley, P. M. Sherrouse, K. M. Stephens, W. M. Ruyten, J. Martinez-Schramm, and Ole Trinks contributed substantially to the work of this project and the preparation of this report.

TABLE OF CONTENTS

	<u>Page</u>
PREFACE	1
1.0 EXECUTIVE SUMMARY	7
1.1 Background	7
1.2 Program Goals	7
1.3 Program Activities	8
1.4 Nonintrusive Diagnostics	9
1.5 Computational Fluid Dynamics	9
1.6 Achievements and Recommendations	10
2.0 INTRODUCTION	12
3.0 THE COOPERATIVE PROGRAM	13
4.0 FACILITY OPERATIONS	15
4.1 The Free-Piston Shock Tunnel	15
4.2 HEG Experiments	19
5.0 COMPUTATIONAL FLUID DYNAMICS AND COMPARISONS WITH TUNNEL DATA	24
5.1 Codes Employed	24
5.2 Tunnel Comparisons	26
5.3 Prediction of Freestream Conditions	27
5.4 Code Validation	28
5.5 Prediction of Model Parameters	30
5.6 CFD Accomplishments	31
5.7 CFD Summary	32
6.0 NONINTRUSIVE DIAGNOSTICS	33
6.1 Introduction	33
6.2 Applications at the AEDC Impulse Facility	34
6.3 Impulse Facility (FPST) Data Analysis	40
6.4 Applications at the DLR HEG	43
6.5 HEG Data Analysis	44
6.6 Development of the Pulsed Electron Beam Fluorescence Technique	49
6.7 NID Summary	52
7.0 SUMMARY OF RESULTS	53
REFERENCES	56

ILLUSTRATIONS

Figure

1. Conditions Required to Duplicate Flight Conditions	60
2. Free-Piston Shock Tunnel Operating Concept	61
3. AEDC Free-Piston Shock Tunnel	62
4. Free-Piston Shock Tunnel Test Section Details	62
5. Particle Stopper	63
6. Calibration Rake	63
7. AEDC Blunt Slender Cone (Electre) Model, 70-percent Scale	64
8. Schematic View of the HEG	65

<u>Figure</u>	<u>Page</u>
9. Double-Ramp Model; Dots Indicate Sensor Positions	66
10. Schematic of Schlieren Apparatus	67
11. Schlieren Pictures of the Double-Wedge Flow Showing Establishment of Separation ($\Delta\tau = 0.6$ msec Between Frames).	68
12. L_u as a Function of Time in Comparison to Pitot Pressure, HEG Run 453, Condition III	69
13. L_u as a Function of Time in Comparison to the Static Pressure for HEG Run 453 and Condition III.	70
14. Results for L_u in High and Low Enthalpy Conditions in Comparison to the Measurements to Ref. 11	71
15. Comparison between AEDC and HEG Heat Flux Calculation Methods	72
16. Computed Spectra.	73
17. Predicted Temperatures in AEDC Impulse Tunnel Nozzle, Run 30	74
18. Vibrational and Rotational Temperatures predicted by the GASP, GIANTS, and LAURA Codes—Fire II.	75
19. Nitrogen Species Predicted by the GASP, GIANTS, and LAURA Codes— Fire II, 1634 sec	76
20. Vibrational and Rotational Temperatures Predicted by the GASP, GPACK, and NEDANA Codes	77
21. Vibrational and Rotational Temperatures Predicted by the GASP and NSHYP Codes—Sphere-Cone, HEG Condition I	78
22. Shock Shape Comparisons, AEDC Run 31	79
23. Shock Shape Comparisons, AEDC Run 34	80
24. Shock Shape Variation with Time	81
25. Run Time Determination Using Shock Shape	82
26. Pressure Coefficient, AEDC Runs 30-35, Electre Model (70 percent)	83
27. Pressure Coefficient, DLR Electre Model in HEG.	84
28. Heat-Transfer Coefficient, AEDC Run 30, Electre Model (70 percent)	85
29. Heat-Transfer Coefficient, AEDC Runs 30-35, Electre Model (70 percent).	86
30. Heat Flux, DLR Electre Model in HEG	87
31. NID Techniques Undertaken for Application at the AEDC Impulse Facility	88
32. Application of LBT at the AEDC Impulse Facility	89
33. Impulse Facility Run 26 Laser Beam Transmission.	90
34. Impulse Facility Run 27 Laser Beam Transmission.	91
35. Impulse Facility Run 28 Laser Beam Transmission.	92
36. Impulse Facility Run 29 Laser Beam Transmission.	93
37. Impulse Facility Run 30 Laser Beam Transmission.	94
38. Impulse Facility Run 31 Laser Beam Transmission.	95
39. Impulse Facility Run 32 Laser Beam Transmission.	96
40. Impulse Facility Run 33 Laser Beam Transmission.	97
41. Impulse Facility Run 34 Laser Beam Transmission.	98
42. Impulse Facility Run 35 Laser Beam Transmission.	99
43. Application of PMIE at the AEDC Impulse Facility	100
44. Application of ES at the AEDC Impulse Facility.	101
45. Application of LDA at the AEDC Laboratory Shock Tube/Tunnel.	102
46. LDA Reduced Data Format—AEDC Laboratory Shock Tube/Tunnel	103
47. Use of Filtered Rayleigh Scattering at the AEDC Impulse Facility.	104

<u>Figure</u>	<u>Page</u>
48. High-Speed Flow Visualization System	105
49. HSFV Setup for Acquiring High-Speed Holograms	106
50. Process for Creating HSFV Digital Movies	107
51. PLIF Setup at the Impulse Facility	108
52. Peak and Average LBT Values During Estimated Good Run Time	109
53. HSFV for Flow Start Process, Impulse Facility Run 30—June 2, 1998	110
54. HSFV for Flow Start Process, Impulse Facility Run 31—June 3, 1998	111
55. HSFV for Flow Start Process, Impulse Facility Run 32—June 4, 1998	112
56. HSFV for Flow Start Process, Impulse Facility Run 33—June 9, 1998	113
57. HSFV for Flow Start Process, Impulse Facility Run 34—June 10, 1998	114
58. HSFV for Flow Start Process, Impulse Facility Run 35—June 12, 1998	115
59. HSFV for Flow Steadiness, Impulse Facility Run 30—June 2, 1998	116
60. HSFV for Flow Steadiness, Impulse Facility Run 31—June 3, 1998	117
61. HSFV for Flow Steadiness, Impulse Facility Run 32—June 4, 1998	118
62. HSFV for Flow Steadiness, Impulse Facility Run 33—June 9, 1998	119
63. HSFV for Flow Steadiness, Impulse Facility Run 34—June 10, 1998	120
64. HSFV for Flow Steadiness, Impulse Facility Run 35—June 12, 1998	121
65. Gas Density from Holographic Interferometry, Impulse Facility Run 35	122
66. Impulse Facility: Planar Laser-Induced Fluorescence Imaging	123
67. PLIF Signal Profiles	124
68. PLIF Signal Ratios	124
69. Impulse Facility Run 26 Emission Spectra	125
70. FPST Emission Spectrum	126
71. HSFV System as Installed on HEG	127
72. PLIF Setup in HEG	128
73. HSFV for Flow Start Process, HEG Run 446—September 25, 1998	129
74. HSFV for Flow Start Process, HEG Run 448—September 28, 1998	130
75. HSFV for Flow Start Process, HEG Run 451—September 30, 1998	131
76. HSFV for Flow Start Process, HEG Run 452—November 1, 1998	132
77. HSFV for Flow Start Process, HEG Run 453—November 1, 1998	133
78. HSFV for Flow Start Process, HEG Run 454—November 2, 1998	134
79. HSFV for Flow Start Process, HEG Run 455—November 2, 1998	135
80. HSFV for Flow Start Process, HEG Run 456—November 5, 1998	136
81. HSFV for Flow Start Process, HEG Run 457—November 5, 1998	137
82. HSFV for Flow Start Process, HEG Run 458—November 1998	138
83. HSFV for Flow Start Process, HEG Run 460—November 1998	139
84. HSFV for Flow Steadiness, HEG Run 446—September 25, 1998	140
85. HSFV for Flow Steadiness, HEG Run 448—September 28, 1998	141
86. HSFV for Flow Steadiness, HEG Run 451—September 30, 1998	142
87. HSFV for Flow Steadiness, HEG Run 452—November 1, 1998	143
88. HSFV for Flow Steadiness, HEG Run 453—November 1, 1998	144
89. HSFV for Flow Steadiness, HEG Run 454—November 2, 1998	145
90. HSFV for Flow Steadiness, HEG Run 455—November 2, 1998	146
91. HSFV for Flow Steadiness, HEG Run 456—November 5, 1998	147
92. HSFV for Flow Steadiness, HEG Run 457—November 5, 1998	148
93. HSFV for Flow Steadiness, HEG Run 458—November 1998	149
94. HSFV for Flow Steadiness, HEG Run 460—November 1998	150

<u>Figure</u>	<u>Page</u>
95. Experimental Setup for HEG PLIF Measurements	151
96. Summary of PLIF Conditions.	152
97. PLIF Images	153
98. Partially Processed Data - Run 454:Condition III	154
99. Partially Processed Data - Run 455: Condition III	155
100. Partially Processed Data - Run 456: Condition III	156
101. Calculated Line Shapes.	157
102. Calculated Signals and Signal Ratios	158
103. Explicit Estimate of Freestream NO Temperature and Density	159
104. Extension of Reference 30 Theory	160
105. Effect of NO in Boundary Layer on Inferred Freestream Parameters	161
106. Sectional Drawing of the Pulsed Electron Gun	162
107. Conceived PEG Application at the FPST.	163
108. Laboratory PEG System	164
109. High-Voltage Pulsed Electronics for the PEG	165
110. PEG Electronic Control and Instrumentation.	166
111. Nitrogen PEBF Spectrum	167

TABLES

1. AEDC FPST Test Conditions	168
2. Size Comparison of DLR and AEDC Free-Piston Shock Tubes.	168
3. HEG Operating Conditions, Conical Nozzle, Air As Test Gas	169
4. Test Matrix for Double Ramp Experiments.	169
5. HEG Freestream Conditions During AEDC Tests	170
6. AEDC FPST Freestream Conditions	171
7. Stagnation Point Heating: Fire II Configuration	171
8. PLIF-NO Measurements of T_{tr}	171
9. AEDC Nonintrusive Diagnostics in the Impulse Facility	172
10. AEDC Nonintrusive Diagnostics in the HEG	173
11. Information Potentially Provided by NID About the Impulse Facility Flow Fields	174
12. Impulse Facility Nonintrusive Diagnostics Data Log	175
13. LBT Measurements at the Impulse Facility.	176
14. Tabulation of Facility Run Time Information	176
15. HEG Nonintrusive Diagnostics Data Log	177

APPENDIXES

1. Project Agreement	178
2. LDA Data Reduction Software	191
3. Shearing and Conventional Interferometry from Holographic Cinematography	197
4. Converting Cordin Camera Film to .AVI Digital Movies	233

1.0 EXECUTIVE SUMMARY

1.1 BACKGROUND

Computational Fluid Dynamics (CFD) codes are vital to the future design of hypersonic flight systems, and adequate data for code validation are essential in the development of the necessary CFD codes. This project was a joint effort between the Arnold Engineering Development Center (AEDC) and the German Research Center (DLR), both of which have active programs to develop the facility and diagnostic technologies needed to provide these data. Each center has chosen an advanced facility concept known as a free piston shock tunnel as a test bed for acquiring the data. However, there are variations in each approach that made a cooperative program of technology development feasible and very attractive. The German facility, called HEG, is one of the largest in the world, while the AEDC Impulse Tunnel (herein called the AEDC FPST for Free-Piston Shock Tunnel) will operate at very high test gas pressure or density. In addition to the pressure and size differences, the nonintrusive diagnostic (NID) techniques employed in the two facilities are somewhat different. Exchanging diagnostic systems provided information to help determine if certain techniques have advantages over others. DLR and AEDC also use different CFD tools. The cooperative program provided an opportunity to compare analysis results using the different CFD methods.

The HEG has been in operation since 1993. Initial shakedown and calibration operation of the FPST began in FY94. The joint program was designed to complement the technology development required to bring the FPST to its full operational capability. The associated diagnostics technology activity was aimed at providing the systems with which to acquire the data needed for validation of CFD codes required for the design of hypersonic vehicles and defense systems.

The joint program involved complementary testing in the AEDC FPST and the HEG Tunnel in Germany. During these tests the relative merits of the different diagnostics systems being used in such facilities were compared.

1.2 PROGRAM GOALS

A goal of the joint program was the faster development of the technologies needed to provide the CFD tools that are required to advance the state of the art in hypersonics. The results from this program will help to make available on a timely basis the experimental and computational capabilities needed by the U. S. aerospace industry to design and produce the hypersonic flight systems of the future. The cooperative program between AEDC and DLR for comparative research and development testing at the two free-piston shock tunnels provided an opportunity to reduce the costs and advance the timeline for acquiring the technologies needed to provide the ground test capabilities required for the development of these future hypersonic flight systems.

Some specific objectives of this project were to:

- Provide data for code validation
- Improve diagnostics capabilities through sharing of different techniques and hardware

- Understand flow and instrumentation anomalies in free-piston facilities
- Evaluate flow quality in the HEG and the AEDC FPST

It is important to note that even though CFD code validation was a major goal of the program, this goal could not be achieved without the flow-field data obtained through the use of nonintrusive diagnostics. Therefore, the development of the NID techniques necessarily constituted a large portion of this program. The successful application of existing NID techniques, including the extension and further development of some, as well as the acquisition of new techniques constitutes a major portion of the success of this joint program.

For both partners the actual test operations in the facilities had several objectives. The collection of data on the various test article configurations was, of course, an important goal. Experimental measurements of the surface parameters on the spherically blunt cone and the flow field around the cone have application in the design of that class of hypersonic flight systems. As mentioned previously, the broadening of the database for hypersonic code validation was a primary reason for the initiation of this project. Of equal importance was the further development of the nonintrusive diagnostics techniques. While the initial work on such systems can be done in the laboratory, the final proof of the applicability and utility of any of these techniques must come from demonstrations in an actual test facility. For AEDC there was a further goal of gaining increased experience in the operation of the AEDC FPST and improving its hardware and operating procedures.

1.3 PROGRAM ACTIVITIES

To accomplish the goals and objectives described above, the following activities were performed:

- Test programs in the HEG and the AEDC FPST at complementary test conditions with similar test article configurations
- Cooperative data analysis
- Parallel CFD analyses to support the experiments
- Joint preparation of summary documentation of the activities and findings for the project

The test program in the HEG produced data on two configurations; a spherically blunt slender cone (designated Electre) and a shock wave/boundary-layer interaction configuration. The original intent of the project was to test the same configurations in the AEDC FPST. However, operational problems (discussed in detail elsewhere in this report) limited the AEDC test program to the Electre model only.

The test program in the AEDC FPST began with a short calibration phase. It was deemed prudent to include these tests because the facility had not been operated as an FPST for some time. In the interim, the configuration had been changed to an impact facility, an impact test program had been conducted, and the configuration had been changed back to the FPST. Four calibration runs were made to verify that the facility was functioning properly. The results of

these tests indicated that the facility operation and the test conditions produced were as seen during the initial calibration tests.

1.4 NONINTRUSIVE DIAGNOSTICS

The high enthalpy and short test times of the FPST present a stiff challenge in making the desired measurements of freestream and model flow-field and surface conditions. Laser-based non-intrusive diagnostics techniques offer the potential for obtaining the needed data, and a number of these techniques have been under development for many years. The nonintrusive diagnostics techniques that were used in various ways in this project included laser beam transmission, planar Mie scattering, witness plates, emission spectroscopy (ES), laser diode absorption (LDA), filtered Rayleigh scattering, pulsed electron beam fluorescence (PEBF), high-speed flow visualization (HSFV), and planar, laser-induced fluorescence (PLIF). Because these techniques are in varying stages of development, the application and results were different for each technique and for the two facilities. Detailed discussions of the nonintrusive diagnostics work are included in the body of this report. As a general summary, this area of activity (NID) was probably the most productive of the entire cooperative program. Both partners were able to develop and use diagnostics systems that had not been available to them previously. This provided data and understanding of real gas flow physics that would not have been possible without the cooperative work. The results in the diagnostics area alone have more than justified the costs and efforts involved in establishing and maintaining this cooperative program.

1.5 COMPUTATIONAL FLUID DYNAMICS

A primary use of free-piston shock tunnels is to obtain data that can be used to validate CFD codes for application to high-energy flows. Such codes will be required in the design and development of high Mach number flight systems, since the flight conditions for such systems often exceed the capability of ground test facilities. The successful development of such flight systems requires that advanced CFD codes be used in conjunction with the limited ground test data. The development and validation of these codes is thus the key to future procurement of advanced high Mach number flight vehicles. Data and code comparisons from the AEDC FPST and the DLR HEG have been reported in a number of publications. However, sharing test information from the HEG and the AEDC FPST provided DLR and AEDC with a larger database for use in evaluating and validating CFD codes. The cooperation also allowed for comparing the results from the different codes used by each institution.

A number of advanced CFD codes were employed in the course of this program. One of the principal CFD codes that has been used in the analysis of data from the AEDC FPST is the three-dimensional, thin-layer Navier-Stokes code, TUFF, developed at NASA Ames. This code solves the strongly coupled species conservation equations and fluid dynamic equations in a finite-volume framework. A sophisticated nonequilibrium radiation solver, NEQAIR, was also used. Several CFD flow-solver codes were used. GASP is a three-dimensional, finite-volume flow solver that contains

options for the Roe or van Leer upwind schemes. GASP solves the integral form of the fluid dynamic equations, including the full Reynolds-averaged Navier-Stokes, thin-layer, parabolized or Euler equations. GASP contains a generalized chemistry model as well as a two-temperature model. Another code that was used was NEDANA, which employs a three-dimensional, locally implicit algorithm for the solution of the thin-layer Navier-Stokes equations expanded for thermochemical nonequilibrium. The numerical flux function is based on the central-difference, flux-limited, artificial dissipation model of Jameson. The scheme combines the simplicity of artificial dissipation with the total variation diminishing property. The flow solver employs the AEDC-developed chemistry package NEQPAK. GPACK is a computer program currently under development that has been applied towards simulating propulsion-generated flow-field phenomena. These simulations treated fully coupled three-dimensional flows with finite-rate chemistry. The CEVCATS-N code used at HEG solves the full Navier-Stokes equations in integral form for mixtures of perfect and reacting gases. Thermochemical equilibrium and nonequilibrium are solved with a numerical scheme consisting of hybrid upwind flux vector splitting and use of a five-stage Runge-Kutta scheme for time integration. Local time stepping, implicit residual averaging, and full multigrid are used to accelerate the convergence process. Viscosity is computed with Sutherland's formula for perfect gases and with Blottner curve fits for reacting gases. The chemical model contains (but is not restricted to) five species. Boundary conditions on the wall allow different temperatures (adiabatic, prescribed, equilibrium). The influence of catalytic effects can also be included. Several tools are used for generation of the structured grids. The computational performance on a NEC SX4/4 (single processor) is about 1.1 GFLOPS.

All of these codes are discussed in some detail in the body of this report, and their use in the program is described. Results of data comparisons with the various codes are also presented.

1.6 ACHIEVEMENTS AND RECOMMENDATIONS

This project has allowed AEDC and DLR to exercise their CFD capabilities in the hypersonics arena and, in addition, develop new capabilities. It was also an opportunity to acquire new data for code validation, as well as an opportunity to reexamine existing data. The exchange of raw data and reduced data allowed for the validation of data reduction techniques. This was especially valuable in the case of heat transfer, which involves considerable calculation. It was found that the AEDC and DLR methods agreed well, but it is noted that the DLR "indirect" method captured the details without the artificial smoothing required by the AEDC "direct" method.

AEDC acquired new CFD capabilities in the course of this effort, including the NEQAIR code, which was installed at AEDC. In the course of this effort AEDC personnel gained valuable experience in the use and development of two-temperature flow codes.

An ambitious, but successful, NID program was executed at the AEDC Impulse Facility as well as at the DLR HEG. All NID techniques pursued for application gave useful results with the exception of the PEBF technique, which, because of time and resource constraints, did not

progress past the laboratory development stage. No FPST-related operational problems were encountered, with the possible exceptions of boundary-layer and recirculation effects on LDA measurements and potential copper absorption effects on HSFV for some conditions. At the DLR HEG the copper absorption effect was significant, but the use of a dye laser pumped by the copper vapor laser was successful at circumventing the absorption problem for HSFV.

It was determined that, in the AEDC facility, flow is established within 0.67 msec from the shock tube gage (ST6) trigger pulse, and that a nominal run time of 2.5 msec free from driver gas effects is available for nozzle stagnation pressures of less than 1000 atmospheres. Facility flow appears optically thick as a result of particulate scattering for nozzle stagnation pressures greater than 1000 atmospheres.

It is clear from the wide range of computational predictions of freestream properties and the lack of agreement of PLIF-NO measurements with any of the predictions, that considerable work is required on CFD physics models, along with a thorough investigation of the current PLIF-NO methodology. Analysis methods using both the laboratory shock tube/tunnel and the newly-acquired high-temperature calibration cell are also required. Future application of LDA requires the use of airtight tubes extending into the boundary layer to eliminate boundary-layer and recirculation effects. It is also recommended that the LDA technique be extended to yield information on flow velocity. As the question of vibrational nonequilibrium has not been resolved, it is recommended that the PEBF technique be developed further, because it can readily give information on vibrational temperature for a number of species simultaneously. Furthermore, the PEBF technique potentially can provide quantitative information on the amount of helium contaminating the test gas.

As a result of this international cooperative program, NID capability for high-enthalpy facilities has been greatly enhanced. The HSFV system is now available for applications to hypersonic air-breathing propulsion, aero-optics, jet interaction, and ballistic range testing. Indeed, the association established during this program with North Dancer Laboratories, Inc. with regard to advancements in high-speed holographic recording has placed AEDC on the leading edge of high-speed visualization capability. The LDA system methodology has already been advanced for use with absorption by O_2 , H_2O , and K, and applications in turbine engine and hypersonic air-breathing propulsion testing as well as aerodynamic testing are forthcoming. Although applications of the PEBF system were not achieved, the capability of the system was greatly advanced, and it will likely become an outstanding diagnostic tool for the high Mach number conditions of AEDC's Tunnel 9.

This international program has promoted the development of excellent working relationships among the engineers at DLR HEG and AEDC. These relationships were expanded to encompass the international hypersonics ground testing community through participation in workshops and symposia. The successes of this program have encouraged the participants to seek other avenues for extending the cooperation into other technical areas.

2.0 INTRODUCTION

In the second half of the 20th century much work has gone into research on and development of hypersonic flight systems, and many such systems have been successfully flown. A recent and ongoing example is the U.S. Space Shuttle. These development programs have been plagued with the problem of obtaining, through ground test or computational simulation, adequate (both in terms of quantity and quality) data on the performance of the systems and subsystems involved. This problem arises because of the difficulty of reproducing in ground test facilities the actual conditions of hypersonic flight. This difficulty is attributable to the very high energies represented by flight at hypersonic Mach numbers. The translation of these high energies to test conditions in a conventional wind tunnel is illustrated in Fig. 1. Flight velocity in thousands of feet per second is representative of the Mach number. As the figure shows, the required tunnel reservoir pressures and temperatures are extreme for Mach numbers greater than about 6. Such pressures and temperatures are difficult to produce and nearly impossible to contain in a conventional wind tunnel.

Because of the problems associated with ground testing of hypersonic systems, the design of future hypersonic flight systems will rely heavily on the use of CFD. A critical step in the development of the required CFD codes is the acquisition of experimental data for validation of the codes. Detailed information about a variety of parameters in the flow field around a hypersonic vehicle is required to validate the codes. To minimize extrapolation of the validated code results it is important to acquire the validation data at conditions as near as possible to the actual flight conditions. To accomplish this and obtain the needed data will require significant advances in the capabilities of ground test facilities and the associated diagnostics techniques.

An approach to producing the tunnel conditions required to obtain test data at hypersonic speeds and provide some of the information needed to develop CFD codes has been the use of so-called "impulse facilities." Such facilities typically use shock waves to process the test gas and produce the pressure and temperature conditions needed. They vary somewhat in the technique used to generate the shock waves. A concept pioneered by Stalker in the 1960s (Ref. 1) is the free-piston shock tunnel (FPST). The basic concept of the FPST is shown in Fig. 2. Here, a piston is driven into and compresses a driver gas to very high pressure and temperature. This gas bursts a diaphragm and thereby generates a shock wave that propagates through and processes the test gas to produce the desired high-pressure and high-temperature nozzle reservoir conditions. Further details of the operation of an FPST are given below.

A relatively small number of FPST facilities have been built. Stalker and associates at the University of Queensland and the Australian National University built Tunnels T1 to T4. In 1990 Tunnel T5 went into operation (Ref. 2) at the California Institute of Technology, in Pasadena. In 1991 what was then the largest FPST in the world was put into operation by the German Aerospace Center (DLR) at the DLR Institute of Fluid Mechanics in Göttingen, Germany (Ref. 3). The Arnold Engineering Development Center (AEDC), in the course of a major upgrade to its Ballistic Range facilities, added an FPST to that facility complex. Initial calibration of the AEDC FPST

(Ref. 4) was accomplished in 1993. The latest addition to the world's complement of free-piston shock tunnels is the High Enthalpy Shock Tunnel (HIEST) at the Kakuda Research Center of the Japanese National Aerospace Laboratory. This is now the largest FPST in the world (Ref. 5). Its primary purpose is the testing of supersonic combustion ramjet engines. There is also a smaller facility, called HEK, at Kakuda, that was the pilot facility for HIEST. The French have the TCM2 facility at Marseille. In recent years, a few small research-scale tunnels have been built at several universities, notably in Japan.

As noted above, FPST facilities are designed to produce very high-energy test conditions. Producing and controlling such conditions leads to some very difficult engineering problems. In the effort to reach the most extreme conditions possible, the facilities are subjected to very high stresses during operation. This can often lead to serious facility damage. Preventing such occurrences and successfully solving the engineering problems can require extensive and expensive research and technology programs. However, development of the required diagnostics systems is a completely different (but also extensive and expensive) task. Many of these systems are laser-based and can be tedious to install and operate. Analysis of the spectral data acquired by these systems is complicated. The CFD codes needed to analyze, correlate, and extrapolate the data are complex and require large computer capabilities. Clearly the complete task of assembling the facility hardware, the diagnostics, and the CFD is a daunting undertaking. Thus any facility technology group that is attempting to develop a complete FPST capability would be expected to be open to the possibility of a cooperative effort with a like-minded group elsewhere.

As can be deduced from the brevity of the above list of FPST facilities that exist worldwide, the community of test centers involved in the operation of these facilities is small. As a consequence, there is a relatively high level of communication between the centers, with sharing of information and discussion of problems. The AEDC group was therefore aware of the status of the other facilities. With knowledge of the NATO International Cooperative Research and Development (ICR&D) Program administered by the U.S. Department of Defense, AEDC could assess potential partnerships in light of the objectives and requirements of the ICR&D program. It was easy to see that there was a very good opportunity for establishing a program of formal cooperation between the DLR and AEDC.

3.0 THE COOPERATIVE PROGRAM

This cooperation arose out of the long-standing Data Exchange Agreement (DEA) 7425, Wind Tunnel Test Techniques and Design, between the U.S. and German governments. Whereas the DEA involves a regular exchange of information, it was thought that a closer collaborative effort involving work sharing in the further development and use of the two high enthalpy shock tunnels, AEDC FPST and HEG, would be mutually most beneficial.

Initial discussions began in 1994 between AEDC and DLR on the possibility of a joint program related to FPST research. Through several exchanges of letters it was agreed that the potential coop-

eration offered a number of benefits to both parties. Whereas AEDC had just completed initial shakedown of an FPST, the DLR had been operating an FPST, known as the High Enthalpy Shock Tunnel Göttingen (HEG), for several years. The DLR therefore brought extensive experience in the operation of such facilities. AEDC had for many years maintained a significant effort in the development of nonintrusive diagnostic systems, and both parties had good capabilities in CFD. In September of 1994, a team from AEDC met with DLR personnel in Göttingen, Germany to discuss the technical issues involved in such a cooperative project. Specific engineering activities for a cooperative program were identified, and a proposed schedule for the work was developed. AEDC then initiated the process of establishing a formal cooperative agreement.

It was determined that establishing a project under the NATO ICR&D Program was the best procedure for creating a cooperative activity between AEDC and the DLR. This program was established by the U.S. Congress to provide an avenue for cooperation between the U.S. and its Allies. One of the stated purposes of the program is to reduce defense RDT&E costs through technology and facility sharing. To initiate the process of establishing such a program, AEDC prepared a Project Nomination Proposal (PNP). This document addresses several key questions about the utility and viability of a proposed cooperative project. These include the commitment of the proposed partners, the anticipated benefits to the participants, the existence of an international agreement under which the project could function, the advantages and disadvantages of a cooperative effort, and the impact on the U.S. defense industrial base. The PNP was approved for ICR&D program funding, and AEDC, in cooperation with HQ AFMC/STI, prepared the necessary documentation. This included a Summary Statement of Intent (SSOI), Project Agreement (PA), and a Data Disclosure Letter (DDL). The SSOI extended the PNP to provide more detailed information about various aspects of the project. These included operational requirements, project objectives, legal authority, project organization and management structure, benefits/risks to the U.S., funding issues, and a proposed schedule of activities. The PA provided more detail about the scope, task sharing and breakdown, and schedule of work. Items such as loan of equipment were also addressed in the PA. In March 1995 the Memorandum of Understanding (MoU) for Research and Technology Projects was concluded between the U.S. Secretary of Defense and the German Ministry of Defense. The FPST PA was submitted under this MoU, and after some negotiation the PA was approved in April 1997. A copy of the PA is included as Appendix 1. Initial funding was received at AEDC in June 1997, and AEDC Job Number 4159 was established to carry out the cooperative work.

The joint program involved complementary testing in the FPST at AEDC and the HEG in the DLR Germany. During these tests the relative merits of different diagnostics systems being used in such facilities were compared. The issues involved here are critical to the validation of the computer codes that will be required for the design of future hypersonic flight systems.

A goal of the joint program was the faster development of technologies needed to provide the CFD tools that are required to advance the state of the art in hypersonics. The results from this program will help to make available on a timely basis the experimental and computational capa-

bilities needed by the U. S. aerospace industry to design and produce the hypersonic flight systems of the future. The cooperative program between AEDC and DLR for comparative research and development testing at the two free-piston shock tunnels provided an excellent opportunity to leverage the resources of the two institutions. The end result will be a reduction in costs and an advance in the timeline for acquiring the technologies needed to provide the ground test capabilities required for the development of future hypersonic flight systems. Some specific objectives of the project were to:

- 1) Provide data for code validation;
- 2) Improve diagnostics capabilities through sharing of different techniques and hardware;
- 3) Understand flow and instrumentation anomalies in free-piston facilities;
- 4) Evaluate flow quality in the HEG and the AEDC FPST.

Activities to accomplish these objectives included:

- 1) Test programs in the HEG and the AEDC FPST at complementary test conditions with similar test article configurations;
- 2) Cooperative data acquisition and analysis;
- 3) Parallel CFD analyses to support the experiments;
- 4) Joint summary documentation of the activities and findings for the project.

4.0 FACILITY OPERATIONS

For both partners the test operations had several objectives. The collection of data on the various test article configurations was of course an important goal. Experimental measurements of the surface parameters on the spherically blunt cone and the flow field around the cone have application in the design of that class of hypersonic flight systems. And as mentioned previously, the broadening of the database for hypersonic code validation was a primary reason for the initiation of this project. Of equal importance was the further development of the nonintrusive diagnostics techniques. While the initial work on such systems can be done in the laboratory, the final proof of the applicability and utility of any of these techniques must come from demonstrations in an actual test facility. For AEDC there was a further goal of gaining increased experience in the operation of the FPST and improving the hardware and operating procedures.

4.1 THE FREE-PISTON SHOCK TUNNEL

4.1.1 Free-Piston Shock Tunnel Description

Referring again to Fig. 2, the designation "free-piston" shock tunnel arises from the fact that the driver of the shock tunnel is exactly that: a piston that slides freely within a tube. The motion of the piston is dictated by the pressure difference between the front and rear faces. At the start of a run, the piston is at rest at the upstream end of the driver tube. Downstream of the piston, the driver tube is charged with a light gas, typically helium, at a relatively low pressure. (In the case

of the AEDC FPST, this pressure is 3 to 7 atm. All subsequent numerical values in this paragraph apply to this facility.) A heavy metal diaphragm separates the driver tube and the shock tube. The shock tube is filled with the test gas, usually air, at a pressure of 0.3 to 1.5 atm. The shock tube is separated from the nozzle by a second diaphragm, which is typically a very thin and light material, since it is only required to hold the relatively low shock tube charge pressure. The nozzle and test section are evacuated to a very low pressure to facilitate the starting process in the nozzle. To initiate a run, pressure is applied to the rear face of the piston. This is usually done by allowing gas from a high-pressure reservoir to enter the driver tube. In the case of the AEDC FPST an explosion of gunpowder provides the piston-driving pressure. The piston travels at high velocity (240 to 500 m/sec) down the driver tube, compressing the helium. When the helium pressure reaches a certain level (which is a function of the thickness and design of the diaphragm) the diaphragm ruptures, and a strong shock wave is initiated in the shock tube. This wave travels through the test gas at speeds of 4000 m/sec or higher. This strong shock wave creates a region of higher pressure and temperature gas behind it. When the wave reaches the end of the tube, it is reflected, at the same time rupturing the secondary diaphragm, and starts back through the shock tube in the other direction. Thus it processes the test gas a second time, causing a further increase in the temperature and pressure. Pressure and temperature in the resulting region of doubly processed test gas can easily approach 2000 atm and 10,000K. This hot, high-pressure slug of gas serves as the reservoir to supply the wind tunnel nozzle. The gas expands through the nozzle into the test section and flows over the test article. The FPST technique produces the high enthalpy flows needed to represent flight at high Mach numbers. One drawback to the use of the FPST facility is that the test times are typically just a few milliseconds. This imposes some limitations on the utility of the FPST in areas such as the operability of an engine system. A few milliseconds is sufficient time, however, for fundamental research in flow-field physics. The FPST has thus become an important tool in the study of high-enthalpy flows.

The AEDC FPST differs from other such facilities around the world in two respects. It has a powder chamber at the upstream end of the driver tube, where the explosive force to drive the piston is produced. It also has a tapered high-pressure section at the downstream end of the driver tube, where the piston comes to rest after impact. All other such facilities use a high-pressure gas to drive the piston, and the piston trajectory is controlled so that it stops by gently impacting the downstream end of the driver tube. From the primary diaphragm on downstream the AEDC FPST is schematically the same as all other such facilities.

The layout of the AEDC FPST is shown in Fig. 3. The shock tube internal diameter is 7.62 cm. The conical nozzle has an 8-deg half angle and an exit diameter of 45.72 cm. Details of the test section area are shown in Fig. 4.

Because of the high energies involved, free-piston shock tunnels experience some difficulty with particles in the flow. These can be produced by erosion of the shock tube walls, particularly at the downstream end, as a result of the high pressures and temperatures generated. Also, the high-pressure diaphragm has a tendency to shed small particles (and sometimes large ones) when

it tears open. In one of the first technology exchanges in the cooperative project, DLR provided AEDC with a design concept, evolved over several years of experimentation, for a particle stopper to be placed at the downstream end of the shock tube. This device, shown in Fig. 5, prevents the larger particles generated in the diaphragm section or the shock tube from passing through the nozzle throat. This reduces potential damage to the throat, which is typically made of expensive material to withstand the severe heat and pressure loads. It also gives some protection to the model installed in the test section. It will not stop all particles immediately, since some with very small mass may blow around it and get into the test section. However, the ability to stop larger particles has been demonstrated. On the first run in the AEDC FPST following installation of the stopper, a relatively large (about 25-mm square) piece of metal shim tore loose from the diaphragm section and impacted the stopper. Without the stopper in place there would have been extensive damage to the expensive throat block.

4.1.2 Free-Piston Shock Tunnel Operation

The AEDC FPST was designed to operate in the mode of a two-stage light-gas gun, in which the piston is sacrificed on each shot by allowing it to impact the high-pressure section. This choice was made with the background of 30 years' experience in the operation of light-gas guns at AEDC. This choice was also dictated by the desire to provide a dual-mode facility: an FPST and a light-gas gun hypervelocity impact ballistics range. The FPST shock tube, nozzle, and test section can be removed and replaced with the launcher of a light-gas gun. In this mode the facility is used for impact testing, which is an important part of the gun range test work at AEDC. From the powder chamber through the high-pressure section, the components are common between the FPST and the impact facility.

A general problem in the operation of a free-piston shock tunnel is the control of the piston travel. If the piston energy is too low, it will be travelling too slowly at the end of its flight and the pressure buildup at the end of the driver tube can cause the piston to rebound. The result will be less than optimum test conditions in the shock tube. If the piston is traveling too fast, it will not stop properly at the end of the driver. For all such facilities except the AEDC FPST, the impact of the piston at the end wall of the driver can result in serious damage to the piston or the driver tube or both. The AEDC FPST piston is made with a plastic outer shell around an inner metal one to provide the required mass. The operation of the facility is designed such that the shell is destroyed on each run by impact with the high-pressure section.

During the initial operation of the AEDC FPST, the heavy internal mass of the piston was made of lead. The lead was much softer than the steel of the high-pressure section; thus when the piston was wedged into that section at the end of its travel, the lead deformed—and piston removal was generally accomplished without much difficulty. This provided some margin of safety when the amount of gunpowder to use for a particular desired shot condition was determined. It was possible to err on the side of over-driving the piston, thus to be sure there was no bounce back. The lead portion of the spent piston was reclaimed and recycled. However, follow-

ing the initial shakedown tests, there were discussions about the possibility of contamination from the lead insert, and because of environmental concerns, the lead component was changed to steel. The tests under this project were the first to be conducted with the new piston design. On the first shot the piston was wedged into the high-pressure section as usual. However, although the steel did deform somewhat, it did not deform as much as did the soft lead. Consequently, the insert essentially welded itself to the inner wall of the high-pressure section. The usual techniques for removing it were unsuccessful, and eventually the entire high-pressure section (19 tons) had to be removed from the facility and taken to the machine shop, where the piston was cut out. After the piston was cut from the high-pressure section, an analysis of the inner steel material showed that it had not been properly heat treated. This error was corrected for all subsequent runs, and there were no further stuck piston problems. The properly heat-treated steel insert can be reused. However, the cost in time and resources to accomplish this piston redevelopment had a serious impact on the planned test program in the AEDC FPST. In the end, only the spherically blunt slender cone configuration was tested at AEDC.

4.1.3 Free-Piston Shock Tunnel Data Acquisition System

Outputs from the tunnel and model transducers were recorded on Norland[®] IQ-300 and LeCroy[®] Model 6810 transient recorders. The channels of these recorders were set at different sensitivities to provide adequate recording ranges for the estimated signal strengths. Specific sampling rates of the recorders were 10 MHz for the IQ-300 and 5 MHz for the 6810. Both machines have twelve-bit resolution. The IQ-300 stores the acquired data on a floppy disk that may be used with a personal computer equipped with an analysis package to convert the data into engineering units. The LeCroy also uses floppy disk storage and is PC-controlled with commercially available software. The recorders have large data memories so that all channels can be triggered at gunpowder ignition, minimizing the possibility of improper triggers and lost data. Model pressures were measured using Kulite High-Temperature Miniature Pressure Transducers XCE-093 having a repeatability of 0.25 percent and combined nonlinearity and hysteresis of 0.5 percent full scale. Heat-transfer measurements were made with Medtherm ISA Type E (chromel-constantan) coaxial thermocouples. The uncertainty associated with heat-transfer measurement is difficult to evaluate; best estimates are ± 7 percent on the temperature measurement and ± 20 percent on the heat-transfer measurement.

4.1.4 Free-Piston Shock Tunnel Test Program

The test program in the AEDC FPST began with a short calibration phase. It was deemed prudent to include calibration tests because the facility had not been operated as an FPST for some time. Also, in the interim the configuration had been changed to an impact facility, an impact test program had been conducted, and the configuration had been changed back to the FPST. For the calibration tests, the rake shown in Fig. 6 was used. On the first run, the stuck piston problem described above occurred. Three additional calibration runs were made to verify that the facility was functioning properly.

The matrix of test conditions for the runs made in the AEDC FPST during this project is shown in Table 1. The four runs with the calibration rake were made to verify the proper operation of the facility following the reconfiguration from the impact test mode. The rake held pressure and heat-transfer probes to measure the nozzle flow-field properties. The results of these tests indicated that the facility operation and the test conditions produced were as seen during the initial calibration tests.

Following the calibration tests, six runs were made with a spherically blunt slender cone that was a 70-percent scale model of the one that had been tested in the HEG. This particular shape has the name Electre. The reduced size of the AEDC model was necessary to better accommodate the smaller AEDC FPST. A sketch of the AEDC Electre model is shown in Fig. 7. As noted in the sketch, the model was instrumented to obtain pressure (9 locations) and heat-transfer distributions (12 thermocouples) along the surface from the nose tip to the aft end. The pressure locations are depicted on the top half of the model, thermocouple locations on the bottom half. The AEDC model was designed to provide the same measurements as were obtained on the HEG model during the test program there. The test parameters for the cone runs are shown in Table 1, along with the parameters for HEG Condition III, which was the condition for the Electre tests. The range of AEDC test conditions included the HEG test conditions, although an exact match was never achieved.

4.2 HEG EXPERIMENTS

4.2.1 The HEG

The free-piston-driven shock tunnel HEG is operated as a reflected-type shock tunnel in tailored mode. The overall facility is 60 m long, and it consists of three main sections: the driver (consisting of an air buffer and a compression tube); the shock, or driven, tube; and the subsequent nozzle/test section. A discussion of HEG operation and its initial calibration is given in Ref. 6. A schematic view of the HEG is shown in Fig. 8. The HEG and the AEDC FPST are compared in Table 2.

The compression tube is separated from the adjoining shock tube by the 8- to 10-mm-thick stainless steel diaphragm. For a test in HEG using operating Condition I (see Table 3), a pressure of 5 MPa in the air buffer is utilized to accelerate a 280-kg piston down the 33-m-long compression tube. During this compression and heating of the helium driver gas, the piston reaches a maximum velocity of about 278 m/sec. When the burst pressure of the 8-mm-thick main diaphragm is reached (50 Mpa or 494 atm), the helium has been heated quasi-adiabatically to approximately 4000K. After diaphragm rupture a strong shock wave is generated and propagates down the 17-m-long shock tube. This shock wave reflects from the end wall, heating the test gas (nitrogen, air, carbon dioxide, etc.) to high-temperature, high-pressure conditions that are given in the upper part of Table 3. When this nozzle reservoir region is formed, the secondary diaphragm (a thin Mylar sheet) ruptures and the test gas expands through the 3.75-m-long convergent-

divergent nozzle. The throat and exit radius of this nozzle are 0.011 m and 0.44 m, respectively, resulting in an area ratio of 1600. The half-angle of the conical nozzle is approximately 6.5 deg.

4.2.2 Determination of Freestream Conditions

The nozzle reservoir conditions (see Table 3) are determined by using the shock tube filling pressure, p_1 (24 kPa for Condition I, and 50 kPa for Condition III), measuring the incident shock wave speed, u_s , and the reservoir pressure, p_0 , and then calculating the shock tube flow using the chemical and thermal equilibrium code ESTC (see Refs. 6 and 7). The shock speed u_s is determined by five ionization gages along the shock tube. Knowing the distance between the ionization gages, the shock speed along the shock tube can be calculated using the points in time recorded when the shock passes each gage. The nozzle reservoir pressure, p_0 , is measured by two transducers, one 6205A Kistler and one Kulite HKS 375M, located in the shock tube end wall. These transducers have an operating range of 0 to 6000 bar, with an accuracy of more than 99 percent. For the determination of the reservoir conditions the average shock speed evaluated between gages 3 and 4 and gages 4 and 5 is used.

As described in Ref. 8, the characterization of the freestream flow in HEG is a combined effort of classical and newly developed measurement techniques and CFD. The nozzle reservoir pressure and temperature are used as input for the DLR Navier-Stokes code, CEVCATS-N, which is used to compute the nonequilibrium nozzle flow. Nominal freestream conditions generated in the HEG test section for operating Conditions I through IV are summarized in the lower part of Table 3.

In high enthalpy testing involving dissociation reactions behind the bow shock wave, the similarity parameter, ρL , must be duplicated in wind tunnel experiments in order to generate similar dissociation relaxation processes in both free flight and ground testing. The high reservoir pressure of approximately 100 MPa causes more severe ablation processes in the nozzle reservoir for Conditions II and IV than for the lower pressure Conditions I and III. Therefore, the majority of tests in HEG are performed using operating Conditions I and III, and consequently a more detailed knowledge of the freestream flow conditions is available for these conditions.

Permanent probes are installed within the test section to monitor the flow conditions during each individual run. The pitot pressure, p_{t2} , and the stagnation point heat-transfer rate, q_{t2} , as well as the heat-transfer rate at 45 and 90 deg from the stagnation point are measured on spheres of diameter 15 and 20 mm, respectively. The sensor used in the pitot probe is a Kulite[®] XCS-062-1.7-bar transducer with an operating range of 0 to 1.7 bar with a full-scale error of 1 percent, and the heat-transfer probe is equipped with ONERA chromel[®]-constantan[®] thermocouples. During the test time window, the axial locations of the stagnation point heat-transfer rate probe and the pitot pressure probe are approximately 140 mm and 162 mm, respectively, behind the nozzle exit. Both probes are located within the core flow at the same radial distance of 200 mm from the nozzle axis. A third permanent probe is used to measure the static pressure (Ref. 9) 131 mm down-

stream of the nozzle exit. The measurement of the temporal development of static pressure in conjunction with the measurement of the pitot pressure and the reservoir pressure is used in HEG not only to monitor the repeatability of test conditions, but also to determine the available test time window. For Conditions I and III, this test time is limited by the starting process of the nozzle flow and the flow past the model as well as by the arrival of helium driver gas in the test section. For operating Condition I, a sleeve is mounted at the end of the shock tube to prevent early driver gas contamination of the test section flow (Ref. 8). The total available test time depends on the operating condition, and it amounts to approximately one millisecond.

4.2.3 Experimental Setup for HEG Test Programs

4.2.3.1 Data Acquisition System

The output of the model sensors, permanent probe sensors, and tunnel sensors was amplified by a bridge amplifier and was acquired with a transient recorder (Eckelmann Industrieautomation TRC 6510) at a sampling rate of 1 MHz, 12-bit depth. A total of 72 data channels are available. The data acquisition was triggered by the shock passing the first ionization gage in the shock tube. The output voltage of the thermocouples was amplified by a factor of 100. Depending on the pressure sensor type and the pressure level to be measured, the power supply was ± 2.5 V up to ± 7.5 V. The output voltage was amplified by a factor of 10 to 1000.

4.2.3.2 HEG Test Articles

Shock interaction tests were done with a double ramp model, shown in Fig. 9. The ramp was equipped with pressure transducers and flush-mounted thermocouples for pressure and heat-transfer distribution measurements. The positions of the sensors are also shown in Fig. 9. There are pressure transducers from Kulite XCS-093 that vary in resolution from 350 to 3500 mbar. They are mounted underneath the surface protected with a heat shield. The holes through which the surface pressure is measured are 0.9 mm in diameter. The cavity slows down the response time, but the system is still fast enough to measure pressure until a steady flow is achieved. The thermocouples are from Medtherm and are fixed into the surface. After installation they are ground to fit the surface exactly. The Electre slender cone model used in the HEG was the full-scale version of the AEDC FPST model shown in Fig. 7. Measurement locations were proportionally the same, and Kulite and Medtherm transducers were also used in this model.

4.2.3.3 Optical Setup for the Double Ramp Model

Primary data for the shock interaction tests came from high-speed photographs. The flow visualization was performed by setting up a schlieren and shadowgraph system, which is shown in Fig. 10. The system is designed for obtaining temporally resolved images of the flow. It consists of a high pulse rate copper vapor laser capable of producing repetition rates up to 50 kHz, together with its companion rotating drum streak camera. While the drum camera is actually a streak camera, the narrow pulse width of the laser performs a pseudoframing function. The setup

uses a Z-path schlieren layout with spherical mirrors having a 1500-mm focal length. The copper vapor laser green line (510 nm) initially was used for visualization purposes, but this led to problems. It was found that the hot copper vapor located behind shocks in the core flow caused strong absorption of the light from the corresponding laser transition of the copper vapor laser, and the result was that some areas had no exposure on the film. To counteract this problem a dye laser was used to shift the wavelength from 510 to 671 nm. This solved the problem, but unfortunately it restricted the experiments to a maximum frequency of 15 kHz for the system and it introduced a reduction in picture quality.

4.2.3.4 Test Matrix for the HEG Test Programs

Table 4 shows the experiments with the double ramp model. Listed in the table are the Run ID for the HEG Experiment and the test type (e.g., condition) as well as the angles used for the ramp. For the tunnel data, the absolute time when the shock is reflected upon the end wall is listed. This time is relative to the tunnel trigger and is always used as the zero point. This means that all other time values are relative to this value (SR). The time lag (TL) defines the time until startup of the flow in the test section. The test gas needs approximately 0.7 msec to travel down the nozzle.

P_0 gives the stagnation value of the tunnel, and p_{t2} the pitot pressure from the permanent probe in the test section. Also listed in the table are the mean values for all runs. They are 45.6 MPa for condition III and 38 MPa for condition I. Since there was no opportunity for conducting double ramp tests at AEDC, there could be no comparison of data between the two tunnels for this configuration.

Test conditions for the HEG Electre tests are shown in Table 5. The results of these tests were compared with the AEDC Electre tests, and this comparison and the results are discussed in Section 5.

4.2.3.5 Double Ramp Test Results

This section presents some results of the experiments which have been performed for initial ramp angles $\Theta = 15$ and 20 deg (see Fig. 9 for nomenclature). Figure 11 shows four frames from HEG run 453 that make the establishment of the separation visible. The time interval between frames is $\delta t = 0.6$ msec.

As seen in Fig. 11, the establishment of the separation bubble is a time-dependent mechanism. To give further insight into this process, the development of the separation length on the first ramp, L_u , was measured from the film. The result is shown in Fig. 12.

The measurement of the development of L_u over time gives an aid in deciding at what time to measure the length L_u . Figure 12 shows a measurement for HEG condition III, run 453, which is the low enthalpy condition, with 12.9 MJ/kg. The angles are $\Theta = 15$ deg and $\Theta_w = 35$ deg. The

pitot pressure is also plotted as a function of time. On first view the development of L_u comes to a stationary value after $t = 2.5$ msec. On the other hand it can be seen that the pitot pressure starts to decrease at that time. If the development of L_u is compared with the static pressure, which is shown in Fig. 13, it is clear that the static pressure has its stationary value around $t = 1.9$ msec (labeled point B). Here, L_u forms a first plateau (P_1) when the static pressure is still in its development (point A). When the static pressure arrives at point B, L_u starts to rise again until it reaches the second plateau (P_2). There seems to be a little time delay between the beginning of rising L_u and the maximum (B) of the static pressure. This time delay should originate from the static pressure probe itself, which produces a time delay because of its construction.

It can be shown here that for the different HEG conditions, the driver gas contamination starts at different points in time. Further details about this can be found in Ref. 10. For run 453, the arrival time of He in the test section is found to be around $t = 2.8$ msec, at which time the steadiness of L_u is destroyed. The arrival of He in the test section for the high enthalpy condition I is generally earlier in time. To compare the two conditions for air flow, it was decided to use a test time window in between $t = 1.8$ and 1.9 msec, on the assumption that the changes in L_u follow the changes in the freestream conditions in a quasi-steady manner. In this way it is possible to compare conditions I and III at a point where driver gas contamination has not yet affected the results and the measured freestream parameters stagnation and static pressure, both indicating good freestream conditions. The term “good freestream condition” is used here in the sense that the values agree with the numerically predicted values that are obtained utilizing nozzle reservoir conditions.

Figure 14 shows the measured values of L_u normalized with the length of the first plate and are for an incident angle $\Theta = 15$ deg. The results of Ref. 11 are compared with the HEG results in Fig. 14. The low enthalpy case (B3) and high enthalpy case (C3) approximately match the HEG run conditions I and III, respectively. It has to be stated, though, that the experiments of Ref. 11 were performed with N_2 as a test gas. The tendency of increasing L_{sep} or increasing L_u with Θ_w is a well-established result.

The discrepancy for the HEG test series between the high and low enthalpy cases is visible. The high enthalpy case decreases L_u slightly, when comparing the above-mentioned quasi steady state. A clear tendency in the data from Ref. 11 for N_2 is not visible. The driving force for the decrease in L_u , which is caused by higher enthalpy, is the dissociation behind the leading-edge shock, which is higher for air than for N_2 , together with the process of recombination. In Ref. 11 one can find measurements at higher angles of attack, where the difference in L_u can be seen more clearly.

5.0 COMPUTATIONAL FLUID DYNAMICS AND COMPARISON WITH TUNNEL DATA

A primary utility of free piston shock tunnels is to obtain data that can be used to validate CFD codes for application to high-energy flows. Such codes will be required in the design and development of high Mach number flight systems, since the flight conditions for such systems often exceed the capability of ground test facilities. To successfully develop such systems, advanced CFD codes must be used in conjunction with the limited ground test data. The development and validation of these codes is thus the key to future procurement of advanced high Mach number flight vehicles. Data and code comparisons from the AEDC FPST (Ref. 12) and the DLR HEG (Ref. 13) have been reported in a number of publications. However, sharing test information from the HEG and the AEDC FPST provided DLR and AEDC with a larger database to use in evaluating and validating CFD codes. The cooperation also allowed for comparing the results from the different codes used by each institution.

5.1 CODES EMPLOYED

One of the principal CFD codes that has been used in the analysis of data from the AEDC FPST is the three-dimensional, thin-layer Navier-Stokes code TUFF (Ref. 14 and 15), developed at NASA Ames. This code solves the strongly coupled species conservation equations and fluid dynamic equations in a finite-volume framework. A time-marching algorithm is used in conjunction with total variation diminishing (TVD) techniques to obtain an asymptotic, steady-state solution. The code has been used in a quasi-one-dimensional form to compute flow in the AEDC FPST nozzle and to predict conditions at the nozzle exit. Two-dimensional axisymmetric computations are subsequently carried out about the blunt-nosed model. The nonequilibrium chemistry model contained in the code is five-species air (O, O₂, NO, N, N₂) with electrons contributed from the ionization of NO. The gas is assumed to be in thermal equilibrium; i. e., the gas can be characterized by a single temperature. The code contains two turbulence models (a Baldwin-Lomax model and a K- ϵ model) in addition to the laminar flow model.

It is generally accepted that the most sophisticated nonequilibrium radiation solver available is NEQAIR (Ref. 16). Generally, it is too costly in terms of computational resources to couple NEQAIR directly to a CFD flow solver; hence, some simpler approach is preferred. The simplest approach is to use NEQAIR in conjunction with some appropriate CFD flow solver in an uncoupled fashion. As a middle-of-the-road approach, radiation codes employing simplifying assumptions (such as LORAN and NOVAR) have been developed (Ref. 17). Also, these radiation codes were coupled with the flow solvers LAURA (Ref. 17) and GIANTS (Ref. 17), respectively. Radiative transport effects have been incorporated into a number of different flow solvers using various simplifying assumptions. Multitemperature models are frequently simplified to a two-temperature model by assuming that the translational and rotational temperatures are in equilibrium and that a single vibrational temperature can be used to describe all the diatomic species. Further, it is usually assumed that the electron temperature is in equilibrium with the vibrational temperature. These

assumptions constitute a minimum acceptable model (Ref. 17) for a CFD code even if the radiation solver is uncoupled. Four additional flow solvers considered and which satisfy these criteria are GASP, NEDANA, GPACT, and NSHYP.

GASP (Ref. 18) is a three-dimensional, finite-volume flow solver and contains options for the Roe or van Leer upwind schemes. GASP solves the integral form of the fluid dynamic equations, including the full Reynolds-averaged Navier-Stokes, thin-layer, parabolized or Euler equations. GASP contains a generalized chemistry model as well as a two-temperature model.

NEDANA (Ref. 19) employs a three-dimensional, locally implicit algorithm for the solution of the thin-layer Navier-Stokes equations expanded for thermochemical nonequilibrium. The numerical flux function is based on the central-difference, flux-limited, artificial dissipation model of Jameson. The scheme combines the simplicity of artificial dissipation with the total variation diminishing property. The flow solver employs the AEDC-developed chemistry package NEQPAK. NEQPAK provides the chemical, thermodynamic, and transport properties that are required to simulate the flow of a gas in thermochemical nonequilibrium. The flow solver also incorporates the Chimera domain decomposition procedure to allow for complex configurations as well as bodies in relative motion. NEDANA uses the two-temperature model of Park (Ref. 20), which characterizes a multicomponent gas by a translational-rotational temperature and a vibrational-electronic temperature.

GPACT is a computer program currently under development that has been applied towards simulating propulsion-generated flow-field phenomena. These simulations have treated fully coupled, three-dimensional flows with finite-rate chemistry. This capability is described and the results of validation studies are reported in Ref. 21. GPACT was derived from a research version of the Generalized Implicit Flow Solver, GIFS (Ref. 22). Since its inception, the GIFS computer program has been systematically and extensively modified under the joint sponsorship of the Air Force Research Laboratory and the Arnold Engineering Development Center. These changes have significantly improved the robustness, the generality of the solution algorithm, the physical model approximations, and the internal databases. This improvement has led to the evolution of the GPACT computer model. Recent efforts have been directed towards improving its overall computational efficiency, including turnaround time and computer memory requirements. Further, modification of the solution technique to strengthen the coupling of numerous physical phenomena occurring in rocket propulsion flow fields that focus on chemical kinetics and two-phase flow with phase change are also being addressed, since these phenomena can significantly impact radiant emission. The objective of future GPACT computer program enhancements is to extend the development of the model beyond the "research" level and eventually to provide an applications-oriented, CFD flow-field simulation tool for use by CFD users in the propulsion community.

The NSHYP flow solver, developed in Germany at the DLR (Ref. 23), solves the time-dependent, thin-layer, Navier-Stokes equations. The numerical algorithm is based on an implicit finite-difference scheme using line Gauss-Seidel relaxation. The resulting system of equations is

solved with the Richtmeyer algorithm. The spatial discretization is formally second order. For the inviscid fluxes a TVD upwind discretization according to Yee & Harten (Ref. 24) is employed, and the spatial derivatives of the viscous fluxes are discretized by second-order central differences. In NSHYP, Roe's approximate Riemann solver (Ref. 25) is used. For the computation of chemically reacting flows the generalized form of Roe's solver according to Liu & Vinokur (Ref. 26) is employed. Air is modeled as a chemically reacting mixture of electrically neutral perfect gases and is assumed to consist of five species, namely molecular and atomic nitrogen (N_2 , N), and oxygen (O_2 , O), and nitric oxide (NO). The chemical reaction rates are taken from Park (Ref. 20). The determination of the vibrational energy of the molecular species is based on the assumption of a harmonic oscillator. The transition of energy between the vibrational modes and the translational modes is approximated using the Landau-Teller formulation. The vibrational relaxation times are obtained from correlations of Millikan & White and Park, and the vibration dissociation coupling according to Park is used. The physical domain considered in the current study is bounded by the body, the inflow and outflow boundaries, and the line of symmetry. On the body, no-slip conditions are applied. The temperature of the fully catalytic, isothermal wall is set to $T_{\text{wall}} = 300\text{K}$. At the inflow boundary, a homogenous hypersonic flow is assumed. At the outflow boundary, the conservative variables are extrapolated from the integration domain by assuming that their slopes in the downstream direction are constant. In order to compute axisymmetric flows with the present 3D flow solver, appropriate symmetry conditions are employed to evaluate the fluxes in the circumferential direction. At the line of symmetry, which for axisymmetric flows represents a singularity, the variables are determined by means of a cubic extrapolation.

The NSHYP code has been largely replaced by the new code CEVCATS-N at DLR. The CEVCATS-N code used at HEG solves the full Navier-Stokes equations in integral form for mixtures of perfect and reacting gases. Thermochemical equilibrium and nonequilibrium are solved with a numerical scheme consisting of hybrid upwind flux vector splitting and use of a five-stage Runge-Kutta scheme for time integration (Ref. 27). Local time stepping, implicit residual averaging, and full multigrid are used to accelerate the convergence process. Viscosity is computed with Sutherland's formula for perfect gases and with Blottner curve fits for reacting gases. The chemical model contains (but is not restricted to) five species. Boundary conditions on the wall allow different temperatures (adiabatic, prescribed, or equilibrium). The influence of catalytic effects can also be included. Several tools are used for generation of the structured grids. The computational performance on a NEC SX4/4 (single processor) is about 1.1 GFLOPS. No results from this code are presented here.

5.2 TUNNEL COMPARISONS

5.2.1 Heat-Transfer Data Reduction

Heat-transfer measurement in high enthalpy facilities, where the heat-transfer rates are large and run times are limited, is often accomplished with a transducer that measures surface temperature as a function of time. A coaxial thermocouple gage has sufficiently fast response for a facility

with millisecond test times. Once the surface temperature-time history has been acquired, semi-infinite body theory is used to infer the heat transfer. The method used at AEDC is a “direct” method that can be traced to Ref. 28. This method involves differentiation and then integration. Since some noise is bound to be present in the experimental data, a special smoothing routine has been incorporated. The method used by DLR is an “indirect” method that involves integration and then differentiation (Ref. 29). A natural smoothing is invoked since the integration is done first. Both methods were applied to typical HEG data, and the results are compared in Fig. 15. The methods yield very similar results. However, it is noted that the indirect method (DLR) does a better job of preserving the details without allowing the noise to dominate.

5.2.2 Spectral Predictions - NEQAIR

The NEQAIR code (Ref. 16) was activated and is available for use at AEDC. A spectrum was computed for an HEG run condition for which a measured spectrum was available. The computed and measured spectra (Fig. 16) indicate that significant emission from contaminants other than air is definitely present. Also shown in Fig. 16 is the emission for Fe for 6000K. It is likely that at least part of the contamination is caused by Fe. It must be concluded that too much contamination is present to allow direct interpretation of HEG (or AEDC) emission spectra. Nevertheless, NEQAIR may prove useful when searching for areas of the spectrum where specific techniques might successfully be applied.

5.3 PREDICTION OF FREESTREAM CONDITIONS

Considerable effort has been expended to define the freestream conditions produced at the nozzle exit (i.e., the entrance to the test section) of the AEDC FPST (Ref. 12) and the DLR HEG (Ref. 13). At AEDC it was discovered that a previously used flow solver, NEDANA, gave a significantly different prediction of vibrational temperature at the nozzle exit when compared to a currently used flow solver, GASP (see Fig. 17). It is noted from Fig. 17 that the vibrational temperature ‘freezes’ early in the nozzle, as is typical of hypersonic nozzles fed from a reservoir. However, the two flow solvers’ predictions of nozzle exit vibrational temperature level (T_v) differ by approximately 900K. The corresponding difference in the translational temperature, T_{tr} , is 70K. Differences of this magnitude in T_v can cause considerable uncertainty in the determination of freestream conditions. In some of the diagnostic techniques presented in Section 6 of this report, the value of T_v must be known before T_{tr} can be computed, or vice versa. Or, alternatively, one must be able to predict the ratio of T_v/T_{tr} with some degree of certainty for the technique to be useful.

5.3.1 Boundary-Layer Effects

Boundary-layer effects are more important in the HEG nozzle than in the AEDC FPST nozzle because the HEG nozzle is physically larger than the AEDC nozzle. During early analysis work at DLR using a Euler code combined with a boundary-layer code, it was found that the boundary-layer transition point was critical for proper interpretation of the results. TUFF solutions were carried out

without accounting for the boundary layer. GASP solutions did account for the boundary layer; in most cases transition was assumed to occur quite early in the nozzle expansion.

5.3.2 Chemical Species Prediction

The chemical species predicted at the nozzle exit plane are shown in Table 5 for HEG conditions I and III and in Table 6 for the typical AEDC FPST run conditions of Runs 16 and 30. It is noted that the species predictions are relatively insensitive to the temperature model (1-T vs. 2-T), and the predictions of the various codes agree relatively well.

5.3.3 Temperature Prediction

Freestream temperature predictions are shown in Table 5 for HEG conditions I and III and for the typical AEDC FPST run conditions of Runs 16 and 30 in Table 6. Predictions made with one temperature (1-T) and two temperature (2-T) codes are shown. Conventional wisdom would lead one to expect some vibrational nonequilibrium, especially at the higher Mach numbers in HEG, thus requiring a 2-T model. DLR calculations with a 2-T code, NSHYP, yield a translational temperature, T_{tr} , of about 800K and vibrational temperatures of 3818K for nitrogen and 2146K for oxygen. The GASP code (calculations performed at AEDC) predicts $T_{tr} = 1176K$ and $T_v = 3400K$ for HEG condition I. This code lumps the oxygen and nitrogen vibrational temperatures together; considering this, the results are in reasonable agreement. However, it is known that flow contaminants can enhance vibrational relaxation and result in thermal equilibrium for conditions where it would not normally be expected. Since some contamination exists in both the HEG and the AEDC FPST, this effect is certainly possible in either facility. Recent DLR experimental results are more consistent with the assumption of thermal equilibrium all the way to the nozzle exit. Assuming thermal equilibrium, NSHYP predicts a temperature of 1144K for condition I and 806K for condition III. The TUFF code (1-T) predicts a temperature of 1011K for condition I and 744K for condition III. This is reasonable agreement with NSHYP in spite of the fact that the TUFF solution was a simple 1-D solution neglecting the boundary layer. A direct measurement of the vibrational temperature will be required to definitively determine whether any vibrational nonequilibrium exists.

The freestream temperatures for the typical AEDC FPST run condition (Run 16 and 30) (see Table 6) is predicted to be 957K by the TUFF code (1-T). The 2-T code predictions are $T_{tr} = 800K$, $T_v = 2250K$ from NEDANA, and $T_{tr} = 708K$, $T_v = 2858K$ from GASP. It is shown in the diagnostics section of this report that the 2-T models yield the most reasonable predictions for these cases. Concern over the significant difference between the T_v predictions by NEDANA and GASP (~600K) lead to the code validation effort described in the following section.

5.4 CODE VALIDATION

5.4.1 Fire II Data

A code validation exercise was carried out utilizing the flight test data from Project Fire II (Ref. 17). This involves a direct comparison of the GIANTS, LAURA, and GASP flow solvers.

A general validation of the GIANTS, LAURA, and GASP flow solvers was attempted by comparing them with the Fire II data at 1634 sec. The translational temperature, T_{tr} , and the vibrational temperature, T_v , are shown in Fig. 18 (flow is from left to right). It can be seen that the GASP results match reasonably well with the GIANTS results. The LAURA flow solver, however, predicts a considerably larger translational temperature through the shock layer. All three flow solvers predict temperature equilibrium midway between the shock and the body. In addition, the predicted species number density for the nitrogen species is shown in Fig. 19. The LAURA flow-solver predictions differ somewhat from the others through the shock layer. Behind the shock, excellent agreement is shown between the species number densities predicted by the GASP, GIANTS, and LAURA flow solvers. Finally, the computed stagnation point heat-transfer rates for the Fire II configuration at 1634 seconds into the flight are compared to the measured stagnation point heat-transfer rate in Table 7. Reasonable agreement is noted, with the GIANTS flow solver prediction differing the most from the experimental value.

5.4.2 HEG and FPST

The other cases considered involve ground test conditions produced by free-piston shock tunnel facilities in the U.S. (AEDC) and Germany (DLR). The NEDANA, GASP, and GPACK flow solvers are used for the AEDC facility conditions, and the GASP and NSHYP flow solvers are used for the DLR facility conditions. The flow conditions for each case are listed in Tables 5 and 6.

In Figs. 20 and 21 the predictions of the various flow solvers are compared for the AEDC Impulse Tunnel Run 30 condition and for the HEG condition I, respectively. The flow was computed through the nozzle of the AEDC Free-Piston Shock Tunnel (nozzle exit Mach number approximately 6.5) and over a sphere-cone model. The centerline shock-layer temperature distributions are shown in Fig. 20. The GASP and GPACK codes produce very nearly the same result at the nozzle exit while NEDANA (as shown in Fig. 17) differs. This is true even though both codes employ nonequilibrium chemistry and two-temperature models. NEDANA also predicts a slightly higher translational temperature through the shock layer. A second case with similar geometry but higher Mach number, approximately 8.2, was computed for the German free-piston shock tunnel HEG Condition I. The temperatures predicted by the NSHYP flow solver are compared to those predicted by GASP in Fig. 21. The NSHYP code has separate characteristic vibrational temperatures for N_2 and O_2 . Allowing for this difference, it appears the two codes predict very similar results.

It has been noted above that the vibrational temperature predicted, measured, or assumed at the facility nozzle exit can have a significant effect on the determination of the flow properties at

that point. This can be seen in the PLIF-NO T_{tr} measurements in the FPST shown in Table 8 and reported in Ref. 30. In order to do the data reduction, T_v must be known or related to T_{tr} . If it is assumed that $T_{tr} = T_v$ in the data reduction routine, then the measured static translational temperature, T_{tr} , is computed to be in the 300 to 400K range and is much lower than that computed with a single temperature flow solver. If the vibrational temperature computed by GASP, $T_v = 3000K$, is used in the data reduction, the computed translational temperature, T_{tr} , is in the range from 600 to 700K, which is in much better agreement with the translational temperature predicted with a two-temperature flow solver such as GASP.

5.5 PREDICTION OF MODEL PARAMETERS

5.5.1 Shock Location

5.5.1.1 Baseline

To establish a data comparison baseline for shock shape, data were analyzed for AEDC Runs 31, 34, and 35, for which the model was a 70-percent scale version of the DLR Electre model. The shock shape was predicted with the TUFF code and compared to the data for Runs 31 and 34 in Figs. 22 and 23, respectively. Agreement is seen to be satisfactory.

5.5.1.2 He Arrival Detection

Run 35 was selected for a more detailed analysis. Shock shapes taken from various camera frames (which can be related to elapsed time) are shown in Fig. 24. For low He percentage, the change in the shock standoff distance with He arrival is quite weak at the stagnation point; however, the sensitivity is greater for the oblique shock on the aftbody. Three locations ($x/r = 2, 3,$ and 5) were selected at which to measure the shock location. These measurements are shown in Fig. 25 as a function of time (referenced to the reservoir pressure jump). The first visible shock is observed at 0.7 msec, indicating the initiation of the flow field about the model. The shock shape remains relatively stable until 3 msec, when a shape change occurs, presumably caused by He arrival. The magnitude of the change is consistent with that predicted by the TUFF CFD code. The shock shape data indicates that He arrival is spread over the 3.0- to 3.3-msec time increment. The facility code predicts He arrival within this band, at 3.15 msec. Other He arrival indicators (Section 6.2.5) are consistent with these results.

5.5.2 Pressure

The data acquired on the blunt cone in the DLR HEG and the AEDC FPST were compared with predictions made with the TUFF, GASP, and GPACK codes. TUFF is a one-temperature code, while GASP and GPACK are two-temperature codes. The pressure coefficient predictions are not sensitive to run conditions, indicating that 'real gas' effects are not significant for pressure prediction on this model.

5.5.2.1 AEDC Cone

Pressure coefficient data for the 70-percent Electre model in the AEDC FPST, Runs 30 to 35, are shown in Fig. 26. Data were obtained for the two pressure ports nearest the stagnation point only for Run 30. Subsequent to Run 30 these two gages either were destroyed or yielded unreliable results. All three codes do a reasonable job of predicting the pressure on the forebody. The two-temperature codes predict a somewhat lower pressure on the aftbody; the two predictions tend to bracket the data.

5.5.2.2 DLR Cone (Electre)

Pressure coefficient data for the DLR Electre model in the HEG are shown in Fig. 27. Again, the TUFF predictions are independent of run condition. If the standard HEG freestream condition is used as the starting point instead of the reservoir conditions, a slight difference is noted on the rear portion of the aftbody. Good general agreement is noted.

5.5.3 Heat Transfer

Heat-transfer predictions using TUFF agreed better with the AEDC data when a catalytic wall was assumed. The HEG data tended to be catalytic at the stagnation point, but less so on the aftbody.

5.5.3.1 AEDC Cone

Heat-transfer calculations for Run 30 using the TUFF code and assuming both catalytic and noncatalytic wall are shown in Fig. 28. It can be seen that the catalytic calculation agrees much better with the data than does the noncatalytic. Thus, the catalytic wall assumption was used in all subsequent calculations. Computed Stanton numbers are compared with the data from AEDC Runs 30 to 35 in Fig. 29. Real gas effects, which are not removed by forming the Stanton number, are evident. The predictions are seen to be in reasonable agreement with the data.

5.5.3.2 DLR Cone (Electre)

Heat-transfer calculations for HEG Runs 110 to 119 made with the TUFF code and assuming catalytic wall are shown in Fig. 30. On the forebody, the catalytic wall assumption gives reasonable agreement with the data. At the shoulder and beyond, the wall may tend to become somewhat noncatalytic since the data are consistently lower than the catalytic predictions.

5.6 CFD ACCOMPLISHMENTS

This project has allowed AEDC and DLR to exercise their CFD capabilities in the hypersonics arena and, in addition, develop new capabilities. It was also an opportunity to acquire new data for code validation, as well as an opportunity to reexamine existing data.

The exchange of raw and reduced data allowed for the validation of data reduction techniques. This was especially valuable in the case of heat transfer, which involves considerable calculation. It was found that the AEDC and DLR methods agreed well, but it is noted that the DLR “indirect” method captured the details without the artificial smoothing required by the AEDC “direct” method.

AEDC acquired new CFD capabilities in the course of this effort. The NEQAIR code was acquired and installed at AEDC. Even though it was discovered that the contaminants present in the AEDC FPST or the HEG make direct comparisons between prediction and data nearly impossible, the acquisition of NEQAIR is a significant capability, which will be useful in the future.

In the course of this effort AEDC personnel gained valuable experience in the use and development of two-temperature flow codes. Hypersonic nozzles are typically susceptible to nonequilibrium effects, one of which is the freezing of the vibrational energy modes at a point somewhat in excess of Mach 2. Since the nozzles involved here are in the Mach 6 to 9 range, one would expect the effect to be present. Since the level of vibrational temperature, T_v , predicted at the nozzle exit varied from code to code, an attempt was made to compare the various codes for a benchmark case.

5.7 CFD SUMMARY

This project has provided an opportunity for AEDC and DLR to compare the various flow codes at their disposal with respect to their underlying assumptions and algorithms as well as the results that they produce. New capability has been established (e.g., the NEQAIR code has been acquired and is operational at AEDC) and has been applied to conditions typical of the AEDC FPST and the DLR HEG. The code can provide useful insight even though flow contaminants render direct data comparison impossible. Data reduction codes have been compared and found to give very similar results. The “indirect” heat-transfer method used by DLR was seen to have some advantages and has potential applicability at AEDC.

The prediction of freestream conditions is nontrivial in a FPST. One of the main areas of uncertainty is the determination of the vibrational temperature. A number of recent indirect measurements and CFD predictions at the DLR HEG indicate that the vibrational temperature, T_v , is in equilibrium with the gas temperature, T_g , at the nozzle exit at Mach 9. Historical evidence gathered at AEDC and other facilities throughout the world indicates that significant vibrational temperature nonequilibrium ($T_v \gg T_g$) should exist at this Mach number level. However, other historical evidence obtained at AEDC in Tunnels F and C shows that contamination (water vapor, in these particular cases, by some as yet undetermined mechanism) can cause the vibrational temperature to return to equilibrium. This problem is one of fundamental importance to high enthalpy, hypersonic ground test facilities, and might be addressed with the pulsed electron beam fluorescence technique (PEBF) to aid in the determination of helium arrival concentration at the end of the facility run time and to provide a direct measurement of the vibrational temperature.

It was found that model parameters could be reasonably predicted with conventional CFD codes. For example, shock wave location can be predicted quite reliably. When used in conjunction with high-speed flow visualization, the observed change in shock shape can be correlated with He arrival. Pressure distributions were reasonably well predicted. It was observed that pressure is relatively insensitive to “real gas” effects. Heat transfer, on the other hand, was found to be sensitive to “real gas” effects. The assumption of a catalytic wall gave a better prediction than that of a noncatalytic wall. Predictions of heat transfer would generally be considered adequate.

6.0 NONINTRUSIVE DIAGNOSTICS

6.1 INTRODUCTION

6.1.1 Background

The utility of free-piston shock tunnels in obtaining data for the validation of CFD codes for the hypersonic regime is dependent on the development of a group of nonintrusive diagnostic techniques. The critical nature of advanced instrumentation for hypersonics research, and the current deficiencies in this area, were made clear during the NATO Advanced Research Workshop on "New Trends in Instrumentation for Hypersonics Research," held in the spring of 1992 at ONERA Le Fauga-Mauzac, France. Many NATO countries are pursuing the same types of diagnostic techniques at significant levels of investment, but with somewhat different methods of application, calibration, and analysis. This cooperative effort provided an opportunity to reduce the costs and time of development of advanced instrumentation. This will lead to a commonality of calibration sources and methods, common procedures for data uncertainty analysis and reporting, and benchmark experiments for evaluating new diagnostic techniques. Activities at the DLR in Göttingen and at AEDC include several areas for such cooperation. Techniques called filtered Rayleigh scattering (FILRAY) and laser diode absorption (LDA) have been applied to measure test gas contamination in the FPST at AEDC and at the HEG, respectively. Other diagnostic techniques, such as planar laser-induced fluorescence (PLIF) and nonabsorptive laser beam transmission (LBT), are being used at both AEDC and the HEG facility. However, different laser systems and data reduction techniques have been developed at the different facilities. This provided another opportunity to exchange systems and obtain comparative data.

The high enthalpy and short test times of the FPST present a significant challenge in making the desired measurements of freestream and model flow-field and surface conditions. Furthermore, the range of freestream static temperature (400 to 3000K) and molecular number density (3×10^{16} molecules/cm³ to 9×10^{16} molecules/cm³) also limit the types of techniques that are applicable and challenge the dynamic range of the measurement system. However, nonintrusive diagnostic techniques offer the potential for obtaining much of the needed information, and a number of these techniques have been in the development process for many years.

6.1.2 Information Potential and Techniques

An integral part of this program was an ambitious plan for the use of nonintrusive diagnostics to provide key information about the flow field. The requirements for NID are to provide multiple, independent measurements to yield information about run time, thermal nonequilibrium, spatial variations of flow properties, flow temporal evolution, and particulate contamination. Numerous NID techniques in various stages of development were considered for application at the AEDC Impulse Facility and the DLR HEG. Some of these techniques are listed in Tables 9 and 10. The tables also note some of the technical details of the different methods. The list of information that can potentially be provided by NID is rather lengthy and is given in Table 11. Unfortunately, cost and timeliness considerations limited the NID techniques undertaken for both the AEDC Impulse Facility and the DLR HEG to those shown in Fig. 31.

6.2 APPLICATIONS AT THE AEDC IMPULSE FACILITY

Nonabsorptive LBT and planar Mie (PMIE) scattering were used to provide information about particulate contamination and its distribution within the flow. These measurements were supplemented by witness plates (WP) to provide identification and size of deposited particulate material. Emission spectroscopy (ES) was used to identify the atomic content of particulate species in the flow as well as to monitor rubidium (Rb) seed material emission as an indicator of helium arrival. LDA was used with Rb seeding of the helium driver gas to indicate helium arrival. A crude version of FILRAY was used as another indicator of helium arrival. High-speed flow visualization (HSFV) was used to provide shadowgraph, schlieren, and holographic interferogram visualizations of the flow around the test articles. PLIF of nitric oxide (NO) was used for rotational temperature and NO concentration measurements.

The NID applications required excellent optical access, and two 30-cm-diam viewing ports at each of the 90-deg positions and one 13-cm-diam viewing port at each of the 45-deg positions provided this. The shock tube gage nearest the nozzle throat (designated ST6) provided the trigger mechanism for all NID electronics.

6.2.1 Laser Beam Transmission

No known atomic or molecular species in the ground state in the Impulse Facility should have an absorption transition at the 632.8-nm wavelength of a He-Ne laser. Therefore, any attenuation of the beam as it crosses the facility would be a result of particulate matter scattering radiation out of the beam. A chopped, 10-mw He-Ne laser beam was transmitted across the exit plane of the facility nozzle just upstream of the test article as indicated in Fig. 32. The transmitted beam passed through a 10-nm laser line filter before impinging on a PIN photodiode operated in the photoconductive mode. The PIN signal was processed in real time by a lock-in amplifier to compensate for flow-induced background light levels and detector bias. The recorded data were normalized post event to produce flow-field transmission versus time. A typical data trace overlaid with the ST6 trace is also shown in Fig. 32. The expected time delay between the peak of reservoir pressure and

the minimum in-beam transmission caused by debris from the flow starting process passing through the 160-cm-long conical nozzle is clearly observed. It is to be noted that the beam transmission stays relatively steady throughout the expected useful run time of the facility, and even into the region where helium driver gas has arrived and flow has broken down. Plots of the resultant attenuation versus time for each of the runs are given in Figs. 33 through 42. It is noted from Figs. 36 and 39 (Runs 29 and 32) that beam transmission does not fully recover, thus indicating that debris is present throughout the expected useful run time.

6.2.2 Planar Mie Scattering

Based on the Impulse Facility flow parameter predictions, it was not believed that enough copper atoms in excited states would exist in the flow freestream to provide absorption of copper vapor laser radiation at 510 nm. Therefore, a copper vapor laser system and beam-shaping optics were used to provide a 3-cm-wide sheet of radiation at a wavelength of 510 nm across the flow. The copper vapor laser output wavelengths are nominally 510 and 578 nm. The 578-nm output was used for filtered Rayleigh diagnostics that are described in another section of this report. The 510-nm radiation was selected using a beamsplitting filter that reflected the 578-nm light and transmitted the 510-nm beam. The physical setup for the application of PMIE is shown in Fig. 43. The laser sheet was transmitted across the flow at the exit plane of the conical nozzle and just upstream of the test article. The optical system was chosen such that radiation scattered from the sheet by flow molecules and particulates would be imaged from the flow centerline out into the nozzle boundary layer. The images were recorded with an intensified charge-coupled device (ICCD), a camera (384 pixels \times 576 pixels) with a gate width of 100 nsec that bracketed the laser pulse width of 40 nsec. A 510-nm, narrow-bandwidth filter was placed before the ICCD camera to eliminate stray 578-nm and other scattered radiation. Spatial dimension calibrations were performed using a rectangular grid pattern. The images were all acquired at 1.6 msec from ST6. Images similar to that shown in Fig. 43 were obtained with the laser sheet propagating across the flow in the reverse direction.

6.2.3 Witness Plates

At least one WP was used on every facility run to monitor the particulates generated by the facility flow process. The plates were electron microscope sample stubs having circular surfaces of 11-mm diameter. For particle entrapment, each plate's surface was coated with either double-sided sticky tape or a soft, conductive carbon material. The plates were mounted on the horizontal 90-deg window ledges, which kept them out of the direct and boundary-layer facility flow. Prior to each facility run, all windows and ledge areas as well as the interior of the conical nozzle were cleaned. Immediately after a facility run, the WP were collected, sealed, and transmitted to the AEDC Chemical Laboratory for analysis.

6.2.4 Emission Spectroscopy

Emission spectroscopy was used to monitor the self-radiation from the Impulse Facility flow and assist in the evaluation of the LDA technique, as shown in Fig. 44. Using a 200-mm focal length lens, radiation from the flow was imaged onto the entrance slit of a 0.275-m focal length spectrometer, and an intensified charge-coupled device (ICCD) (384 pixels \times 576 pixels) was used for detection. The system was focused using an incandescent light at the observation volume and was aligned using a HeNe laser; the slit was imaged 1 mm upstream of either the calibration rake's hemispherical probe or the nose of the test article, and at the vertical centerlines of the articles. For all runs, a 1200-groove/mm holographic grating, a central wavelength of 780 nm, and a 250- μ m entrance slit width were used. The resultant spectral resolution was approximately 1.0 nm FWHM, and the spectral range was from 765 to 795 nm. The intensifier gate width was nominally 100 μ sec. Various sampling times were used. Through pixel binning, eight 5.44-mm vertical regions for the calibration rake or eight 6.10-mm vertical regions for the test article were observed (the pixel heights were magnified 4.93x and 5.52x, respectively, onto the observation volume). This provided spectra from the bow shock region out into the freestream.

6.2.5 Laser Diode Absorption

Non-naturally occurring Rb was seeded into the Impulse Facility driver gas, and the presence of the Rb was detected with absorption spectroscopy using a tunable laser diode operating at a nominal 780.2 nm that accesses the $5S_{1/2} \rightarrow 5P_{3/2}$ transition of Rb. This technique had been previously demonstrated at the DLR/HEG (Ref. 31).

The Rb was obtained as $RbNO_3$ (rubidium nitrate) that was precisely dissolved in water to facilitate the seeding process. A precise volume of the mixture, which determined the grams of Rb seed, was applied either on the driver gas diaphragm or on the "insert wall" just upstream of the diaphragm. Rb seed levels ranged from 143 micrograms to 30 milligrams.

Prior to application at the Impulse Facility, the LDA technique was demonstrated in the AEDC laboratory shock tube/tunnel as shown in Fig. 45. The LDA system consists of a GaAlAs single-mode laser diode operating at approximately 5-mw continuous laser power. The laser is wavelength tuned across the Rb absorption transition at 780.2 nm at a 15-kHz rate by varying the laser diode current. The laser wavelength is monitored by directing a portion of the laser beam through a Rb reference cell. Absorption in both the reference cell and the test facility is monitored by silicon photodiodes, and the output is recorded on a high-speed digital oscilloscope. In the laboratory shock tube/tunnel, the laser beam path was through the shock region just in front of a small-scale model. Shown in Fig. 45 is a raw data trace from a laboratory shock tunnel run with seeding of the driver gas. The arrival of the helium driver gas is clearly shown.

Because the laser diode wavelength is being scanned in time and the amount of absorption and laser power is also a function of time, the LDA data are three-dimensional. Special software was developed for the LDA data reduction process and is presented in detail in Appendix 2.

Reduced data are presented in the formats shown in Fig. 46. The three-dimensional data are presented with laser frequency (wavelength) as the ordinate, time or scan number as the abscissa, and beam transmission value as a color scale. At any selected tunnel run time, an absorption profile can be obtained. A multiparameter fit of a spectrophysical model to this profile can yield static pressure and temperature information. By integrating the transmission over the absorption profile the arrival of the helium in the laboratory shock tunnel can be more clearly seen.

The LDA apparatus was set up at the Impulse Facility as it was for the laboratory shock tunnel. However, in this case the laser beam was directed through the test cell freestream approximately 4.5 in. (11.4 cm) below the test article tip. The operating procedure for the Impulse Facility was essentially the same as that for the shock tunnel. The RbNO_3 solution was “painted” onto the driver gas diaphragm or on the “insert wall” using a very small brush and then dried using a heat gun. Drying time was dependent on the amount of solution applied, and this time ranged from two to ten minutes. This seed insertion was done just prior to final assembly or “loading” of the Impulse Facility. The optical alignment of the laser beam through the test cell and alignment onto the absorption photodetector were verified as final evacuation of the test facility was implemented. In addition to optical alignment, the laser operating frequency and scan range were verified by monitoring the real-time absorption feature obtained from the Rb reference cell located with the laser. Adjustment of the laser frequency was accomplished with a small adjustment in the laser temperature. However, the laser frequency stability, after a 30-minute warmup, was extremely reliable and seldom, if ever, required adjustment. The only adjustment sometimes made was to ensure that the laser frequency scan was centered on the Rb absorption signal out of the Rb reference cell. Once the test area was evacuated no further adjustments were possible, as there were no remote-control systems associated with the LDA system. As noted earlier in this report, the data acquisition system consisted of a high-speed digital oscilloscope. At completion of the facility run, the data from the oscilloscope were downloaded as either an ASCII or binary file and then transferred to a PC system for plotting using standard plotting routines for initial data reduction. The data were then transferred to a workstation for more detailed analysis and presentation, as described in Appendix 2.

6.2.6 Filtered Rayleigh Scattering

The physical layout for the FILRAY application is shown in Fig. 47. The 578.2-nm beam from the copper vapor laser was brought into the Impulse Facility in a direction almost directly opposed to the general flow velocity vector in order to maximize the Doppler shift of Rayleigh-scattered radiation. The Rayleigh scattering from a point along the laser beam in the flow core was collected and imaged through a gaseous iodine filter onto a photomultiplier tube (PMT). The spectral line shape of the copper laser overlaps a number of molecular iodine transitions as shown in Fig. 47, and the use of this filter serves to prevent laser radiation scattered from test cell surfaces from reaching the PMT. When facility flow is established, the Doppler-shifted, Rayleigh-scattered light is transmitted by the iodine filter. The iodine filter was heated to 100°C in order to maintain a fully vaporized state and prevent condensation of the iodine on the filter windows. Because the Rayleigh-scattering cross section for the helium driver gas is approximately 80 times smaller than that for the test gas, the Rayleigh signal should drop steadily as the helium driver gas arrives. This

technique was successfully demonstrated in the laboratory shock tube/tunnel using an argon-ion laser output at 514.5 nm, which was a near perfect match to an iodine filter absorption line. Unfortunately, in the highly self-radiating environment of the Impulse Facility, a pulsed laser such as the copper vapor laser system had to be used. The copper vapor laser was operated at a replate of 15 kHz with pulse energy of approximately 1 mJ and a pulsewidth of 25 nsec. The PMT output was recorded using two gated integrators, each with a 200-nsec gatewidth. One integrator was centered around the laser pulse, and the other integrator recorded the background signal between the laser pulses. The gated integrator output was recorded on a digital oscilloscope. The oscilloscope was triggered by the output from a pressure transducer at the nozzle entrance.

6.2.7 High-Speed Flow Visualization

The HSFV system for obtaining temporally resolved shadowgraph, schlieren, and holographic interferometry images of the flow over the test article is shown in Figs. 48 and 49. The heart of the system is a copper vapor laser system and its companion rotating drum streak camera. The copper vapor laser can operate at a pulse rate up to 50 kHz with a pulse width of 25 nsec. The laser has a dual line output of 35 w at a 20-kHz pulse rate. The wavelengths of the outputs are 510 nm (67 percent of power) and 578 nm (33 percent of power), and the beam diameter is approximately 25 mm. The camera drum rotates at a maximum rate of 300 rps (18,000 rpm) and carries a 1.0-m length of 35-mm film. Image height (across the filmstrip) is fixed at 25 mm. Image length (along the filmstrip) can be adjusted by selecting either a 17-, 10-, or 6-mm mask, corresponding, respectively, to a maximum of 58, 100, or 166 frames per filmstrip. By choosing a laser pulse rate, mask size, and appropriate drum rpm, the user can optimize the image acquisition either toward maximum image FOV/resolution or toward time-sequence duration.

6.2.7.1 Shadowgraph/Schlieren

The shadowgraph/schlieren system utilized a 12-in. (~300-mm)-diam, Z-path spherical mirror layout (see Fig. 48). The mirror focal lengths are 90 in. (2.29 m). Because the window clear aperture was 11 in. (280 mm), the system F-number was approximately 8. The copper vapor laser's green output (wavelength = 510 nm) was used while the yellow output (wavelength = 578 nm) was used for another diagnostics technique. A correction optic was employed on the receiver side to reduce the astigmatism induced by the Z-path spherical optics system. The entire system was mounted on vibration-isolation optical tables. The image aperture and drum speed were selected on the basis of the number of frames and the frame rate desired. It is important to remember that the camera is actually a streak camera with the laser strobing action performing a pseudo-framing function. Imaging was performed in the shadowgraph or schlieren mode.

6.2.7.2 Holographic Interferometry

The physical layout of the holographic interferometry (HI) system is shown in Fig. 49. The copper vapor laser beam was first filtered longitudinally and spatially, and reduced to one polarization. It was then split into reference and object beams. The object beam was then expanded by a

lens, collimated by the 12-in. spherical mirror and transmitted through the test section, where it interacted with the flow field. On the receiver side of the tunnel, the second 12-in. diameter spherical mirror condensed the object beam. Researchers at North Dancer Laboratories, Inc. (NDL) provided the holographic camera. Although the copper vapor laser system is a multimode laser, NDL developed proprietary techniques to record the holograms. The holographic camera's rotating film disk was placed at the point where the beam reached a diameter of 5 mm. The reference beam was relayed around the test section to the receiver side of the tunnel and also was reduced to a diameter of 5 mm and co-impinged on the holodisk. In addition, schlieren images, created by placing a knife edge at the focal point of the object beam after it passed through the transparent holodisk, were recorded using the drum camera. Both holographic cinematography and schlieren data were acquired in this way during Impulse Facility Runs 33 and 35. The data sets consist, respectively, of 34 and 31 flow-field images recorded at 8 kHz.

The holographic data were processed by NDL personnel using a phase-shift interferometry technique to extract the time-resolved distribution of gas density across the nozzle flow. An optical system, including a reference beam and shearing interferometer, was set up. Shearing distance/angle of the phase-shifting apparatus was calibrated using optical geometry and fringe visualization. Holograms were reconstructed, and three phase-shifted 640×480 digital interferogram images were acquired for each time frame, including one "no-flow" frame. Digitized images were aligned using the test article shadow. Phase maps were extracted for each time frame by masking out the object, calculating the modulo 2π phase, subtracting the "no-flow" phase map, phase unwrapping, and integrating the sheared phase. Gas number densities were calculated based on the refractive index from phase map, tube geometry, and wavelength. For comparison, densities were computed for a limited number of time frames using conventional interferometry (i.e., creating interferograms by physically overlaying the "no-flow" and "flow-on" holograms). Complete details of the holography data processing are in Appendix 3.

6.2.7.3 Digital Movies

The process for creating digital movies from the drum camera film is illustrated in Fig. 50. After exposure of the 1.0-m-long strip of 35-mm film, the filmstrip is chemically processed in a developing canister and dried. A flatbed scanner is used to acquire high-resolution digital images of the filmstrip negative. Because of scanner length limitations, the image is acquired as several overlapping subimages. Custom software is used to locate and crop each individual frame from the subimages. The unique images are batch processed (mirrored left to right, made film positive, and enhanced) and saved under temporally significant filenames. A title frame is added, and a digital movie is created using commercially available software. The complete details of this process are given in Appendix 4.

6.2.8 Planar Laser-Induced Fluorescence

The physical setup for PLIF is shown in Fig. 51. Dual Nd:YAG/dye/frequency-mixing laser systems and beam-shaping optics were used to generate two overlapping sheets of laser radiation

at nominal 226-nm wavelengths, exciting selectable transitions in the NO gamma bands. Wavelengths were determined using an NO reference cell and a pulsed UV wavemeter. From measurements of the fluorescence signals and their ratios, rotational temperature and number density of NO can be determined. The observed PLIF sheet dimensions are typically 3 cm wide and 17.5 cm in length, with the sheet thickness maintained at approximately 0.5 mm to prevent saturation of the excitation transitions. The sheets impinge on the test article at a selected distance from the nose-tip region in order to avoid interference from the strong radiation from this region. The two laser pulses are temporally separated by approximately 300 nsec. Fluorescence images were obtained with a pair of ICCD cameras (384×576 pixels) with intensifier gatewidths set at 300 nsec. The ICCD cameras were turned such that the 576-pixel dimension was vertical. The PLIF images were obtained at a nominal 1.6 msec from the ST6 pulse. A static calibration cell with known NO concentrations was placed over the nose of the model. A series of calibration measurements was made at different pressures and NO densities. Energy differences between the two lasers were eliminated by recording the energy of the individual laser pulses and normalizing the PLIF images. Transmission losses through the optics and test-cabin windows were measured to be approximately 70 percent for each beam.

6.3 IMPULSE FACILITY DATA ANALYSIS

6.3.1 Impulse Facility NID Data Log

A log of the nonintrusive data obtained in the AEDC Impulse Facility is shown in Table 12.

6.3.2 Flow Particulate Contamination

Two WPs (one of each coating type) from Run 26 were analyzed with a scanning electron microscope (SEM) and using SEM x-ray energy dispersive analysis. Subsequently, SEM instrumentation failures prevented further analysis of the WP. The sizes, populations, and elemental constituencies of the particles on each WP were very similar. The particle population was reported as low, with sizes ranging from ~ 5 to ~ 300 μm and shapes ranging from rectangular to spherical. Some particles were composed primarily of Fe, and many were composed primarily of two or more elements such as Fe, Ca, Si, K, Al, S, and Cr. Other trace elements detected were Cl, Mn, Ti, Ni, and Cu. Several organic particles and one Si fiber were identified. Possible sources of the particles include tunnel walls, diaphragms, the piston, and residual test section matter.

Table 13 gives a tabulation of the LBT data obtained from facility Runs 23 through 35 for which the nozzle throat material was Fansteel 60, a tantalum-tungsten steel alloy which has proved to be the most durable throat material used to date. For Runs 26 through 35 the facility particle stopper was in place to prevent large particles from impinging directly on the test article. As can be seen from the table, the time from ST6 to the minimum transmission peak correlates with the average flow time through the nozzle within ± 12 percent.

When a plot of average beam transmission during the estimated run time of the facility versus nozzle stagnation pressure is constructed, as shown in Fig. 52, it appears that a nozzle stagnation pressure of 1000 atm is almost like a barrier. That is, if the pressure is less than 1000 atm, the beam transmission is excellent; if the pressure is greater than 1000 atm, then the flow is optically thick.

Assuming a geometric extinction cross section, a 50- μm -diam monodisperse particulate size distribution based on witness plate sample analysis, and a uniform spatial distribution, an average particle number density of 57.2 particles/cm³ can be estimated for the flow during the predicted run time as long as nozzle stagnation pressure remains less than 1000 atm. Assuming a 5-msec erosion/ablation period and iron as the predominant material, then approximately 15 g are eroded per run.

Based on the PMIE results shown in Fig. 43, a two-layer model can be invoked. Using this model, the core particle number density is 8.1 particles/cm³, and the shear layer density is 339.6 particles/cm³.

6.3.3 Flow Start Process

High-speed shadowgraph/schlieren flow visualization was performed for six Impulse Facility runs with the copper vapor laser operating at from 8 to 25 kHz. Each image sequence consisted of nominally 100 frames, representing from 12.5 to 4.0 msec, respectively, of elapsed time. The choice of the 10-mm mask provided a relatively long time record without severely compromising image resolution. The laser pulse string was initiated by the shock tube gate (rise in nozzle reservoir pressure, ST6). Representative image sequences, selected to illustrate the Impulse Facility flow start process, are presented for Runs 30 through 35 in Figs. 53 through 58. Corresponding plots of nozzle reservoir pressure and model nose temperature and pressure are included. The traces indicate that flow reaches the model nose within approximately 0.3 msec of the rise in reservoir pressure. Another 0.3 to 0.7 msec is required for establishment of the target flow condition, depending upon the run parameter values selected. Data for the runs indicate that under normal operation the starting process is completed in less than 1.0 msec after the indicated reservoir pressure rise.

6.3.4 Flow Steadiness

Representative image sequences, selected to illustrate the Impulse Facility flow steadiness, are presented for Runs 30 through 35 in Figs. 59 through 64. The included model nose temperature and pressure data traces indicate that the flow condition was relatively constant during the nominally 1.0-msec measurement window. Figure 65 shows holographic imaging data that indicate the steadiness of freestream number density during the nominal measurement window.

6.3.5 Helium Arrival

HSFV images were also utilized to detect He arrival. Shock shapes taken from various camera frames from Impulse Tunnel Run 35 (see Fig. 64) were related to elapsed time and shown previ-

ously in Fig. 25. The shock shape data indicate He arrival is spread over the 3.0- to 3.3-msec time increment. As noted earlier, the facility code predicts He arrival within this band, at 3.15 msec.

Table 14 is a tabulation of information on helium arrival provided by LDA, FILRAY, and HSFV. The earliest detection of Rb by LDA is nearly as early as the flow establishment time. It is speculated that residual Rb circulating in the test section as a result of prior seeding experiments is causing a false indication of helium presence at these early times. LDA peak absorption times as well as FILRAY rollover time indicate helium arrival at 2.5 msec past ST6.

6.3.6 Flow Static Properties

PLIF images were taken on Runs 30 through 35 at NO excitation wavelengths of 225.134 and 225.716 nm. A collage of the raw images (in pseudo color) is shown in Fig. 66. Flow is left to right; laser beam propagation direction is top to bottom. Images for Run 30 are centered on the bow shock and cover an area of about 5.1 in. in height. All other images are centered above the shock and cover an area of about 7.5 in. in height. No signal was measured for Run 34 on image (a). The image for Run 35 (b) shows a dark band at the bottom where the laser sheet penetrates the shock. Otherwise, nonuniformity of the signals can be attributed to nonuniform energy distribution in the laser sheets, attenuation of the laser sheet because of absorption, and noise. The image for Run 34(b) appears to show some additional nonuniformity, but is suspect considering the absence of a measurable signal on the corresponding image for Run 34 (a). Thus, for the most part, the PLIF images point toward a uniform freestream.

For Run 35, a calibration was performed as well (see images on far right in Fig. 66). This calibration was attempted by enclosing the test article with a cell with optical access ports in the top and the side. The cell was filled with a mixture of NO in nitrogen. However, signal levels were so low that they could not be used for an absolute calibration of the PLIF images from Run 35.

Quantitative analysis of the images from Runs 33 and 35 was performed by 1) performing a background subtraction, 2) integrating signals across the widths of the laser sheets, and 3) scaling the resulting values by the measured laser pulse energy. The resulting signal profiles are shown in Fig. 67, in which laser propagation direction is right to left. Clearly, laser absorption plays an important role, accounting for a drop in signal of about a factor of two between the point where the laser sheets enter the imaging region and the bow shock. Signal ratios are shown in Fig. 68. Different behaviors are observed for Runs 33 and 35. For Run 35, a constant signal ratio is obtained in the freestream. This would seem to indicate a uniform temperature in this region. However, the same is not the case for Run 33, where the signal ratio is found to rise steadily along the propagation direction of the laser sheets. Also, a marked change in signal ratio is observed for Run 35 when the laser sheets cross the bow shock. The same effect is not observed for Run 33. For Run 35, if the predicted freestream value of 690K is assigned to the uniform region, then the PLIF signal ratio indicates a peak temperature of 1300K in the shock.

6.3.7 Flow Self-Emission

The Run 26 emission spectra in the limited 765- to 795-nm Fig. 69 showed, except for two K lines, negligible freestream emission but, in second order, strong Fe emission near the probe's nose (in the bowshock). The spectroscopic presence of Fe is consistent with the finding of iron filings on model noses after runs. All succeeding runs used a long-wavelength pass filter to eliminate second-order spectra. Weaker first-order Fe emissions were later recorded in the brightest shock regions. Except for the occasional appearance of the 793.313-nm Cu atomic line and the above-mentioned Fe lines, the only spectral lines recorded were the two K lines at 766.491 and 769.898 nm and Rb lines at 780.023 and 794.760 nm. A typical spectrum is shown in Fig. 70. No other species emission was found overlapping the 780.023 nm Rb line. In general, concerning Rb emission: 1) its strength was a direct function of Rb seed level; 2) relative to freestream, it was strong in the shock; and 3) it was detected between 2.6 and 3.6 msec past the ST6 trigger. The effects of residual tunnel Rb seed were evident in succeeding runs.

6.4 APPLICATIONS AT THE DLR HEG

In September and October of 1998 a team of AEDC instrumentation engineers traveled to Göttingen to participate in a part of a shock/boundary-layer interaction test program in the HEG. Several diagnostic systems were carried for application in the HEG. These included lasers for obtaining PLIF data on freestream properties in the HEG, the AEDC High-Speed Flow Visualization system to record shock wave patterns in the interaction region, and the Laser Beam Transmission System for monitoring flow particulate contamination.

A double wedge model (see Fig. 9) was used to generate the shock/boundary-layer interaction. The width of the model was 340 mm, and the length of the first and second plates was 170 and 150 mm, respectively.

6.4.1 Laser Beam Transmission

The same setup used in the AEDC Impulse Facility was installed on the HEG facility. From the beginning, difficulties were experienced with the system. The system experienced equipment failures (laser), loss of system trigger and timing troubles, and finally a series of unresolved null data sets (possibly caused by shock deflection). These, coupled with the pressure of a pressing schedule and the need to give priority to the other diagnostics led to, in effect, an abandonment of the LBT system. The end result: no useful data were produced.

6.4.2 High-Speed Flow Visualization

The HEG facility sports a dedicated vibration isolated optical system used for Schlieren, shadowgraph, and holography. In the current campaign it was set up to acquire Schlieren images employing the same Cu Vapor laser and drum camera as was used as in the AEDC work. The system, as shown in Fig. 71, has 1500-mm focal length spherical mirrors in a Z-path configuration to

obtain a 300-mm diam viewing area. Although several framing rates were tried early on, 30 KHz was settled upon for the majority of the runs before the frequency shifting technique was employed. A 510-nm laser line filter was used at the camera to exclude flow incandescence.

During the first phase of the test it was noticed that for high angles of attack the flow field behind the downstream shocks (where the flow had the highest density and temperature) became opaque, or “blacked out” in the images. HEG personnel identified the problem as absorption caused by copper vapor contamination in the flow stream. To overcome this, a dye laser was used to frequency shift Cu-vapor output of 510 to 671 nm.

One innovation apparently developed by personnel at the DLR and adopted by the AEDC team was the use of “gray edges.” A glass photographic plate was exposed in such a way that when it was developed it exhibited transparency on one half, total blockage on the other, and a region between the two halves with a linear ramp (gradient) from one to the other. This gray edge was used in place of the knife-edge to soften the otherwise overly stark contrast. It was postulated that a variable gray edge could be constructed which exhibited a variation in gradient along the edge. When such a gray edge was placed on a traversing mount that allowed for its adjustment along the “edge,” the contrast could be varied. Further, gray edges could be fabricated to have a stepwise variation, or any other nonlinear profile desired.

6.4.3 Planar, Laser-Induced Fluorescence

The setup is shown in Fig. 72. Dual Nd:YAG/dye/frequency-mixing laser systems and beam-shaping optics were used to generate two overlapping sheets of laser radiation at nominal 226-nm wavelengths. Transitions in the NO gamma bands were again excited. Wavelength identification was accomplished using a pulsed wavemeter. Calibrations were performed by filling the HEG with a known mixture of NO and N₂ gas. Instrument timing triggers were provided by using a pressure transducer signal that occurred approximately 150 μsec prior to flow arrival. The trigger signal was further delayed until flow arrival using a delay generator. The two laser pulses were temporally separated by approximately 300 nsec. Fluorescence images were obtained with a pair of ICCD cameras (384 × 576 pixels) with intensifier gatewidths set at 200 nsec. The intensifier gates were turned on approximately 50 nsec before the laser pulse. Each camera’s optics also included a 50-nm bandpass filter centered at 254 nm and a Schott UG-5 filter that was used to block scattered laser light. Spatial calibrations were performed by imaging a rectangular grid pattern.

6.5 HEG DATA ANALYSIS

6.5.1 HEG NID Data Log

The HEG NID data log for those HEG shots for which AEDC personnel were present is given in Table 15.

6.5.2 Flow Particulate Contamination

No usable data were obtained (see Section 6.4.1).

6.5.3 Flow Start Process

High-speed shadowgraph/schlieren flow visualization was performed for eleven HEG runs with the copper vapor laser operating at 15 kHz. Each image sequence consisted of either 54 or 99 frames, representing, respectively, 3.5 or 6.6 msec of elapsed time, depending on the selected camera mask and drum rpm. Choice of the smaller mask and lower drum rpm provided a longer time record (more images per length of film), but at the expense of image resolution. The laser pulse string, delayed to capture the desired portion of the run, was initiated by the rise in nozzle reservoir pressure, STP1. Representative image sequences, selected to illustrate the HEG flow start process, are presented for Runs 446 through 460 in Figs. 73 through 83. Corresponding plots of nozzle reservoir and test section pitot pressure are included. Because of the long delay selected for Runs 452, 453, and 454, supersonic flow over the test article was already established when the laser pulse sequence began. The start processes of the HEG and AEDC Impulse Facility are quite different. Arrival of the flow at the test article after the reservoir pressure rise (~ 0.75 msec) is significantly later in the HEG than in the AEDC facility (~ 0.3 msec), primarily owing to the longer HEG nozzle. The longer time constant is also apparent in the time required for the establishment of the target flow condition (1.4 to 2.0 msec in the HEG, compared to 0.7 to 0.95 msec in the AEDC facility). A significant amount of secondary flow around the ends of the wedge test article is indicated and is discussed in the following section. The adverse effect of copper absorption, observed in the Impulse Facility, was also a problem during the HEG runs. The effects of both secondary flow and copper absorption are illustrated in the last three frames of Fig. 75.

6.5.4 Flow Steadiness

Representative image sequences, selected to illustrate the HEG flow steadiness during the measurement window period, are presented for Runs 446 through 560 in Figs. 84 through 94. Corresponding plots of nozzle reservoir and test section pitot pressure are again included. The target flow condition is established at nominally 2.0 msec after the shock reflects from the tunnel end wall (indicated by the rise of reservoir pressure, STP1). The flow condition remains relatively constant for at least 0.4 msec, during which time the primary measurements are acquired.

6.5.5 Helium Arrival

Initial evaluation of the HEG images indicates that it will be difficult to determine shock locations accurately. Copper absorption in the high-temperature areas and/or end effects causes these areas to appear dark in the images. In some cases the nose and even the remainder of the model and the shock are obscured. The influence of driver gas detection on shock location has since been exhaustively treated and presented in Ref. 8.

6.5.6 PLIF-NO Data

The experimental arrangement for the PLIF measurements in the HEG is shown in Fig. 95. This configuration was used on Run 453 and following runs, with two spatially overlapping, temporally coincident beams. The PLIF measurement volume is that imaged by the upper of the two cameras. Prior to Run 453, spatially overlapping, temporally separated sheets were used, with each beam imaged by a separate camera. However, signals from one of the cameras were found to be nonexistent or too small to be used for analysis. The distances from the top (93 mm) and bottom (169 mm) of the imaging region are measured along the laser beams to the edge of the flow. For this purpose, the flow diameter was assumed to be 55 cm, as defined by HEG personnel for HEG Conditions I and III.

The three NO excitation wavelengths used in the PLIF measurements (henceforth referred to simply as λ_1 , λ_2 , λ_3) are listed in Fig. 96. The first of these is the same as those used in Ref. 32, which discusses fluorescence thermometry in optically thick flow. HEG personnel supplied the HEG freestream parameters. The NO densities and temperatures were used to perform the calculations to be shown subsequently in this report. Condition IV is the high-pressure condition at which optical flow blockage occurred (on Runs 449 and 450). A summary of the PLIF measurements is given, from which the most important point is that good data were obtained on Runs 454, 455, and 456.

PLIF images for Runs 454-457 are shown in Fig. 97. Flow direction and laser propagation direction are indicated with arrows. Wavelengths from Fig. 96 are indicated. The reflected spot from the Cu-vapor laser is identified, and the absence of the λ_1 beam for Run 457 due to a missed trigger is noted.

Figures 98 through 100 illustrate partially processed data. For each of the three Runs 454, 455, and 456, five steps were required to obtain vertical signal profiles. First a background signal was determined, and it was verified that this background was roughly constant outside the laser beams. Second, the background was subtracted from the signals everywhere in the image. Third, left and right boundaries were defined for each laser beam, parallel to the beam, and the signals between the two boundaries were integrated for each row of pixels. The result is a single signal value for each beam for each row of pixels (384 values per beam per image). Fourth, the signal values were energy normalized by converting them to a net pulse energy in the tunnel of 1 mJ per pulse (measured just inside the tunnel window, before attenuation by the flow field). Finally, the data were plotted as a function of the propagation distance of the lasers into the flow, measuring from the edge of the presumed 55-cm-diam flow field. Also shown in Figs. 98, 99, and 100 are the ratios of the resulting signals as a function of the same propagation distance. Average ratios with associated statistical uncertainties are indicated.

To assess the importance of laser absorption and spectral hole burning upon propagation of the laser beams through the flow, the model from Ref. 32 was used. Results are shown in Fig. 101

for the mildest (in terms of laser absorption) of the three calibration conditions, condition III and condition I, using the freestream parameters from Fig. 96. The results are arranged by excitation wavelength. Note the very severe absorption effect in the calibration measurements. This effect is attributable to the relatively high NO concentration (5 percent NO in N₂) and, especially, the much longer absorption path in the calibration measurements (425 to 501 mm—see Fig. 95) versus the tunnel runs (93 to 169 mm). As a result it is exceedingly difficult to interpret the PLIF data for the calibration measurements quantitatively. As the calculated line shapes in Fig. 101 show, the overlap integral of the spectral line shape and the absorption line shape are entirely dominated by the wings of the profiles. Correct modeling of those requires the inclusion of species-dependent, pressure-broadening effects. Also, contributions from neighboring spectral lines (with different temperature dependence) cannot be ignored, even if these lines are negligible in optically thin flow. In conclusion: the calibration measurements did not provide a meaningful calibration. However, spectral hole burning is significant for tunnel run conditions III and I, but at a level that is manageable by the theory from Ref. 32.

Continuing with the theory from Ref. 32, signal profiles and signal ratio profiles were calculated for the HEG-supplied freestream parameters. These profiles are to be compared with the experimental profiles from Figs. 98, 99, and 100. The average signal ratios from those pages are shown in the lower plots of Fig. 102 and are seen to be in excellent agreement with the theoretical predictions. This implies that the PLIF measurements are consistent with the HEG-supplied freestream parameters. Comparison of the predicted and measured signal curves also looks good: See for example the trends for λ_1 (strong attenuation upon propagation) and λ_2 (much less attenuation) for Run 454 (compare leftmost two plots of Fig. 98 and top-left plot of Fig. 102).

At this point there are three items that can be identified for followup work:

- 1) An explicit calculation of the NO temperature and density in the freestream region from the experimental PLIF data, following the optically thick laser absorption model that is developed in Ref. 32;
- 2) An exploration of an extension of Ref. 32 to more fully take into account the observed laser sheet attenuation in the PLIF images;
- 3) A sensitivity study to look at the possible effect of a boundary layer on the measured NO densities and temperatures.

Using the theory from Ref. 32, an explicit estimate was made of the NO density and temperature for run condition III. This was accomplished by combining the measured PLIF signal ratios from Runs 454 and 455, both taken at condition III. The energy-normalized PLIF signal ratios from these two runs were $R_{31} = 0.938 \pm 0.008$ for Run 454, and $R_{21} = 0.434 \pm 0.009$ for Run 455 (see Figs. 98 and 99). The subscripts refer to the wavelengths that are indicated in Fig. 96. Each of the two PLIF signal ratios determines a set of three curves in the temperature-density diagram shown in Fig. 103. In each set, the central curve is determined by the measured signal ratio (e.g.,

$R_{31} = 0.938$ for Run 454). The other two curves are determined by the 1-sigma-adjusted signal ratios (e.g., $R_{31} = 0.938 + 0.008$ and $R_{31} = 0.938 - 0.008$ for Run 454). An underlying assumption of this calculation is that the freestream flow has a top-hat profile with a diameter of 55 cm. By combining the two sets of curves, an explicit estimate is obtained for the temperature ($T = 582 \pm 19\text{K}$) and NO density [$n_{\text{NO}} = (5.30 \pm 0.23)\text{E}+15/\text{cc}$] of the freestream flow. It should be emphasized that this estimate is independent of the CFD calculations. It *does* depend on the assumption that vibrational and rotational temperatures of the NO molecules are equal. If this were not the case, a different NO density would result. However, the derived NO (rotational) temperature is believed to be independent of this assumption (see the discussion in Ref. 32).

Figure 104 summarizes the attempt to modify the two-run, three-line fluorescence thermometry technique from Ref. 32 mentioned above to a single-run, two-line technique. Though the attempt proved unsuccessful, it deserves further study for future work. The central idea of the attempted extension is as follows: Rather than working with the measured PLIF signal ratios only (which are measured at a single point in the flow), observed attenuation factors of the laser sheets should be included. The attenuation factors were determined for the PLIF images for Runs 454, 455, and 456. For example, for Run 454, the following attenuation factors were found for the two laser wavelengths (“1” and “3”) used: $\beta_1 = 6.04 \pm 0.31/\text{m}$ and $\beta_3 = 5.56 \pm 0.27/\text{m}$. These factors were determined by curve-fitting a straight line to the log of the PLIF signal ratios as a function of propagation distance into the flow (see plots on Figs. 98, 99, and 100, in which the PLIF signal is plotted on a linear scale). Just as in the case of the measured PLIF signal ratios, the measured values of the absorption coefficients determine a set of curves in the temperature-density plots shown in Figs. 103, 104, and 105. By combining two measured attenuation coefficients (one for each wavelength) and one PLIF signal ratio, a set of three curves is obtained. These sets of three curves are shown in Fig. 104 for Runs 454, 455, and 456, separately. Ideally, each set of three curves should yield unique NO density and temperature values. However, because there are three measured quantities (two attenuation factors and one PLIF ratio) but only two to-be-determined quantities (NO temperature and density), an overdetermined system results. For Run 454, the three sets of curves come close to having a common intersection. However, no common intersection is found for Runs 455 and 456. Thus, at this point, it is not clear how the extended theory can be of benefit. One possibility that cannot be rejected out of hand is that the extended theory is sound, but points to a yet undiscovered problem with the PLIF measurements.

Fig. 105 shows the results of a second extension to the theory in Ref. 32. Rather than assuming that the freestream flow has a top-hat NO density profile with a diameter of 55 cm, it is assumed that there is, in addition, a boundary layer, in which the NO density and temperature fall linearly from the (to-be-determined) freestream values to the values at the edge of the boundary layer (zero NO density and ambient temperature = 293K). Using this alternate model, the explicit calculations of NO temperature and density were repeated for boundary-layer thicknesses of 50 and 100 mm. In both cases, PLIF signal ratios from Runs 454 and 455 were combined to arrive at an estimate of the NO temperature and density in the freestream. The results are indicated in Fig. 105. It is found that there is relatively little variation in the derived NO temperatures. However,

there is a larger effect on the inferred NO density. What is expected is that: by adding NO to the boundary layer, a smaller NO density in the freestream should result while the same laser attenuation effect is maintained. Note that for a full interpretation of these results, an independent estimate of the actual boundary-layer thickness must be supplied.

6.6 DEVELOPMENT OF PULSED ELECTRON BEAM FLUORESCENCE TECHNIQUE

6.6.1 Description of PEBF Technique

As a flow diagnostic technique, electron beam fluorescence (EBF) has been widely used for measurements of densities, temperatures, and velocity distribution functions in a variety of low density gases (Refs. 33 and 34). For the technique, fluorescence from atoms and molecules excited by a narrow electron beam is spectroscopically analyzed. All gas species present are accessed simultaneously under electron excitation. The bulk of EBF work has used continuous wave (cw) electron guns whose output currents are typically less than 10 ma. For most gases, collisional quenching, in which electron-excited states are depopulated by collisions with other atoms or molecules before emission can occur, limits the measurable upper density level to about 10^{16}cm^{-3} . For certain species, slightly higher densities can be measured with the application of known quenching rate constants.

PEBF promises extension of the EBF diagnostic technique to densities up to approximately 10^{18}cm^{-3} . This is made possible by the development of pulsed electron guns (PEG) that emit a high-current electron pulse in times of a few tens of nanoseconds. If fluorescence is measured during the initial portion of a PEG pulse, which time is short relative to the quenching timescale, spontaneous emission occurs before quenching collisions become of effect, enabling, in many gases, a linearity, or known relationship between fluorescence strength and density up to 10^{18}cm^{-3} . Also, the short pulse enables "instantaneous" measurements in fast-changing flows or flows of a transient nature. Gated, intensified CCD cameras are well suited as detectors for PEBF.

A PEG pulse is generated by a pseudospark discharge, the physics of which is discussed in Refs. 35 to 38. In this peculiar process, electrons are forced to follow field lines that take the longer path between electrodes and, by using a stacked set of circular electrodes with aligned orifices, electrons are accelerated through the orifices and gain enough ballistic energy to detach from the field at the gun exit.

Faculty and students at the University of Southern California (USC) proposed using PEBF for flow diagnostics (Refs. 39 and 40). Several years later, USC faculty and Integrated Applied Physics Inc. (IAP) jointly developed an advanced PEG, and a duplicate PEG was purchased for testing at AEDC. USC's PBF experience has been reported in, e.g., Refs. 41 to 43. PEBF has been used by other investigators for, as an example, flow visualization in an ONERA wind tunnel.

A cutaway drawing of the PEG is shown in Fig. 106. The PEG requires a specific level of vacuum (a differential pumping station will be required during application, as shown in Fig. 107).

The anode flange does not show two ports, one for introducing a working gas and the other to provide gun pumping. A high-voltage trigger electrode initiates the hollow cathode discharge, and the electron pulse is formed and accelerated through the stacked electrode set. Before passing the current-sensing Rogowski coil, the electron pulse passes through a 3-mm-diam orifice in the anode. Nominal beam characteristics are given in the figure. The PEG is expected to be capable of generating several pulses at a 300-Hz rate. To power and control the PEG, a high-voltage pulse generator (HVPG) and delayed trigger generator were also purchased from IAP.

The flow density of the FPST is on the order of 10^{17}cm^{-3} , high enough to warrant a PEG application, as envisioned in Fig. 107. Only one or two PEG pulses could be used during the several-millisecond useful flow time. After passing through the observation volume, the electron beam must be collected by a current-measuring Faraday cup. To protect the PEG from harmful gases and excessive pressures, a differential pumping section or fast-acting gate valve (or both) would be necessary. PEG shielding would be required to reduce the pulse's generated electromagnetic interference to levels noninterfering to other instrumentation.

6.6.2 Laboratory Development

An existing laboratory cylindrical vacuum tank was refurbished for initial testing of the PEG. Fig. 108 is a sketch of the assembled system. Measuring 30 cm in diameter and 65 cm in length, the tank is fitted with a window, turbomolecular pump, pressure gages, gas entry needle valve, and gate valve. A cylindrical differential pumping section, having a pumping port and removable orifice plate, was designed and fabricated to fit between the PEG and gate valve. A copper, gridless electron cup, insulated from the tank, was positioned at the bottom of the tank to capture the electron beam. The PEG was pumped by another turbomolecular pump through small diameter tubing. This pump and two pressure gages were mounted on a cylindrical, flanged, pipe section. The PEG was pumped to 10^{-4} torr and the tank to 5 mtorr before any firings were attempted. The tank was then filled with some 100 mtorr of dry nitrogen and the gun with 10 to 50 mtorr of either purified argon or nitrogen.

Initiation of the pseudospark discharge in the PEG requires that a negative high-voltage pulse be applied to the cathode. This pulse, on the order of 30 kV, is generated by the HVPG shown in Fig. 109.

Long before any PEG current pulses were ever detected, many modifications were made to the factory HVPG, mainly because of failures of the four silicon-controlled rectifier (SCR) switches. In several steps, SCRs having a greater rate of change of current with respect to time and di/dt capability were installed before the HVPG could be made operational. The SCRs are represented in Fig. 109 as SCR switches 1, 2, 3, and 4. The high-current pulse generator was also modified to provide the high drive currents required by the high di/dt SCRs. In addition, it was necessary to retrofit the Transmission Line Transformer into a container filled with transformer oil to suppress high-voltage breakdown discharges within the transformer.

A PEG pulse can be initiated either by the manual pushbutton start indicated in Fig. 109 or by an externally applied timing pulse. The Digital Pulse Generator (DPG), implemented by a Stanford Research Systems, Inc. Model DG535 Digital Pulse Generator, produces two simultaneous trigger pulses. The first pulse causes the high-current pulse generator to supply gate drive currents to the four SCR switches. The SCRs simultaneously produce high-current pulses to drive the primary windings of the transmission line transformer. In response to the primary current pulses, a high-voltage pulse is produced in both the shield and center conductor of the transformer secondary winding. The shield of the secondary winding provides the requisite high-voltage pulse to the PEG cathode.

The second pulse produced by the DPG drives the delayed trigger generator (DTG) which, in turn, produces a negative 4-kV pulse, which adds to the high-voltage pulse induced in the center conductor of the transformer secondary winding. This combination pulse is applied to the PEG trigger electrode and is identified in Fig. 109 as the high-voltage trigger pulse. A time delay circuit in the DTG permits the negative 4-kV pulse to be precisely delayed so that its peak value is simultaneous with the peak value of the high-voltage cathode pulse. The 4-kV differential between the trigger electrode and the surrounding hollow cathode causes an electrical discharge to be established in a smaller hollow cathode structure which encloses the trigger electrode and incorporates a small exit orifice. This discharge then initiates the pseudospark discharge.

A Rogowski coil assembly attached to the PEG is used to monitor the electron beam. The copper electron cup is also used to monitor, as well as terminate, the electron beam produced by the PEG. A 0.1-ohm, zero-inductance, sense resistor senses electrical current flowing from the electron cup to ground.

After many firing attempts, indications of PEG current began. It may be that the PEG electrodes had been undergoing a conditioning process, as reported in pseudospark gun literature. Upon an inspection of the anode exit orifice flange, it was noticed that the beam had impinged randomly about the orifice, being as much as 5 mm off axial centerline. This is consistent with the observation that only occasional significant current pulses were being measured. Typical electronic waveforms associated with PEG operation are shown in Fig. 110. The trigger signal initiates the sequence of events. The pseudospark pulse occurs some 6.9 msec after application of the trigger signal and persists for a period of 10 to 20 nsec. Since a calibration constant has not yet been established for the Rogowski coil, only its output voltage characteristic is shown in the figure. The waveforms were recorded at a sampling interval of 10 nsec/div so that the electron cup signal, which lasts only 10 to 20 nsec, is undersampled. Therefore, the true peak values of the electron cup signal are not known. However, the peak recorded voltage of 4 volts and the sense resistor value of 0.1 ohm leads to an indicated peak value for the electron beam current of 40 amp. New maximum values of current were gradually established as firings continued.

To record PEBF, a 200-mm focal length lens focused fluorescence through the tank's fused silica window onto the slit of an Acton Research Corporation 0.275-m spectrometer, which was

fitted with a Princeton Instruments, Inc. ICCD camera. The camera was gated with the PEG current pulse. A PEBF spectrum is shown in Fig. 111, which is the N_2^+ First Negative System's (0,0) band at 391.4 nm.

6.7 NID SUMMARY

6.7.1 Technical Conclusions

An ambitious but successful NID program was executed at the AEDC Impulse Facility as well as at the DLR HEG. All NID techniques pursued for application gave useful results with the exception of the PEBF technique, which, because of time and resource constraints, never progressed past the laboratory development stage. No Impulse Facility-related operational problems were encountered, with the possible exceptions of boundary-layer and recirculation effects on LDA measurements and potential copper absorption effects on HSFV for some conditions. At the DLR HEG the copper absorption effect was significant, and the use of a dye laser pumped by the copper vapor laser was successful at circumventing the absorption problem for HSFV.

It was determined that the AEDC Impulse Facility flow is established within 0.67 msec from the shock tube gage (ST6) trigger pulse, and a nominal run time of 2.5 msec free from driver gas effects is available for nozzle stagnation pressures less than 1000 atm. Facility flow appears optically thick as a result of particulate scattering for nozzle stagnation pressures greater than 1000 atm. By way of contrast, the HEG flow requires a longer time to establish, some 1.4 msec, and the optically thick threshold is never reached since the HEG operates below 1000 atm.

6.7.2 Technical Recommendations

It is clear from the wide range of computational predictions of freestream properties and the lack of agreement of PLIF-NO measurements with any of the predictions, that considerable work is required on CFD physics models. A thorough investigation of the current PLIF-NO methodology and analysis methods using both the laboratory shock tube/tunnel and the newly acquired high-temperature calibration cell is also required. Future application of LDA requires the use of airtight tubes extending into the boundary layer to eliminate boundary-layer and recirculation effects. It is also recommended that the LDA technique be extended to yield information on flow velocity. As the question of vibrational nonequilibrium has not been resolved, it is recommended that the PEBF technique be developed further, because it can readily give information on vibrational temperature for a number of species simultaneously. Furthermore, the PEBF technique can potentially provide quantitative information on the amount of helium contaminating the test gas.

6.7.3 Benefits to AEDC

As a result of this international cooperative program, AEDC NID capability has been greatly enhanced. The HSFV system is now available for applications to hypersonic air-breathing propulsion, aero-optics, jet interaction, and ballistic range testing. Indeed, the association with ND, L,

Inc. with regard to advancements in high-speed holographic recording has placed AEDC on the leading edge of high-speed visualization capability. The LDA system methodology has already been advanced for use with absorption by O_2 , H_2O , and K , and applications in turbine engine and hypersonic air-breathing propulsion testing, as well as aerodynamic testing, are forthcoming. Although applications of the PEBF system were not achieved, the capability of the system was greatly advanced, and it probably will become an outstanding diagnostic tool for the high Mach number conditions of AEDC's Tunnel 9.

This international program has promoted the association with colleagues at DLR HEG and the international hypersonics ground testing community through participation in workshops and symposiums.

6.7.4 Benefits to DLR

The early ties with AEDC through the still ongoing Data Exchange Agreement 7425 have been further developed and reinforced through the collaborative efforts in this project. From the DLR point of view, it was a true collaboration. (Each party contributed to the other through expertise, know-how, and hardware/software knowledge in areas where the other may have had little or less or even no prior experience.) This was an excellent example of work sharing (union of effort) stretching across not only organizational but also international boundaries. Of particular interest and benefit to the DLR in NID was the implementation and successful testing of HSFV on HEG. This proved to be a most powerful tool in studying unstationary effects (boundary-layer growth, separation, and interactions) in flow development.

7.0 SUMMARY OF RESULTS

This program has been a lengthy, in-depth, and very fruitful cooperative effort between the engineering staffs at AEDC and the DLR Institute for Fluid Mechanics in Göttingen. From the initial discussions in 1994 through to the final laboratory work on the PEBF in 2000, the project has been marked by some significant successes as well as the not unexpected, and usual for such a complex technology program, problems and difficulties. The most notable positive result for the individuals working on the project has been the excellent relationships developed and the high degree of cooperation on the part of all involved. The opportunity to learn about, and from, each other has been a great benefit.

The project began with some ambitious goals involving complementary testing in the FPST and the HEG, NID techniques development and CFD code validation. As work progressed it became clear that a reduction in the preliminary list of proposed activities was necessary. The development of a mass spectrometer diagnostics system was eliminated from consideration because of the resources and time needed. These same considerations led to assigning a lower priority to the PEBF system. During the course of the test work in the AEDC FPST, hardware failures forced a reduction in the planned test program. While such problems were not unexpected

because of the nature of the facility, it was nonetheless a disappointment. However, even with these setbacks the program produced a number of significant accomplishments.

In all facility development and CFD code validation activities the key issue is the availability of appropriate, accurate, and reliable data on the parameters of interest. As a result, the development of NID techniques became the controlling activity of the program. The successful application of existing NID techniques, including the extension and further development of some of these, and the acquisition of new techniques constitutes a major portion of the success of this joint program.

Since the advancement of CFD capabilities was a primary goal of the project, there was a significant effort to use the test data acquired with conventional instrumentation and also the data acquired with the advanced NID techniques to test and compare the CFD codes used by the partners. There was also the opportunity to reexamine existing data. The exchange of raw and reduced data allowed for the validation of data reduction techniques. This was especially valuable in the case of heat transfer, which involves considerable calculation. It was found that the AEDC and DLR methods agreed well, but it is noted that the DLR "indirect" method captured the details without the artificial smoothing required by the AEDC "direct" method.

AEDC acquired new CFD capabilities in the course of this effort. The NEQAIR code was acquired and installed at AEDC. In the course of this effort, AEDC personnel gained valuable experience in the use and development of two-temperature flow codes.

An ambitious but successful NID program was executed at the AEDC Impulse Facility, as well as at the DLR HEG. All NID techniques pursued for application gave useful results with the exception of the PEBF technique that, because of time and resource constraints, did not progress past the laboratory development stage. No FPST-related operational problems were encountered, with the possible exceptions of boundary-layer and recirculation effects on LDA measurements and potential copper absorption effects on HSFV for some conditions. At the DLR HEG the copper absorption effect was significant, and the use of a dye laser pumped by the copper vapor laser was successful at circumventing the absorption problem for HSFV.

Important issues in the operation of shock-driven test facilities are the time required to establish steady flow and the duration of quality test flow. Using data obtained with the HSFV system acquired under this project it was determined that Impulse Facility flow is established within 0.67 msec from the shock tube gage (ST6) trigger pulse, and a nominal run time of 2.5 msec free from driver gas effects is available for nozzle stagnation pressures of less than 1000 atmospheres. This conclusion is supported by the initial results with the LDA system. Facility flow appears optically thick as a result of particulate scattering for nozzle stagnation pressures greater than 1000 atmospheres. Consequently, AEDC will need to develop some means to circumvent this problem in order to use NID techniques at higher stagnation pressures. The HEG flow requires a longer time to establish, some 1.4 msec, while the nominal run time is somewhat shorter than the 2.5

msec of the Impulse Facility. The optically thick threshold is never reached since the HEG operates below 1000 atm.

Another major issue in the operation of high enthalpy facilities is the thermo-chemical state of the flow as it expands through the nozzle. An important indicator of the state is the vibrational temperature. One result of the CFD analysis done under this project is the determination that the measurement of T_v with existing techniques and the prediction with current CFD codes do not result in agreement on the level of T_v . It is clear from the wide range of computational predictions of freestream properties and the lack of agreement of PLIF-NO measurements with any of the predictions, that considerable work is required on CFD physics models, along with a thorough investigation of the current PLIF-NO methodology. Analysis methods using both the laboratory shock tube/tunnel and the newly-acquired high-temperature calibration cell are also required. Future application of LDA requires the use of airtight tubes extending into the boundary layer to eliminate boundary-layer and recirculation effects. It is also recommended that the LDA technique be extended to yield information on flow velocity. Another aid in resolving the T_v question would be the further development of the PEBF technique. This technique can readily give information on vibrational temperature for a number of species simultaneously. Furthermore, the PEBF technique potentially can provide quantitative information on the amount of helium contaminating the test gas.

While questions still remain about the determination of the nozzle freestream conditions, the CFD analyses and code comparisons accomplished under this project showed that model parameters could be reasonably predicted with conventional CFD codes. For example, shock wave location can be predicted quite reliably. When used in conjunction with high-speed flow visualization, the observed change in shock shape can be correlated with He arrival. Pressure distributions were reasonably well predicted. It was observed that pressure is relatively insensitive to "real gas" effects. Heat transfer, on the other hand, was found to be sensitive to "real gas" effects. The assumption of a catalytic wall gave a better prediction compared to that of a noncatalytic wall. Predictions of heat transfer would be generally considered adequate.

An integral part of this program was an ambitious plan for the use of nonintrusive diagnostics to provide key information about the flow field. The requirements for NID are to provide multiple, independent measurements to yield information about run time, thermal nonequilibrium, spatial variations of flow properties, flow temporal evolution, and particulate contamination. Numerous NID techniques in various stages of development were considered for application at the AEDC Impulse Facility and the DLR HEG, and the list of information that can potentially be provided by NID is rather lengthy. Unfortunately, cost and timeliness considerations limited the NID techniques undertaken for the AEDC Impulse Facility as well as the DLR HEG.

If the old adage "a picture is worth a thousand words" is true, then a major accomplishment under this project was the acquisition and implementation of the High-Speed Flow Visualization System. With this system, an image sequence of nominally 100 frames could be obtained during a tunnel run. Depending on the laser framing rate, this would cover from 4.0 to 12.5 msec of tunnel

run time. From these pictures it was possible to clearly observe the flow establishment in the test section. As previously noted, the change in the flow field around the model could also be correlated with the arrival in the test section of contamination by the helium driver gas.

As noted in the CFD discussions, the wide range of computational predictions of freestream properties and the lack of agreement of PLIF-NO measurements with any of the predictions clearly shows that considerable work is required on CFD physics models. A thorough investigation of the current PLIF-NO methodology and analysis methods using both the laboratory shock tube/tunnel and the newly acquired high-temperature calibration cell is also required. Further development of LDA is needed to eliminate boundary-layer and recirculation effects and to yield information on flow velocity. As the question of vibrational nonequilibrium has not been resolved, it is recommended that the PEBF technique be developed further, because it can readily give information on vibrational temperature for a number of species simultaneously. Furthermore, the PEBF technique potentially can provide quantitative information on the amount of helium contaminating the test gas.

As a result of this international cooperative program, AEDC NID capability has been greatly enhanced. The HSFV system is now available for applications to hypersonic air-breathing propulsion, aero-optics, jet interaction, and ballistic range testing. Indeed, the association with ND, Inc. with regard to advancements in high-speed holographic recording has placed AEDC on the leading edge of high-speed visualization capability. The LDA system methodology has already been advanced for use with absorption by O_2 , H_2O , and K , and applications in turbine engine and hypersonic air-breathing propulsion testing as well as aerodynamic testing are forthcoming. Although applications of the PEBF system were not achieved, the capability of the system was greatly advanced, and it probably will become an outstanding diagnostic tool for the high Mach number conditions of AEDC's Tunnel 9.

REFERENCES

1. Stalker, R. J. "The Free-Piston Shock Tube." *The Aeronautical Quarterly*, Vol. 17, November 1966, pp. 351-370.
2. Hornung, H., et al. "Performance Data of the New Free Piston Shock Tunnel T5 at GALCIT." 18th Symposium on Shock Waves and Shock Tubes, 1991.
3. Eitelberg, G., McIntyre, T. J., Beck, W. H., and Lacey, J. "The High Enthalpy Shock Tunnel in Göttingen." AIAA Paper 92-3942, July 1992.
4. Blanks, J. R. "Initial Calibration of the AEDC Impulse Tunnel." AEDC-TR-95-36 (ADA311751), August 1996.

5. Itoh, K., Ueda, S., Komuro, T., Sato, K., Takahashi, M., Miyajima, H., and Koga, K. "Design and Construction of HIEST (High Enthalpy Shock Tunnel)." Proceedings of the International Conference on Fluid Engineering, Vol. 1, 1997, pp. 353-358.
6. Eitelberg, G. "First Results of Calibration and Use of the HEG." AIAA-94-2525, June 1994.
7. McIntosh, M. "Computer Program for the Numerical Calculation of Frozen and Equilibrium Conditions in Shock Tunnels." Department of Physics, School of General Studies, Australian National University, Canberra, 1968.
8. Hannemann, K., et al. "The Influence and the Delay of Driver Gas Contamination in HEG." AIAA 21st Aerodynamic Measurement Technology and Ground Testing Conference, Denver, CO, June 19-22, 2000.
9. Kindl, H. and Olivier, H., "Development of a Static Pressure Probe." HT-SF-E34-711-RWTH, Shock Wave Laboratory, Aachen, Germany.
10. Hannemann, K., et al. "Combined Experimental and Numerical Characterization of the HEG Test Section Flow." Proceedings of the 22nd International Symposium of Shock Waves, London, UK, 1999.
11. Davis, J. P. "High Enthalpy Shock/Boundary Layer Interaction on a Double Wedge." PhD Thesis, California Institute of Technology, 1999.
12. Maus, J., Blanks, J., and DeWitt, J. "Calibration Test of a New Free-Piston Shock Tunnel." AIAA-93-5003, December 1993.
13. Krek, R. M., and Eitelberg, G. "Classical Characterization of HEG (Nozzle, Freestream Flow Field)." DLR-IB-223-94 A 50, 1994.
14. Maus, J. R., and Rock, S. G. "Computational Results for AEDC Free-Piston Shock Tunnel and Comparison with Calibration Data." AIAA-95-6039, April 1995.
15. Molvik, G. A., and Merkle, C. L. "A Set of Strongly Coupled, Upwind Algorithms for Computing Flows in Chemical NonEquilibrium." AIAA-89-0199, January 1989.
16. Park, C. "Nonequilibrium Air Radiation (NEQAIR) Program: Users Manual." NASA TM-86707, July 1985.
17. Olyneck, D. R., et al. "Comparisons of Coupled Radiative Navier-Stokes Flow Solutions with the Project Fire II Flight Data." AIAA-94-1955, June 1994.
18. Walters, R. W. "GASP Version 3 Users Manual." Aerosoft, Inc., Blacksburg, VA, May 1996.
19. Rock, S. G., and Tramel, R. W. "A Three-Dimensional Thermo-Chemical Nonequilibrium Chimera Flow Solver for Moving Grids, Part I: Steady State." AIAA-95-0151, January 1995.

20. Park, C. "Convergence and Computation of Chemical Reacting Flows." 'Thermophysical Aspects of Re-Entry Flows,' *Progress in Astronautics and Aeronautics*, Vol. 103, 1986, pp. 478-513.
21. Ebrahimi, Houshang B. "Numerical Investigation of Twin-Nozzle Rocket Plume Phenomenology, Part II." AIAA-98-0924, January 1998.
22. Holcomb, J. Eric. "Development of an Adaptive Grid Navier-Stokes Analysis Method for Rocket Base Flows." AIAA-88-2905, July 1988.
23. Brenner, G., Gerhold, T., Hannemann, K., and Rues, D. "Numerical Simulation of Shock/Shock and Shock-Wave/Boundary Layer Interactions in Hypersonic Flows." *Computers and Fluids*, Vol. 22, 1993, pp. 427-439.
24. Yee, H. C., and Harten, A. "Implicit TVD Schemes for Hyperbolic Conservation Laws in Curvilinear Coordinates." *AIAA Journal*, Vol. 25, 1987, pp. 266-274.
25. Roe, P. L. "Approximate Riemann Solvers, Parameter Vectors and Difference Schemes." *Journal of Computational Physics*, Vol. 43, No. 2, 1981, pp. 357-372.
26. Liu, Y., and Vinokur, M., "Upwind Algorithms for General Thermo-chemical Nonequilibrium Flows." AIAA-89-0201, January 1989.
27. Brück, S., Radespiel, R., and Longo, J. M. A. "1997 Comparison of Nonequilibrium Flows Past a Simplified Space Shuttle Configuration." AIAA 97-0275, January 1997.
28. Cook, W. J., and Felderman, E. J. "Reduction of Data from Thin-Film Heat-transfer Gages; a Concise Numerical Technique." *AIAA Journal*, Vol. 4, March 1966, pp. 561-562.
29. Neumann, R. D. "Aerothermodynamic Instrumentation." Special Course on Aerothermodynamics of Hypersonic Vehicles, AGARD R-761, 1988.
30. Williams, W. D., et al. "Non-intrusive Diagnostics for the AEDC Impulse Facility, Application and Results." 18th International Congress on Instrumentation for Aerospace Facilities Record, Toulouse, France, June 14-17, 1999.
31. Trinks, Ole. "Diode Laser-Atomic Absorption Spectroscopy of Atomic Rubidium in the High Enthalpy Tunnel HEG for Determining Flow Velocities and Gas Temperatures." DLR-IB 223-97 A31, September 1997.
32. Ruyten, W. M., Smith, M. S., Price, L. L., and Williams, W. D. "Three-Line Fluorescence Thermometry of Optically Thick Shock-Tunnel Flow." *Applied Optics*, Vol. 37, No. 12, April 20, 1998, pp. 2334-2339.
33. Muntz, E. P. "The Electron Beam Fluorescence Technique." NATO AGARDograph 132, 1968.

34. Gochberg, Lawrence A. "The Electron Beam Fluorescence Technique in Hypersonic Aerothermodynamics." AIAA-94-2635, June 20-23, 1994.
35. Christiansen, J., and Schultheiss, C. "Production of High Current Particle Beams by Low Pressure Spark Discharges." *Z. Physik*, Vol. A290, 1979, pp. 35-4.
36. Frank, K., and Christiansen, J. "The Fundamentals of the Pseudospark and Its Applications." *IEEE Transactions on Plasma Science*, Vol. 17, No. 5, October 1989, pp. 748-753.
37. Benker, Winfried, Christiansen, Jens, Frank, Klaus, Gundel, Hartmut, Hartmann, Werner, Redel, Thomas, and Stetter, Michael. "Generation of Intense Pulsed Electron Beams by the Pseudospark Discharge." *IEEE Transactions on Plasma Science*, Vol. 17, No. 5, October 1989, pp. 754-757.
38. Christiansen, J. "The Properties of the Pseudospark Discharge." *Physics and Applications of Pseudosparks*, edited by M. A. Gundersen and G. Schaefer, Plenum Press, New York, 1990, pp. 1-13.
39. Wojcik, Radoslaw M., Schilling, John H., and Erwin, Daniel A. "Rarefied Flow Diagnostics Using Pulsed High-Current Electron Beams." AIAA 90-1515, Seattle, WA, June 18-20, 1990.
40. Erwin, Daniel A., Kunc, Joseph A., and Muntz, E. Phillip. "A New Technique for Temperature and Specie Concentration Measurements in Unseeded Supersonic and Hypersonic Gas Flows." AFOSR-TR-91-0808 (ADA241536), August 9, 1991.
41. Lutfy, F. M., and Muntz, E. P. "Initial Experimental Study of Pulse Electron Beam Fluorescence." *AIAA Journal*, Vol. 34, No. 3, March 1996, pp. 478-482.
42. Muntz, E. P., Lutfy, F. M., and Boyd, I. D. "The Study of Reacting, High Energy Flows Using Pulsed Electron Beam Fluorescence." AIAA 96-1986, New Orleans, LA, June 17-20, 1996.
43. Lutfy, Fred M., and Muntz, E. P. "Spectroscopic Survey of Gases Found in Hypersonic Flows Using Pulsed Electron Beam Fluorescence." AIAA 99-2452, Los Angeles, CA, June 20-24, 1999.

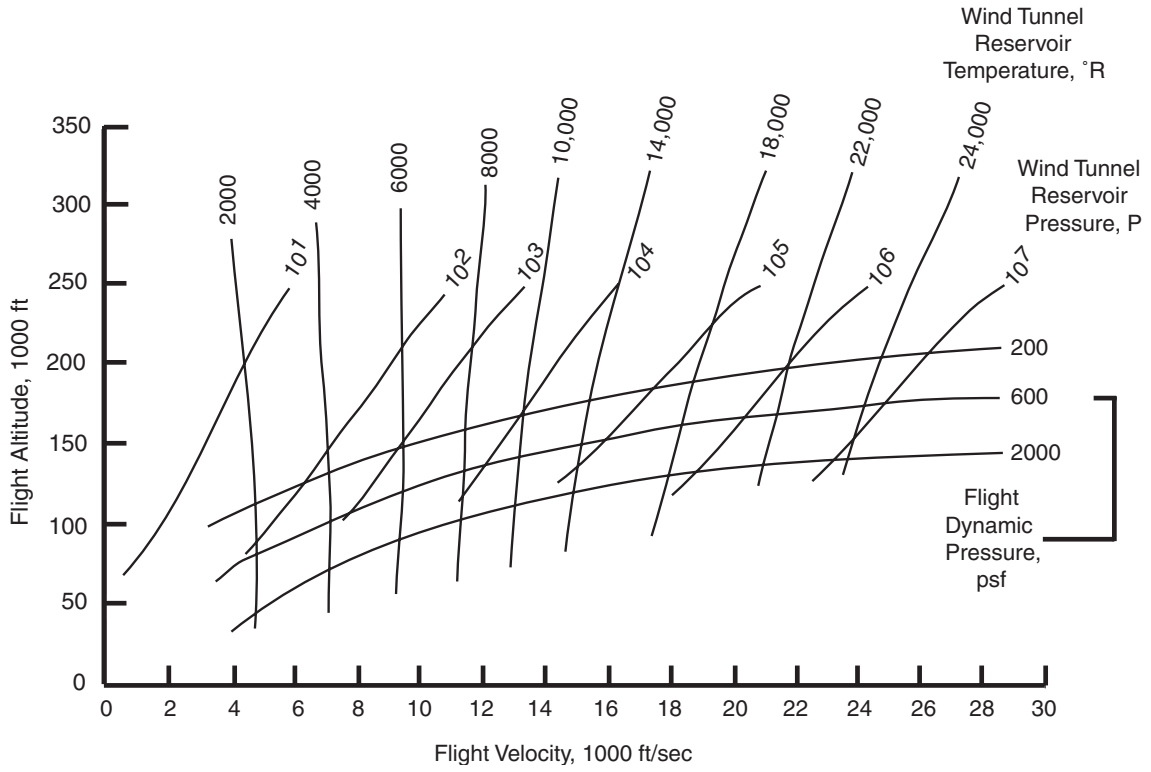


Figure 1. Conditions Required to Duplicate Flight Conditions

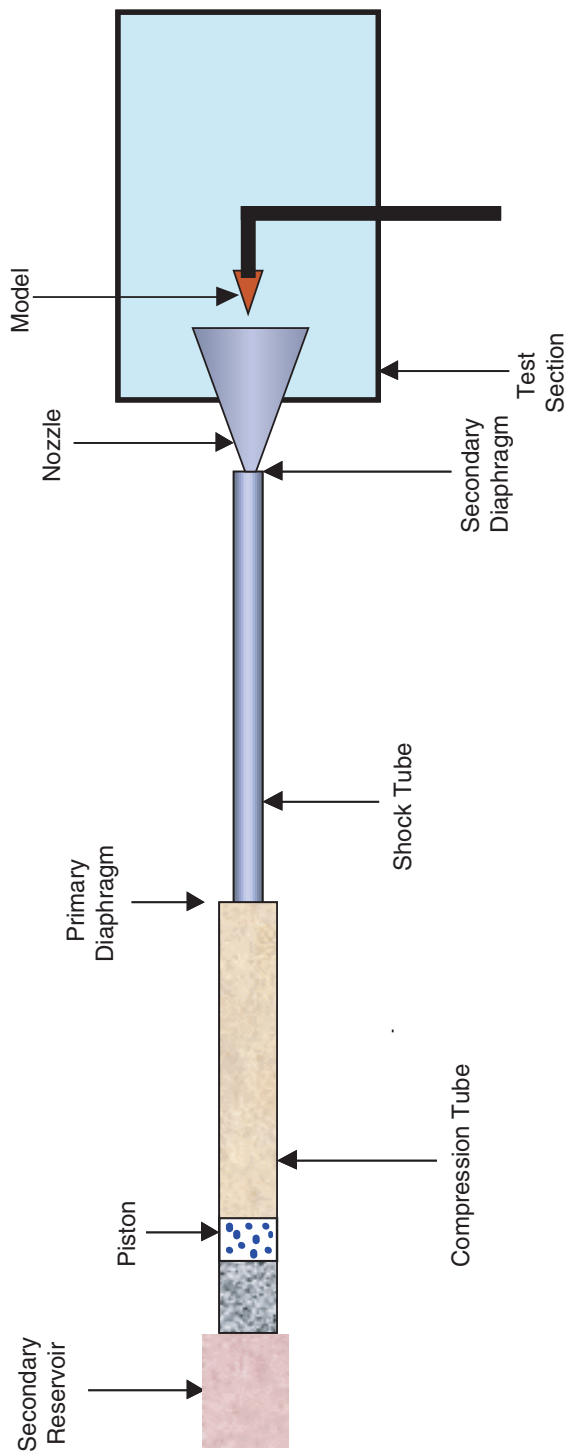


Figure 2. Free-Piston Shock Tunnel

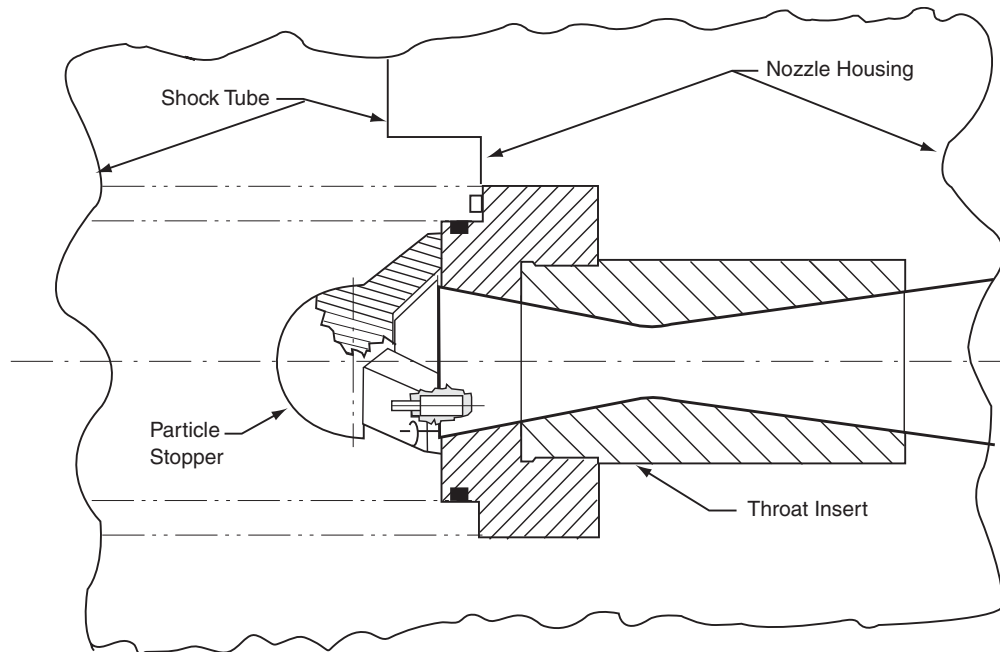


Figure 5. Particle Stopper

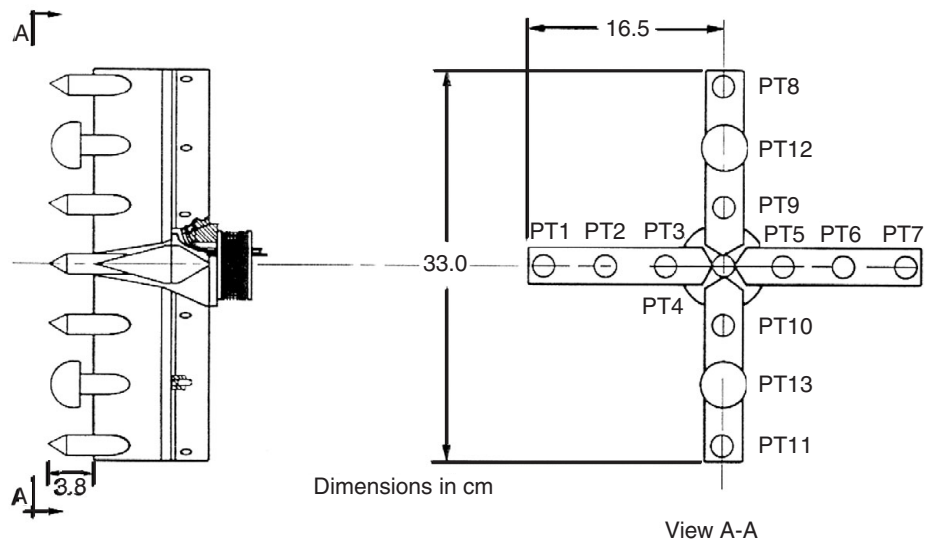


Figure 6. Calibration Rake

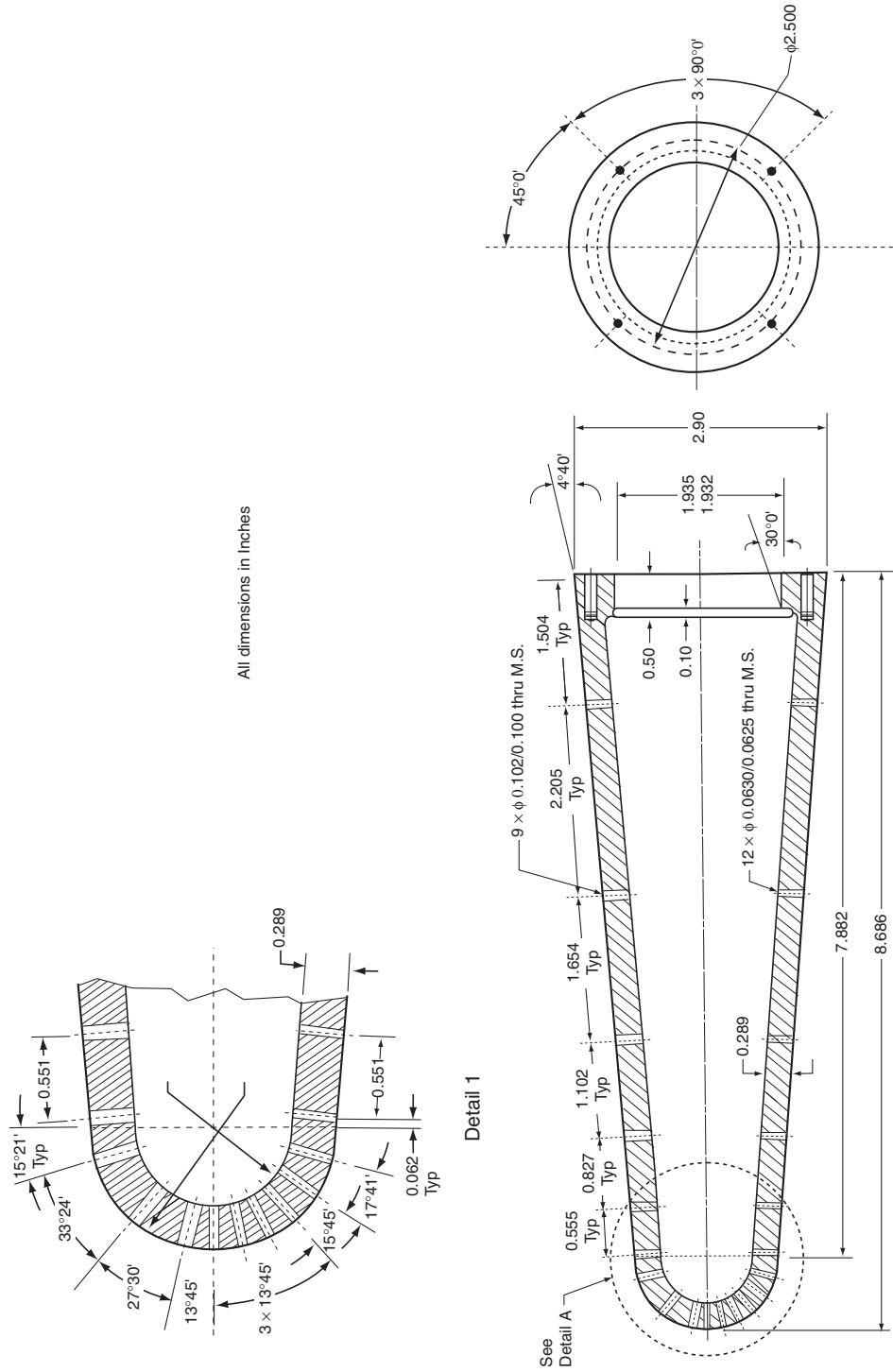
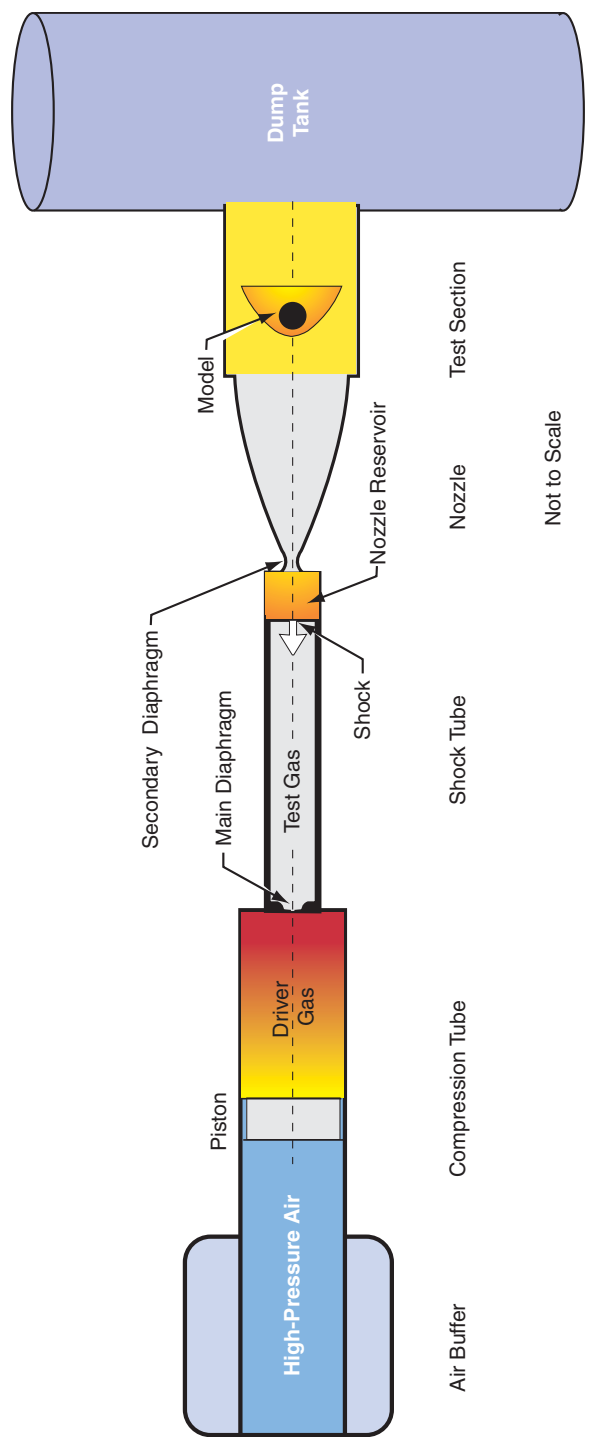


Figure 7. AEDC Blunt Slender Cone (Electre) Model, 70-percent Scale



Not to Scale

Figure 8. Schematic View of the HEG

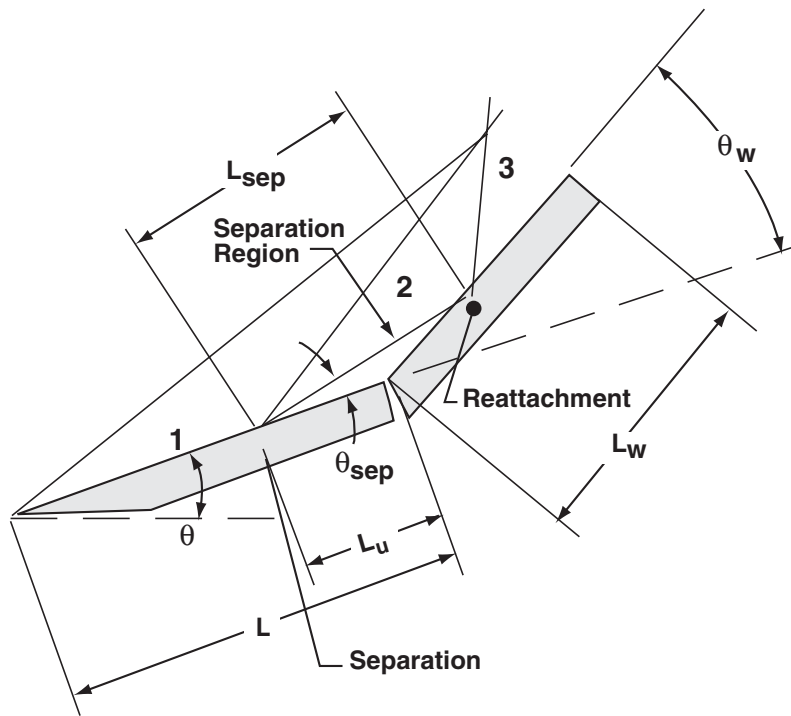
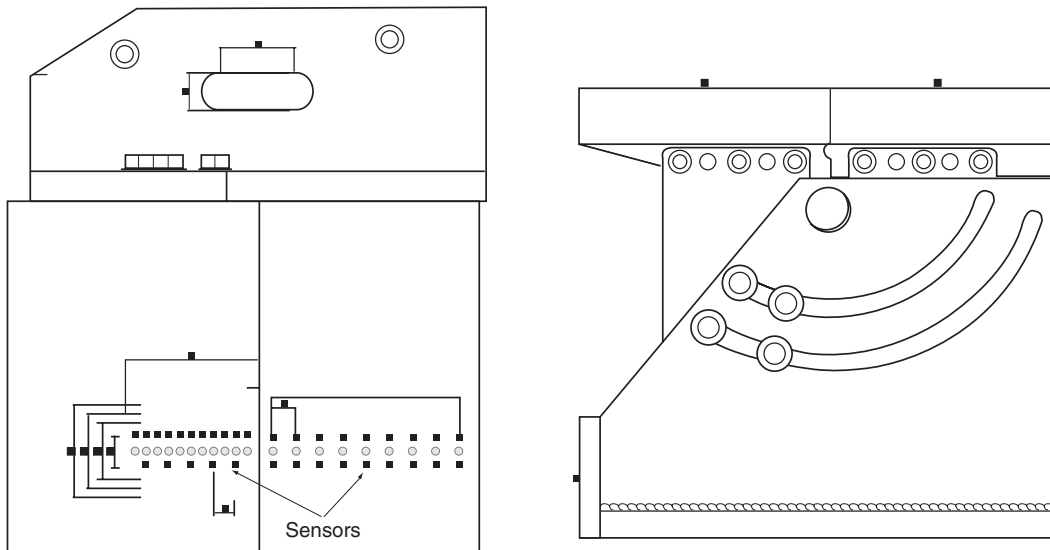


Figure 9. Double-Ramp Model; Dots Indicate Sensor Positions

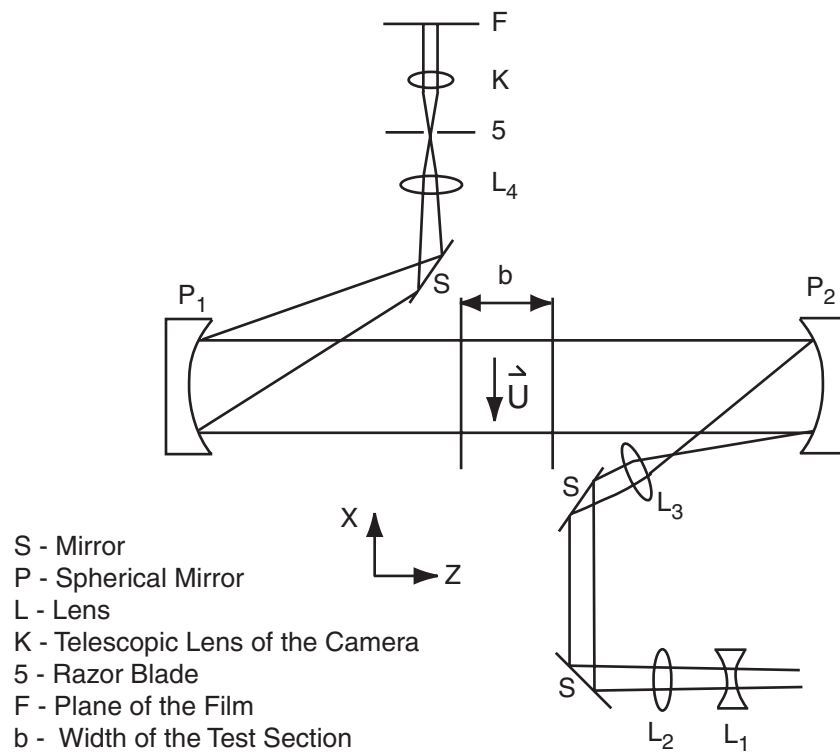


Figure 10. Schematic of Schlieren Apparatus

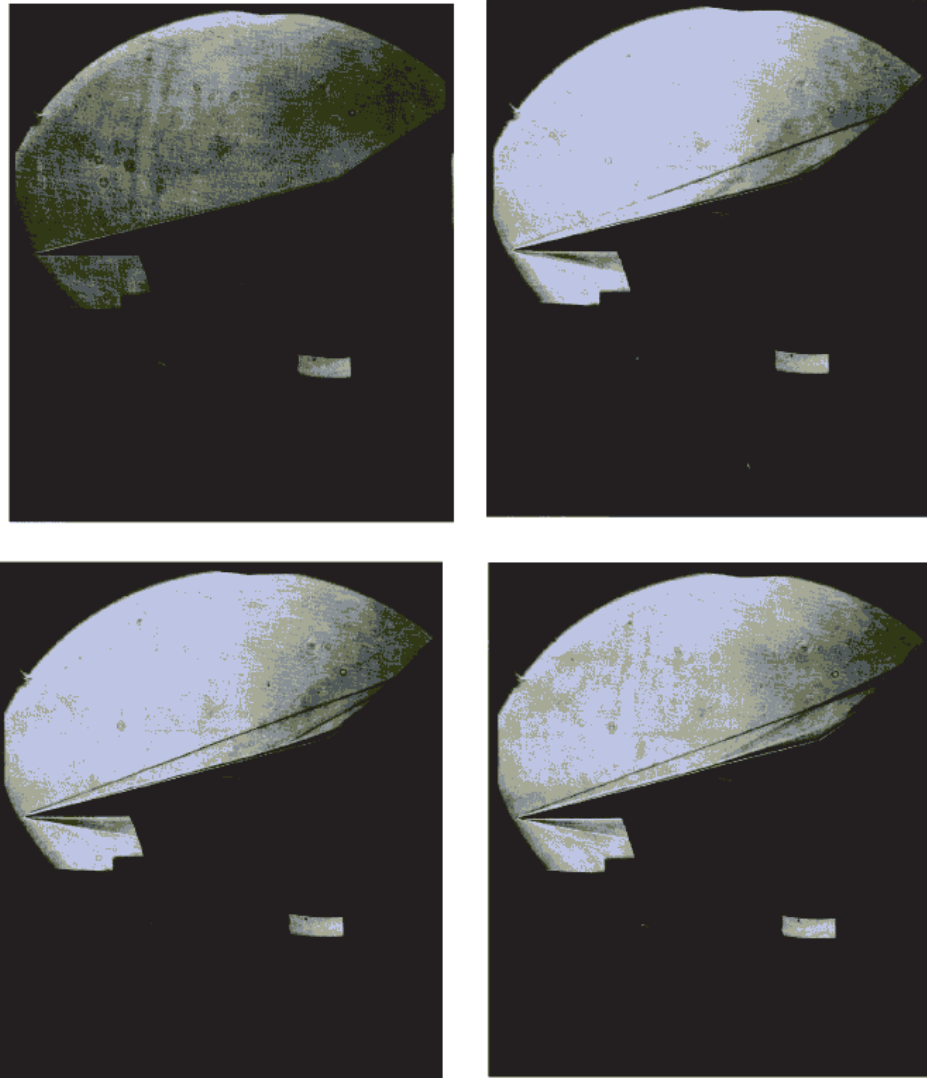


Figure 11. Schlieren Pictures of the Double-Wedge Flow Showing the Establishment of Separation ($\Delta t = 0.6$ msec Between Frames)

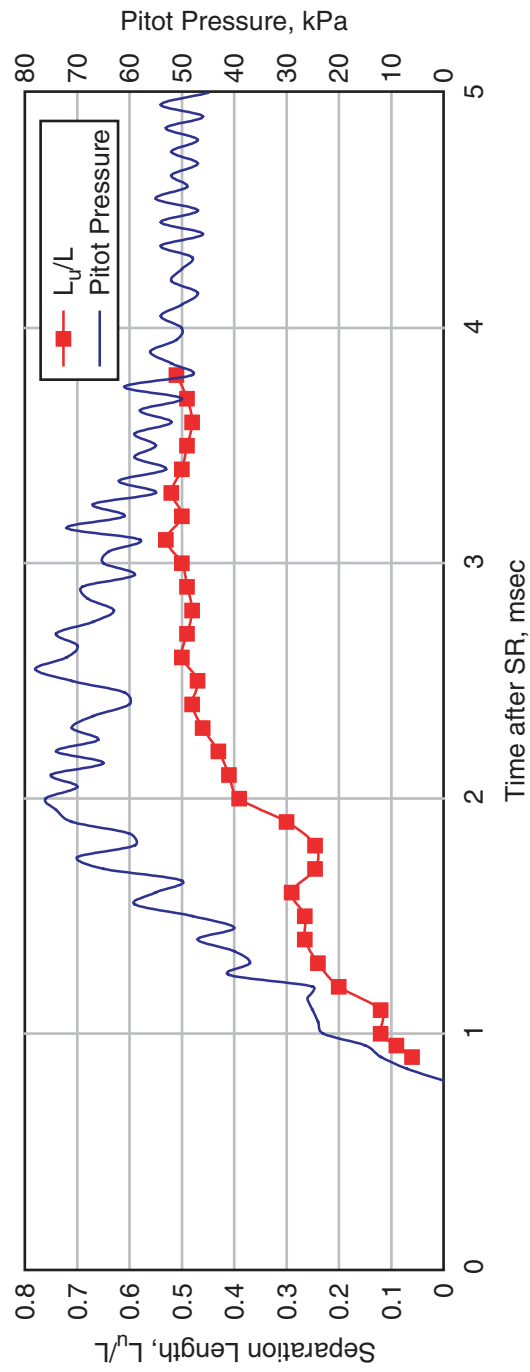


Figure 12. L_u as a Function of Time in Comparison to Pitot Pressure, HEG Run 453, Condition III

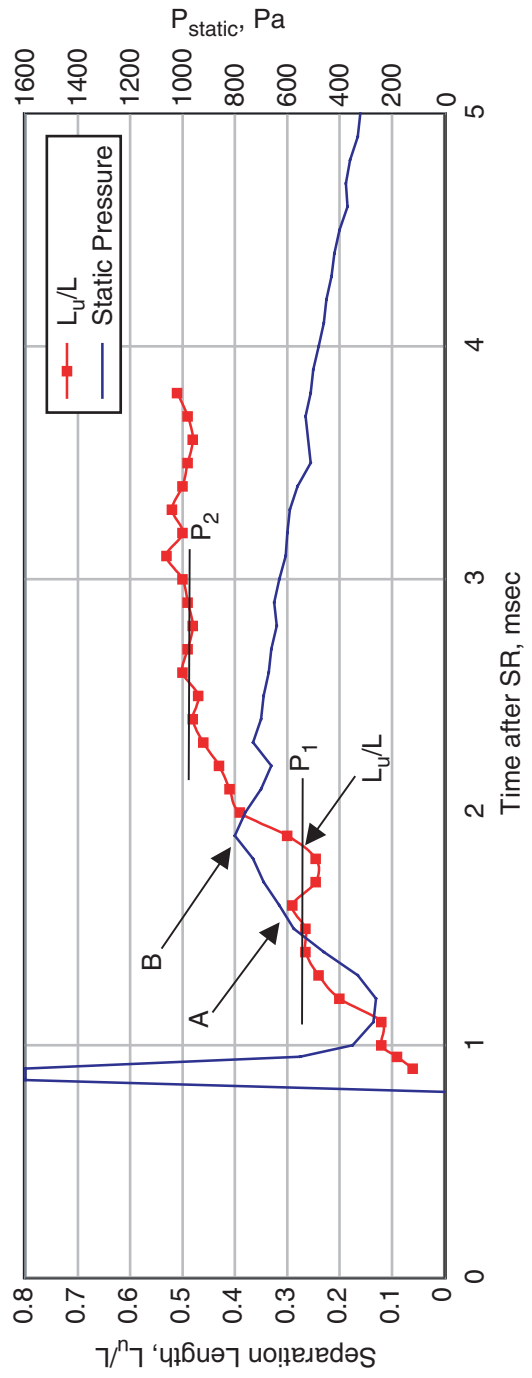


Figure 13. L_u as a Function of Time in Comparison to Static Pressure for HEG Run 453 and Condition III

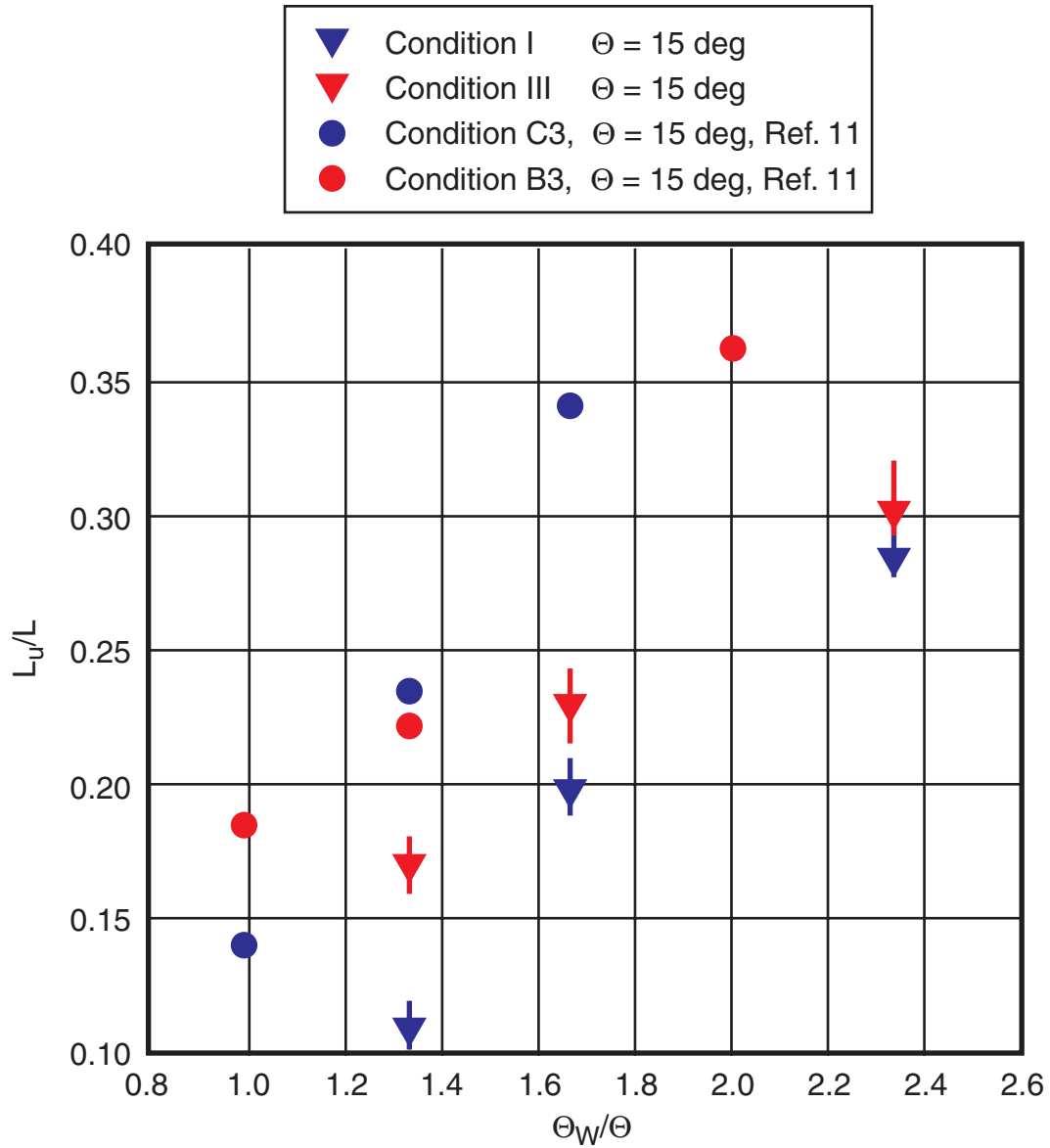


Figure 14. Results for L_u in High and Low Enthalpy Conditions in Comparison to the Measurements to Ref. 11

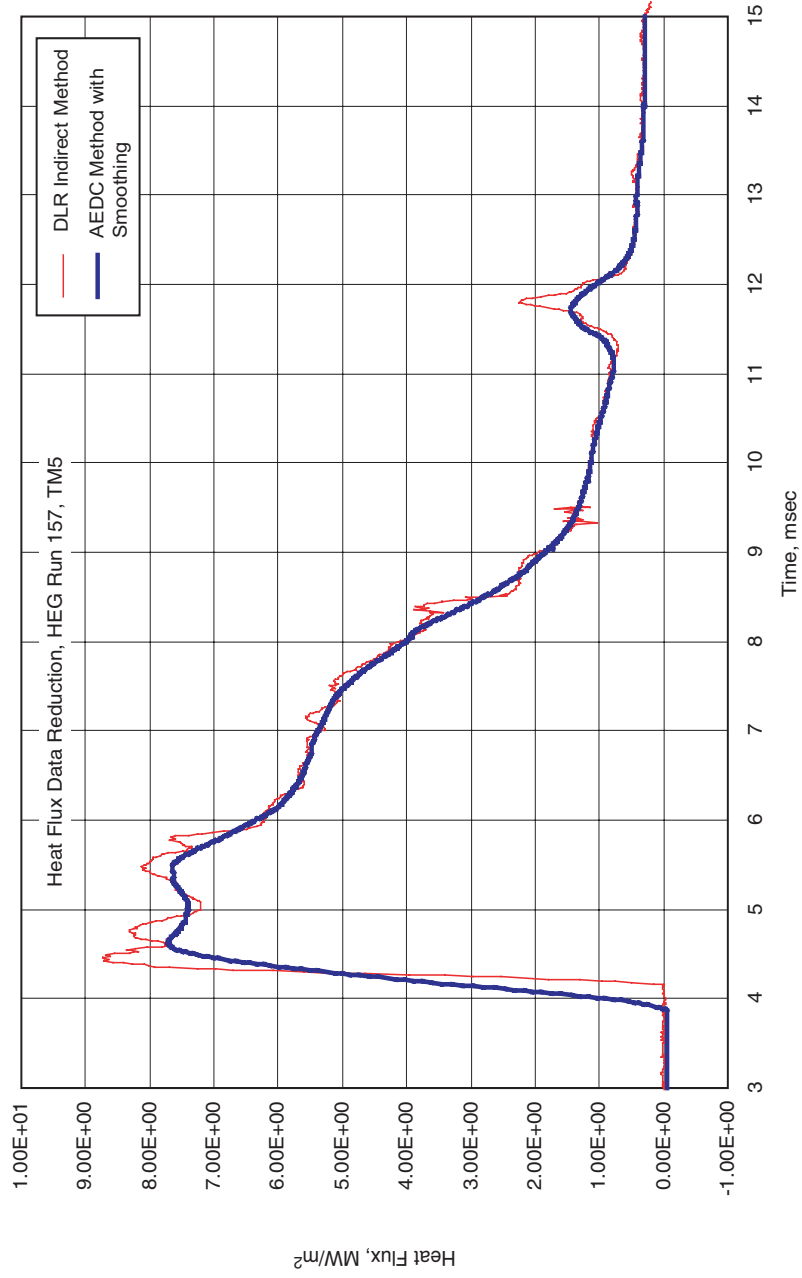


Figure 15. Comparison Between AEDC and HEG Heat Flux Calculation Methods

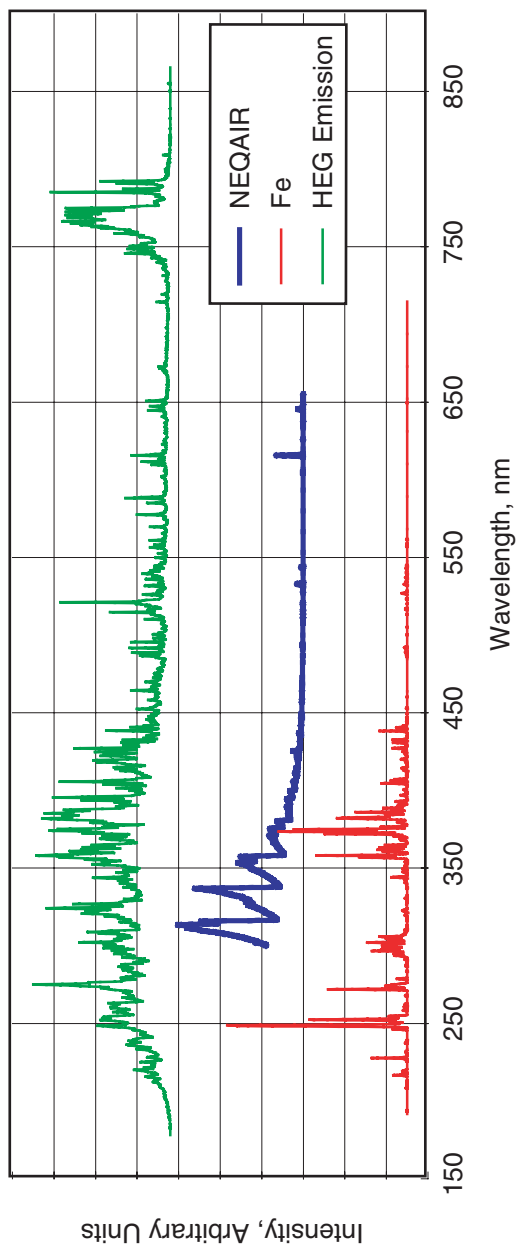


Figure 16. Computed Spectra

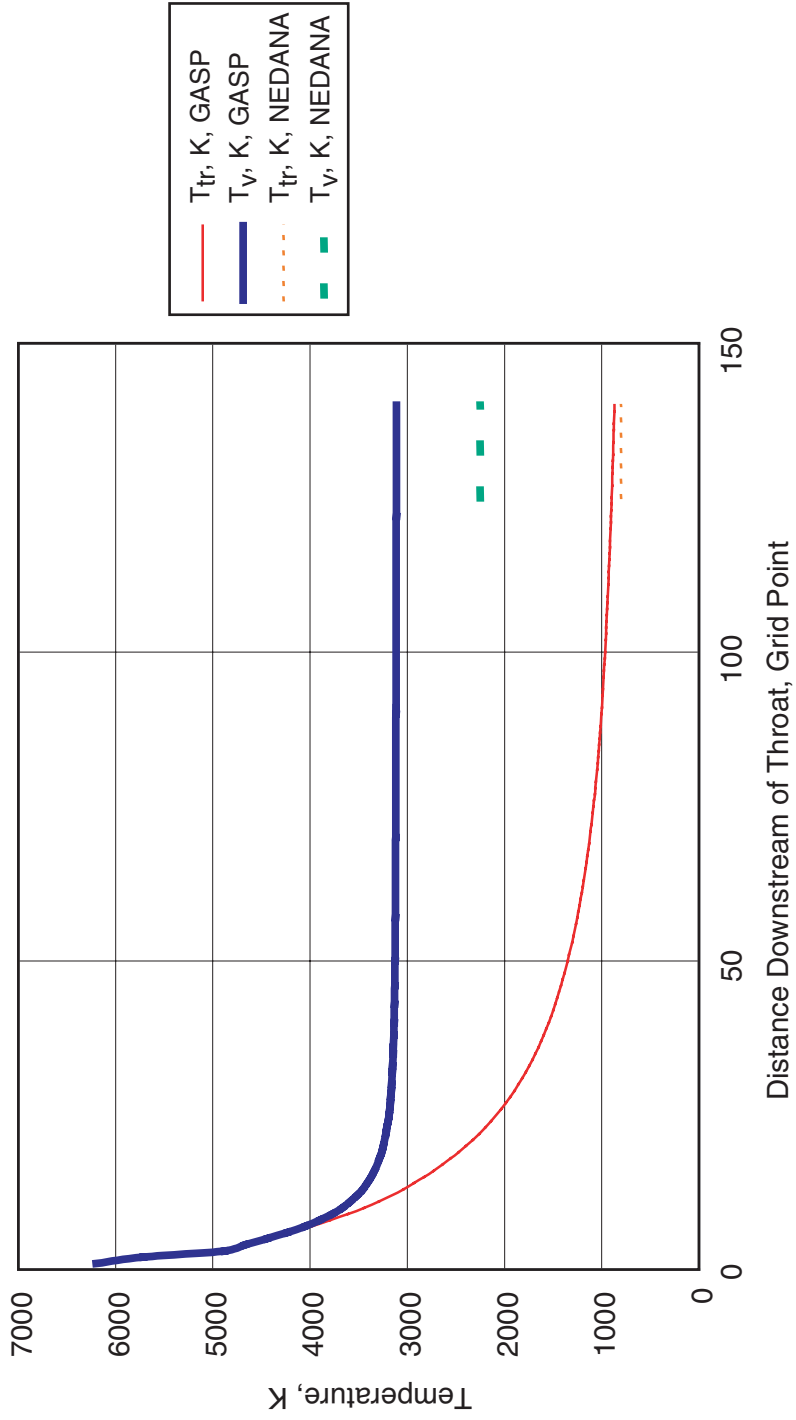


Figure 17. Predicted Temperatures in AEDC Impulse Tunnel Nozzle, Run 30

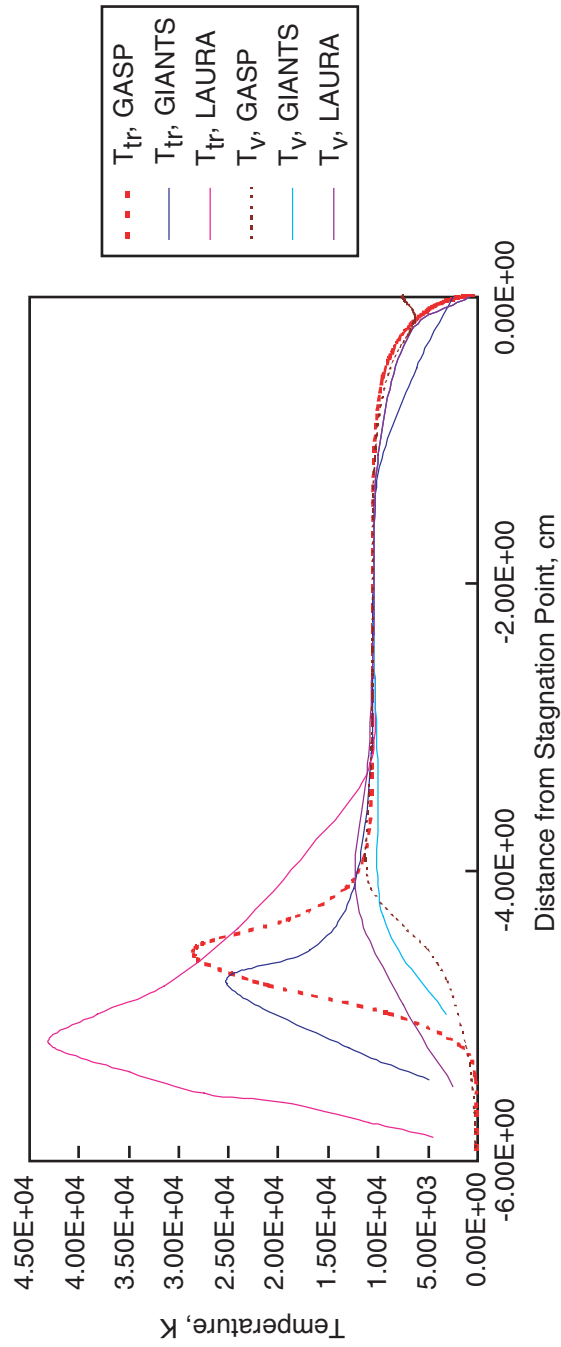


Figure 18. Vibrational and Rotational Temperatures Predicted by the GASP, GIANTS, and LAURA Codes - Fire II

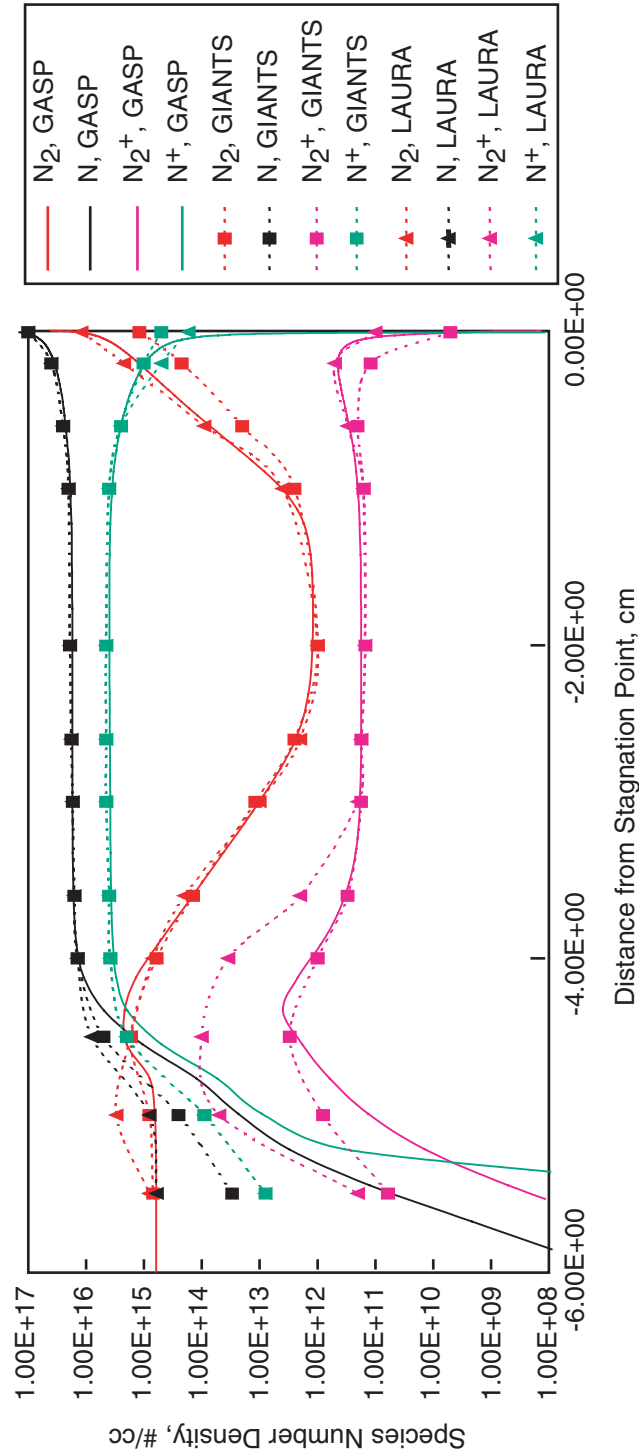


Figure 19. Nitrogen Species Predicted by the GASP, GIANTS, and LAURA Codes - Fire II, 1634 sec

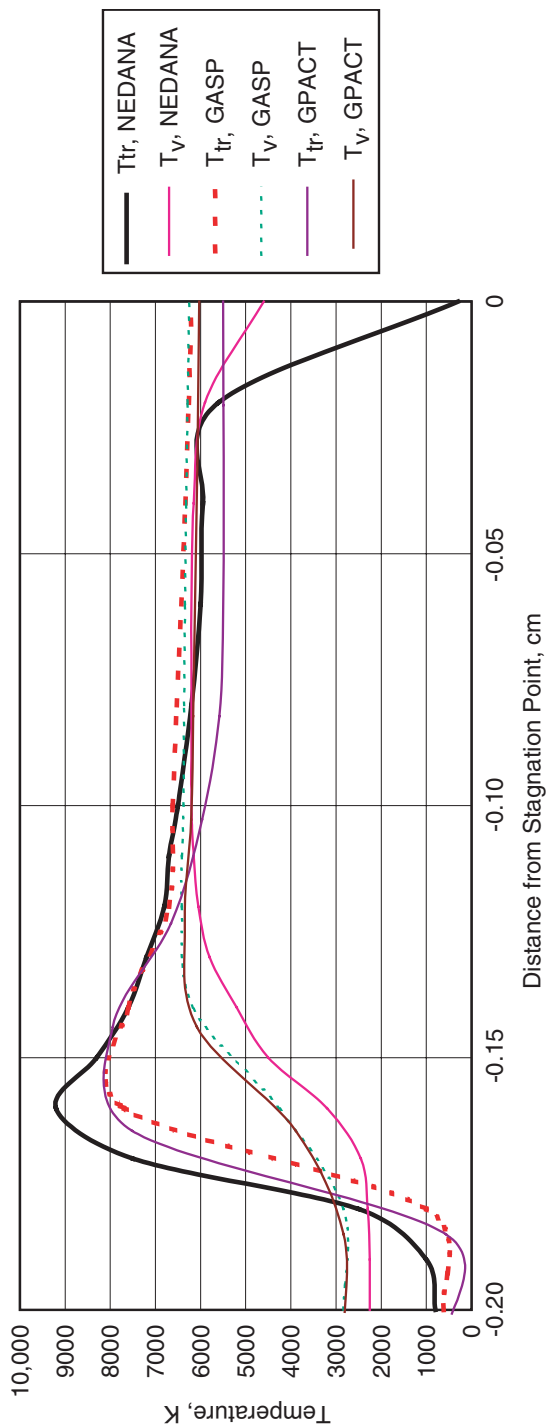


Figure 20. Vibrational and Rotational Temperatures Predicted by the GASP, GPACK, and NEDANA Codes

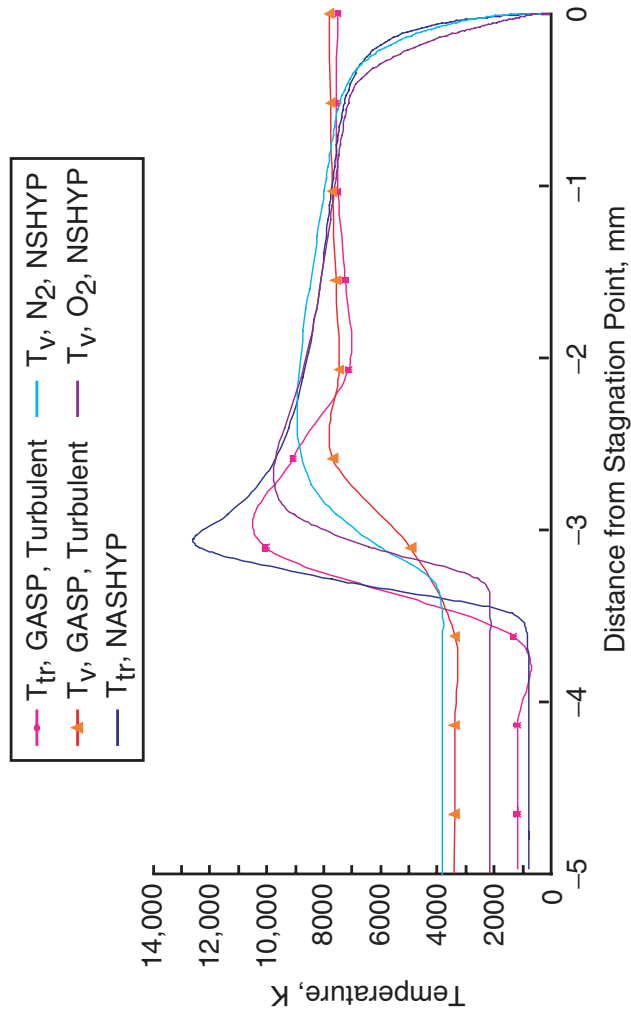


Figure 21. Vibrational and Rotational Temperatures Predicted by the GASP and NSHYP Codes — Sphere-Cone, HEG Condition I

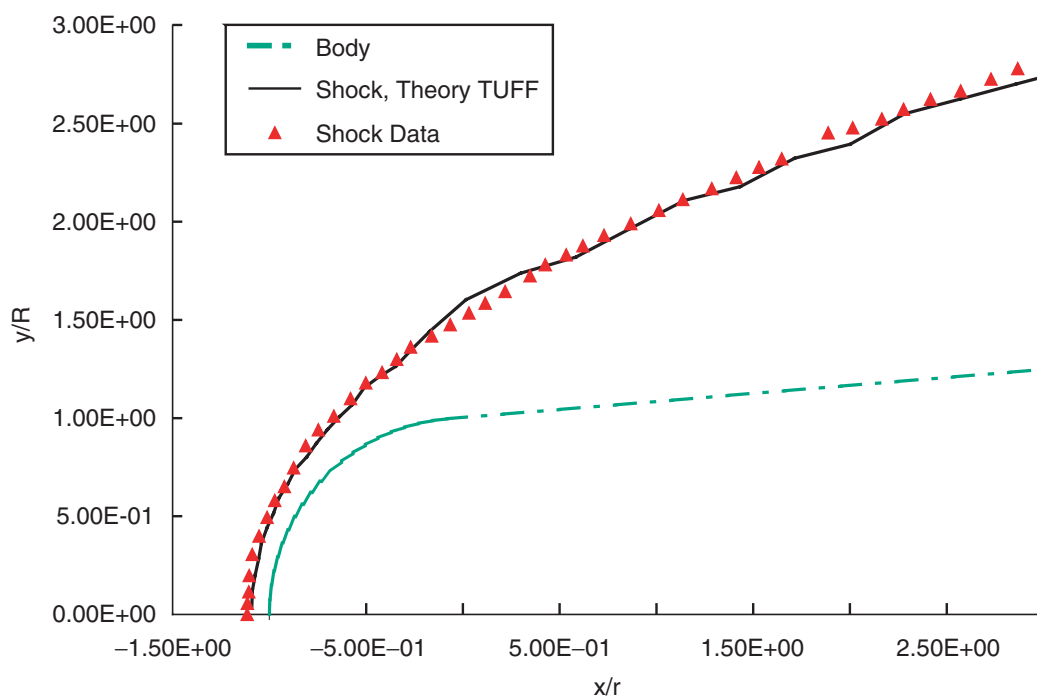


Figure 22. Shock Shape Comparisons, AEDC Run 31

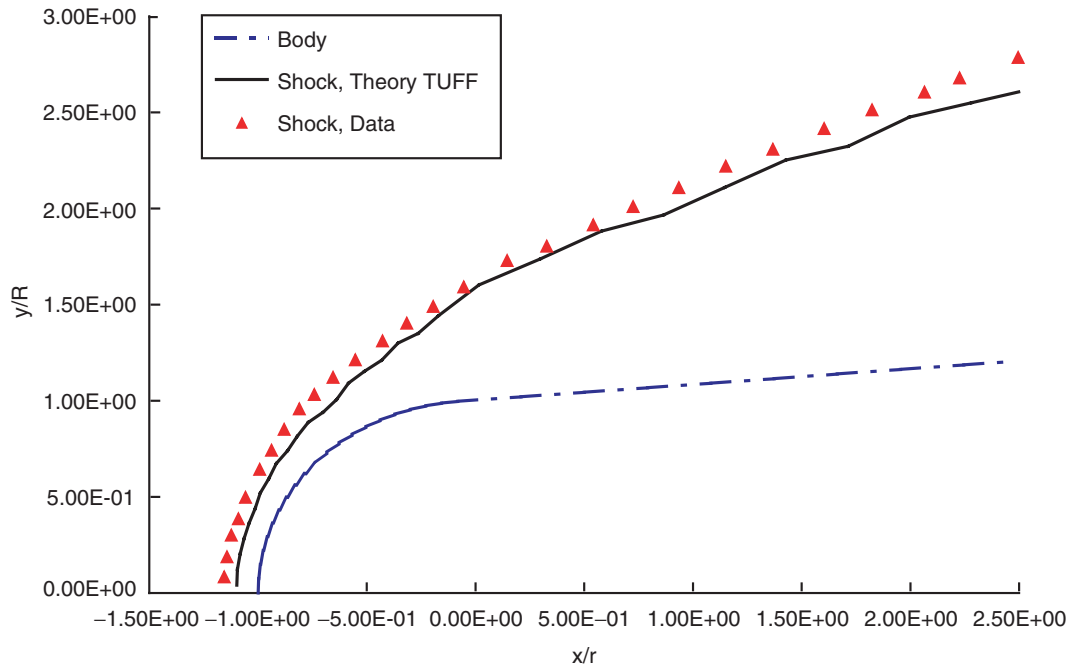


Figure 23. Shock Shape Comparisons, AEDC Run 34

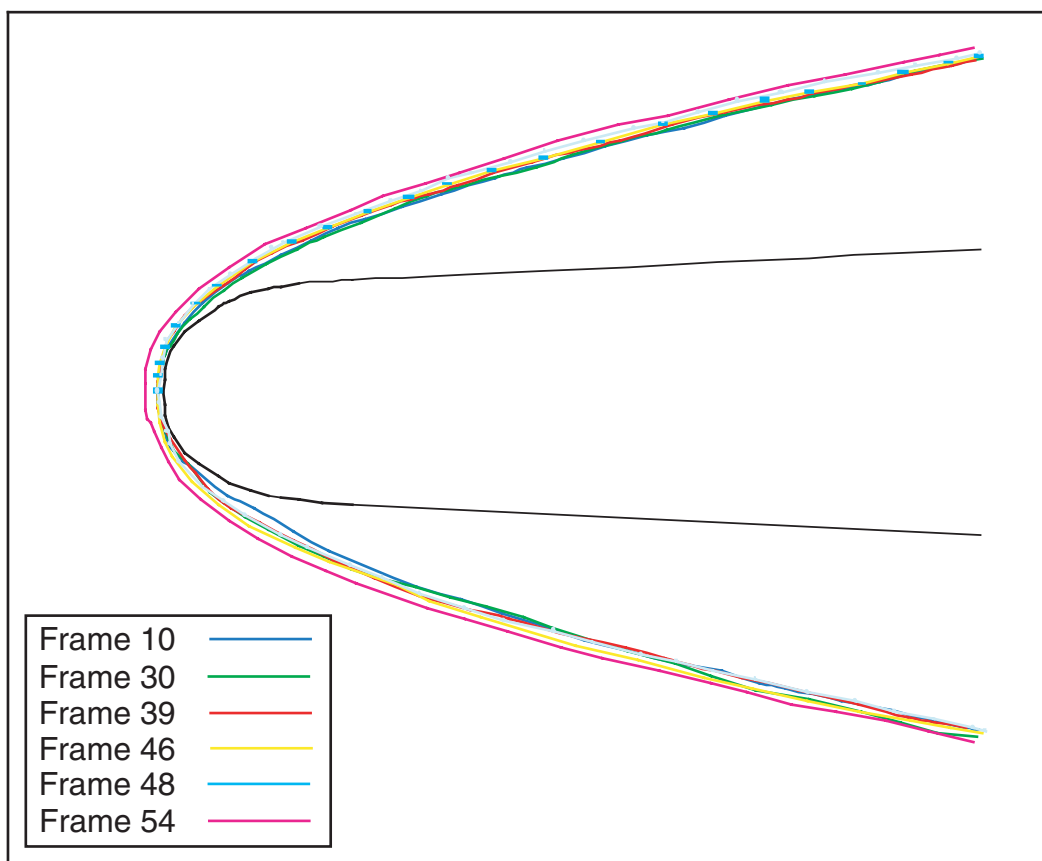


Figure 24. Shock Shape Variation with Time

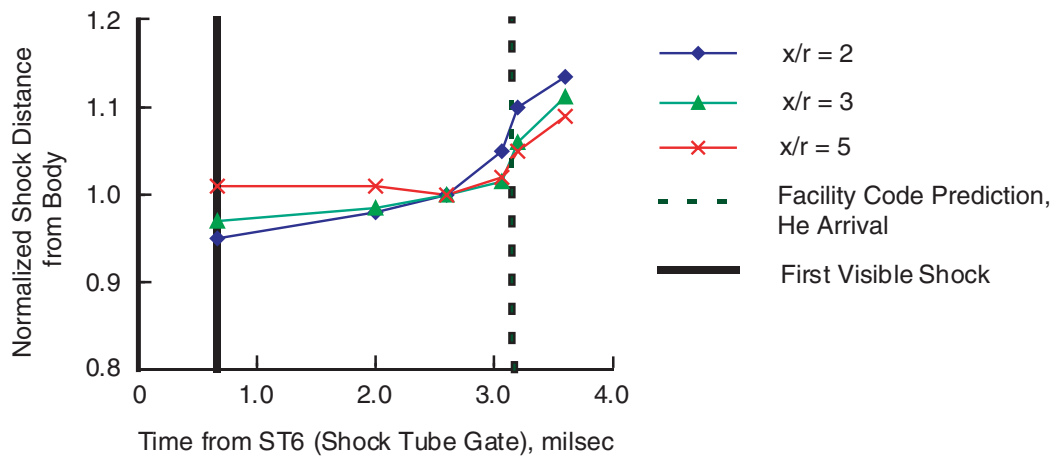


Figure 25. Run Time Determination Using Shock Shape

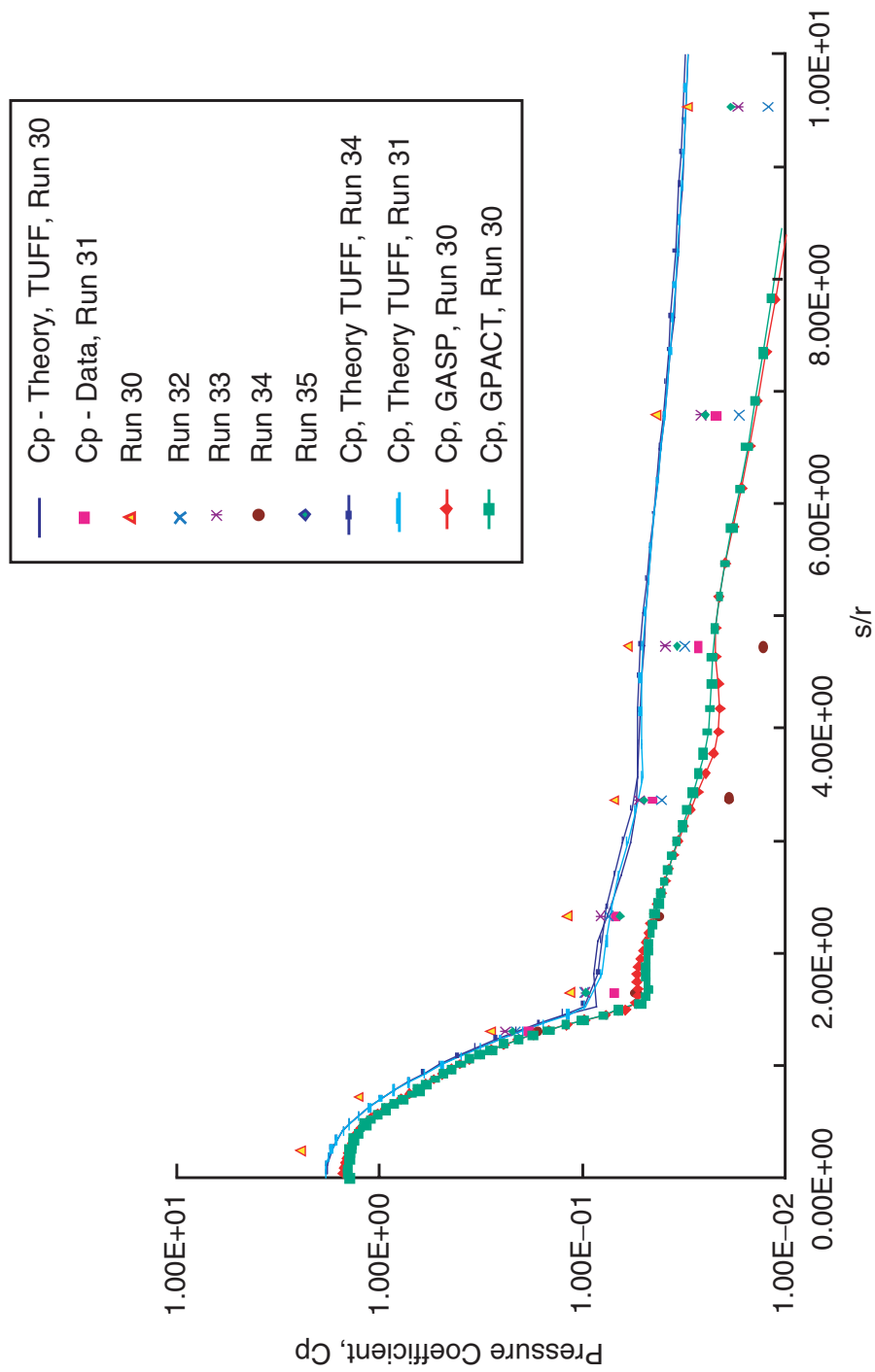


Figure 26. Pressure Coefficient, AEDC Runs 30-35, Electre Model (70 percent)

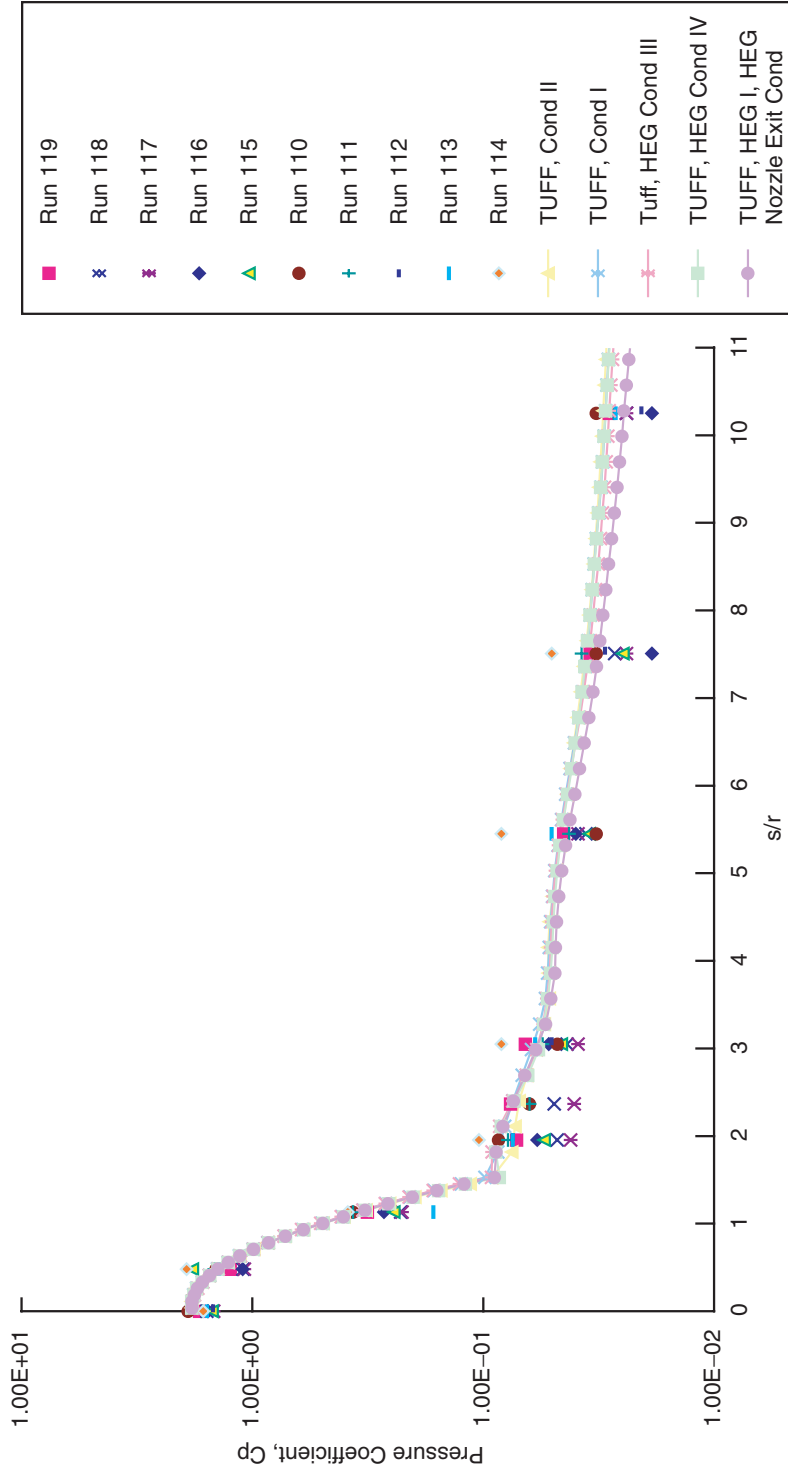


Figure 27. Pressure Coefficient, DLR Electre Model in HEG

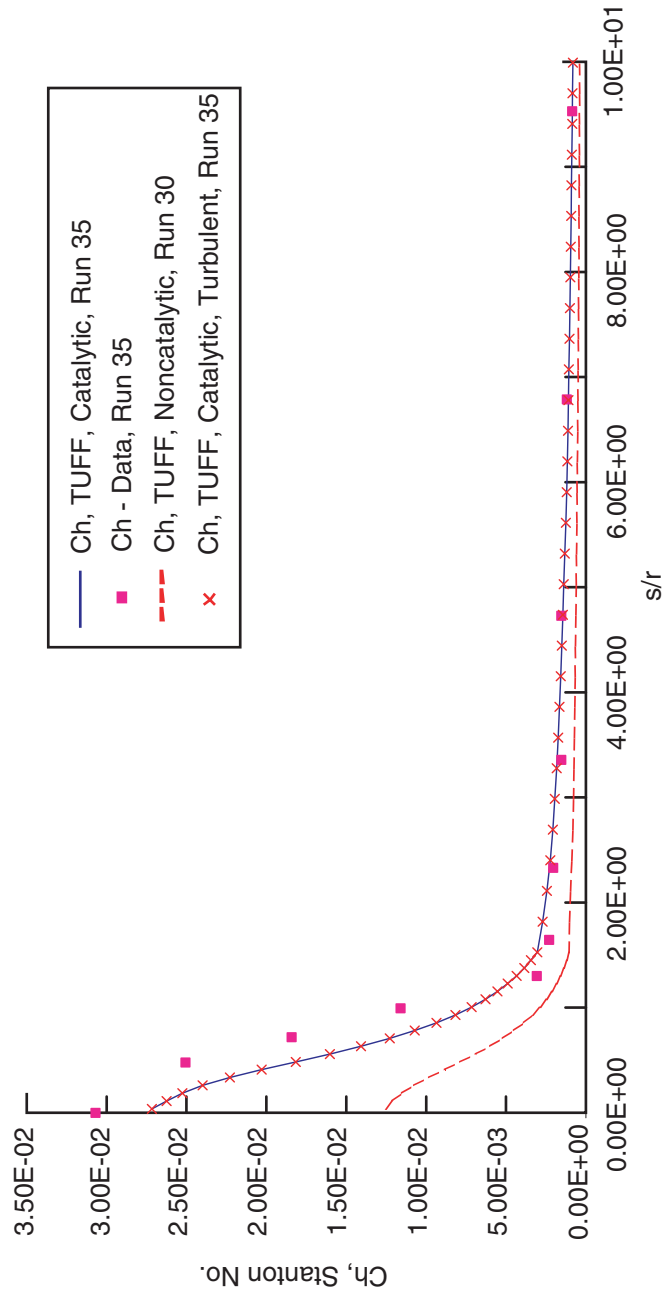


Figure 28. Heat-Transfer Coefficient, AEDC Run 30, Electre Model (70 percent)

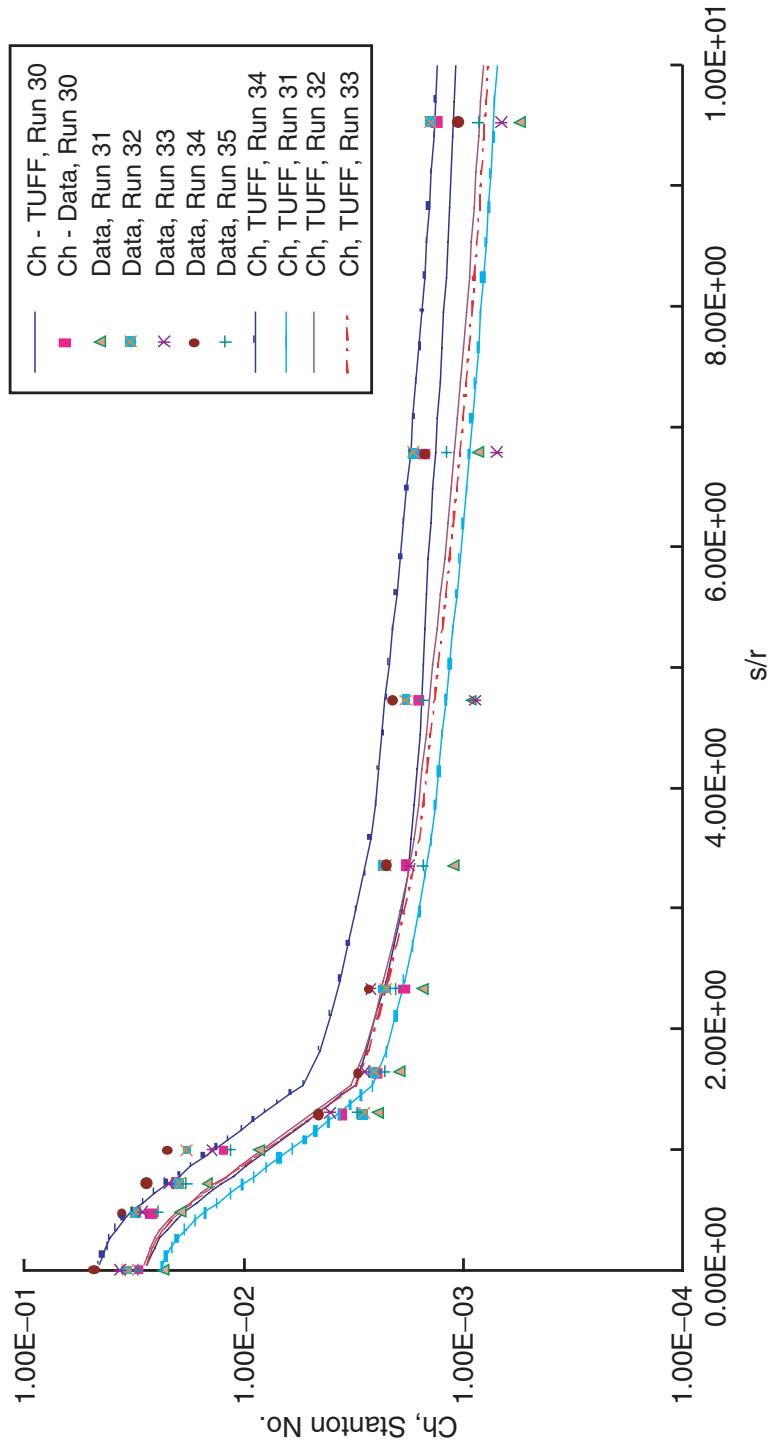


Figure 29. Heat-Transfer Coefficient, AEDC Runs 30-35, Electre Model (70 percent)

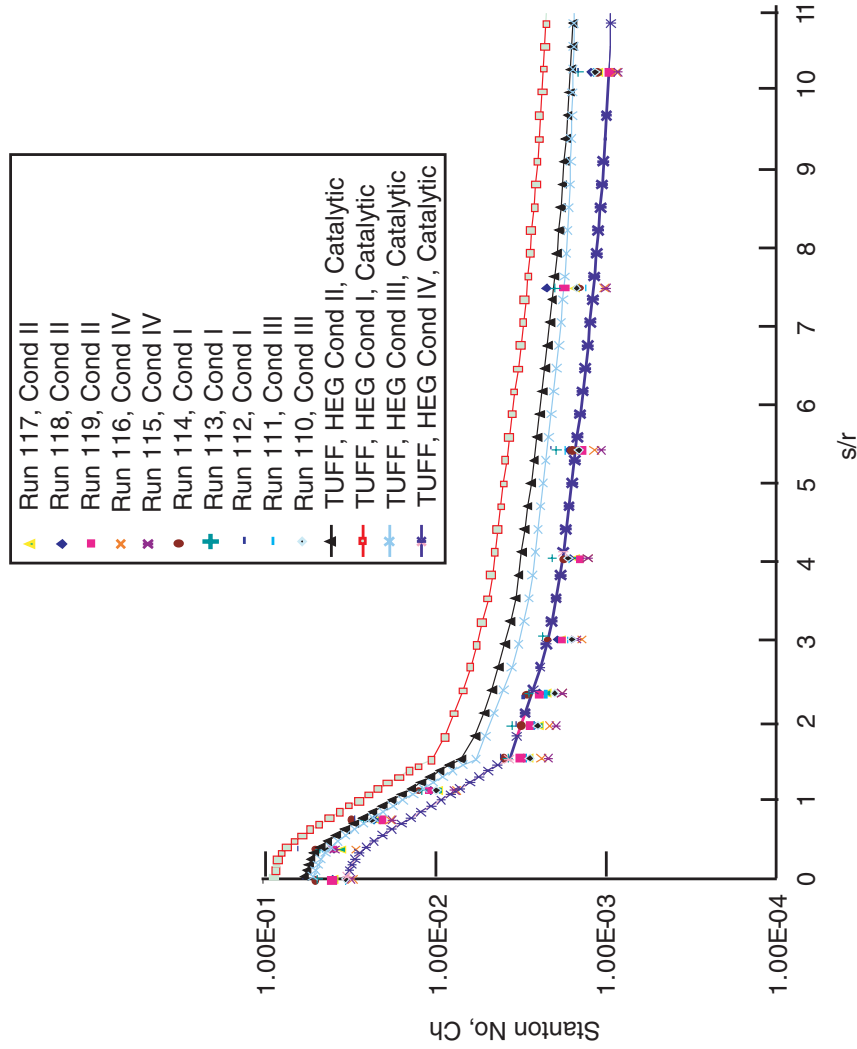


Figure 30. Heat Flux, DLR Electre Model in HEG

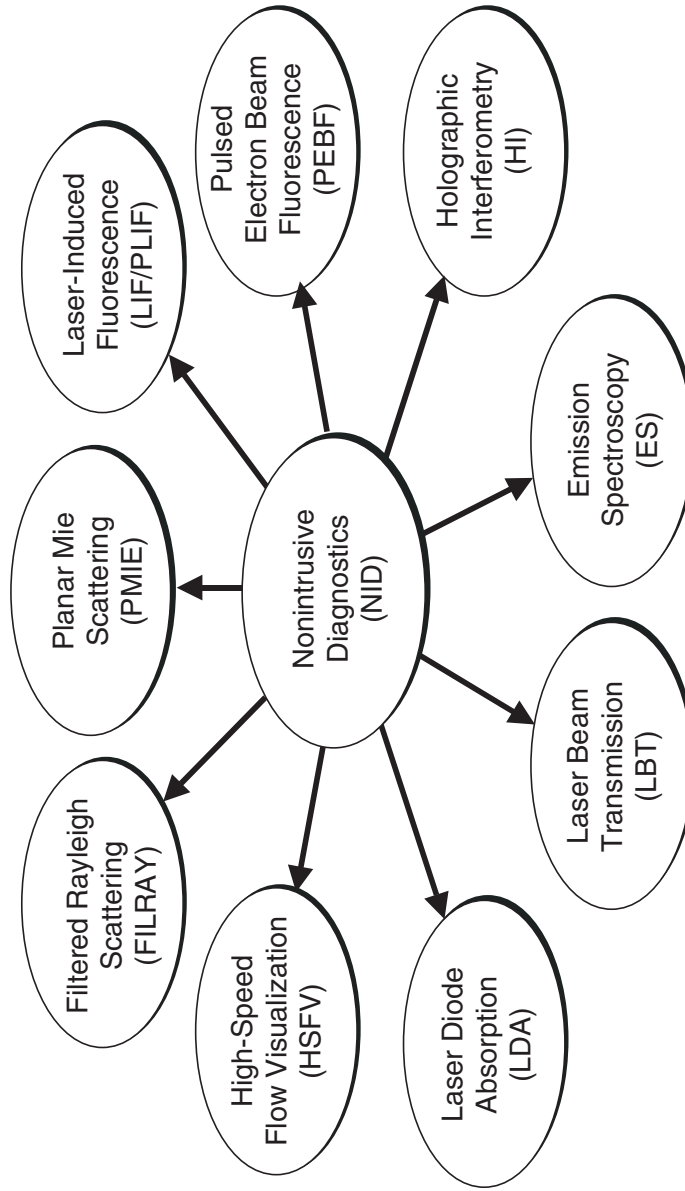


Figure 31. NID Techniques Undertaken for Application at the AEDC Impulse Facility

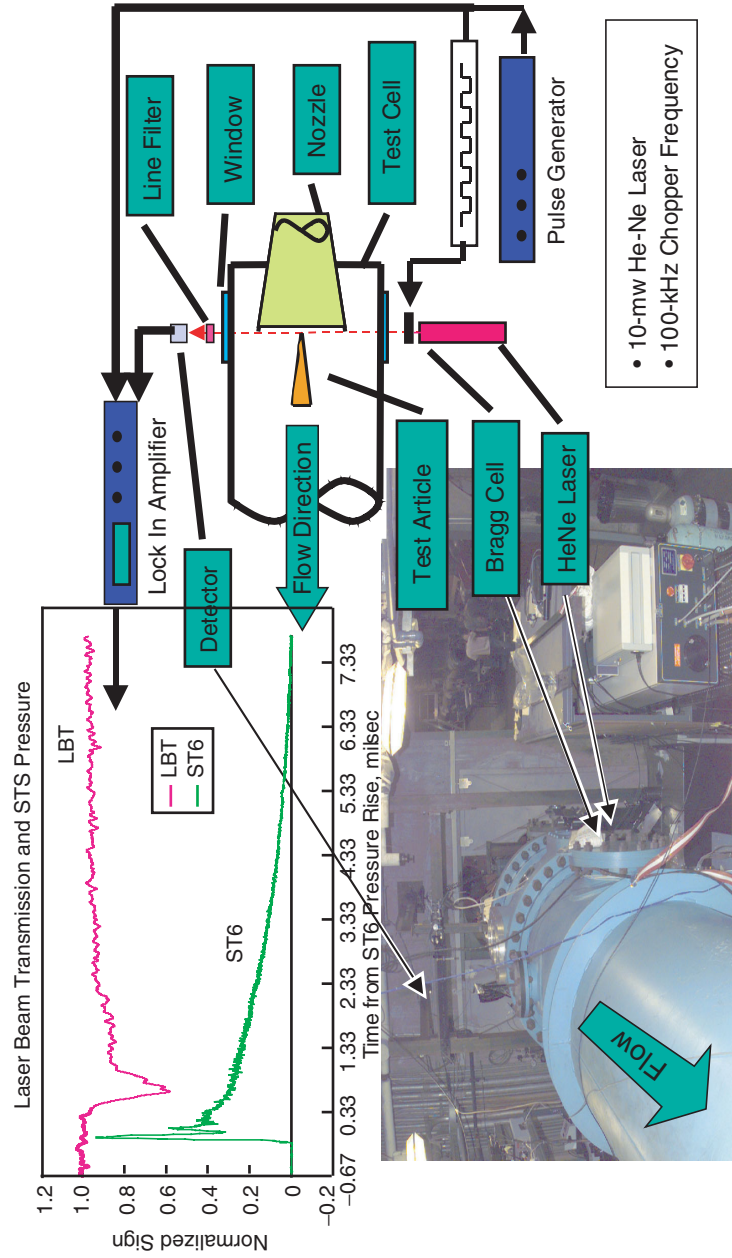


Figure 32. Application of LBT at the AEDC Impulse Facility

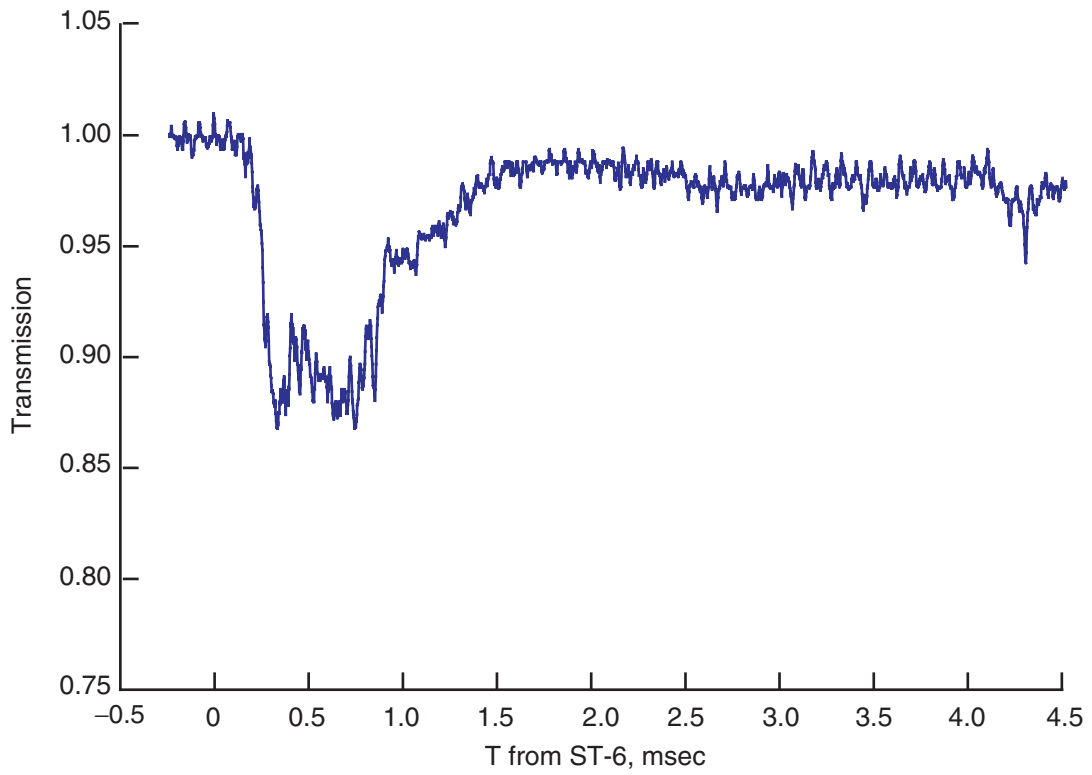


Figure 33. Impulse Facility Run 26 Laser Beam Transmission

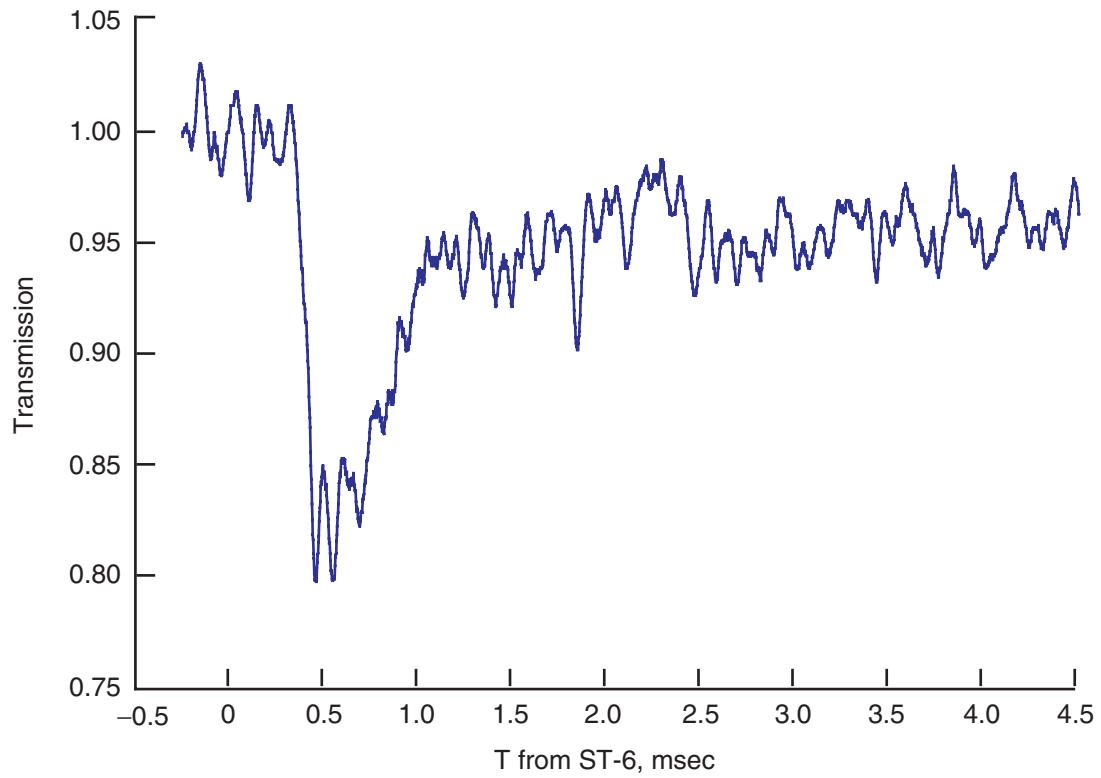


Figure 34. Impulse Facility Run 27 Laser Beam Transmission

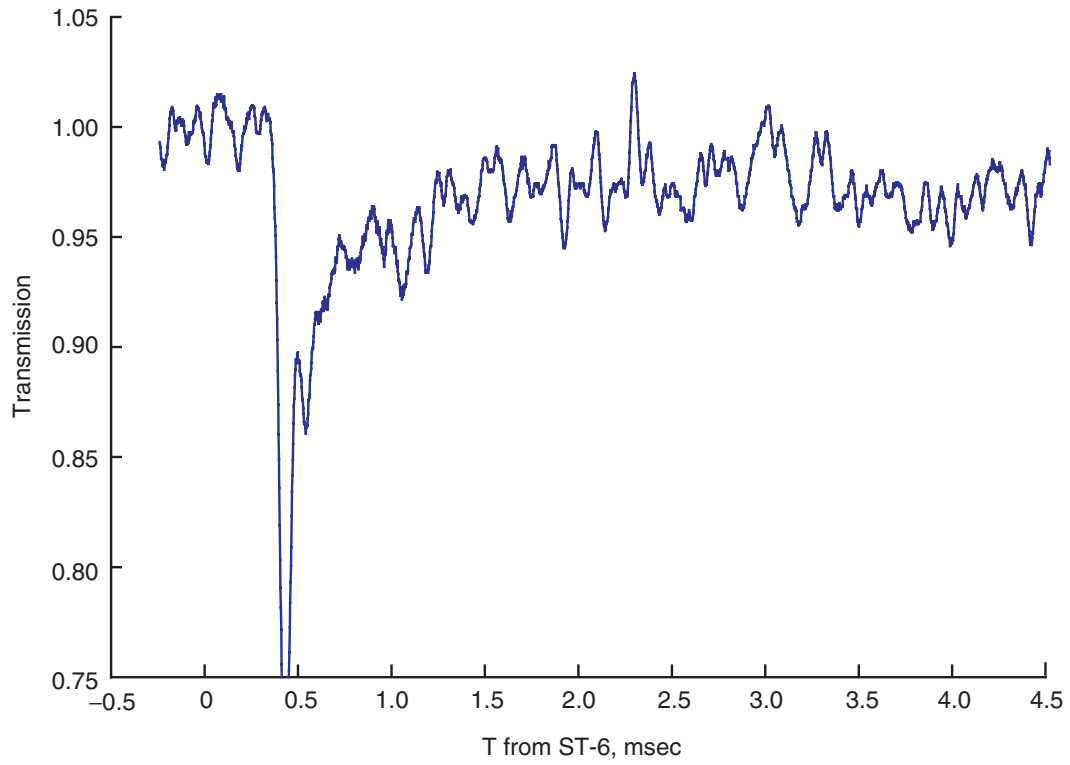


Figure 35. Impulse Facility Run 28 Laser Beam Transmission

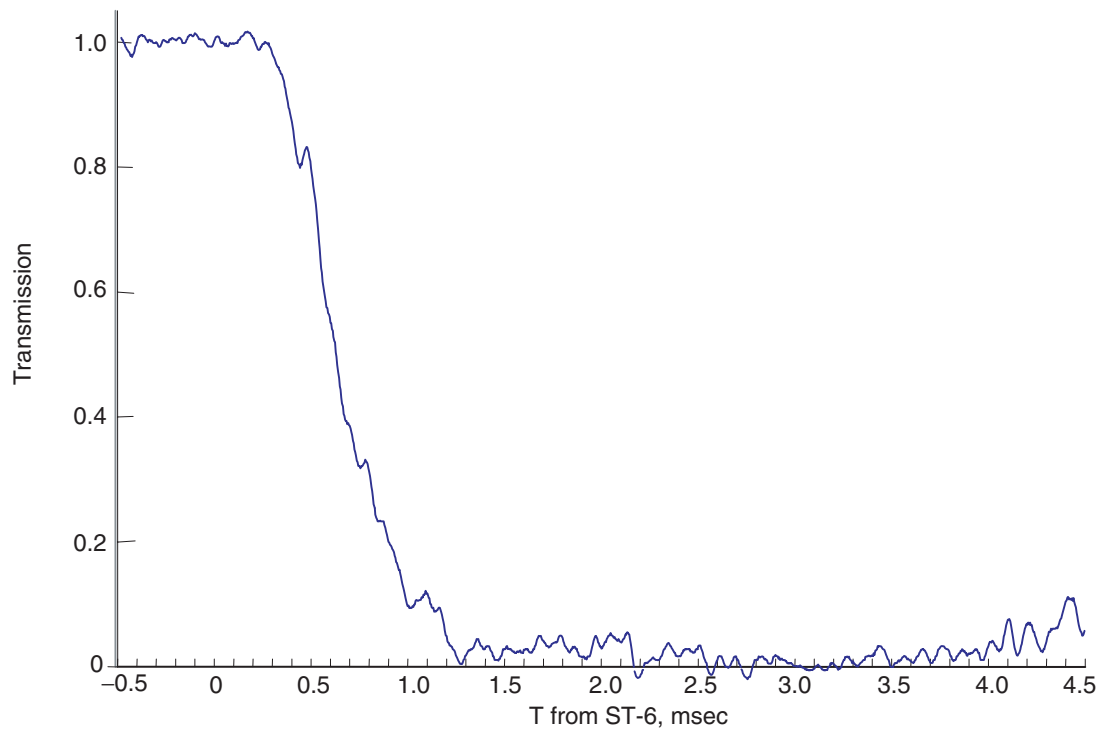


Figure 36. Impulse Facility Run 29 Laser Beam Transmission

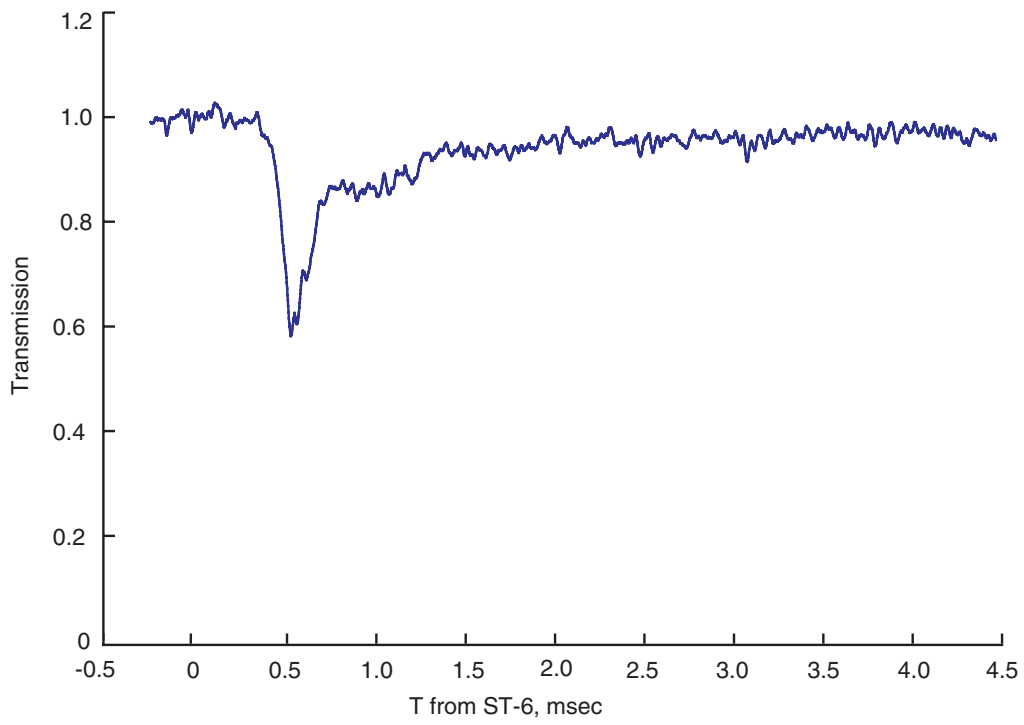


Figure 37. Impulse Facility Run 30 Laser Beam Transmission

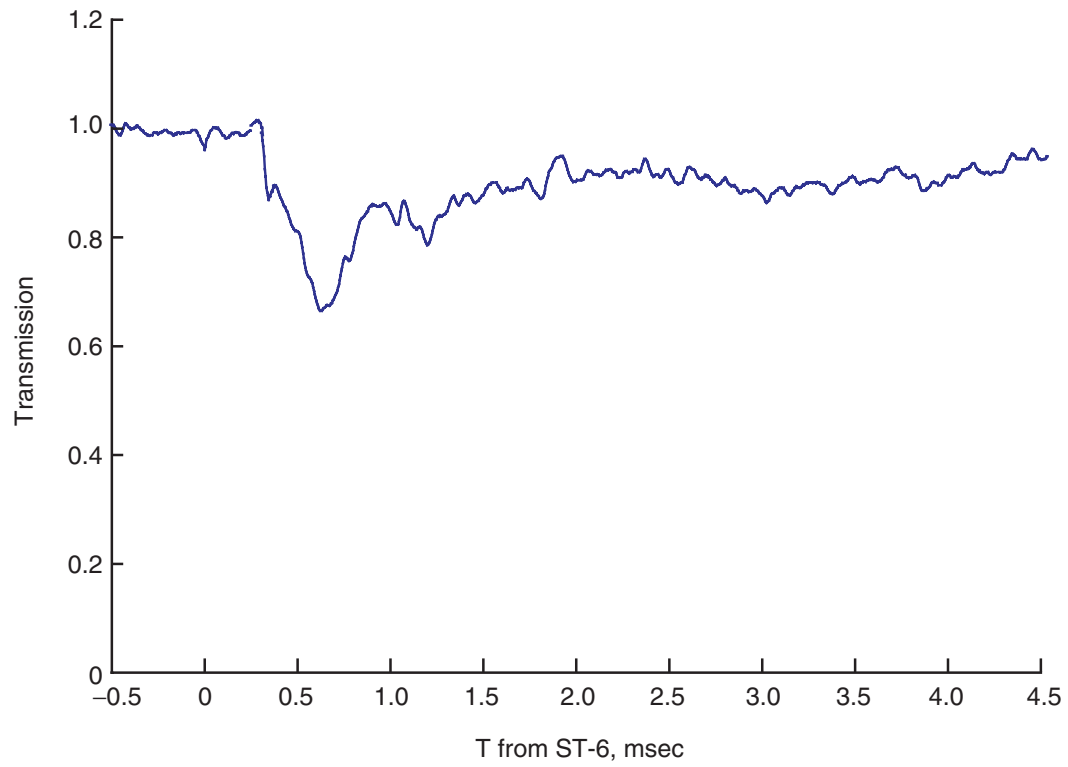


Figure 38. Impulse Facility Run 31 Laser Beam Transmission

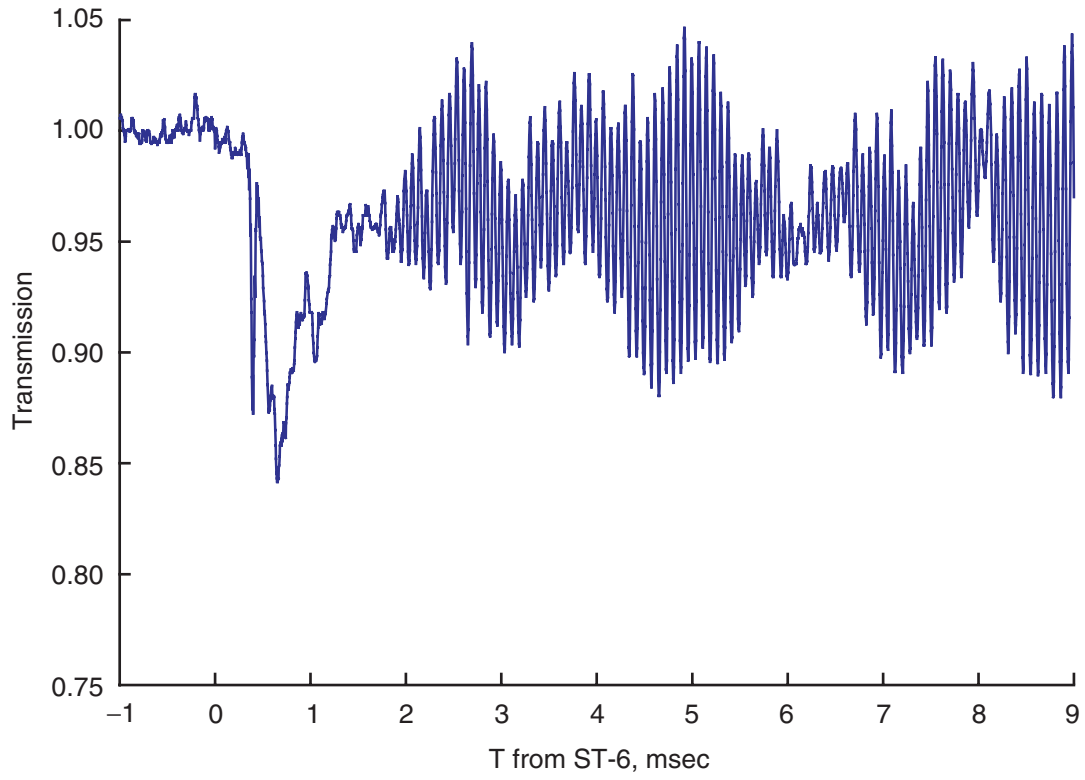


Figure 39. Impulse Facility Run 32 Laser Beam Transmission

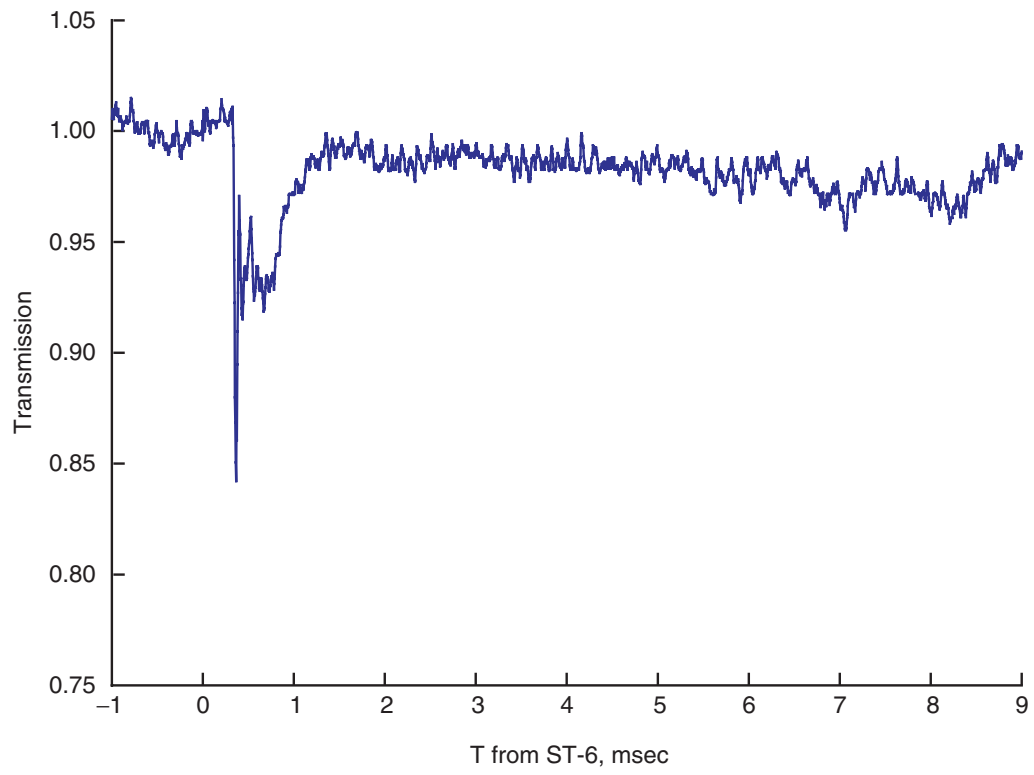


Figure 40. Impulse Facility Run 33 Laser Beam Transmission

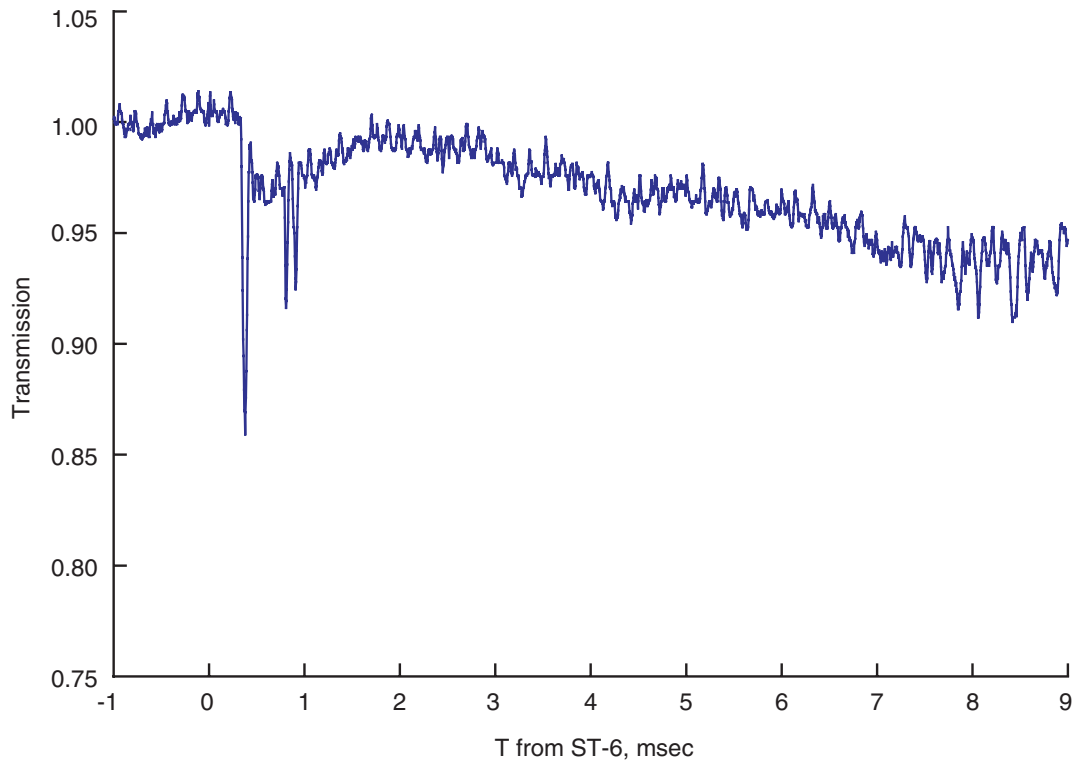


Figure 41. Impulse Facility Run 34 Laser Beam Transmission

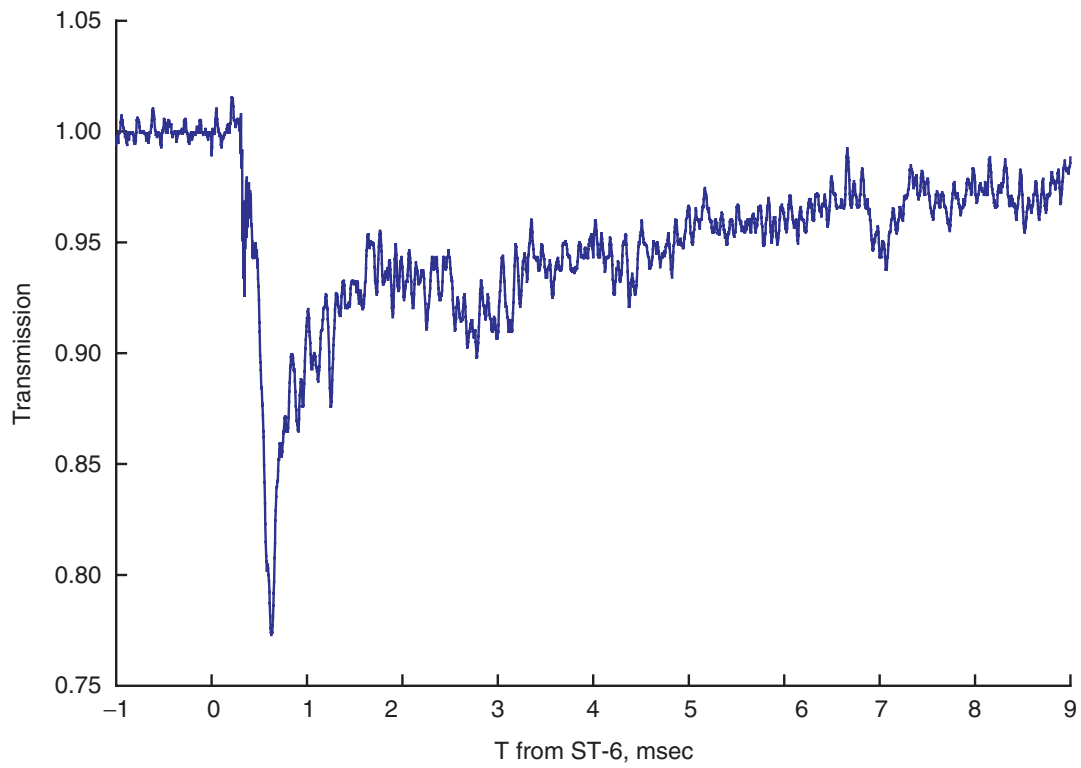


Figure 42. Impulse Facility Run 35 Laser Beam Transmission

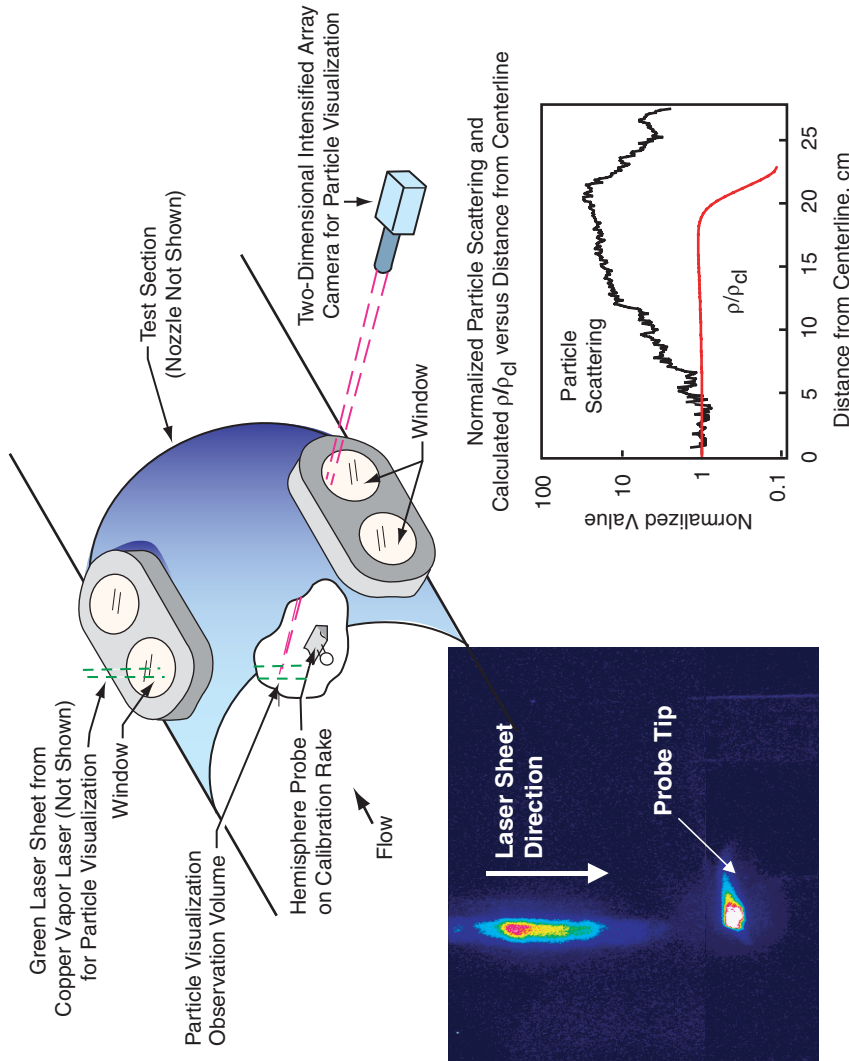


Figure 43. Application of PMIE at the AEDC Impulse Facility

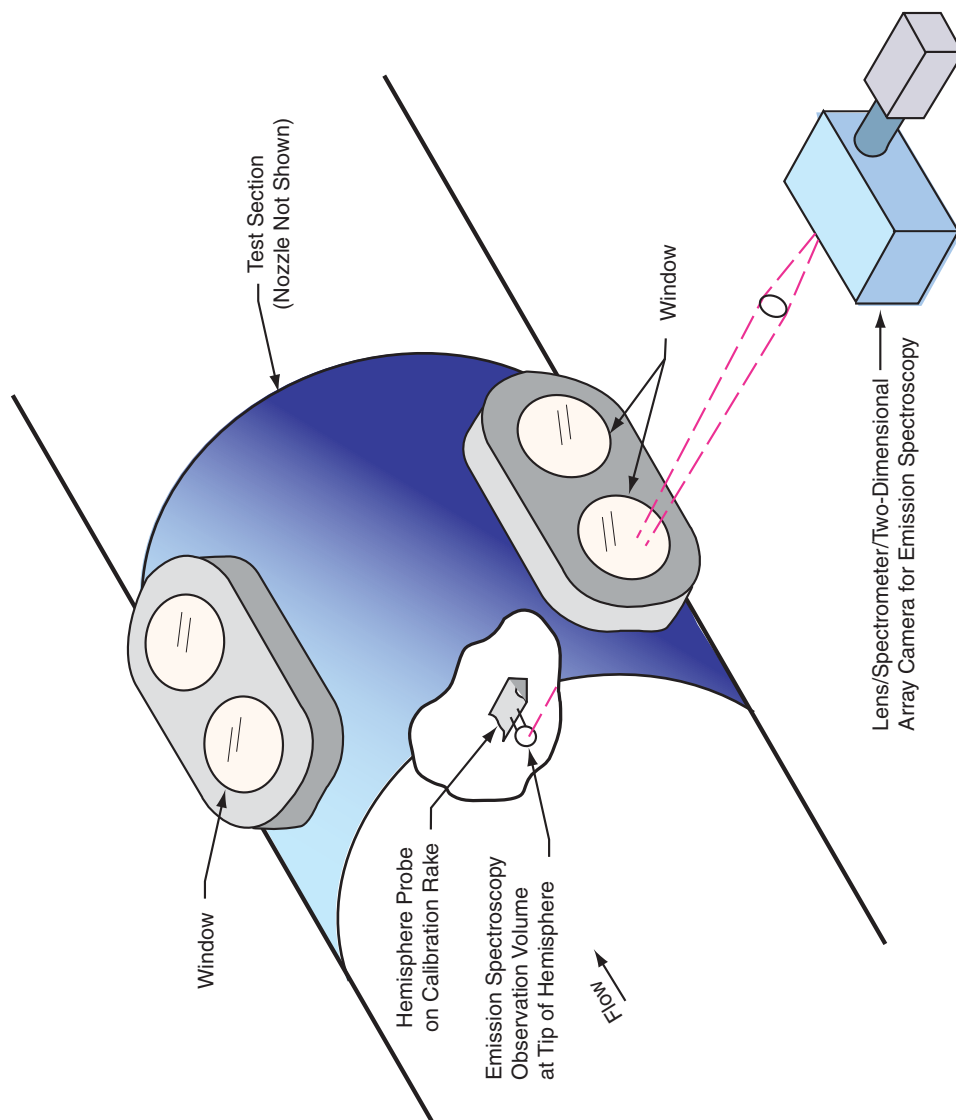


Figure 44. Application of ES at the AEDC Impulse Facility

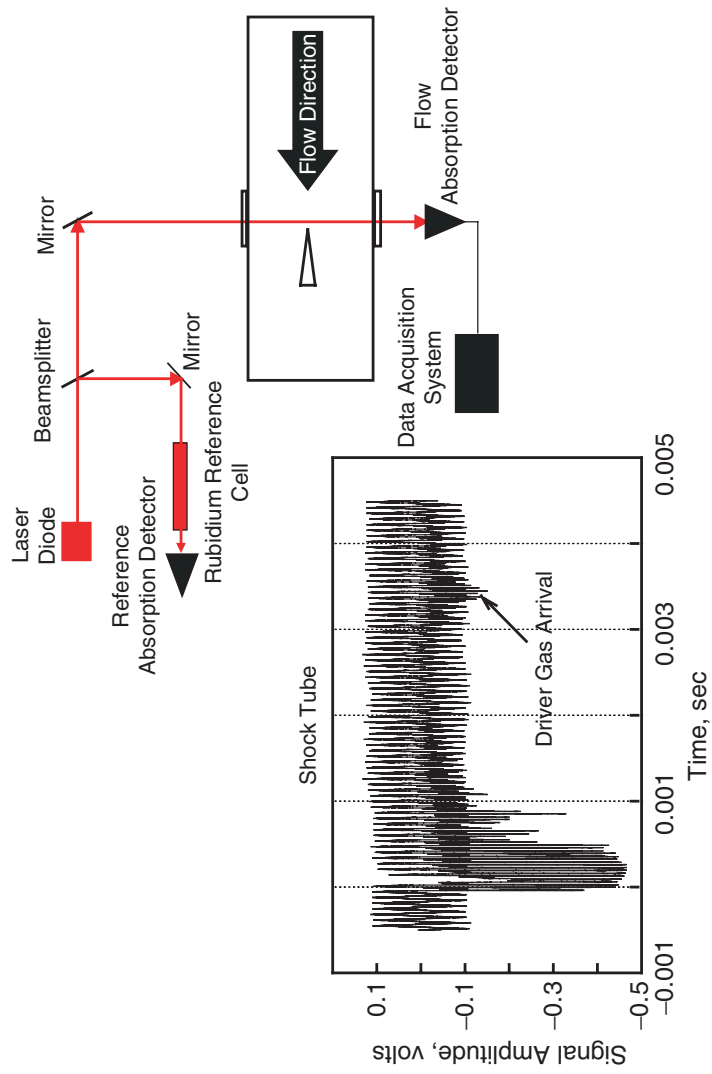


Figure 45. Application of LDA at the AEDC Laboratory Shock Tube/Tunnel

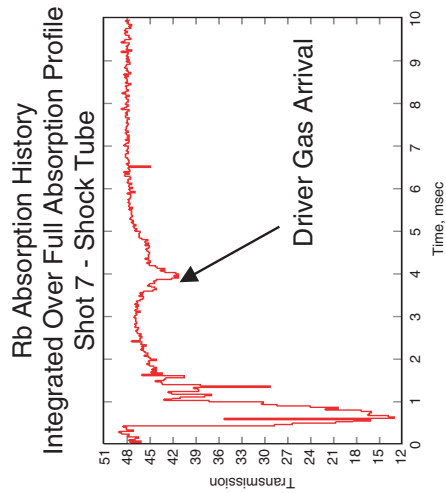
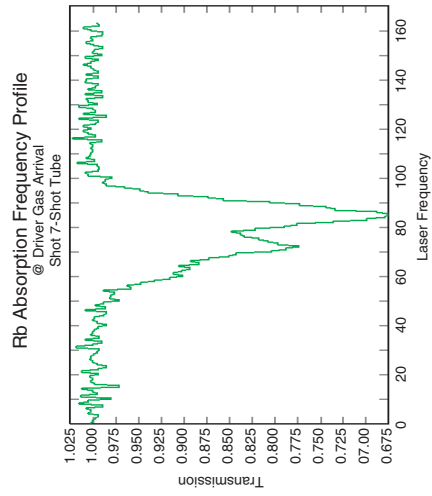
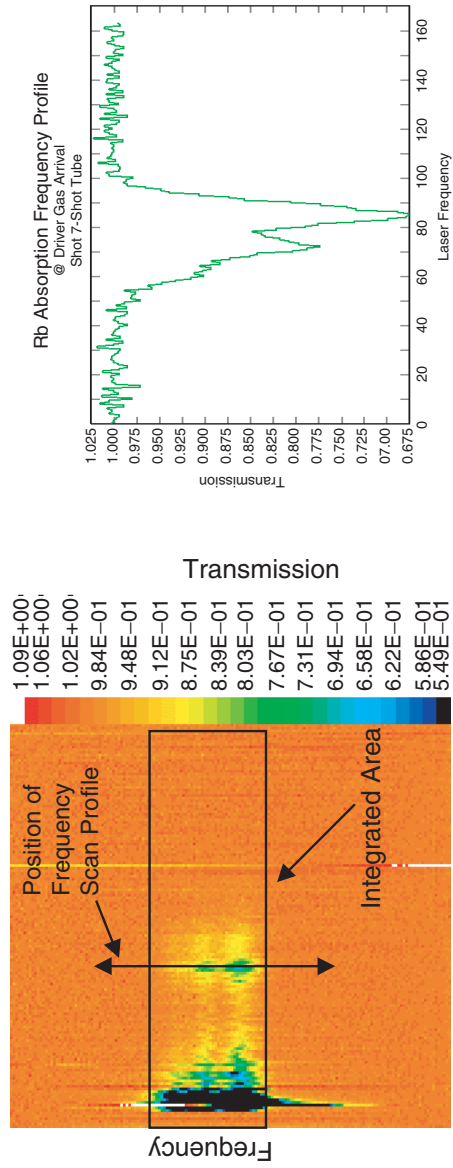


Figure 46. LDA Reduced Data Format—AEDC Laboratory Shock Tube/Tunnel

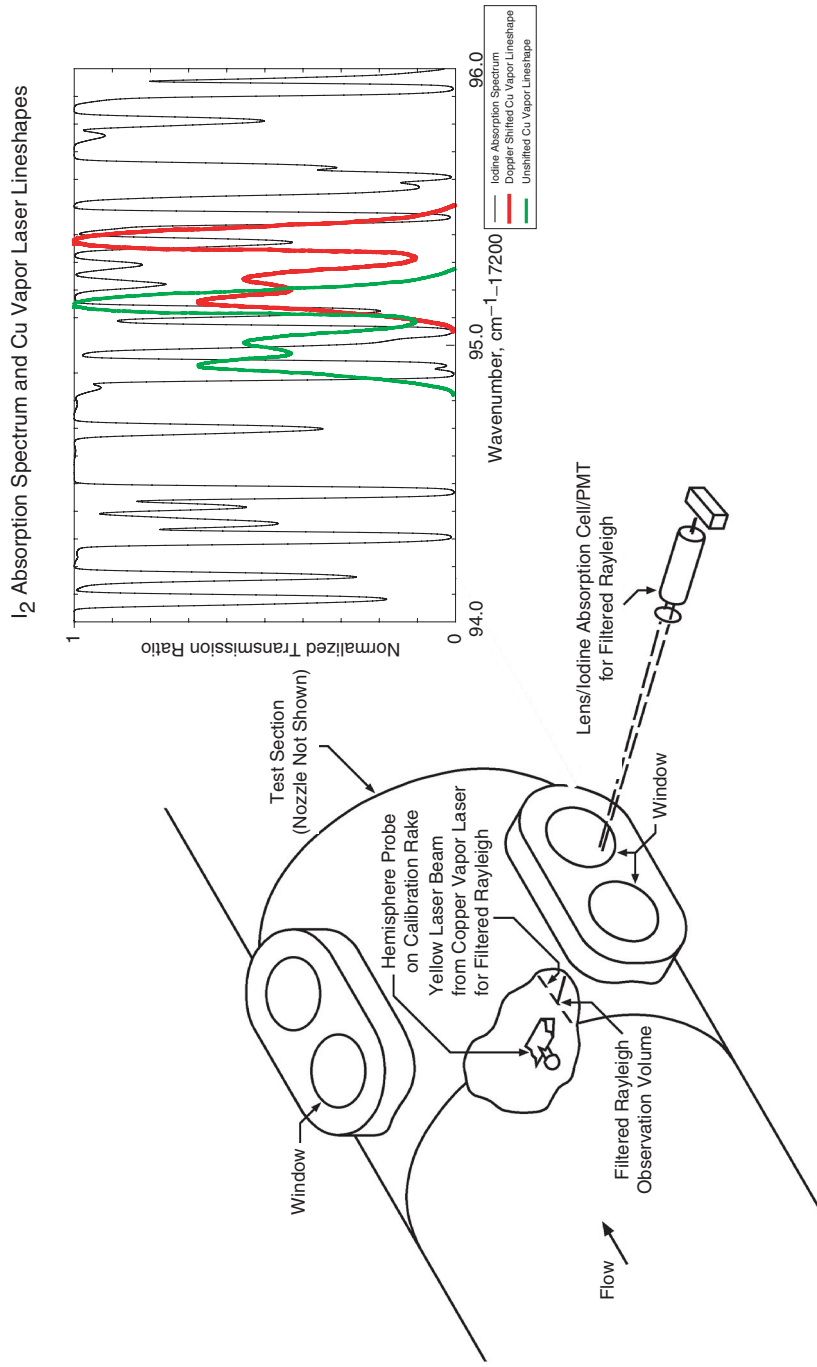


Figure 47. Use of Filtered Rayleigh Scattering at the AEDC Impulse Facility

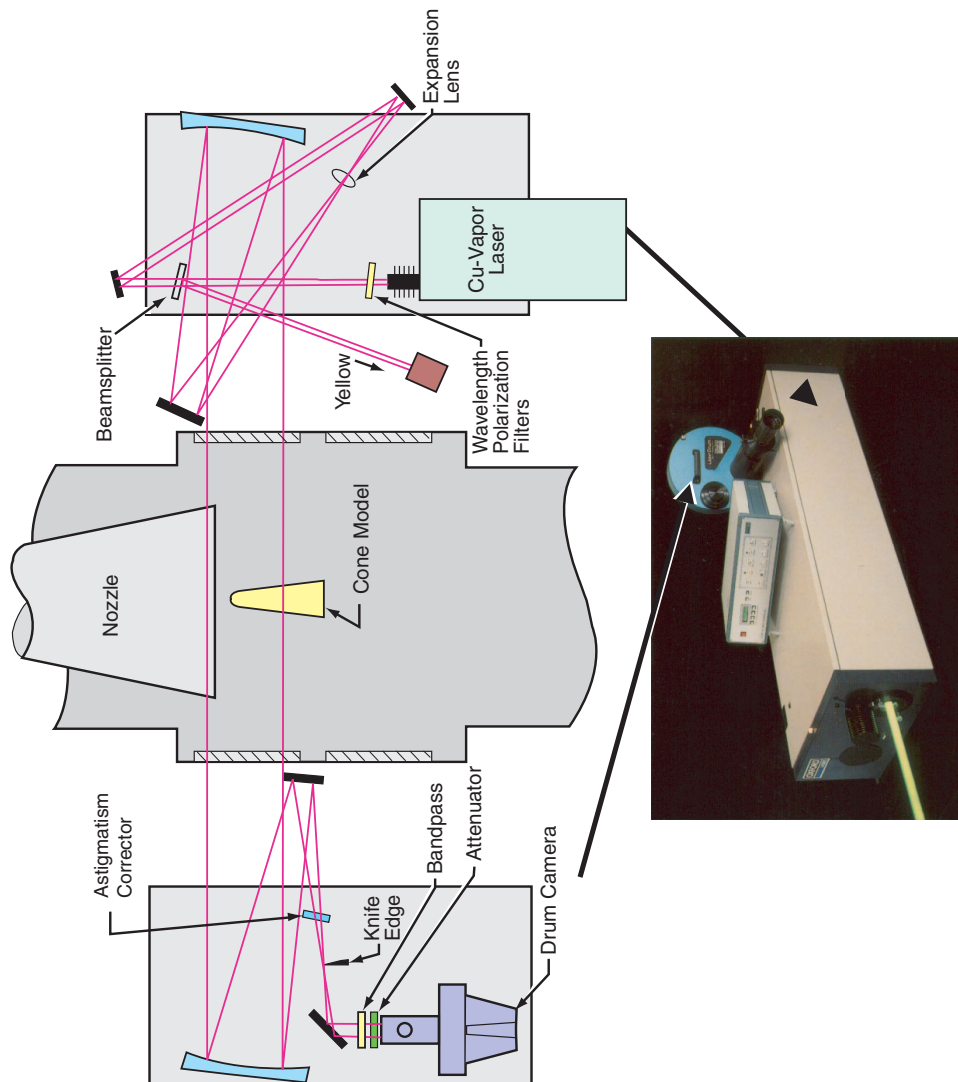


Figure 48. High-Speed Flow Visualization System

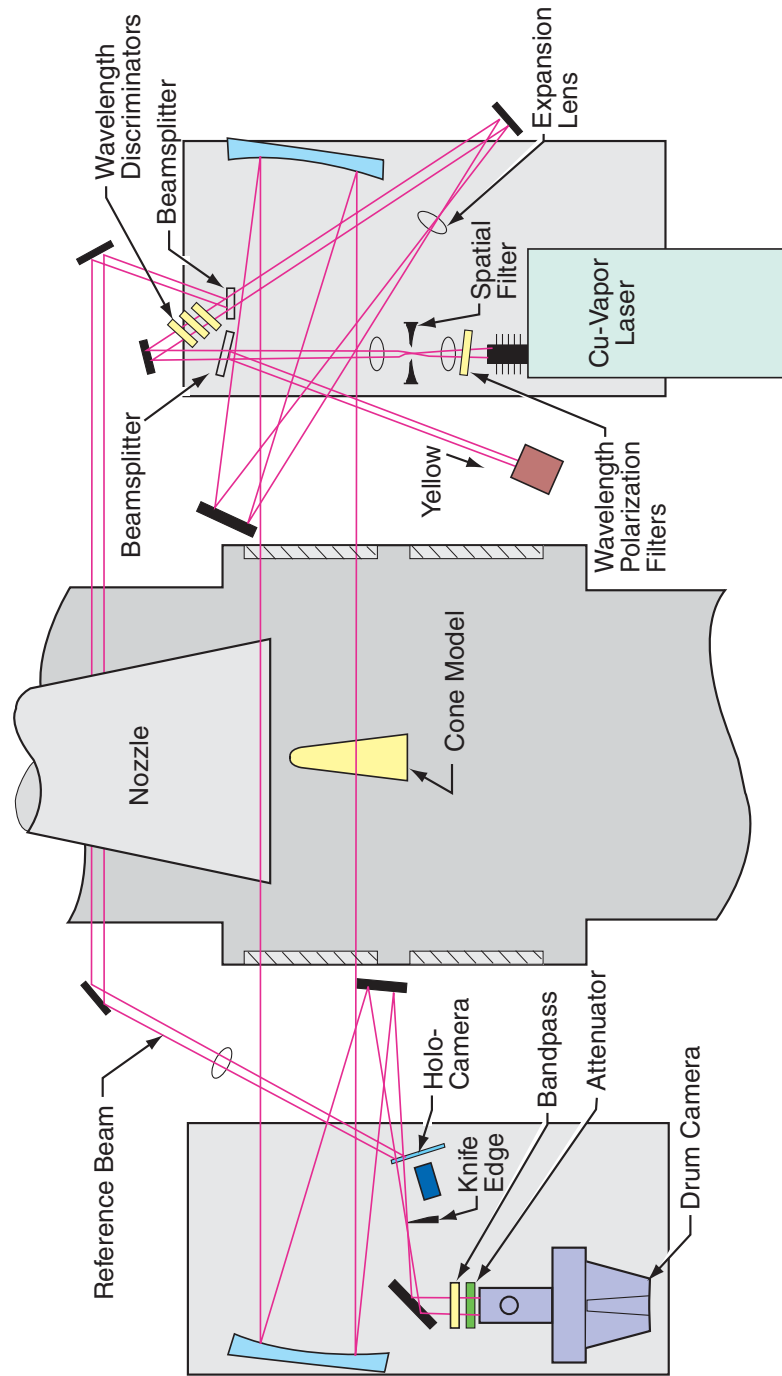


Figure 49. HSFV Setup for Acquiring High-Speed Holograms

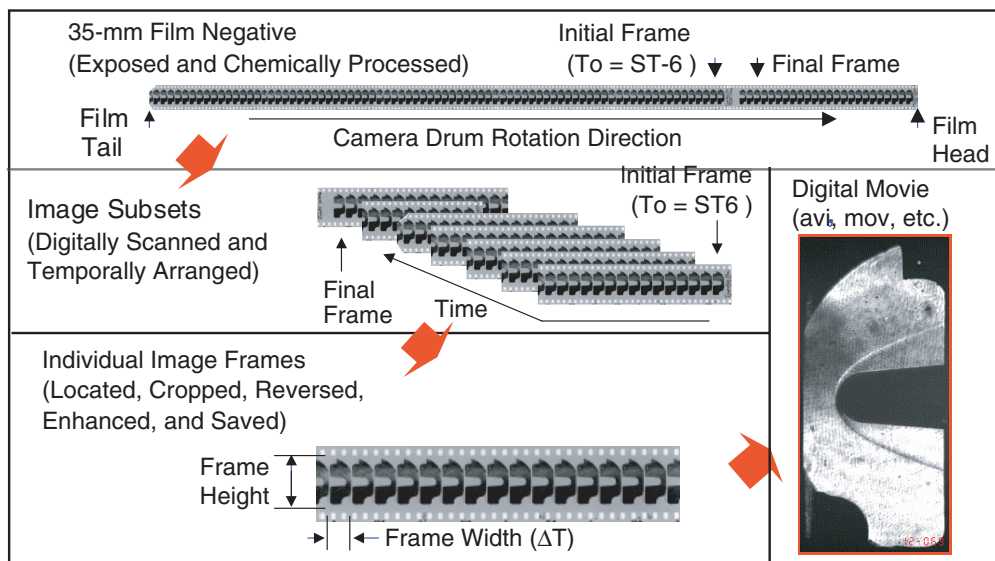


Figure 50. Process for Creating HSFV Digital Movies

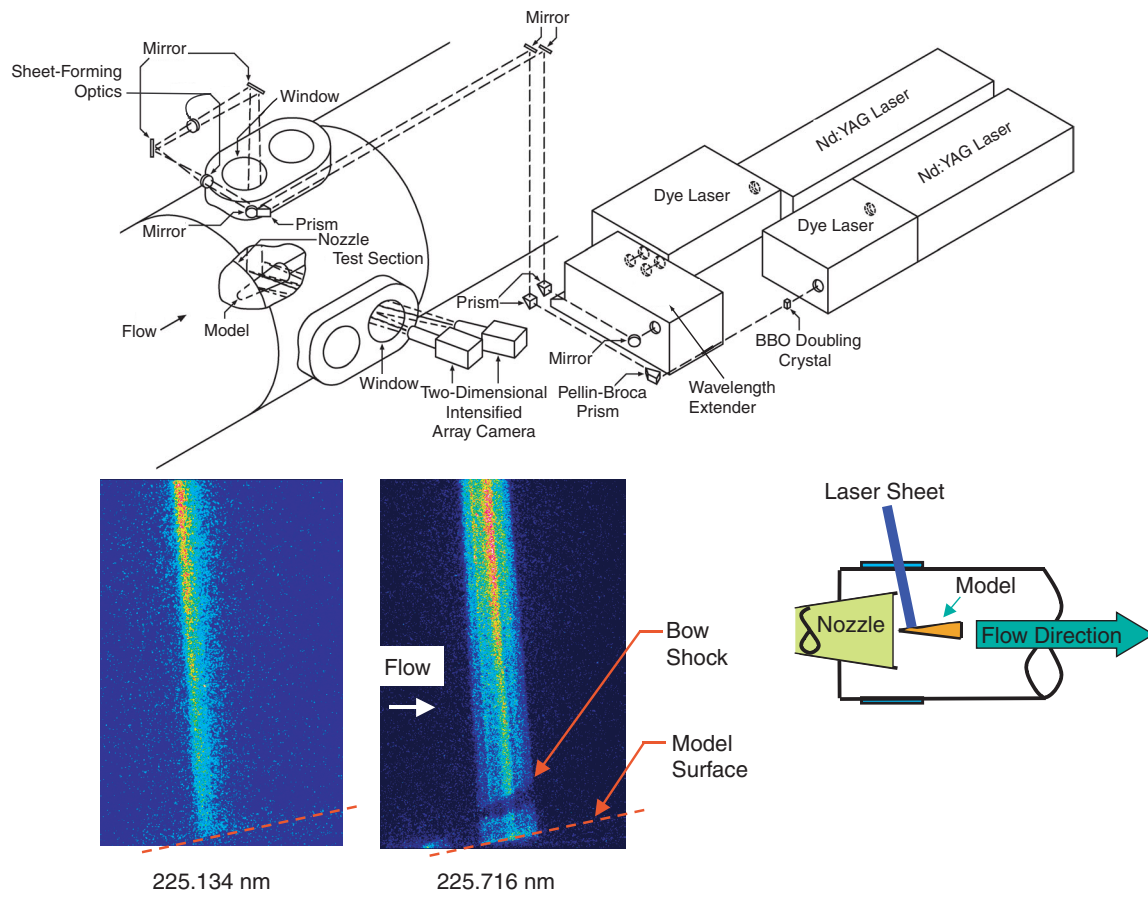


Figure 51. PLIF Setup at the Impulse Facility

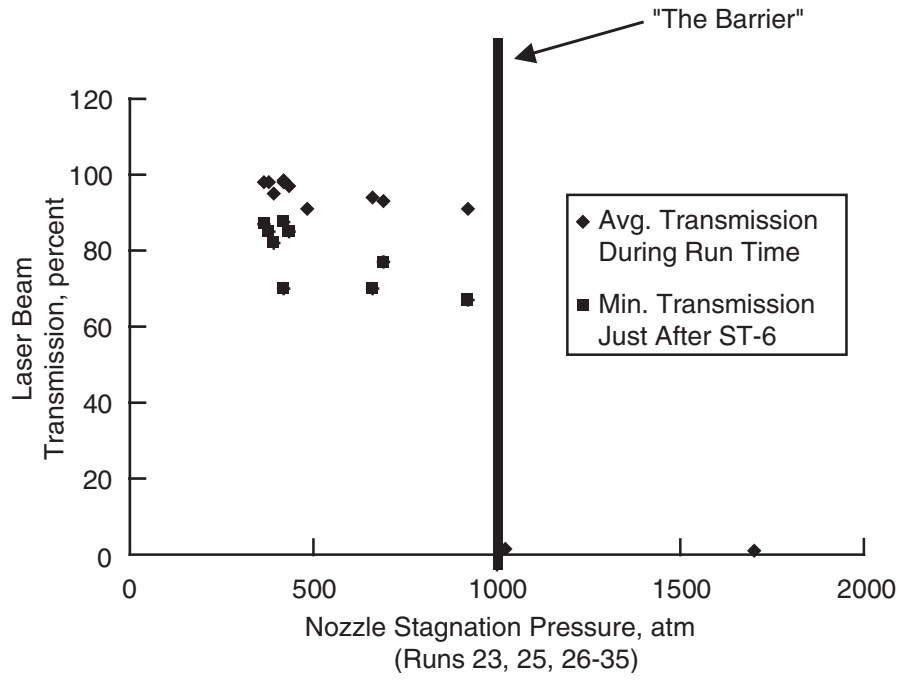


Figure 52. Peak and Average LBT Values During Estimated Good Run Time

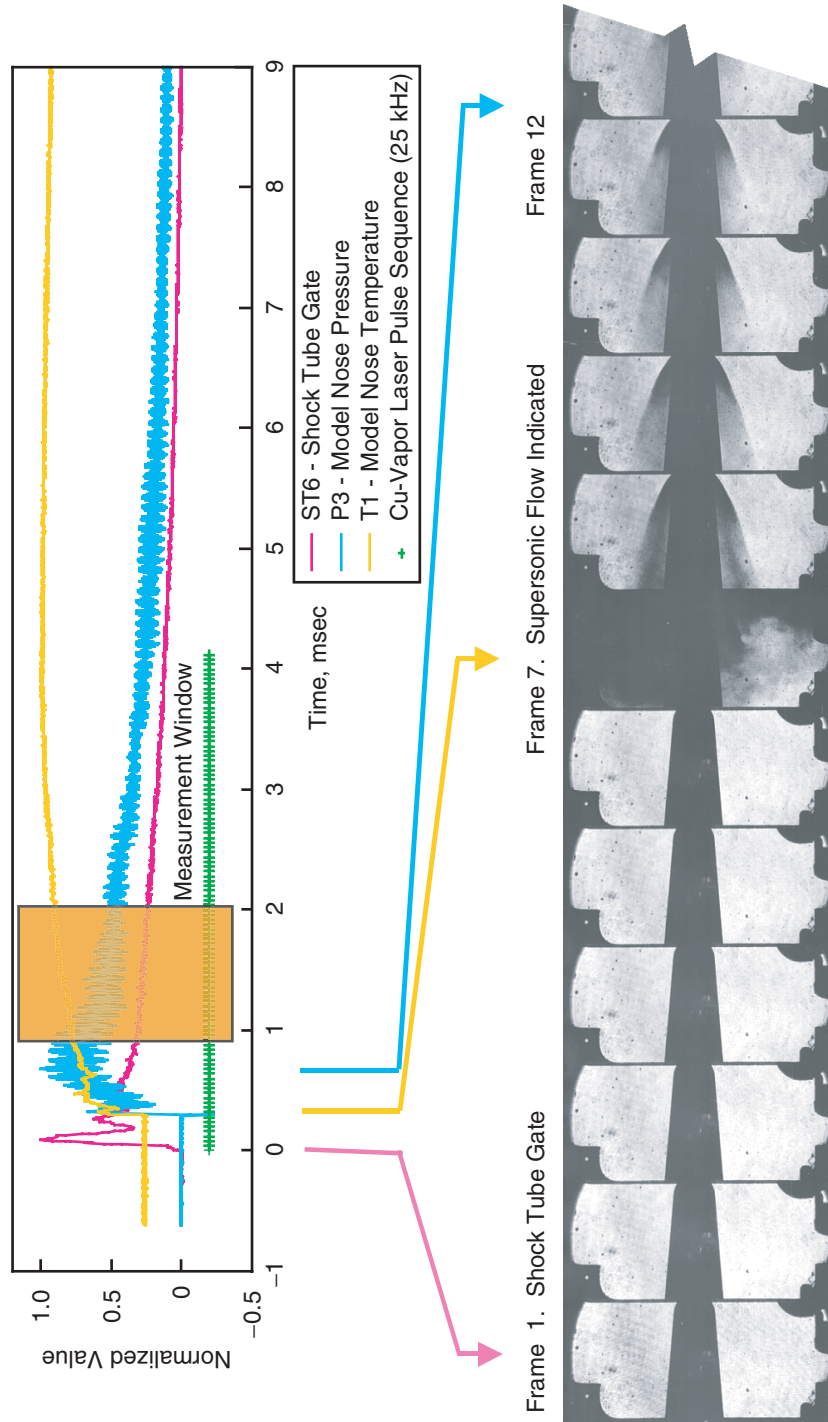


Figure 53. HSFV for Flow Start Process, Impulse Facility Run 30—June 2, 1998

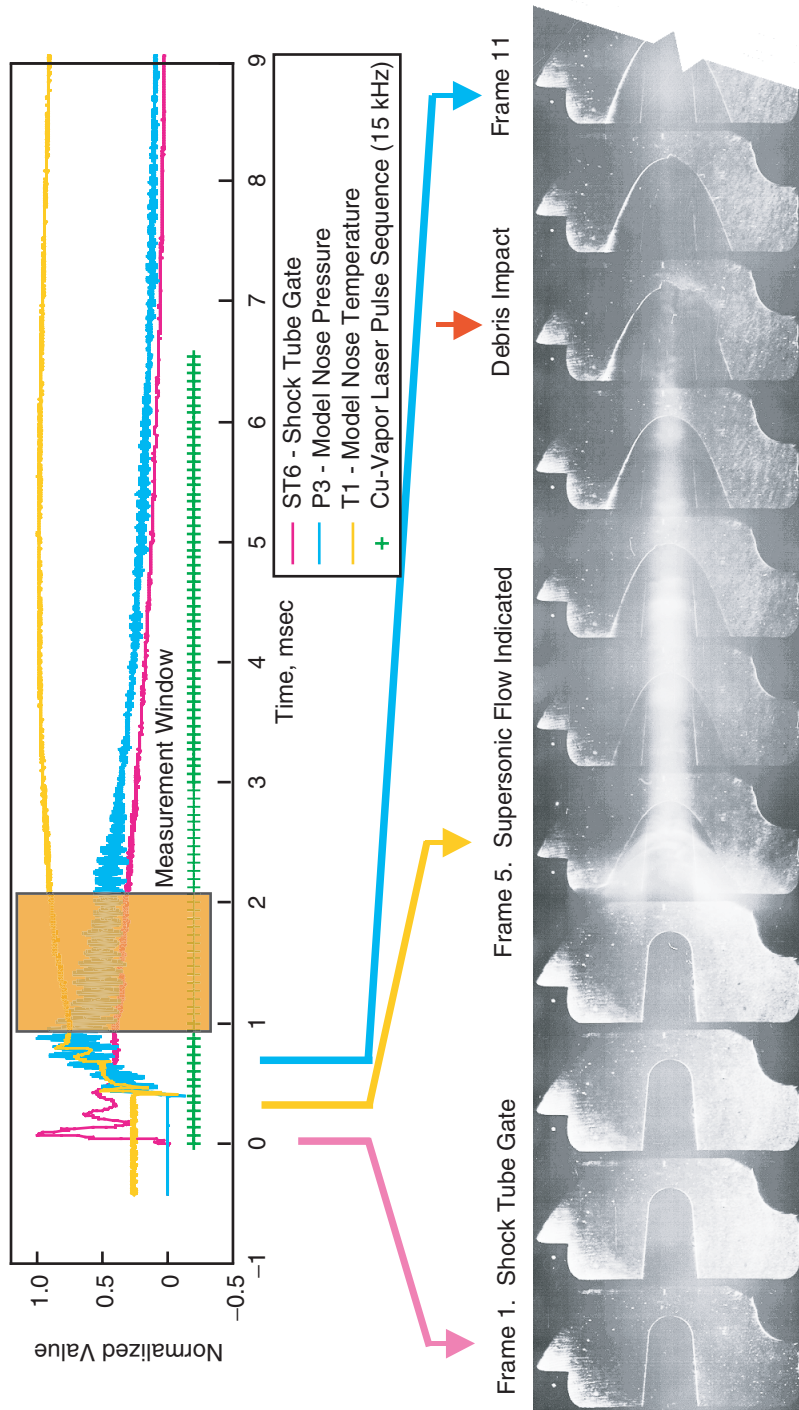


Figure 54. HSFV for Flow Start Process, Impulse Facility Run 31—June 3, 1998

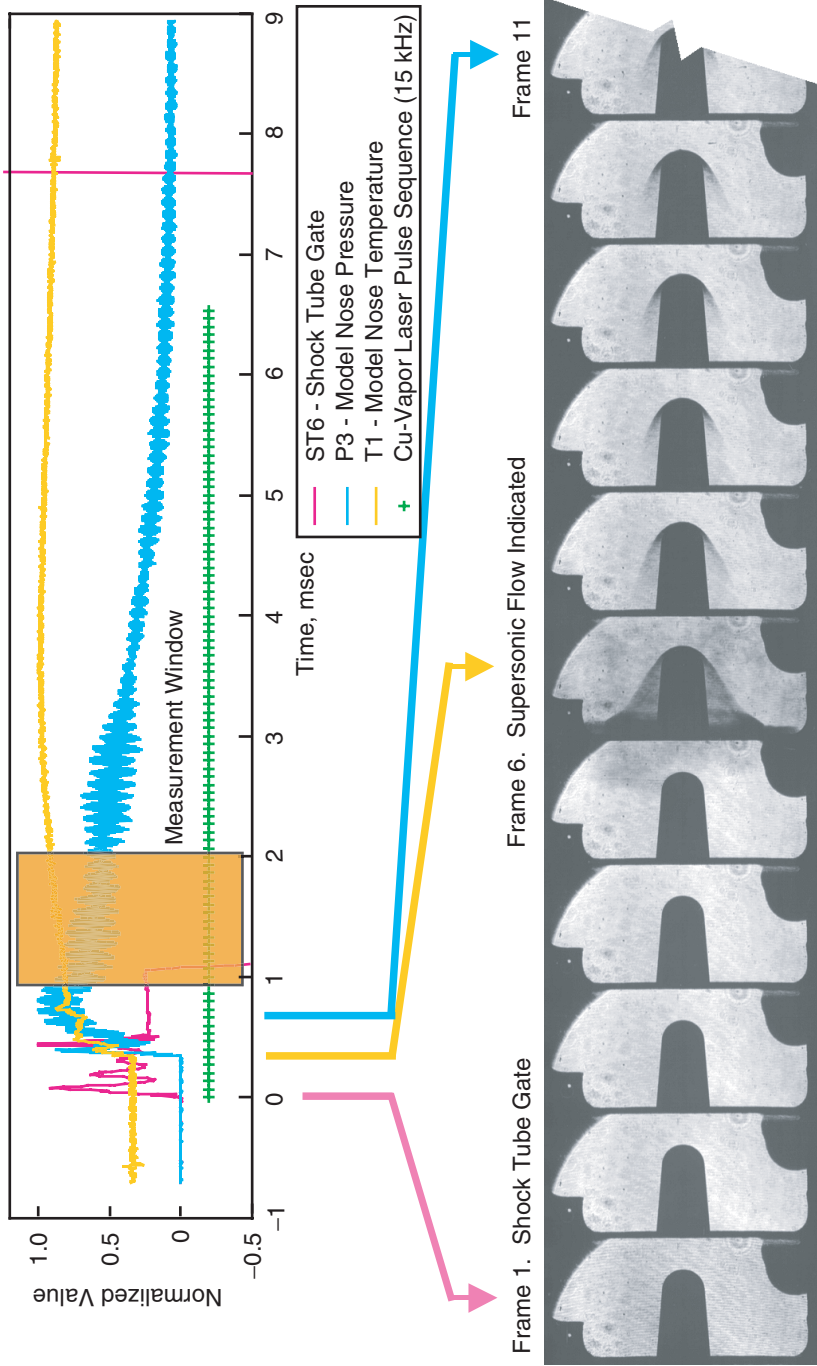


Figure 55. HSFV for Flow Start Process, Impulse Facility Run 32—June 4, 1998

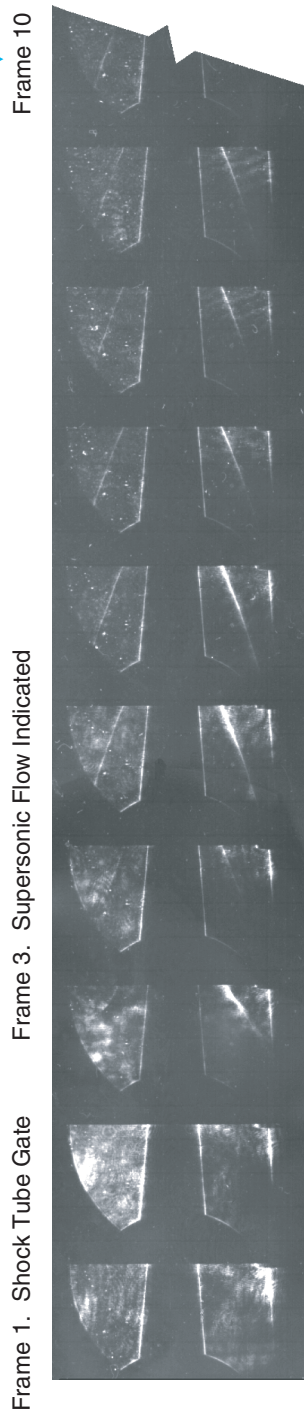
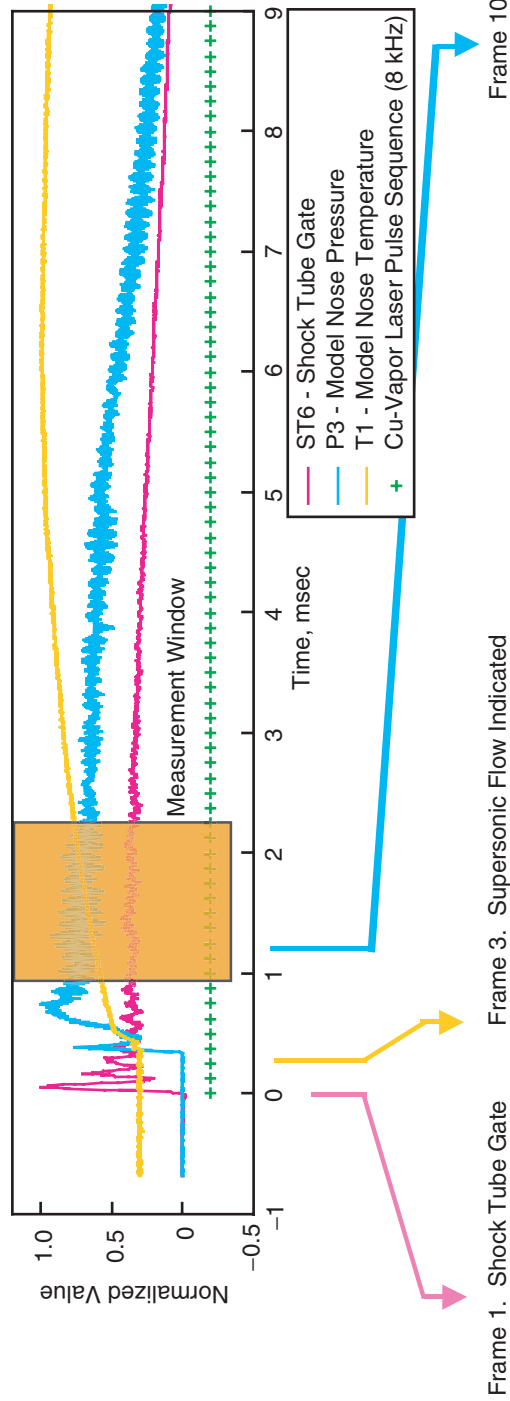


Figure 56. HSFV for Flow Start Process, Impulse Facility Run 33—June 9, 1998

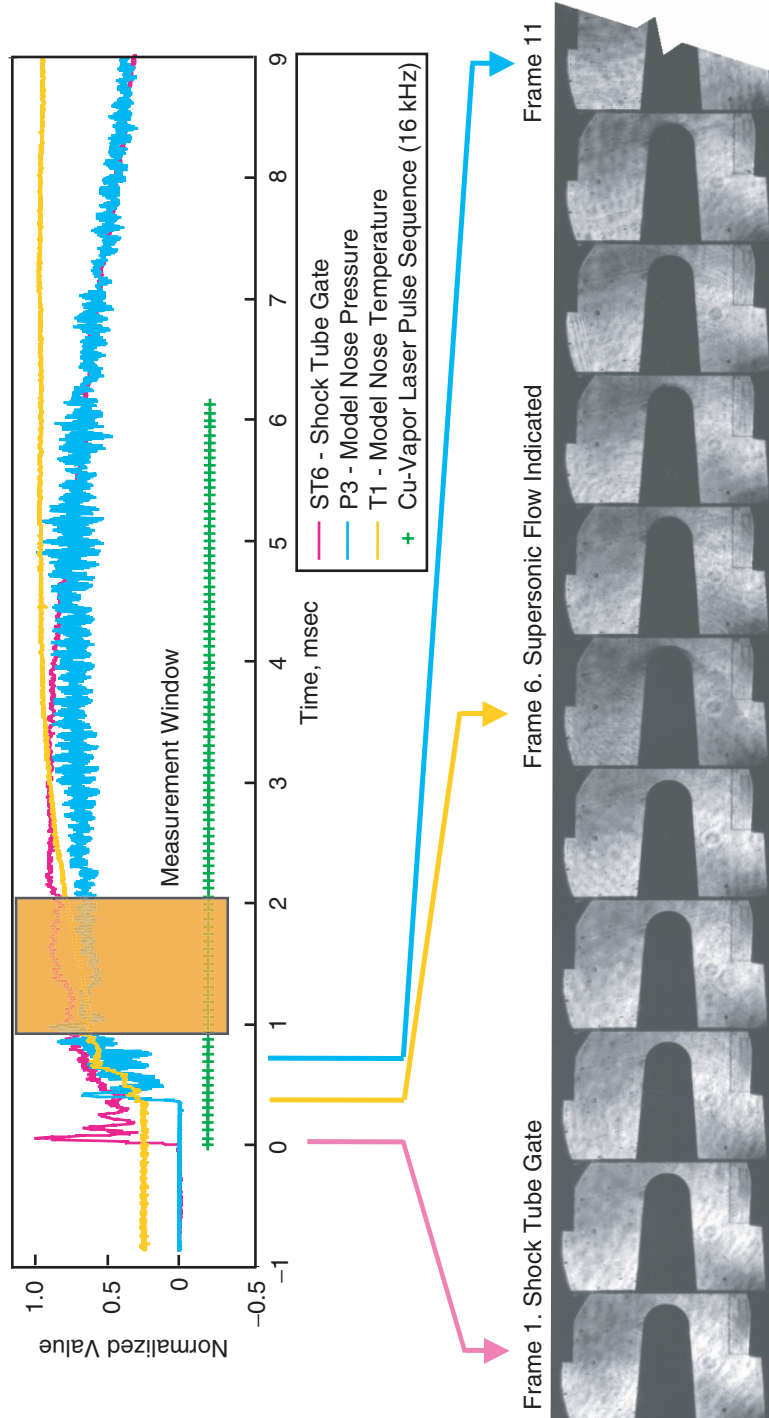


Figure 57. HSFV for Flow Start Process, Impulse Facility Run 34—June 10, 1998

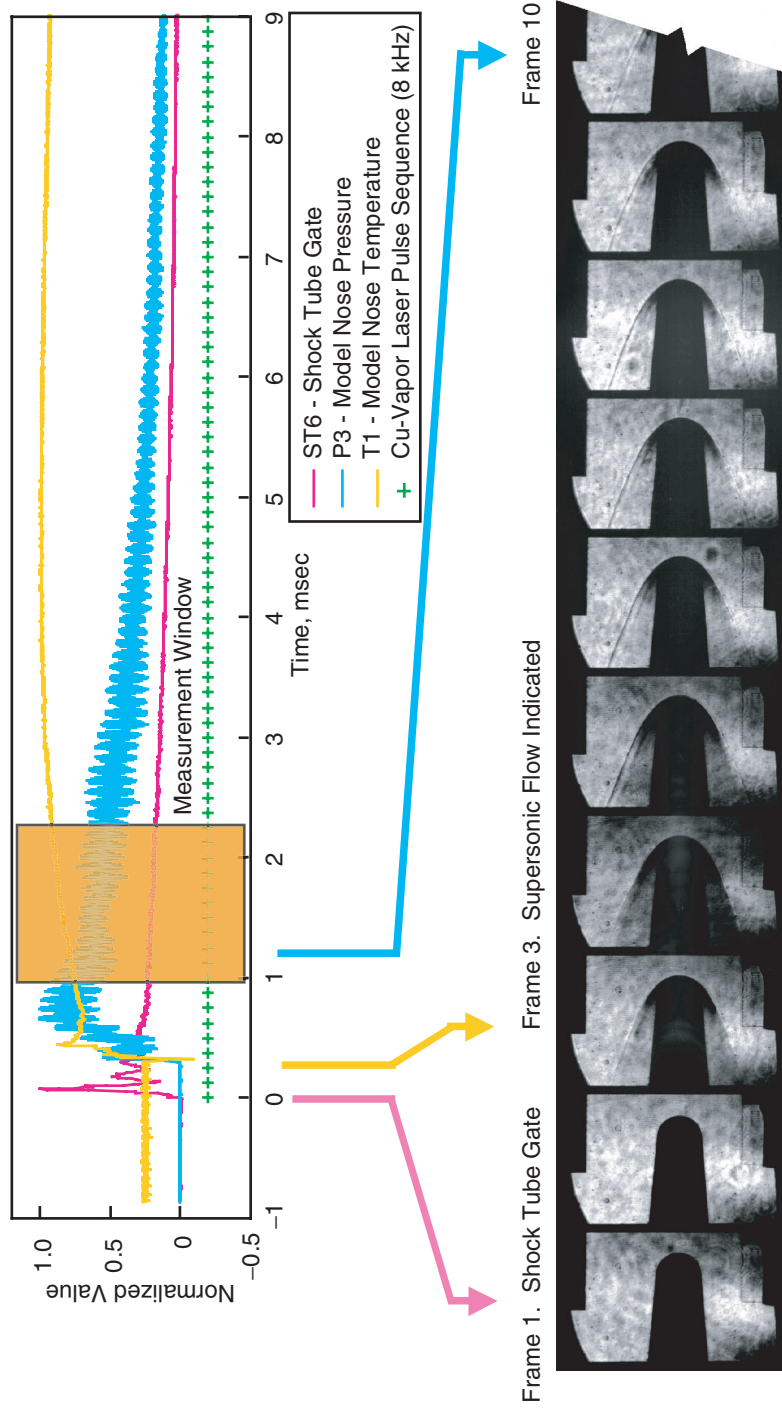


Figure 58. HSFV for Flow Start Process, Impulse Facility Run 35—June 12, 1998

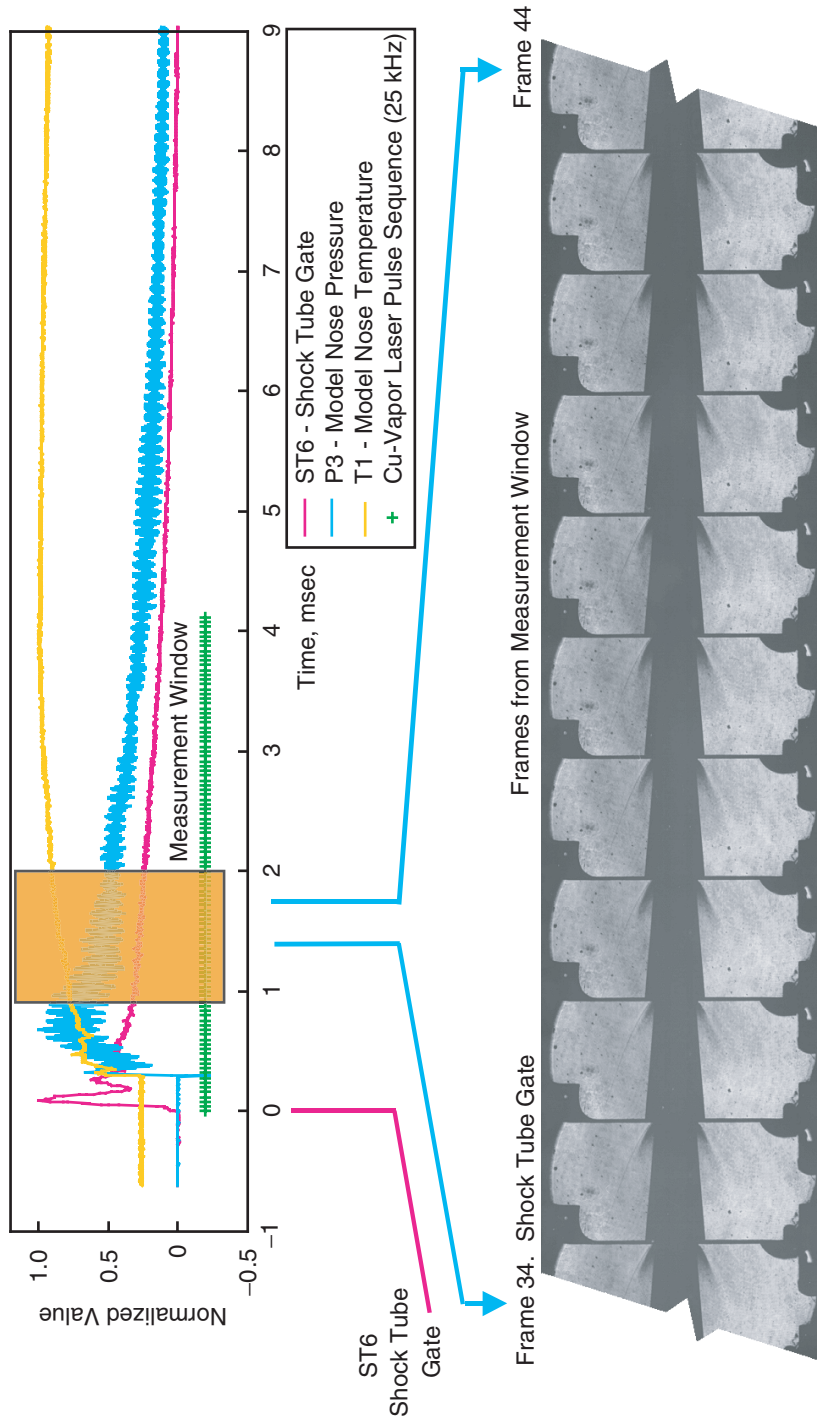


Figure 59. HSVF for Flow Steadiness, Impulse Facility Run 30—June 2, 1998

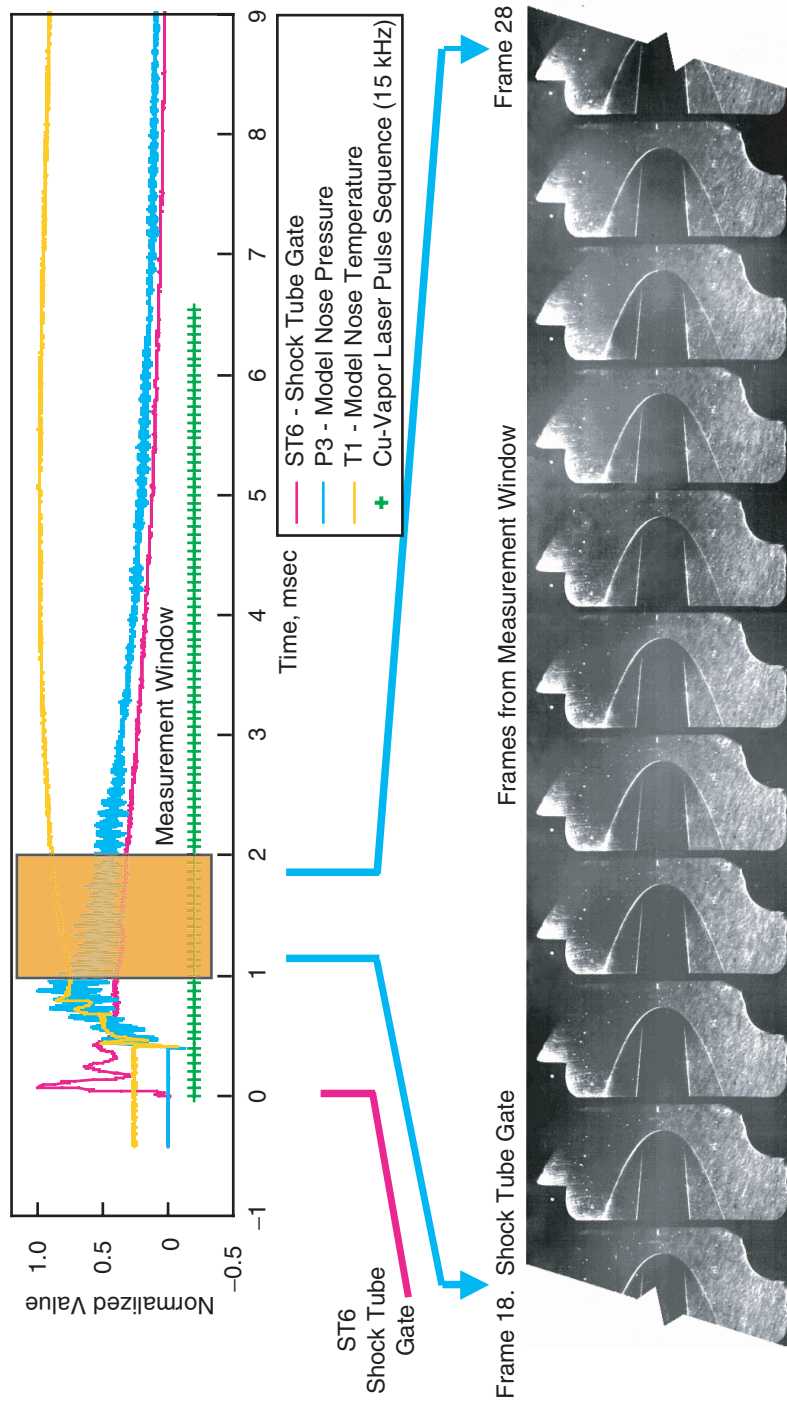


Figure 60. HSFV for Flow Steadiness, Impulse Facility Run 31—June 3, 1998

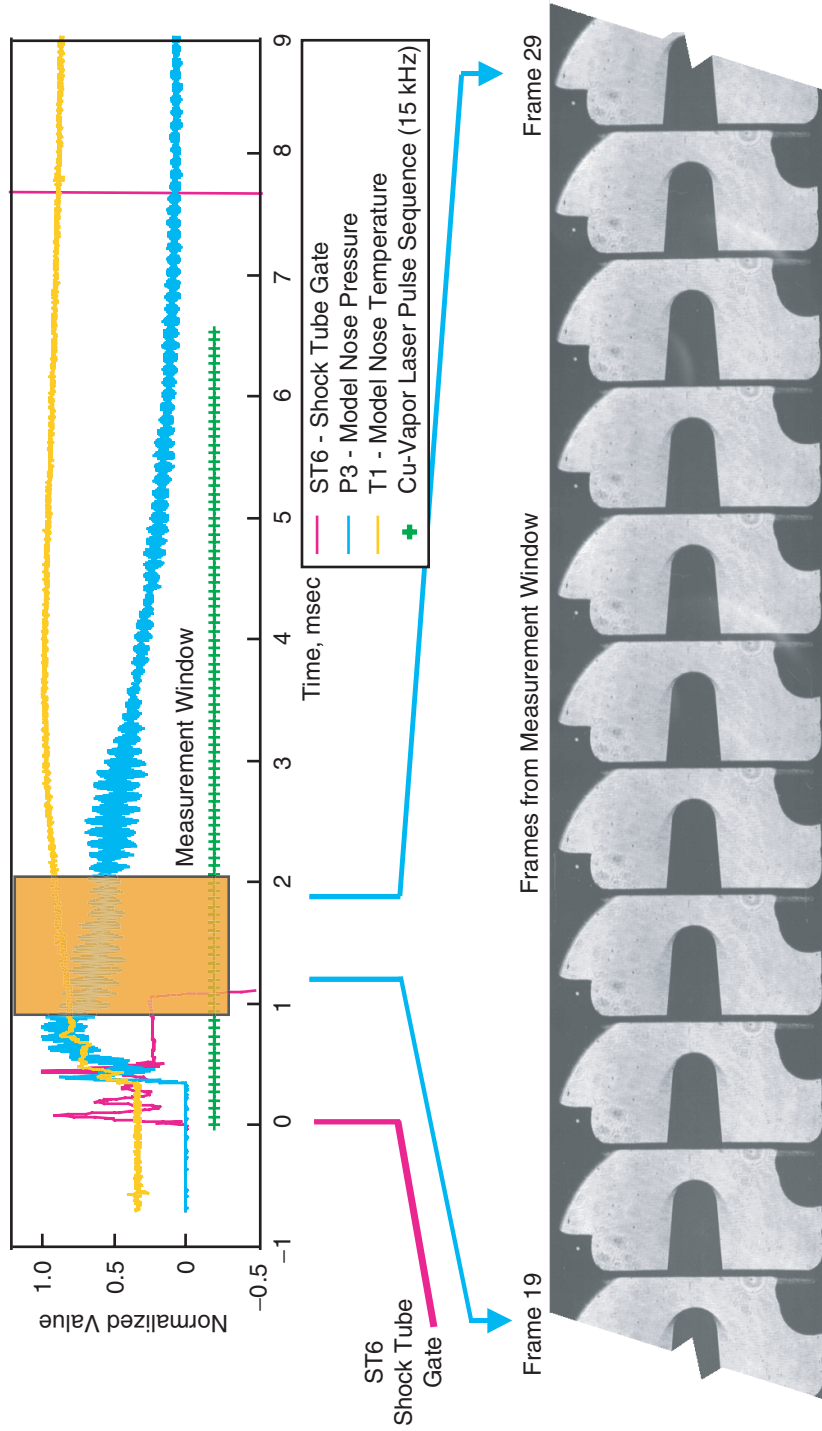


Figure 61. HSFV for Flow Steadiness, Impulse Facility Run 32—June 4, 1998

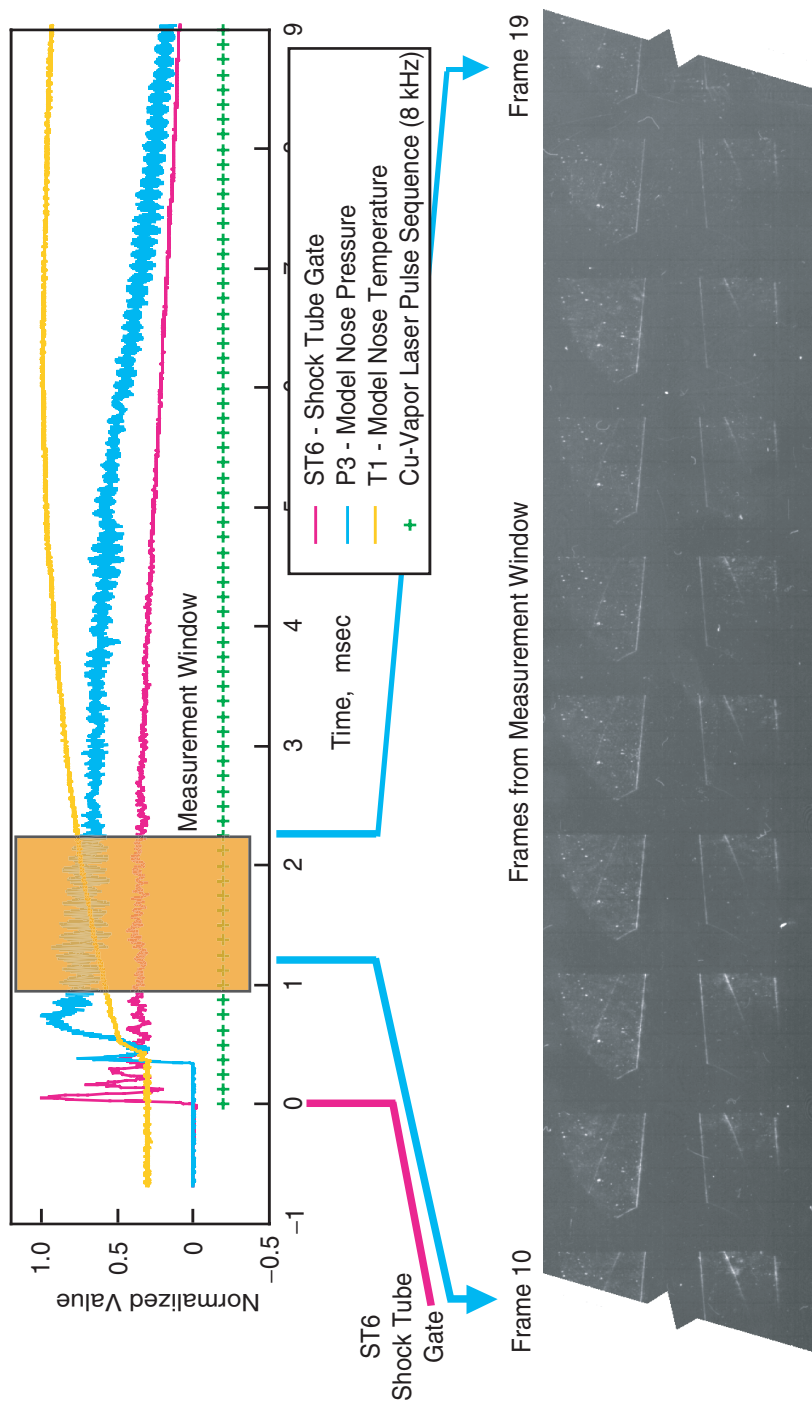


Figure 62. HSFV for Flow Steadiness, Impulse Facility Run 33—June 9, 1998

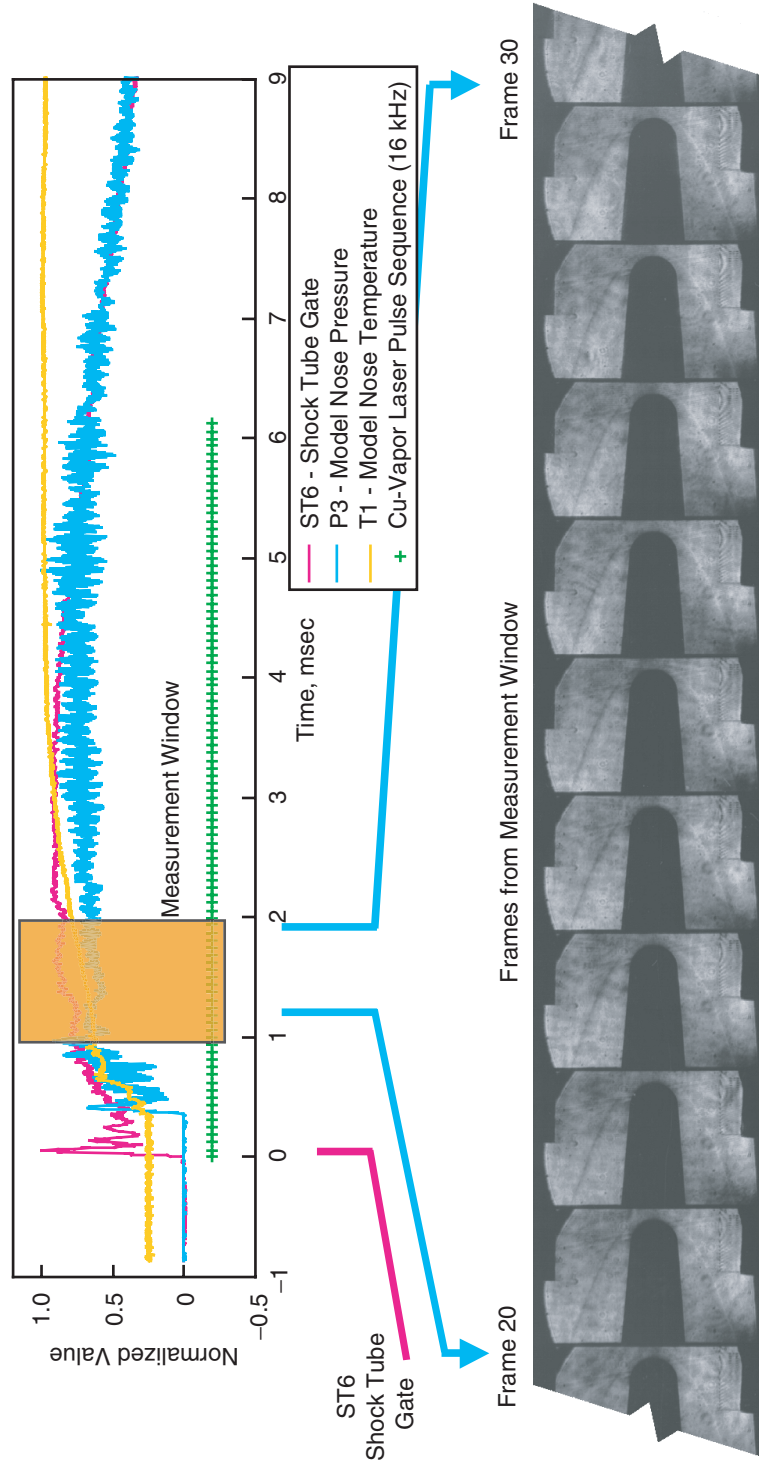


Figure 63. HSFV for Flow Steadiness, Impulse Facility Run 34—June 10, 1998

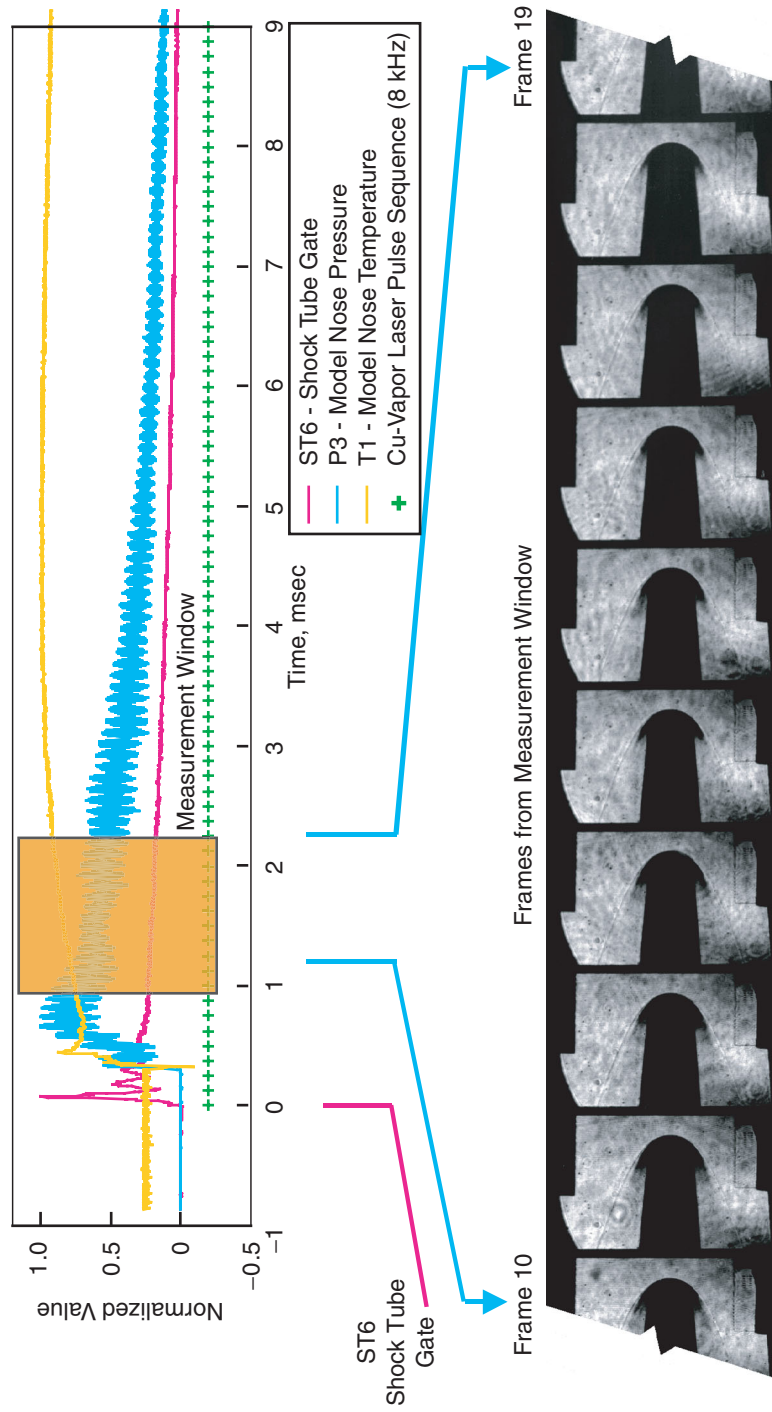


Figure 64. HSFV for Flow Steadiness, Impulse Facility Run 35—June 12, 1998

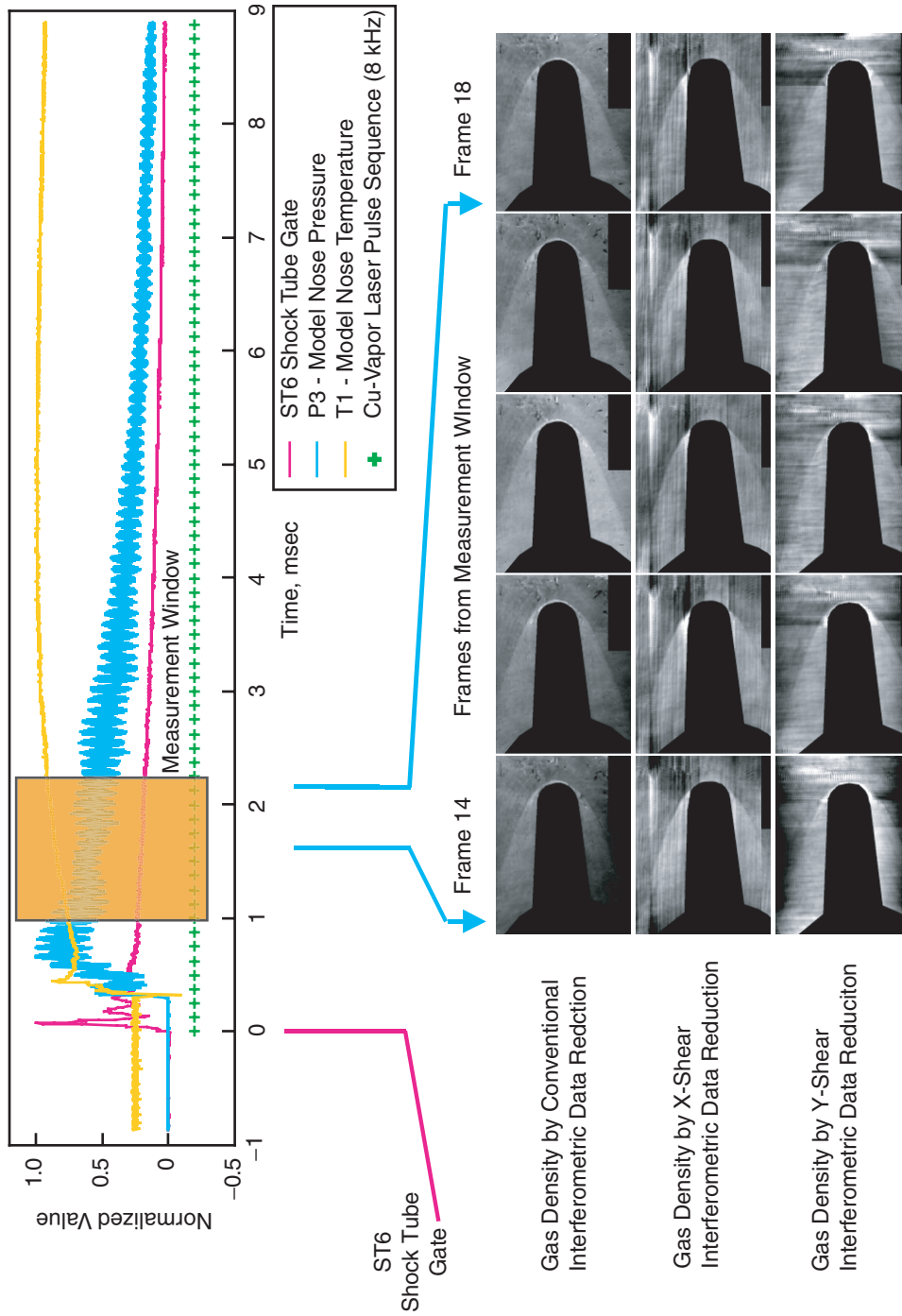
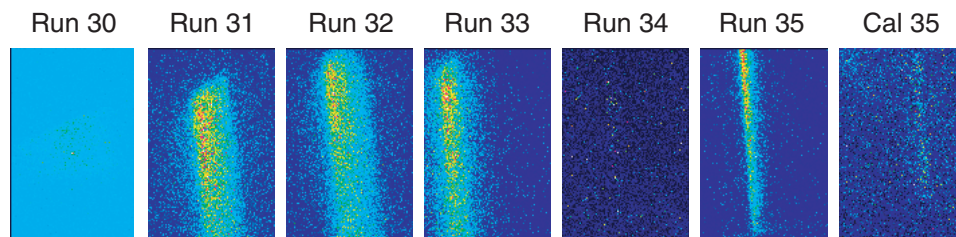
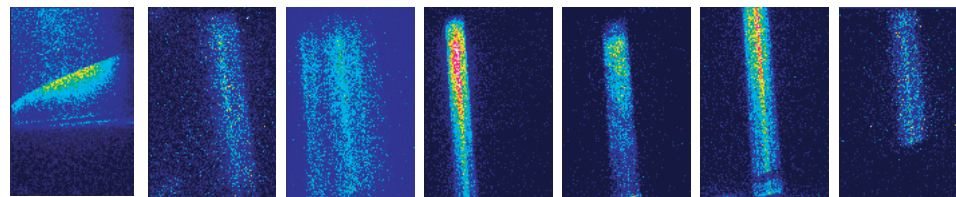


Figure 65. Gas Density from Holographic Interferometry, Impulse Facility Run 35—June 12, 1998



a. 225.134 nm



b. 225.716 nm

Figure 66. Impulse Facility: Planar Laser-Induced Fluorescence Imaging

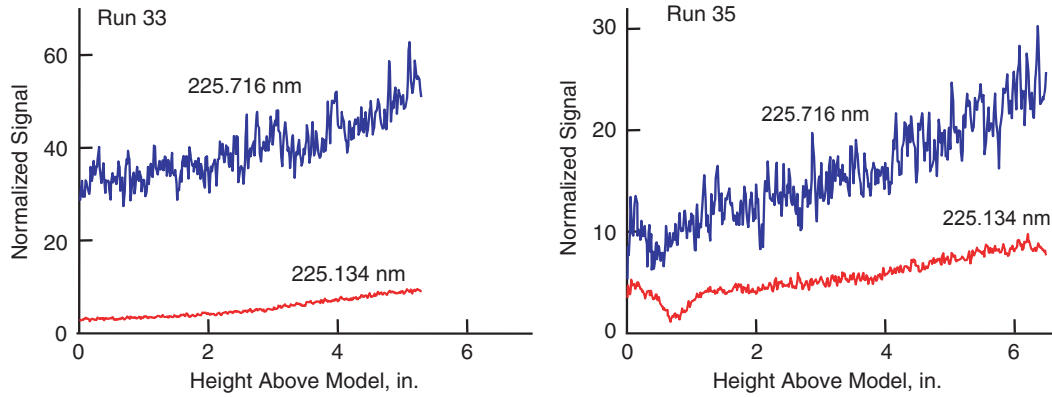


Figure 67. PLIF Signal Profiles

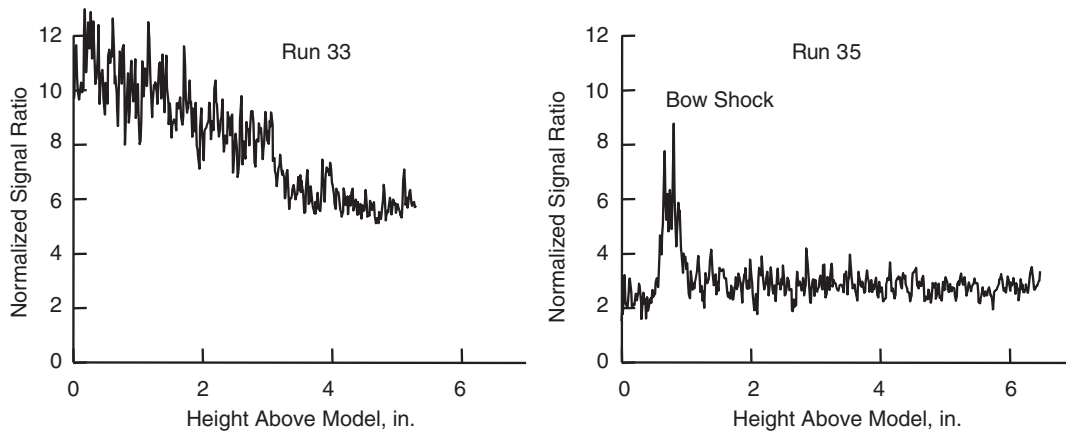


Figure 68. PLIF Signal Ratios

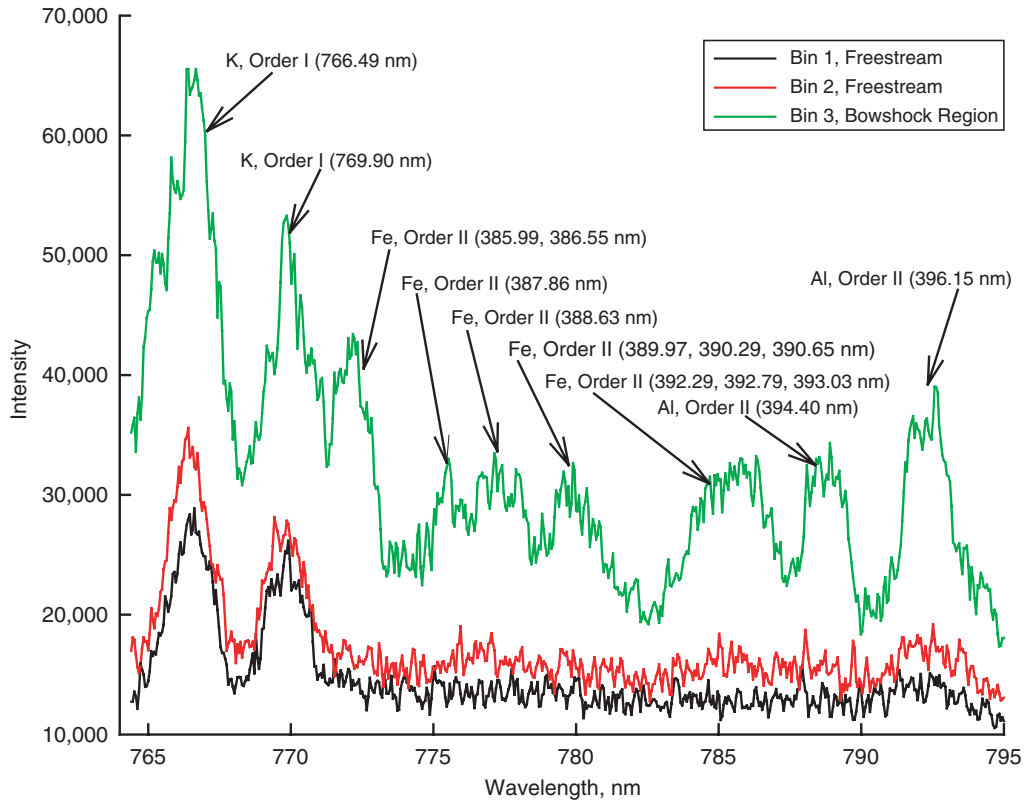


Figure 69. Impulse Facility Run 26 Emission Spectra

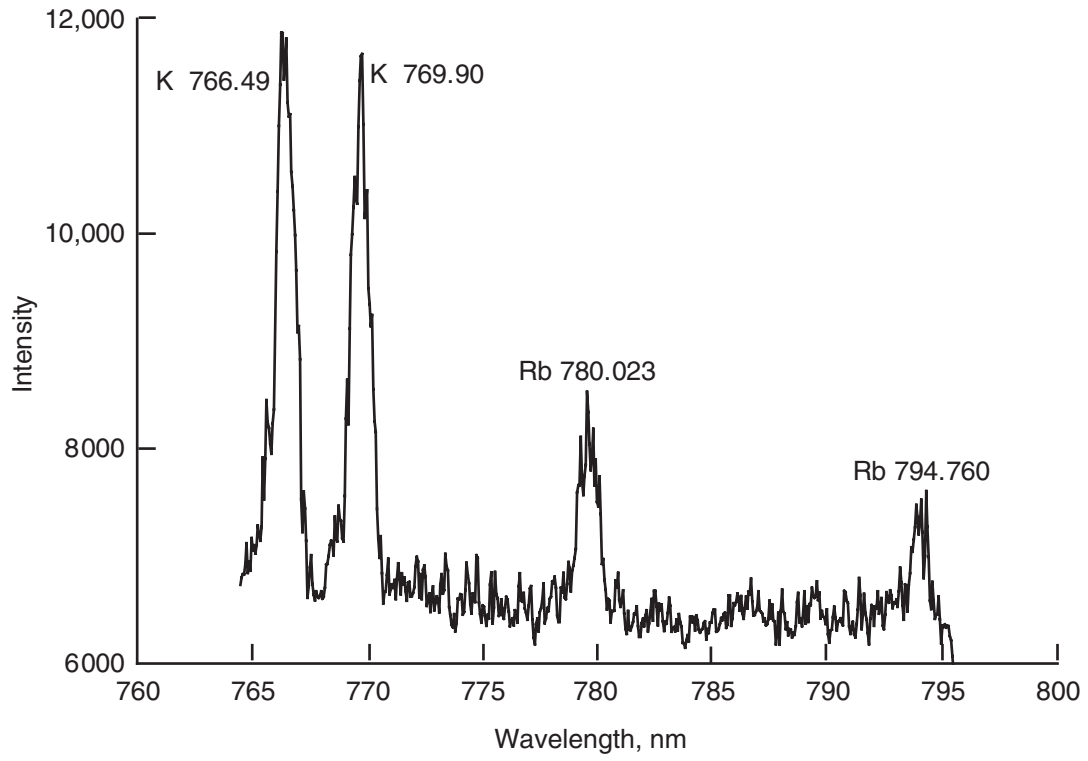


Figure 70. FPST Emission Spectrum

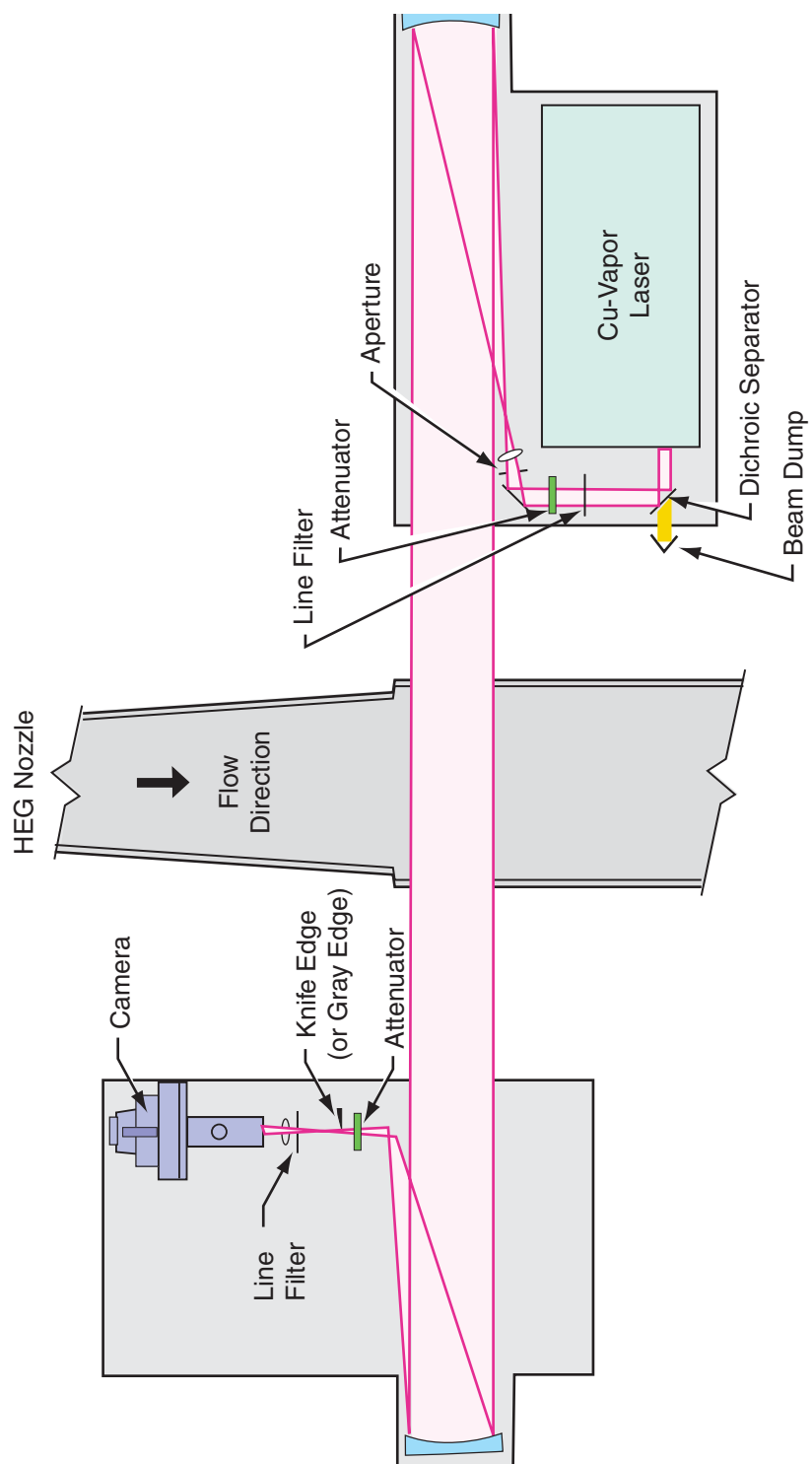


Figure 71. HSFV System as Installed on HEG

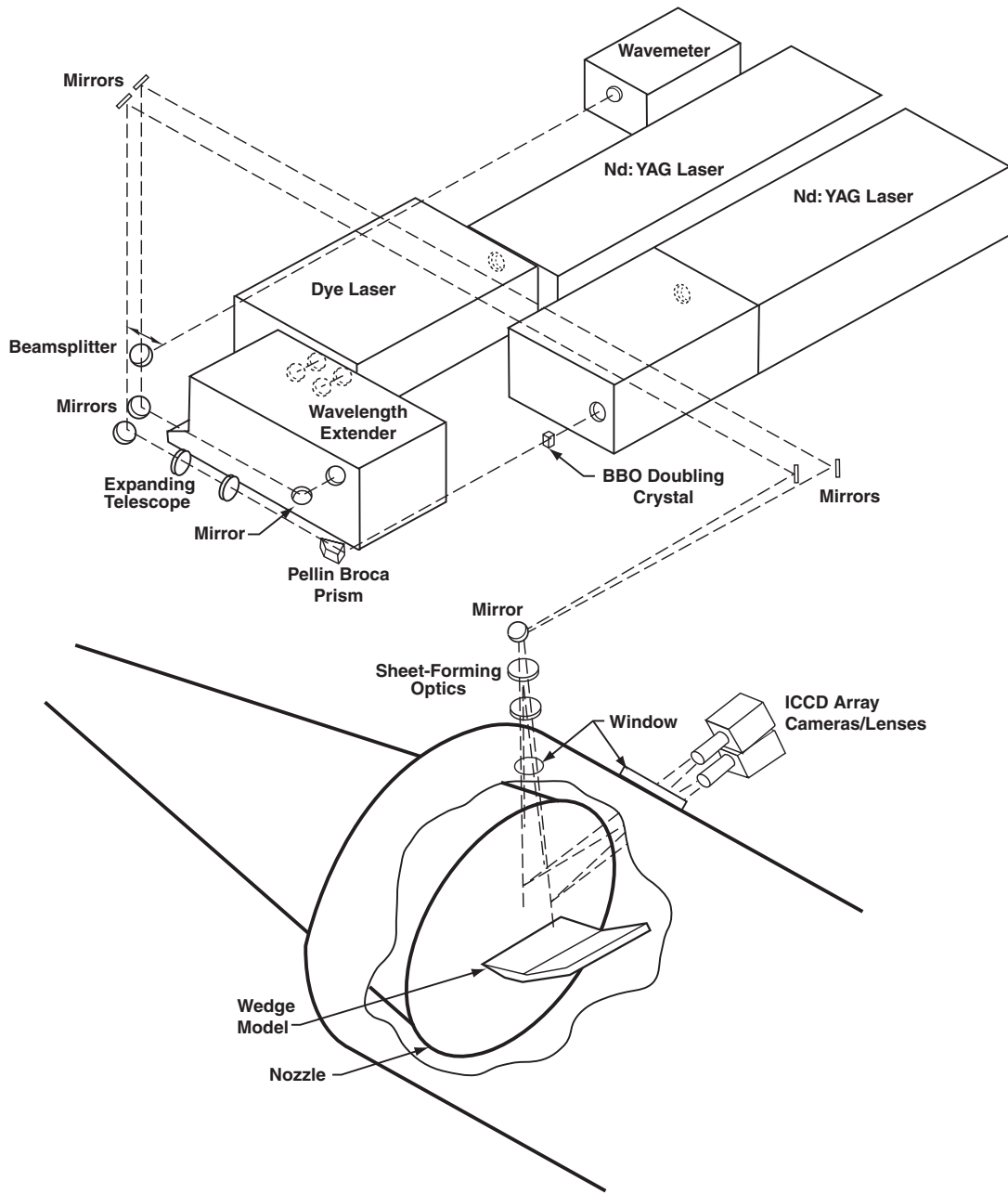


Figure 72. PLIF Setup in HEG

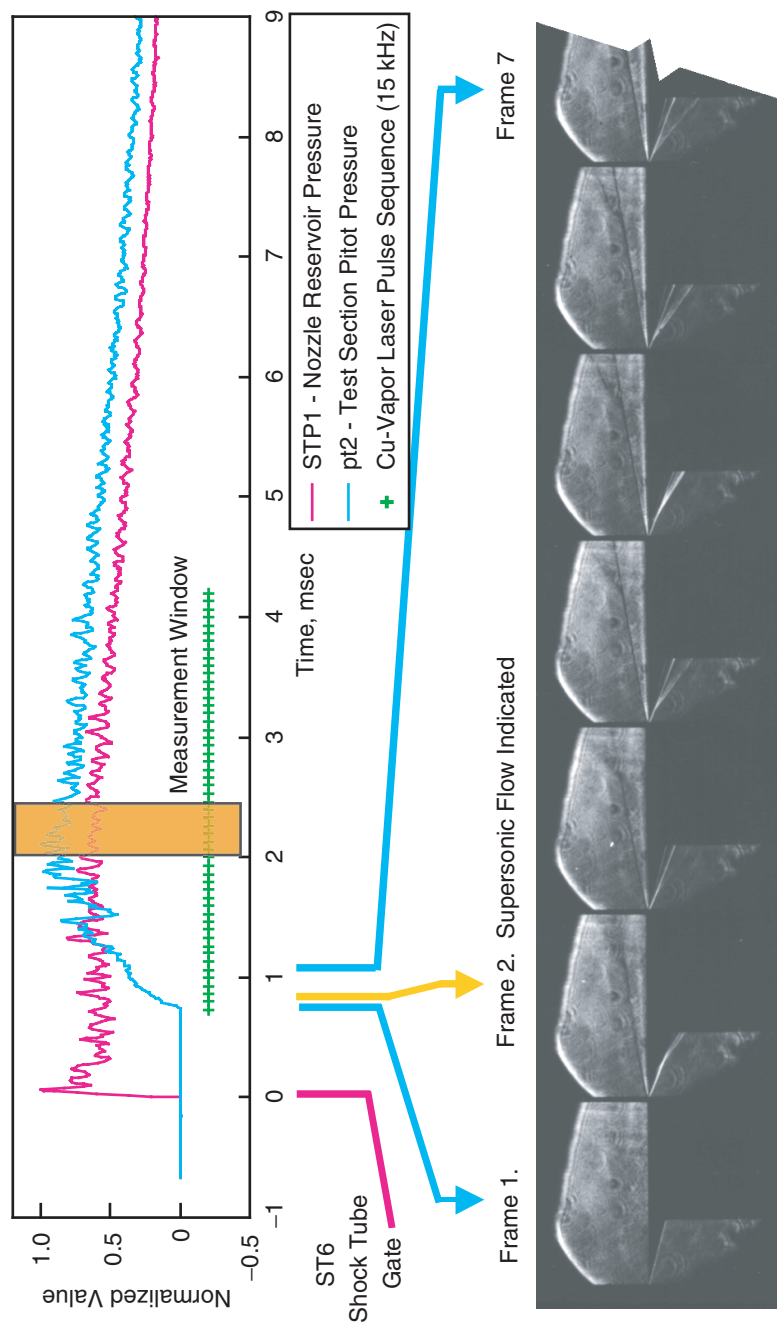


Figure 73. HSFV for Flow Start Process, HEG Run 446—September 25, 1998

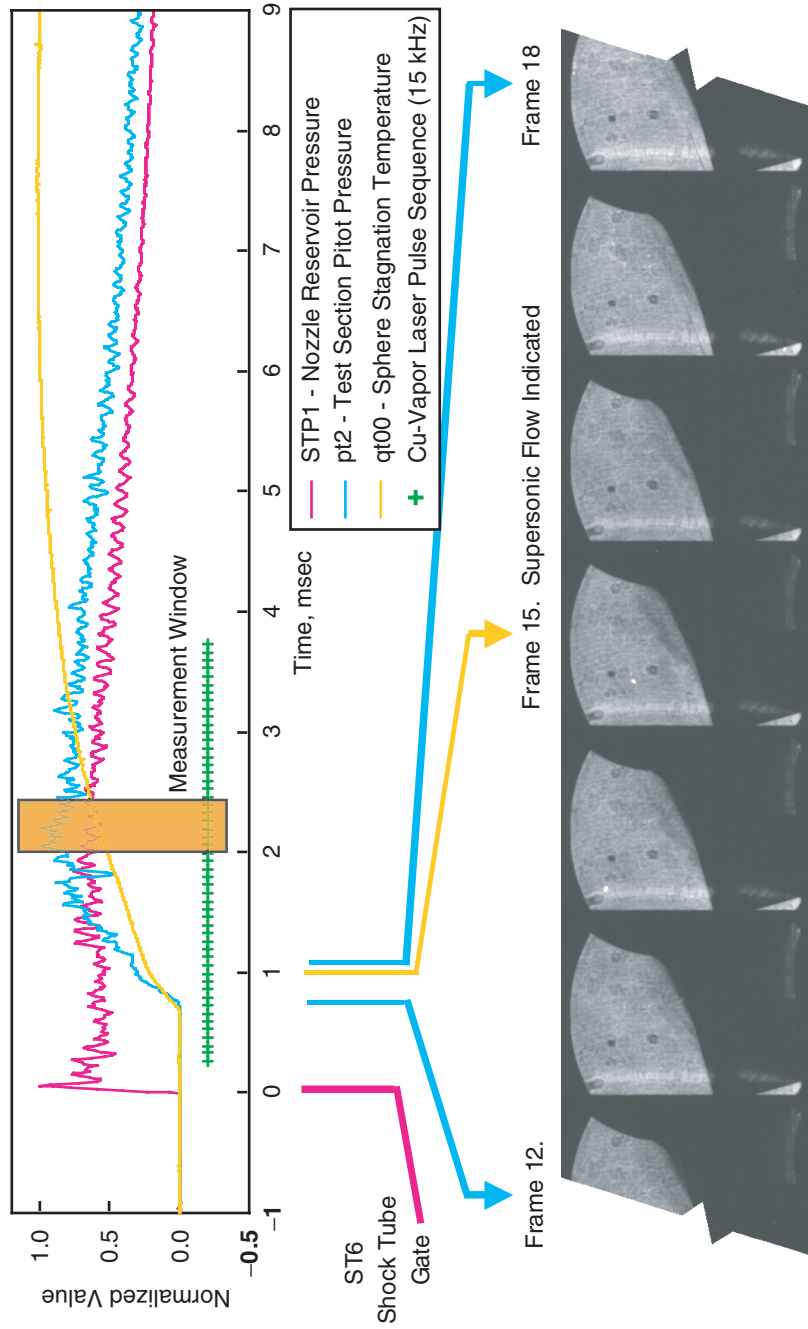


Figure 74. HSFV for Flow Start Process, HEG Run 448—September 28, 1998

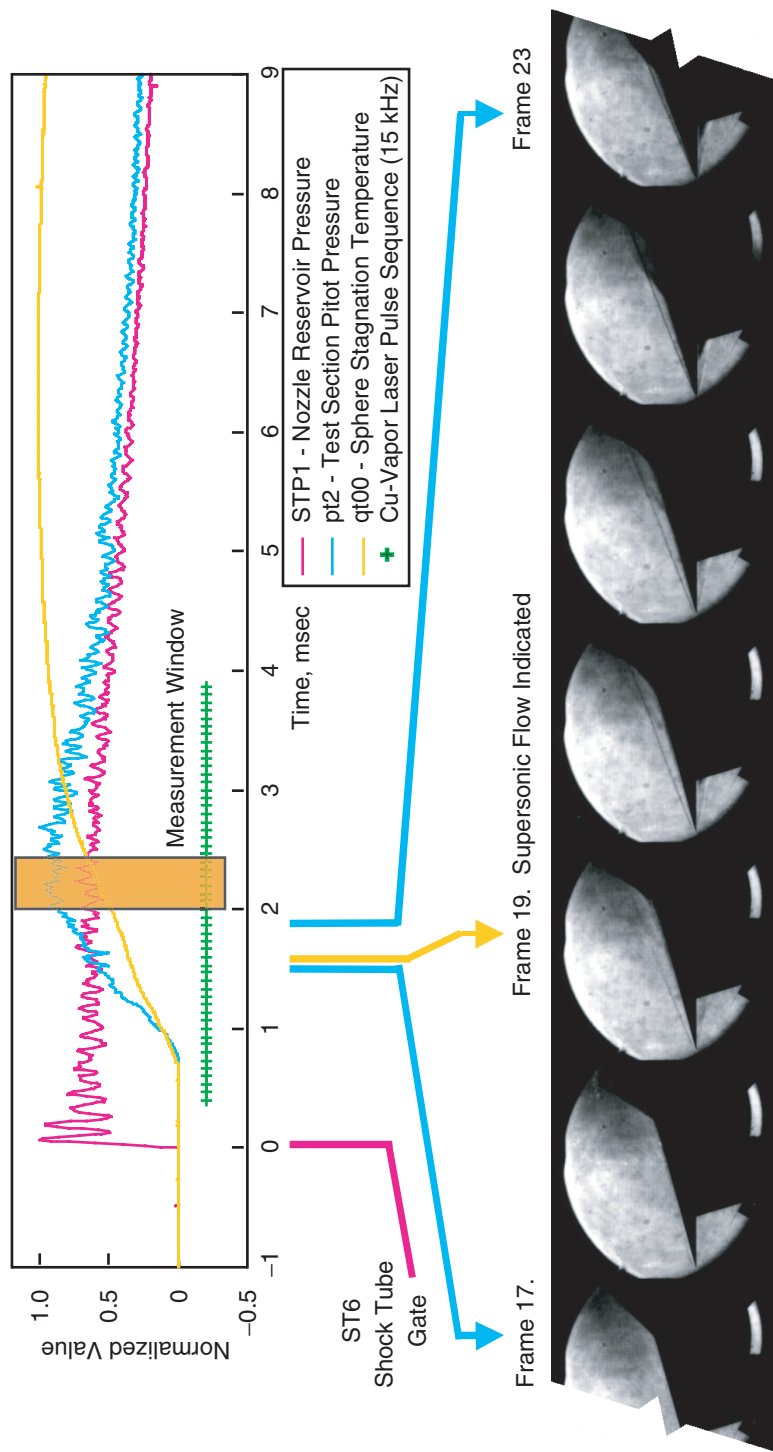


Figure 75. HSFV for Flow Start Process, HEG Run 451—September 30, 1998

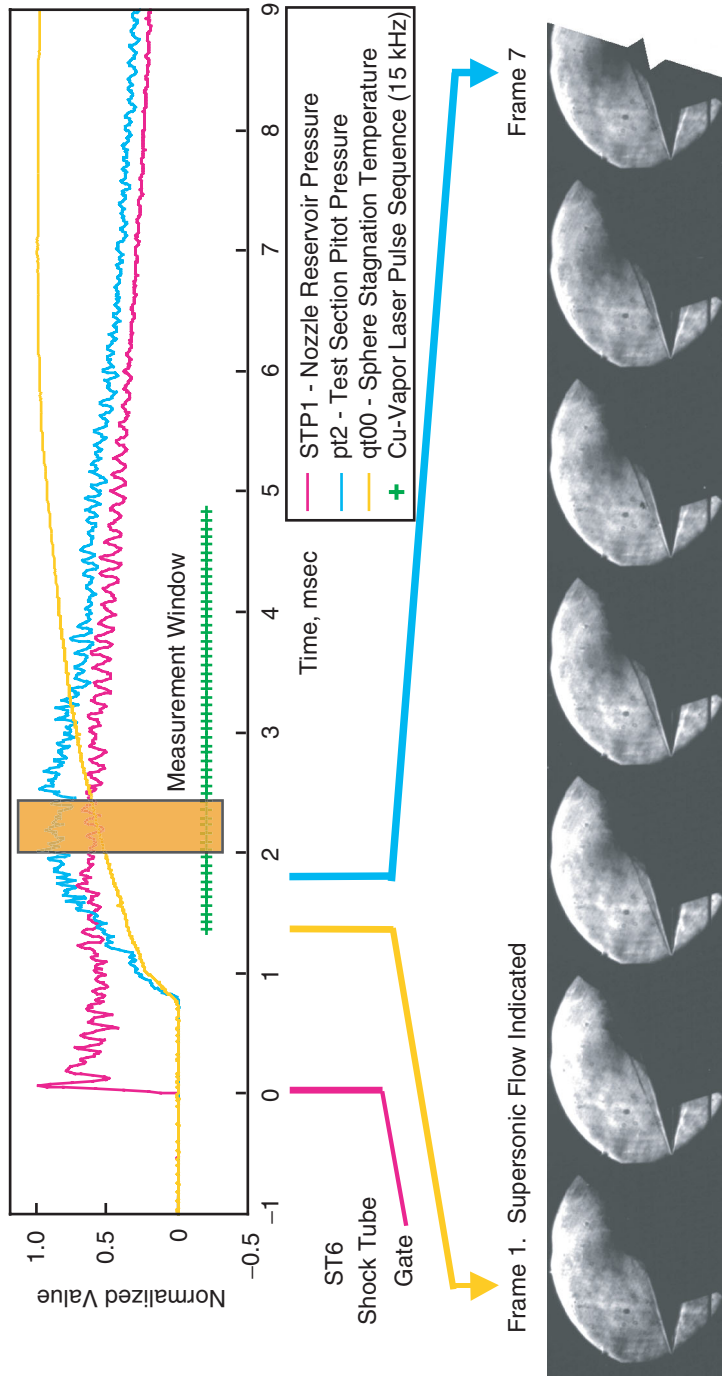


Figure 76. HSFV for Flow Start Process, HEG Run 452—November 1, 1998

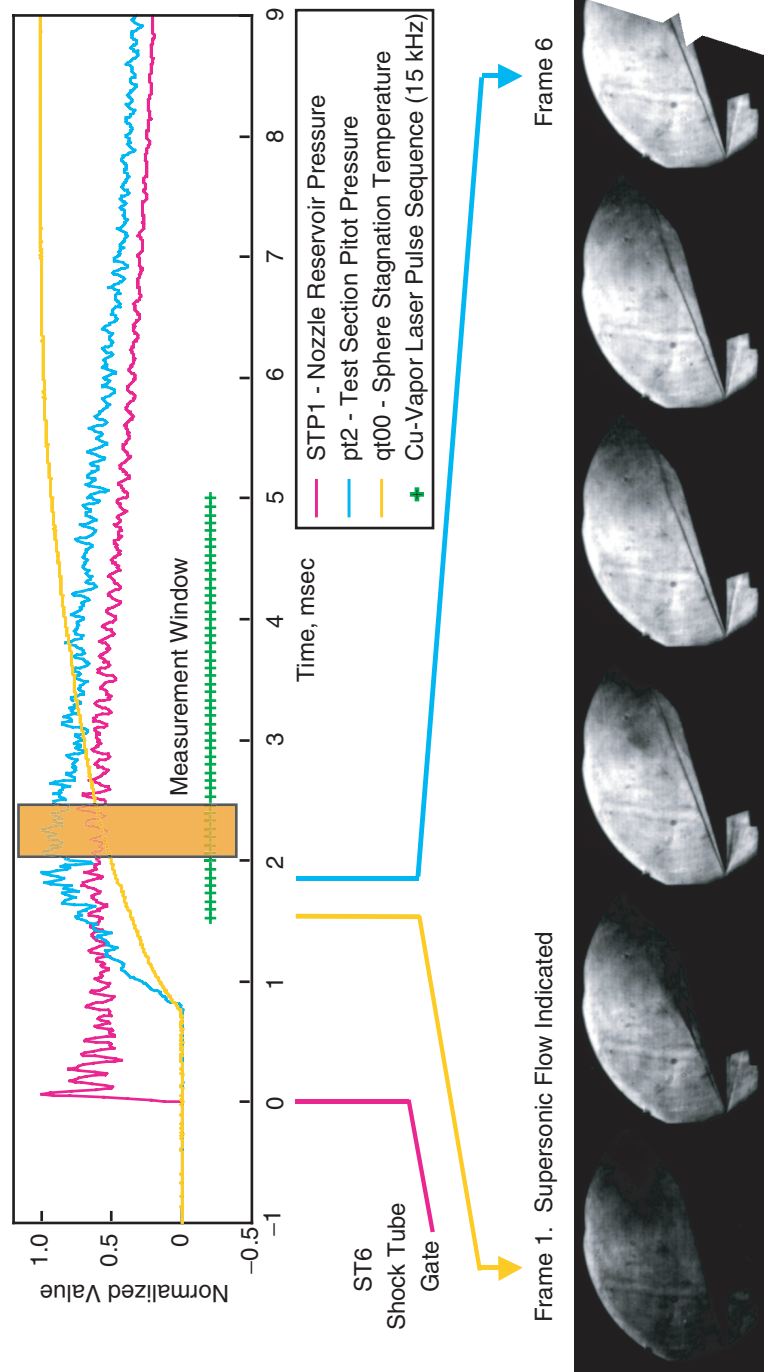


Figure 77. HSFV for Flow Start Process, HEG Run 453—November 1, 1998

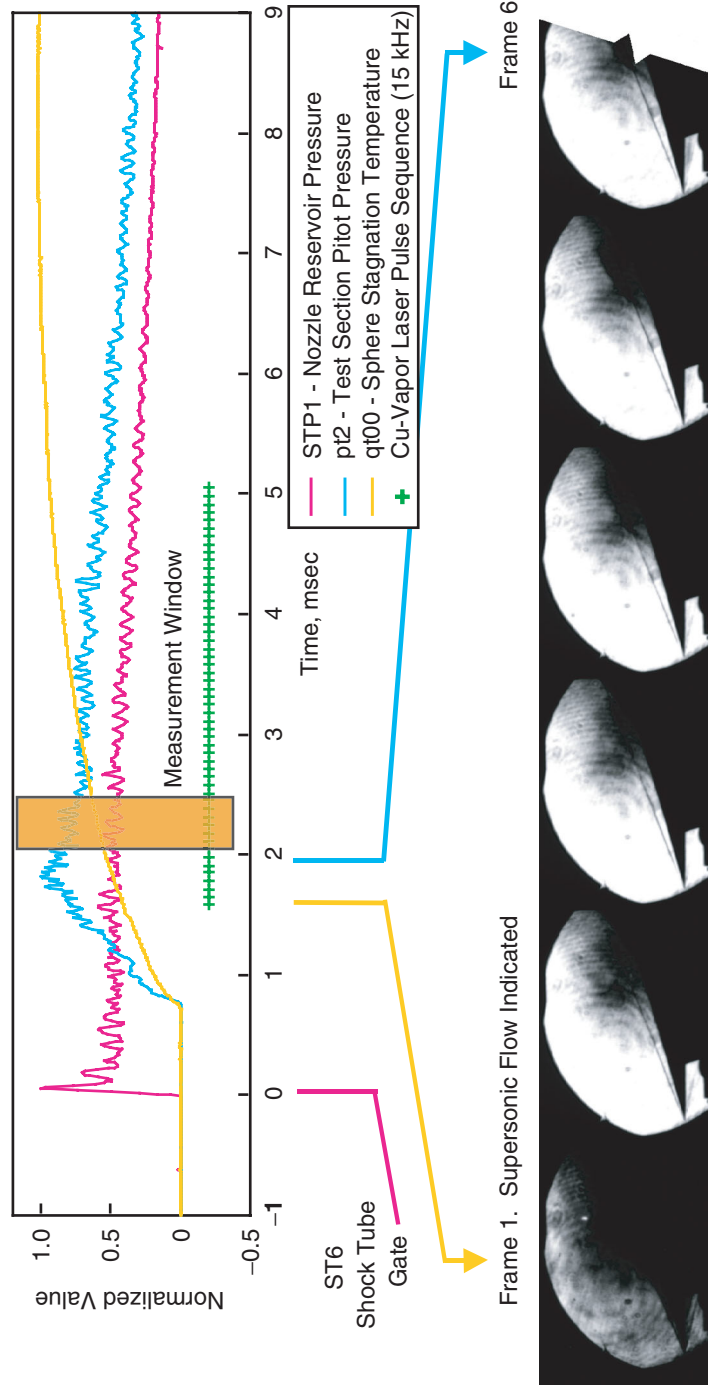


Figure 78. HSFV for Flow Start Process, HEG Run 454—November 2, 1998

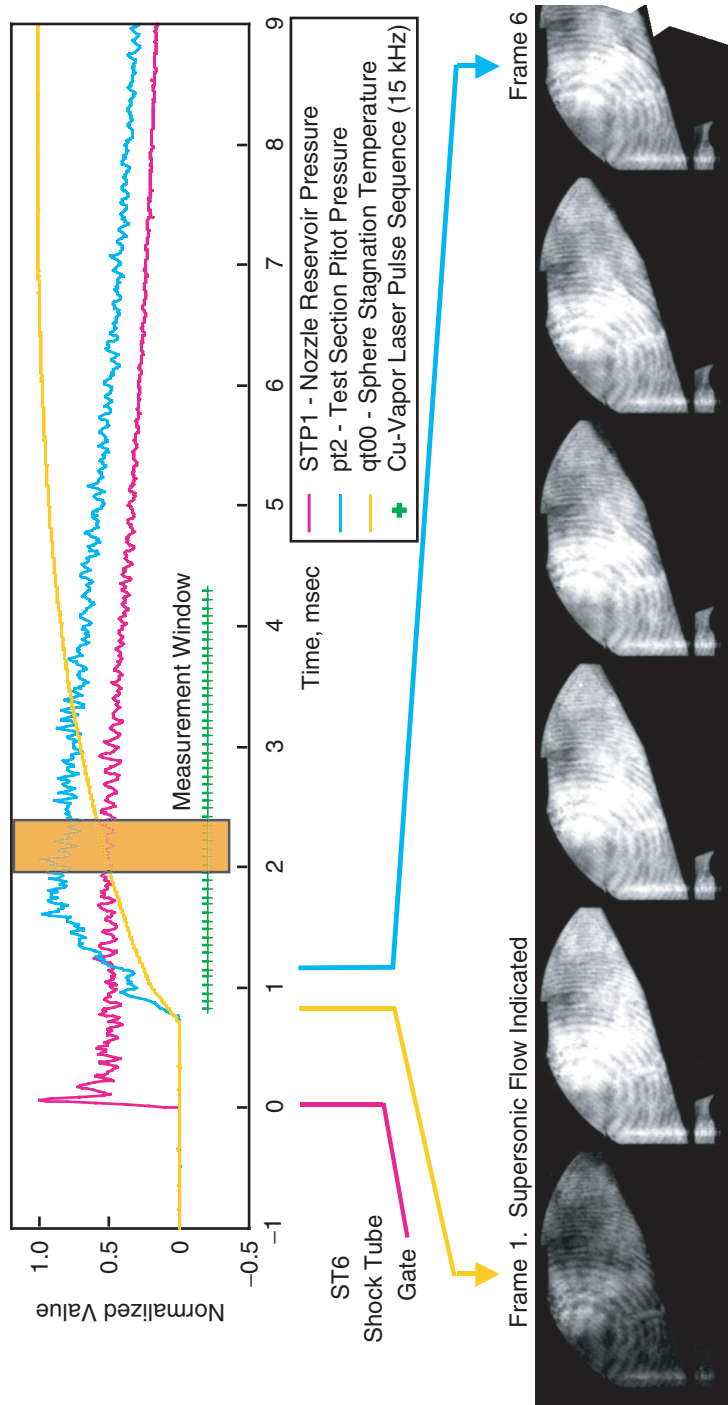


Figure 79. HSFV for Flow Start Process, HEG Run 455—November 2, 1998

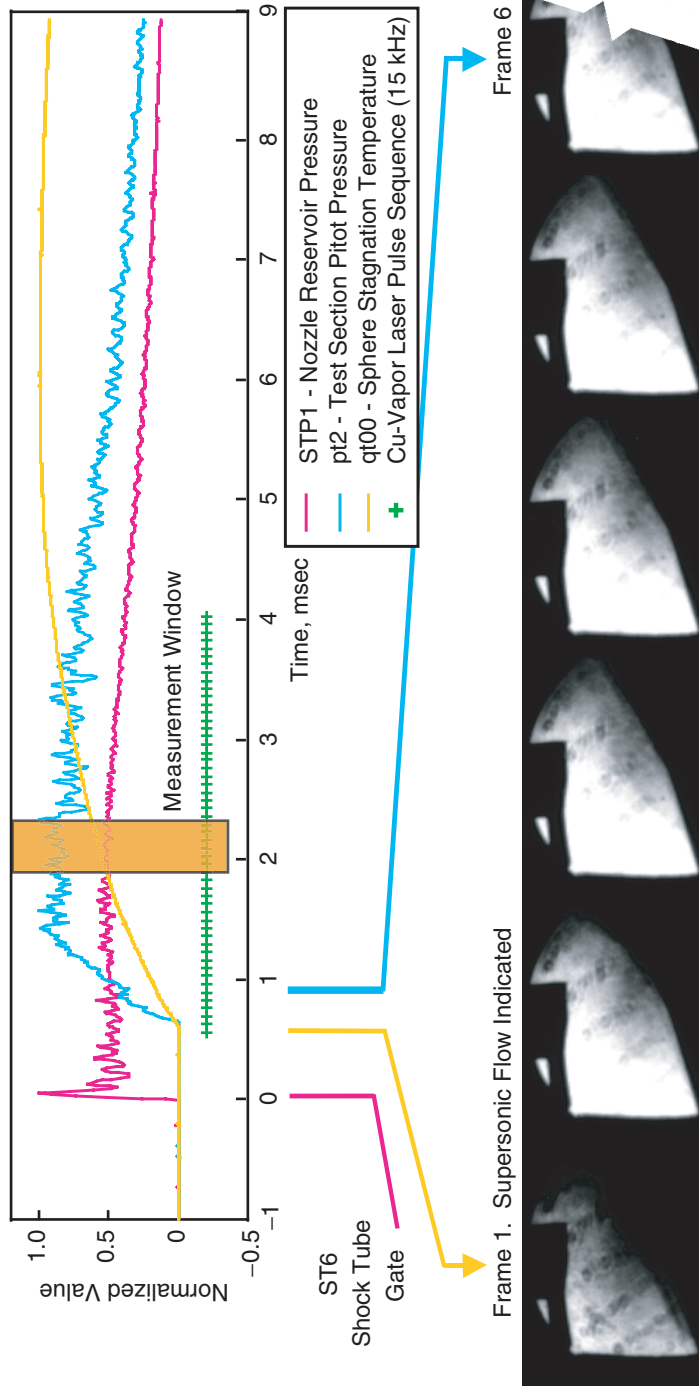


Figure 80. HSFV for Flow Start Process, HEG Run 456—November 5, 1998

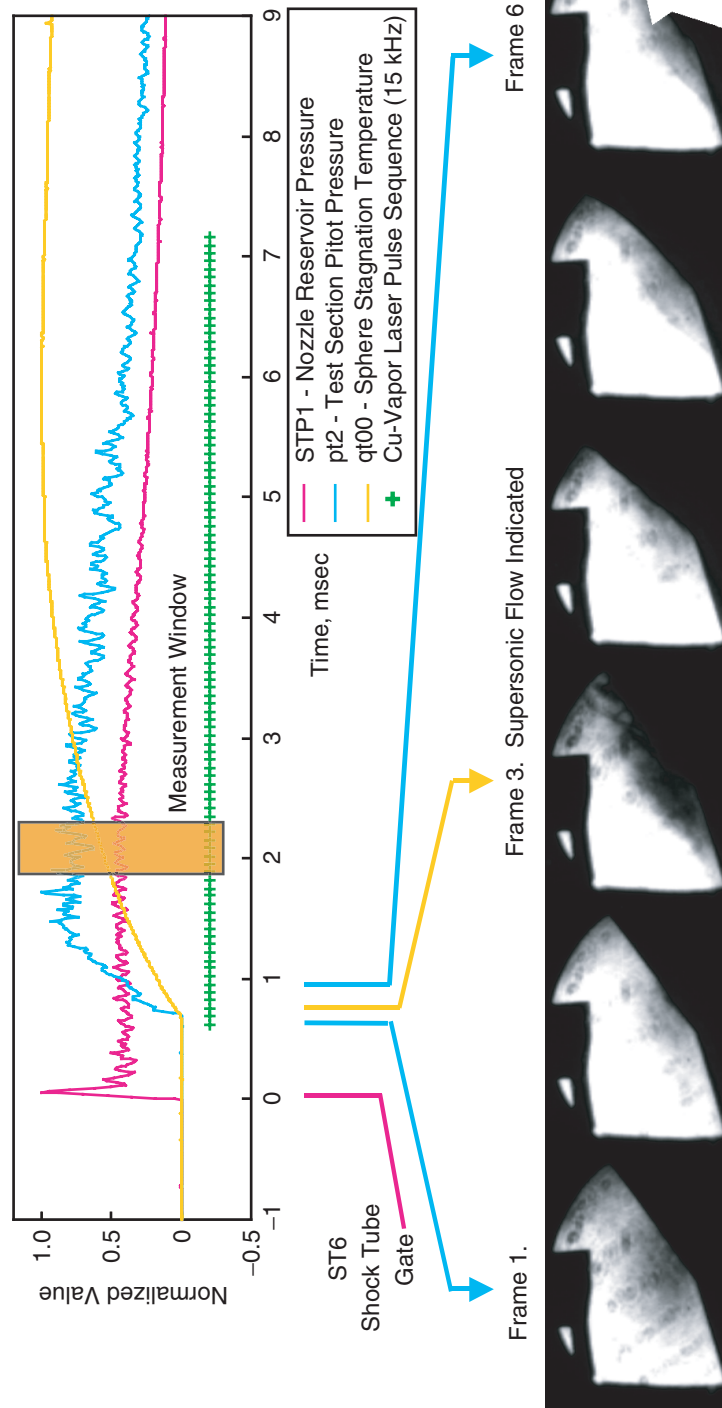


Figure 81. HSFV for Flow Start Process, HEG Run 457—November 5, 1998

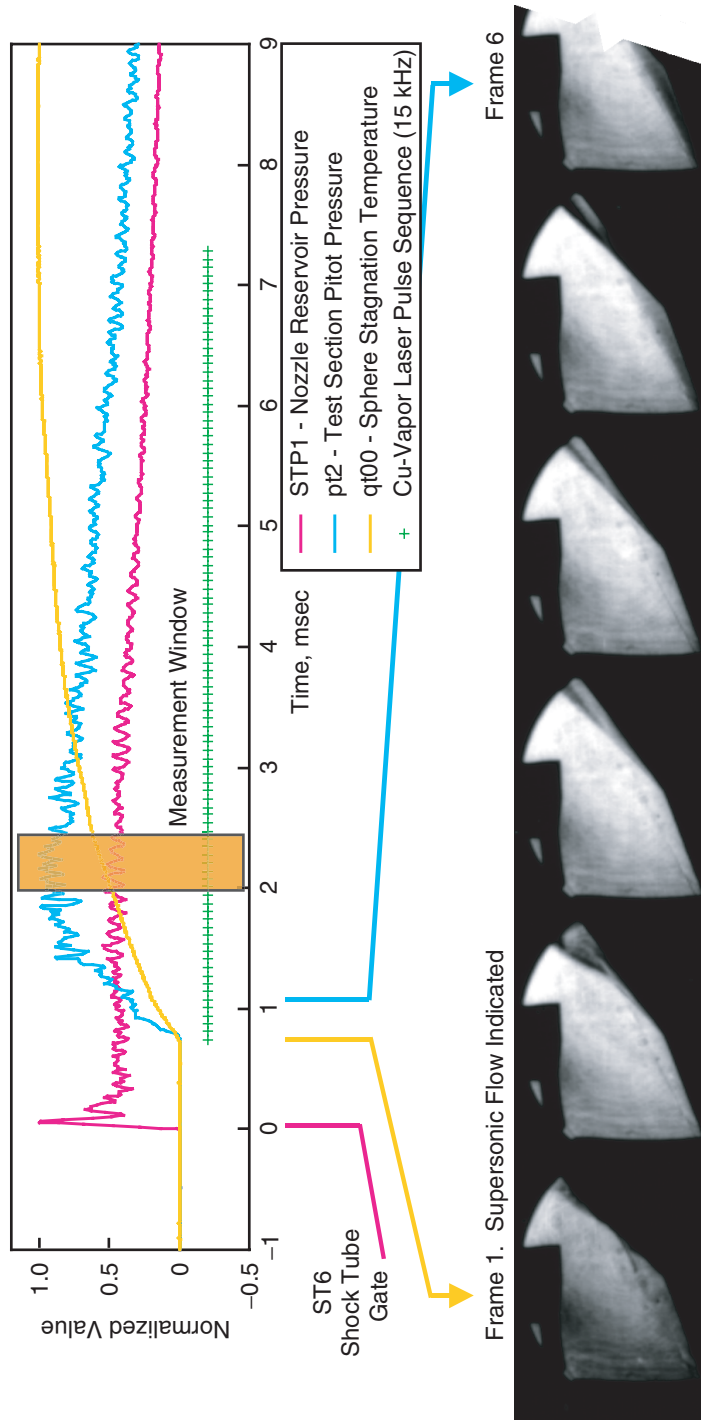


Figure 82. HSFV for Flow Start Process, HEG Run 458—November 1998

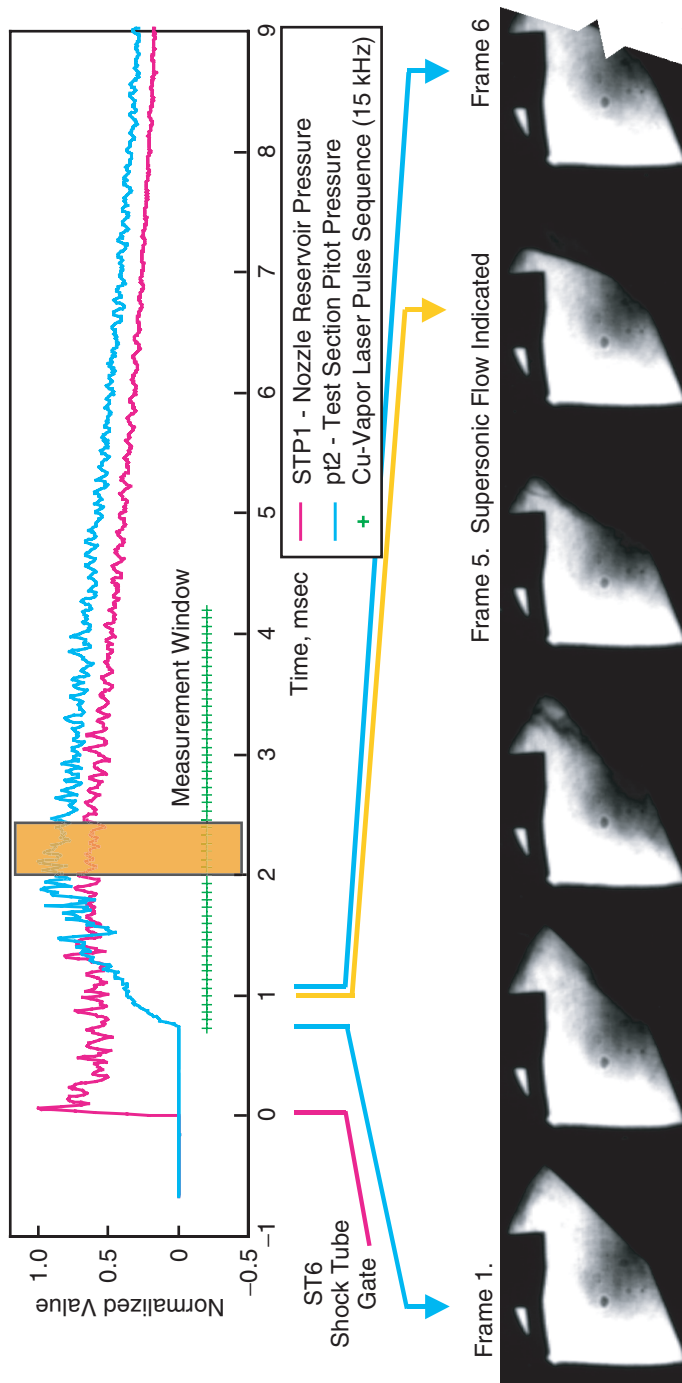


Figure 83. HSFV for Flow Start Process, HEG Run 460—November 1998

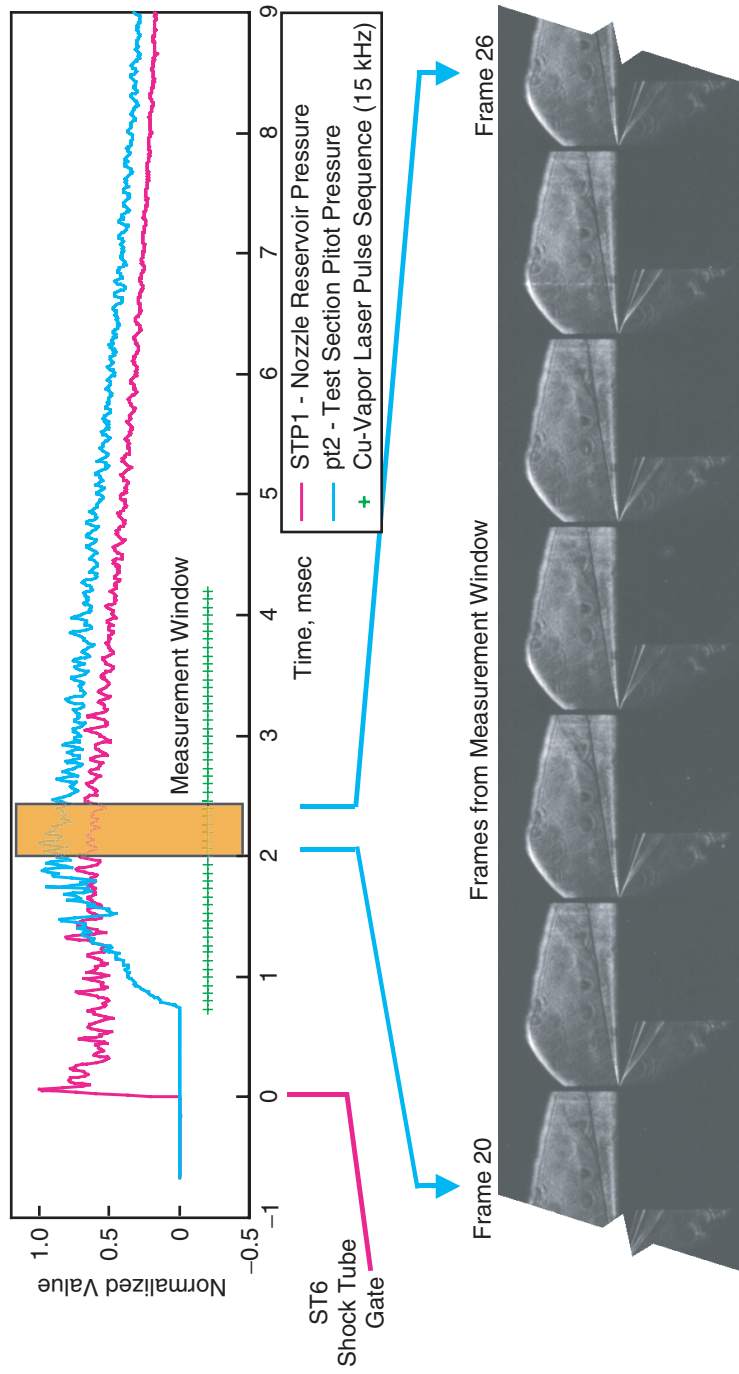


Figure 84. HSFV for Flow Steadiness, HEG Run 446—September 25, 1998

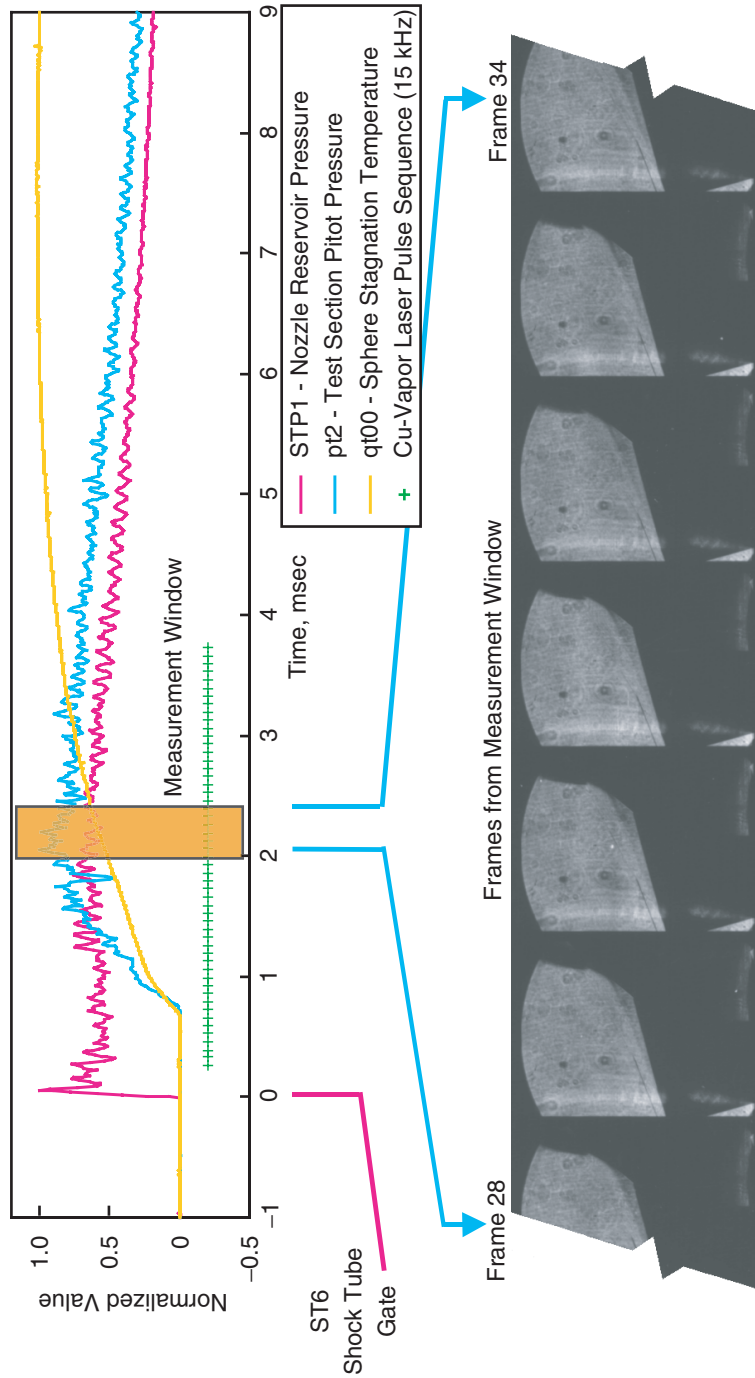


Figure 85. HSFV for Flow Steadiness, HEG Run 448—September 28, 1998

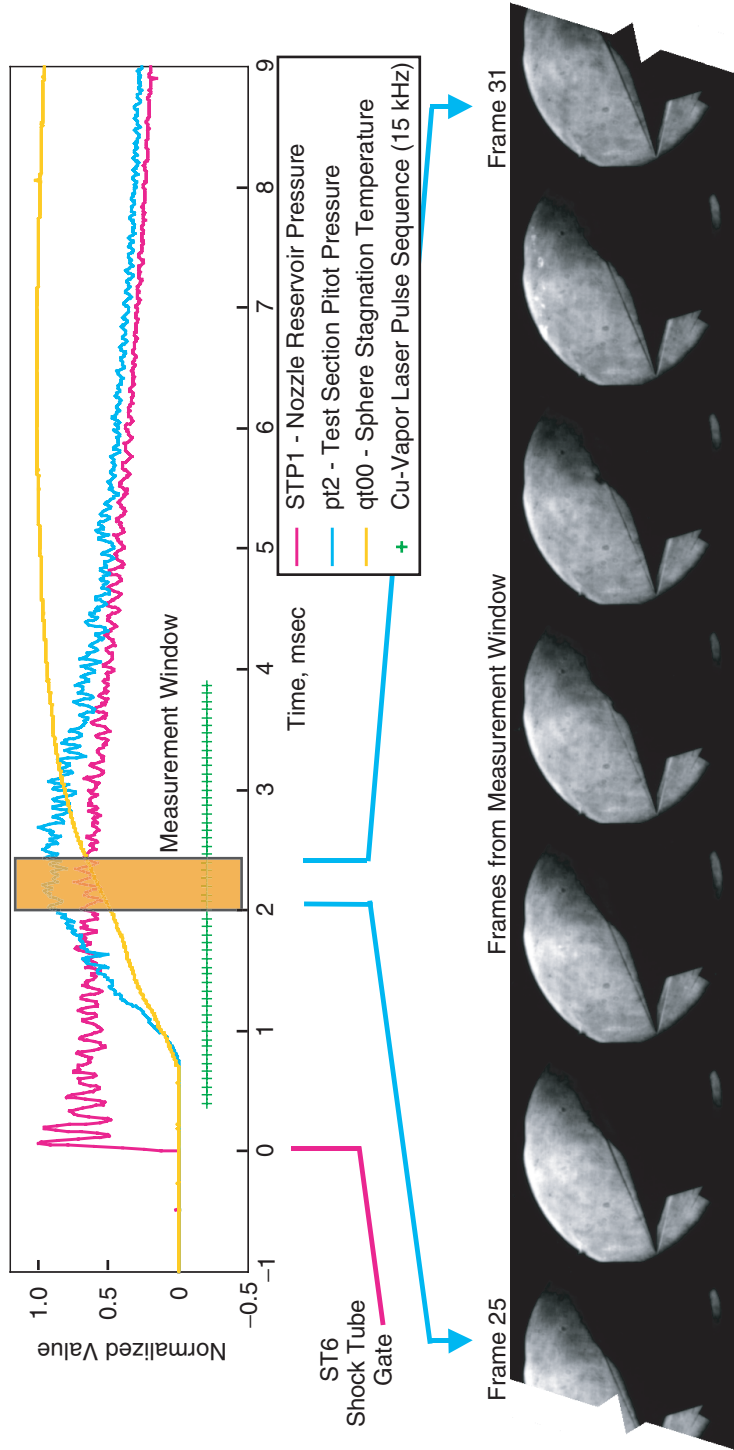


Figure 86. HSFV for Flow Steadiness, HEG Run 451—September 30, 1998

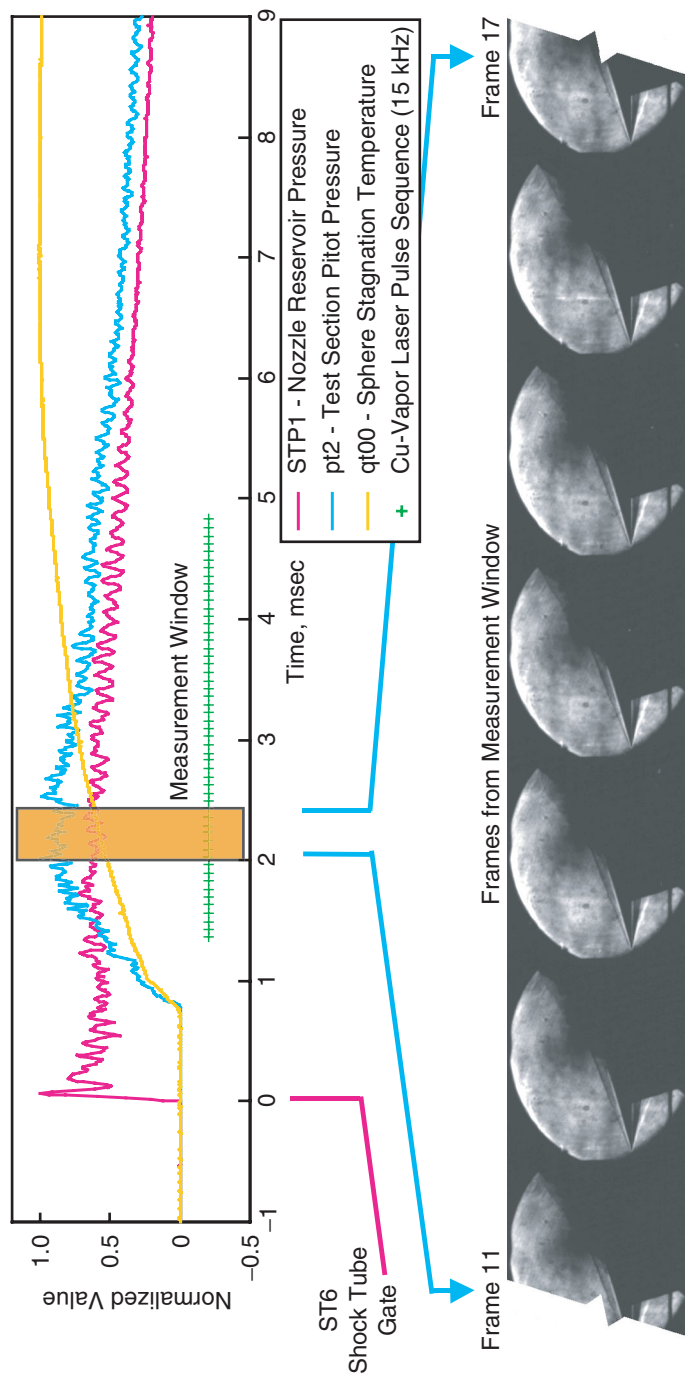


Figure 87. HSFV for Flow Steadiness, HEG Run 452—November 1, 1998

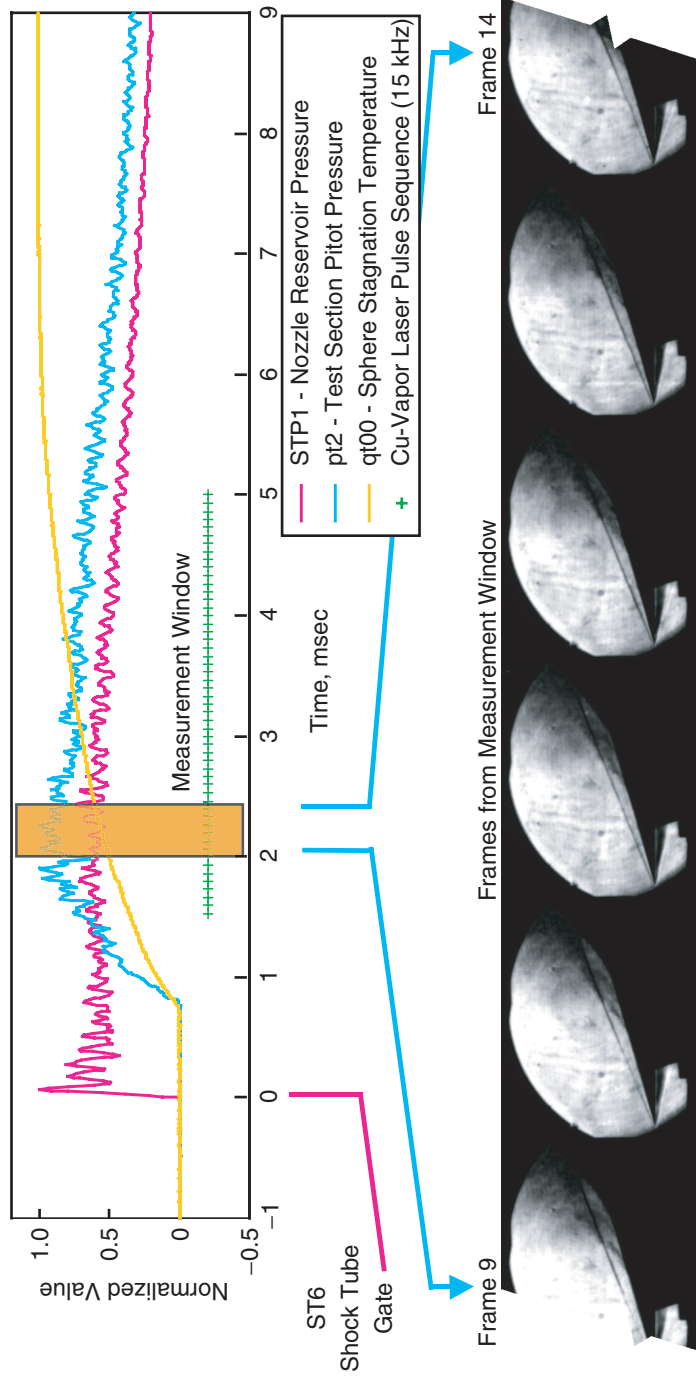


Figure 88. HSFV for Flow Steadiness, HEG Run 453—November 1, 1998

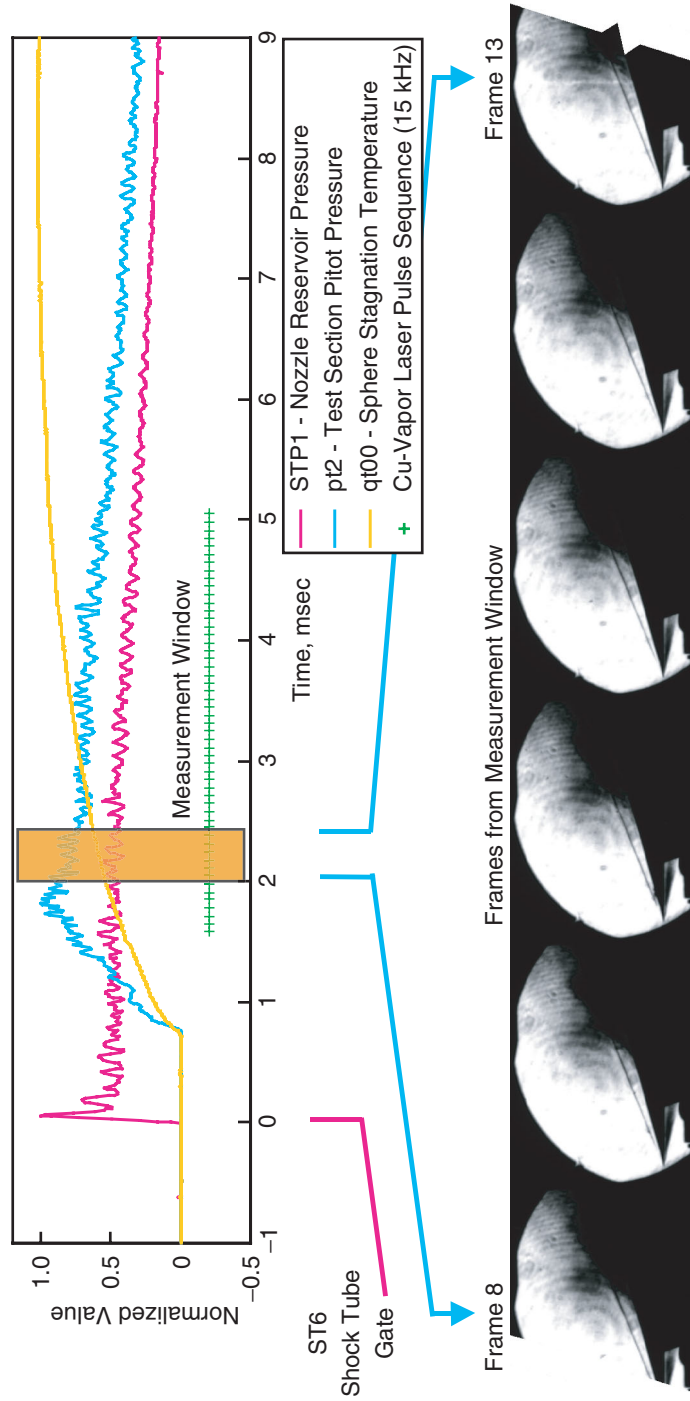


Figure 89. HSFV for Flow Steadiness, HEG Run 454—November 2, 1998

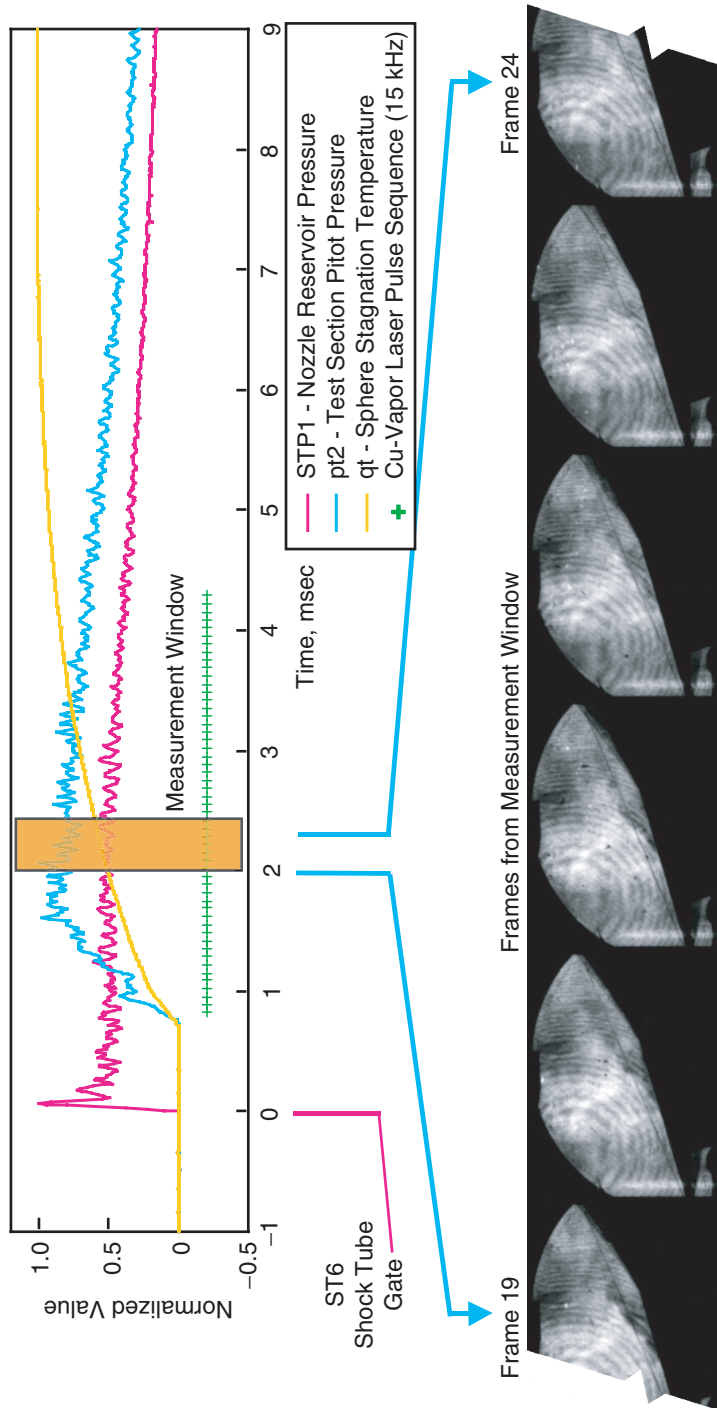


Figure 90. HSFV for Flow Steadiness, HEG Run 455—November 2, 1998

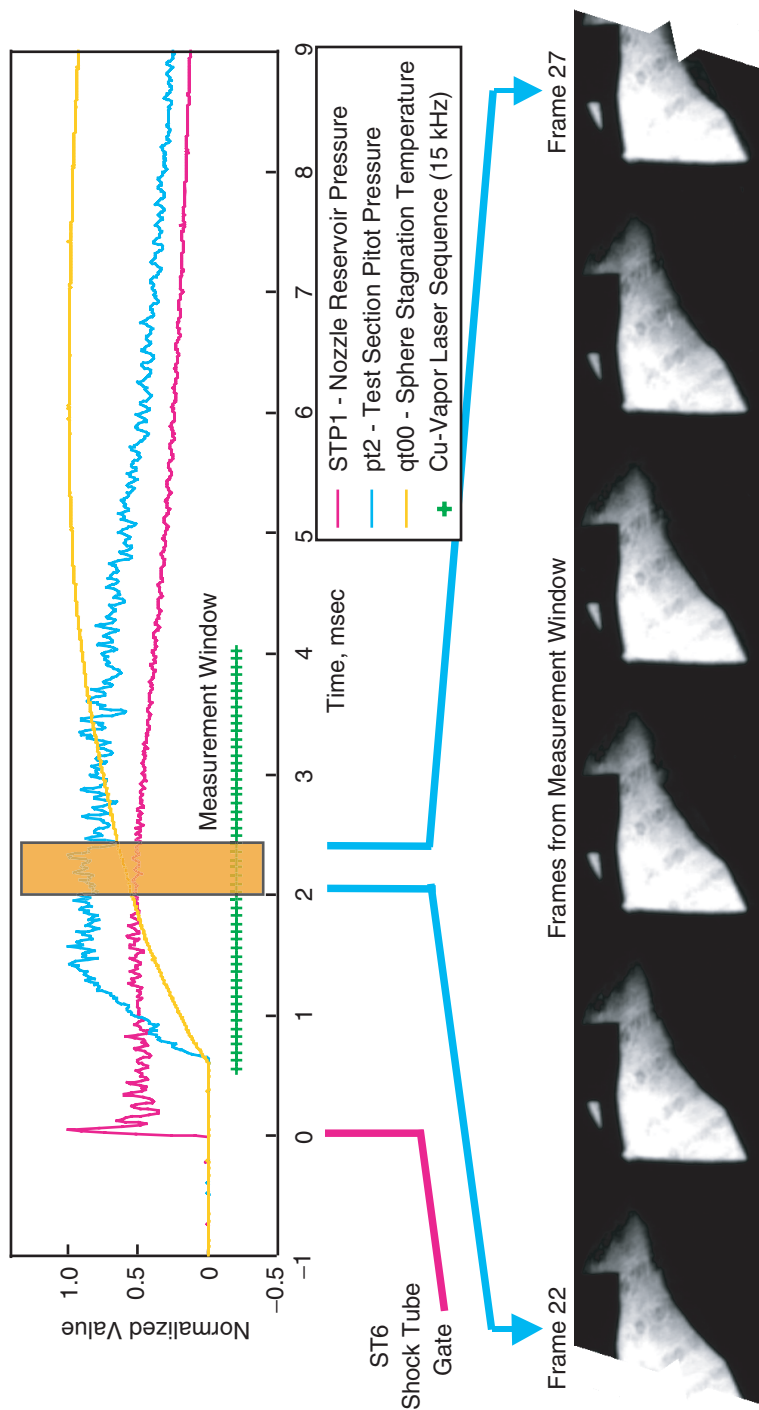


Figure 91. HSFV for Flow Steadiness, HEG Run 456—November 5, 1998

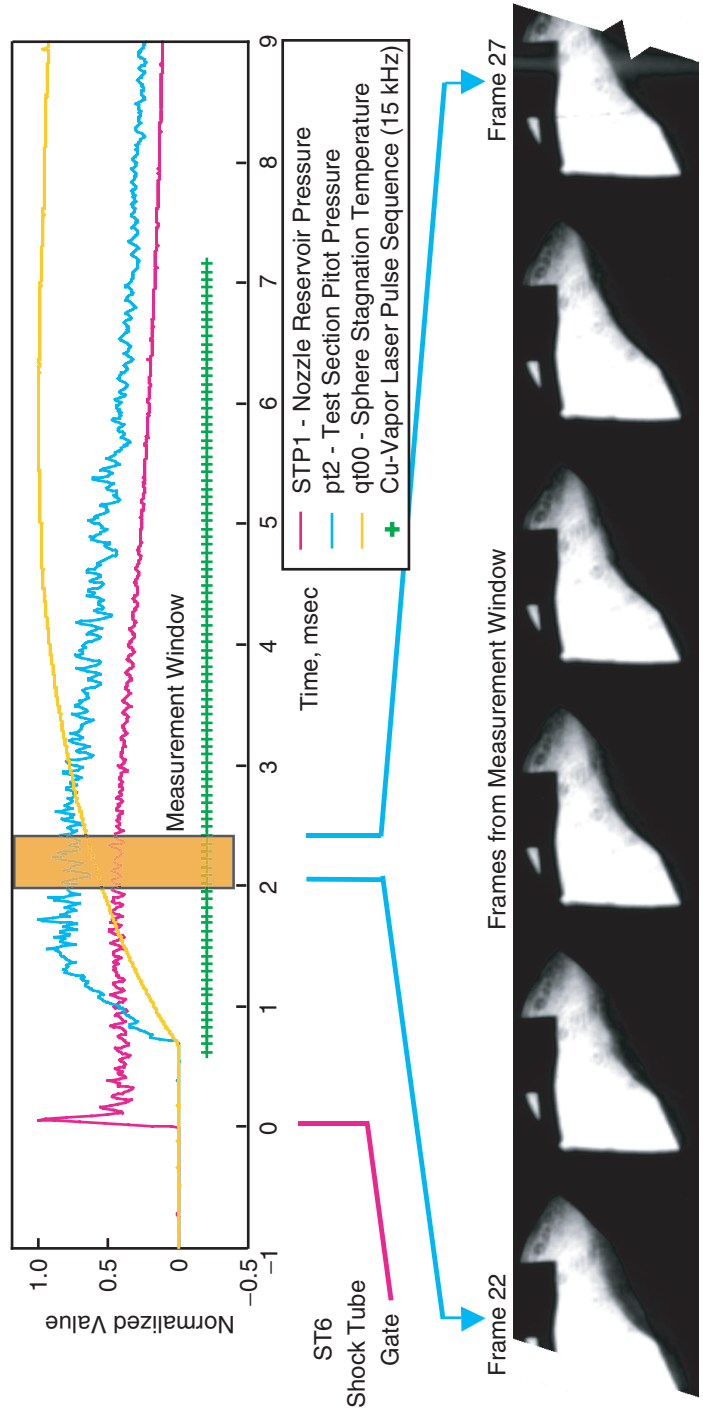


Figure 92. HSFV for Flow Steadiness, HEG Run 457—November 5, 1998

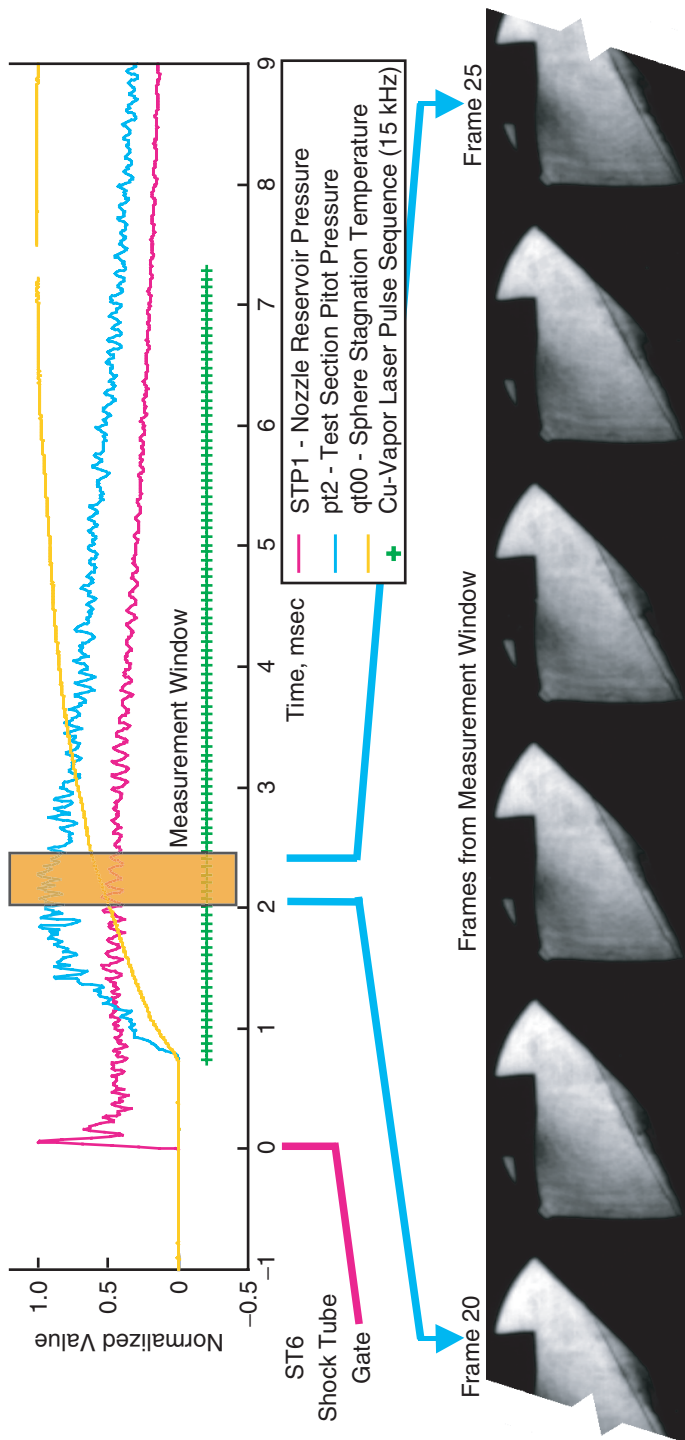


Figure 93. HSFV for Flow Steadiness, HEG Run 458—November 1998

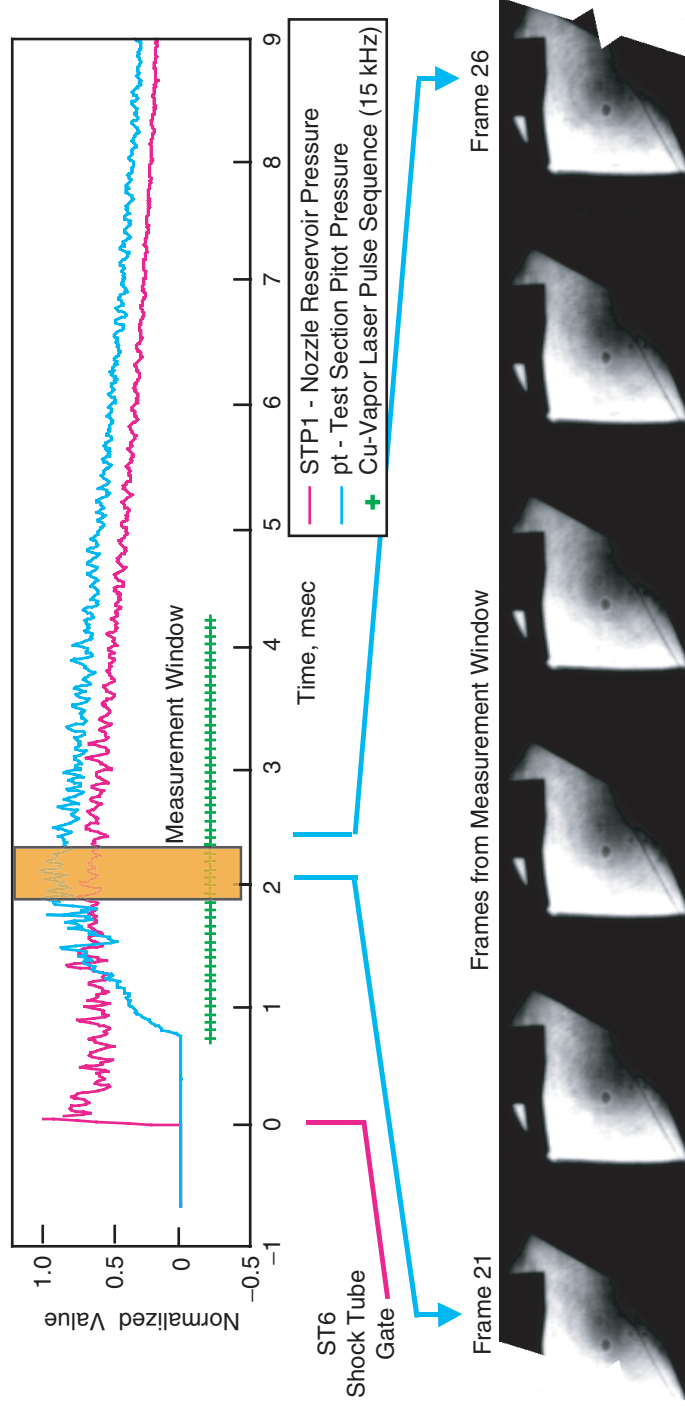
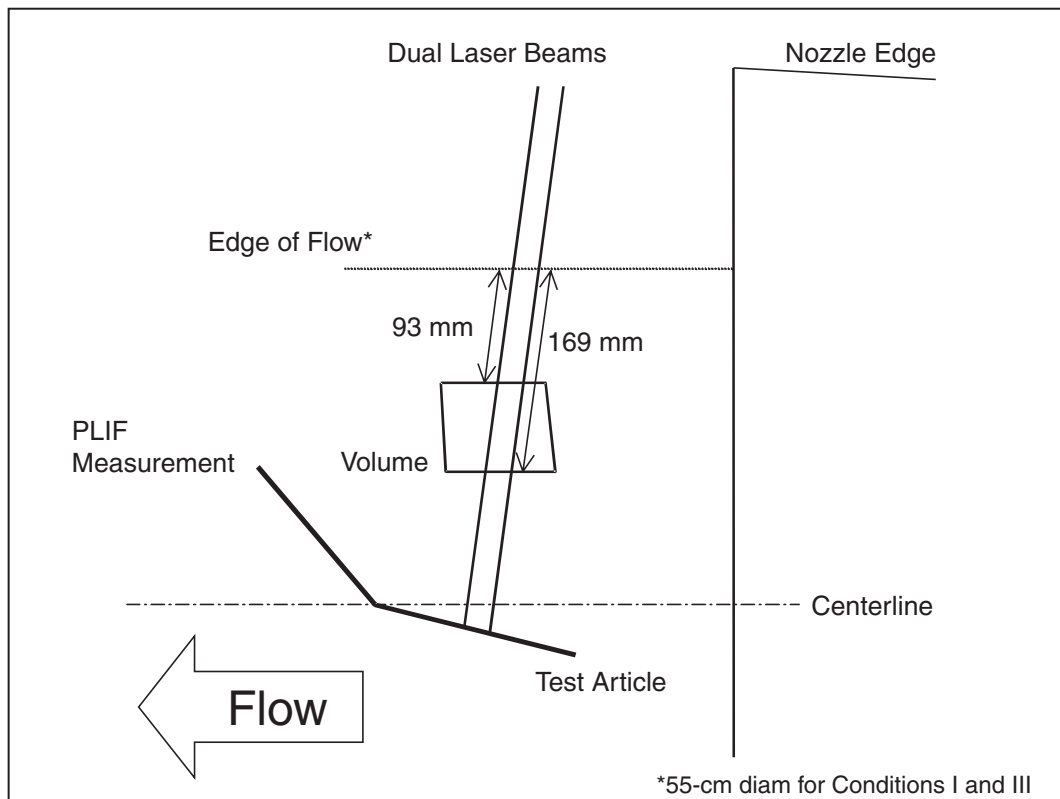


Figure 94. HSFV for Flow Steadiness, HEG Run 460—November 1998



Note: Estimated distance from top, bottom of PLIF imaging region to tunnel window in calibration measurements: 425 mm, 501 mm

Figure 95. Experimental Setup for HEG PLIF Measurements

NO Excitation Wavelengths

$\lambda 1$: 225.716 nm, R11 + Q21(13.5) -- same as "line 1" in Ref. 32
 $\lambda 2$: 225.134 nm, P21 + Q11(28.5) -- same as "line 2" in Ref. 32
 $\lambda 3$: 225.473 nm, R11 + Q21(17.5) -- not "line 3" in Ref. 32

HEG Freestream Conditions (Supplied by HEG)

Condition I: 1.07 mol/kg NO (1.49×10^{15} cc⁻¹ NO), 807K
Condition III: 2.28 mol/kg NO (5.20×10^{15} cc⁻¹ (NO), 612K
Condition IV: 1321 Pa (vs 517 Pa for Cond I, 642 Pa for Cond III)

Summary of PLIF Measurements

Runs 446, 447, 448, 451, 452 (Condition III): only single λ in image
(no signal on other camera)
Runs 449, 450 (Condition IV): optical blockage of flow
Run 453 (Condition III): data were lost
Calibrations with 5-percent NO in N₂ in tunnel: too much laser absorption
Runs 454, 455 (Condition III): good data with two λ in image
Runs 456, 457 (Condition I): same, except laser mistrigger for 457

Figure 96. Summary of PLIF Conditions

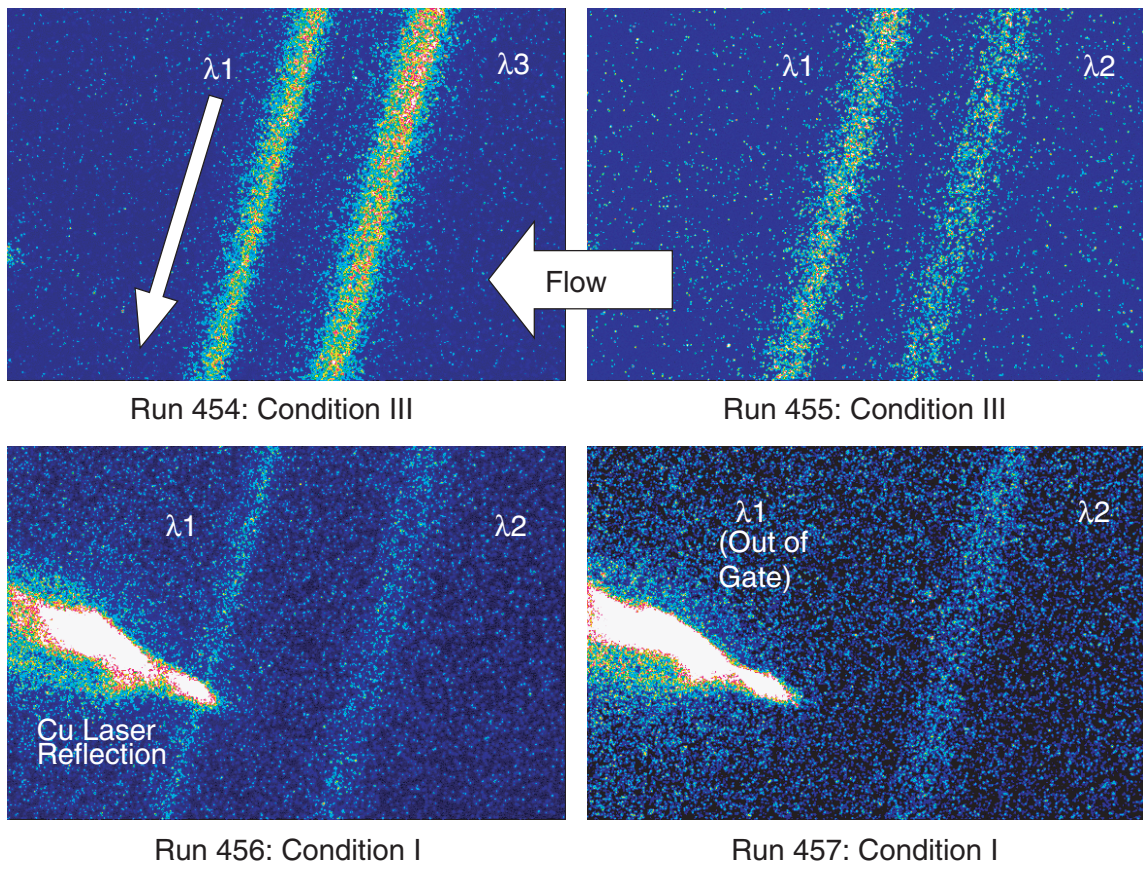
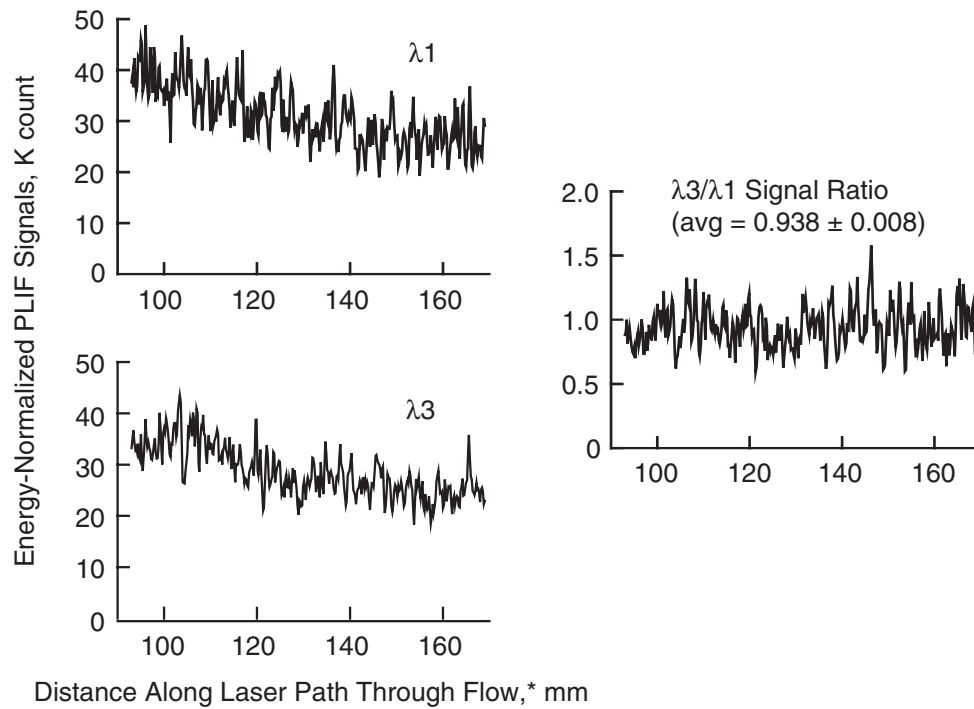
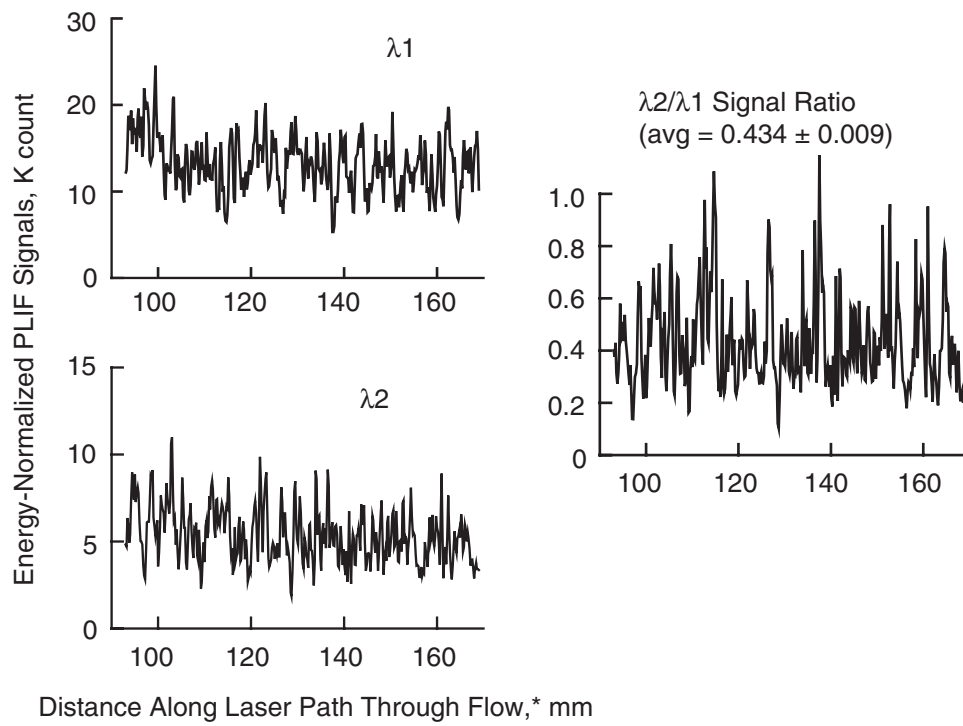


Figure 97. PLIF Images



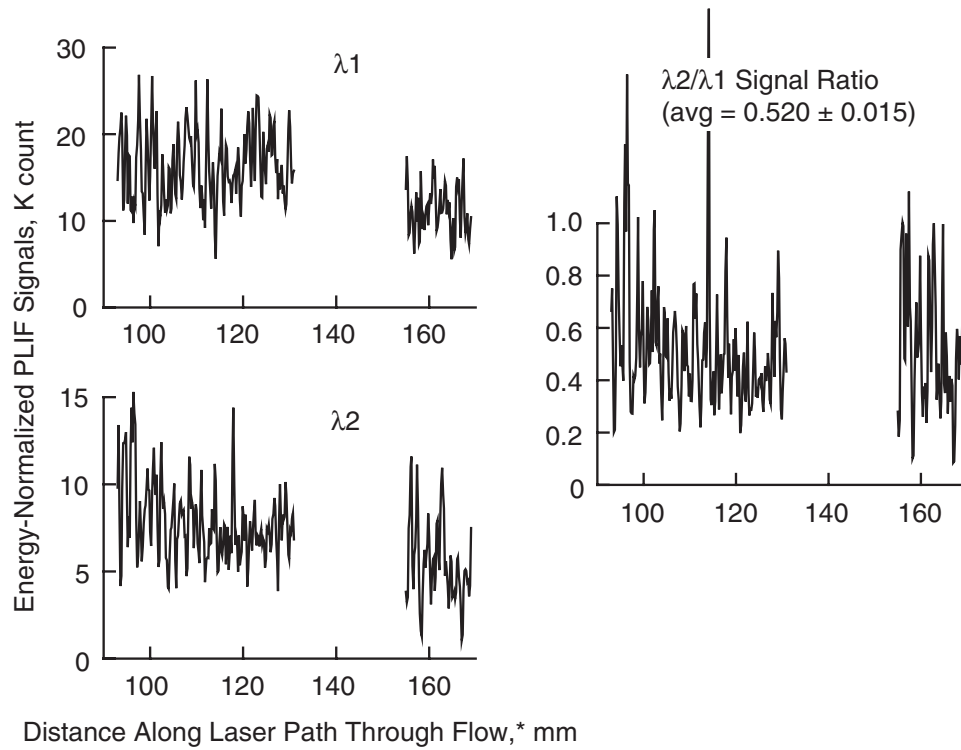
*Assuming 55-cm Square-Hat Core Flow Diameter

Figure 98. Partially Processed Data - Run 454 Condition III



*Assuming 55-cm Square-Hat Core Flow Diameter

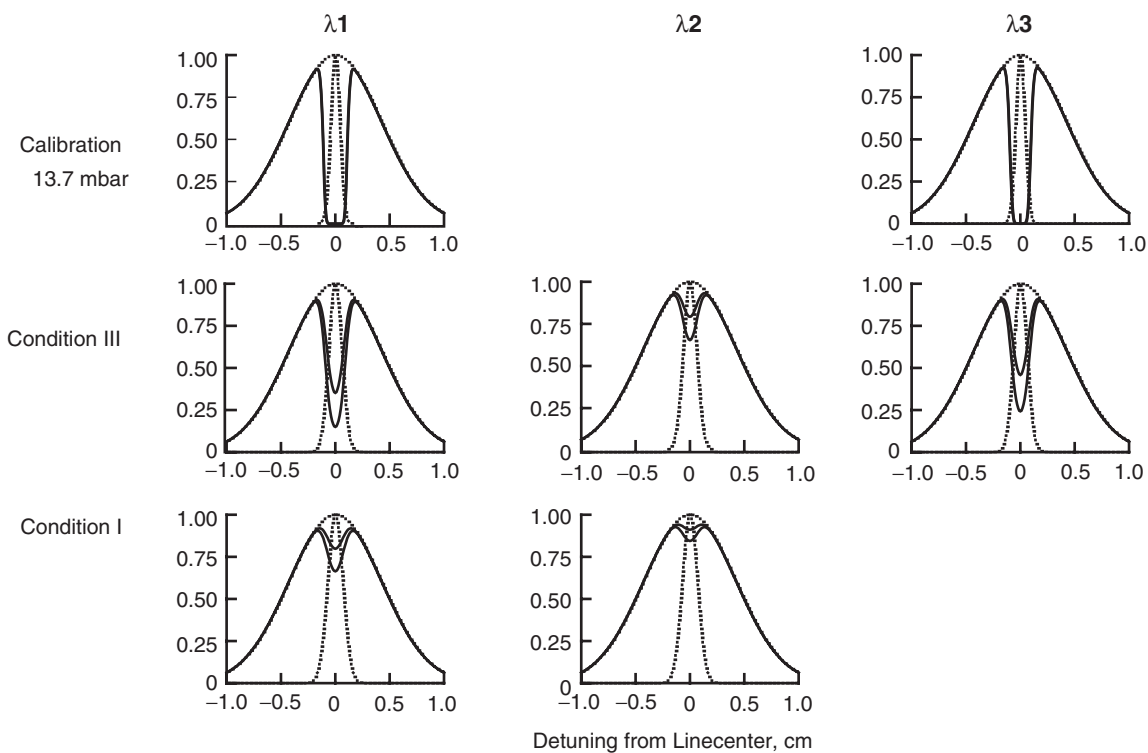
Figure 99. Partially Processed Data - Run 455 Condition III



*Assuming 55-cm Square-Hat Core Flow Diameter

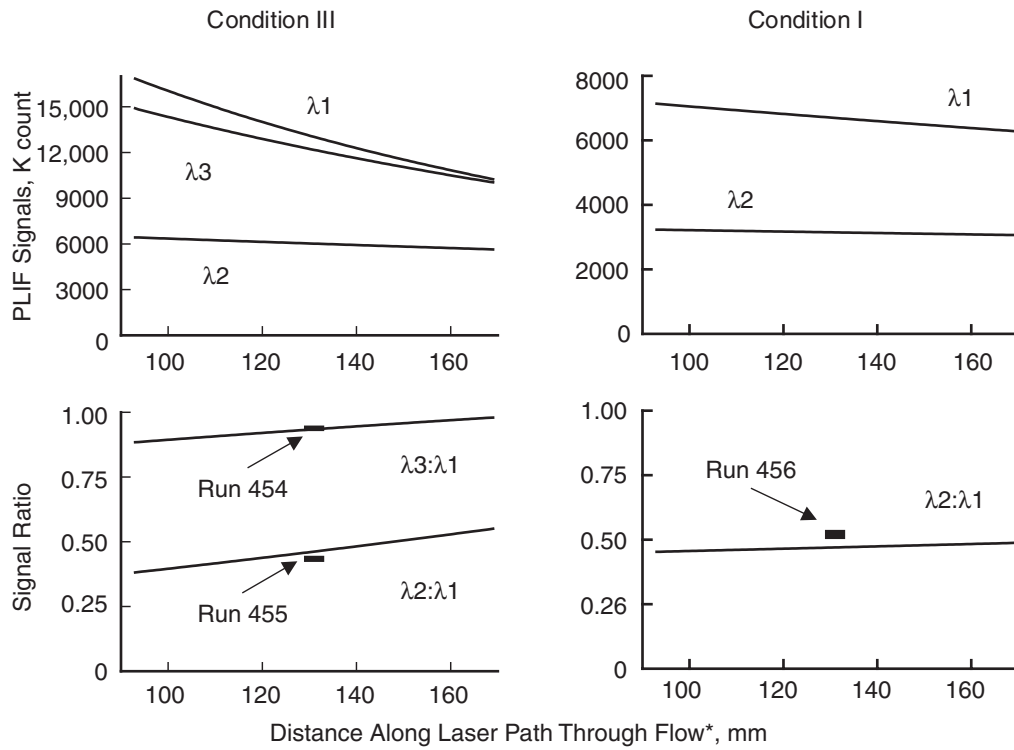
Figure 100. Partially Processed Data - Run 456 Condition III

Calculated Laser Line Shapes at Top and Bottom of PLIF Images*



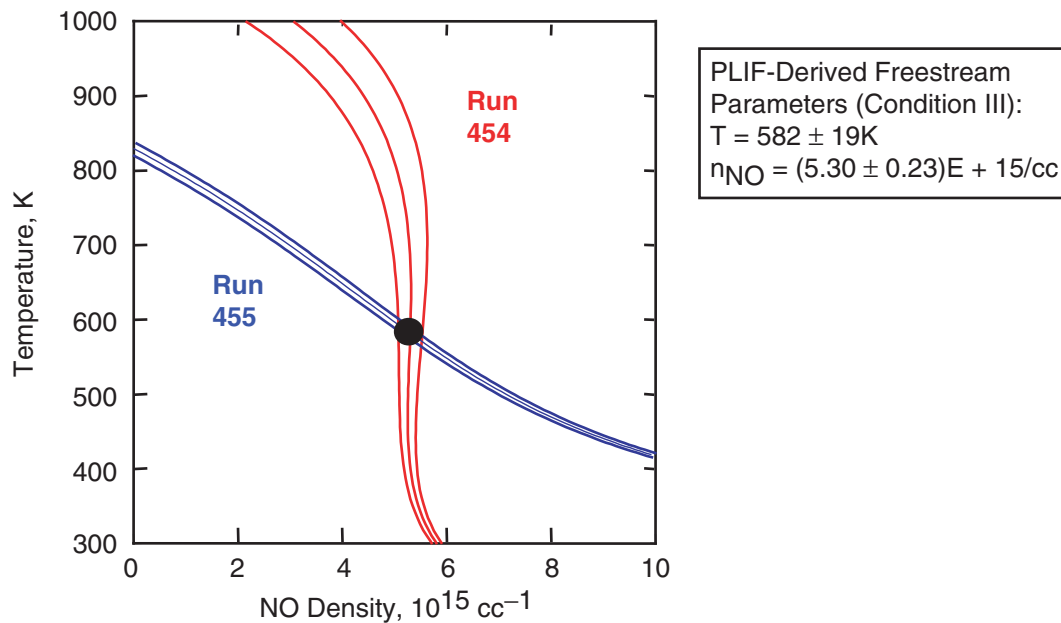
*Unattenuated laser line shapes and absorption line shapes shown as dashed lines

Figure 101. Calculated Line Shapes



*Assuming 55-cm Square-Hat Core Flow Diameter

Figure 102. Calculated Signals and Signal Ratios



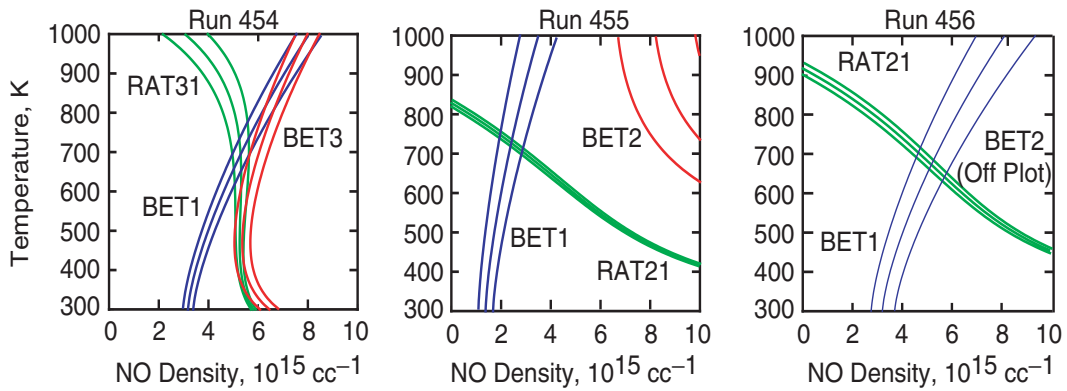
Assumptions:

1. Uniform freestream flow, 55-cm diam
2. Identical run conditions for Runs 454 and 455 (Condition III)
3. Run 454 PLIF ratio is given by $R_{31} = 0.938 \pm 0.008$
4. Run 455 PLIF ratio is given by $R_{21} = 0.434 \pm 0.009$
5. Results are independent of CFD prediction

Figure 103. Explicit Estimate of Freestream NO Temperature and Density

Key Points:

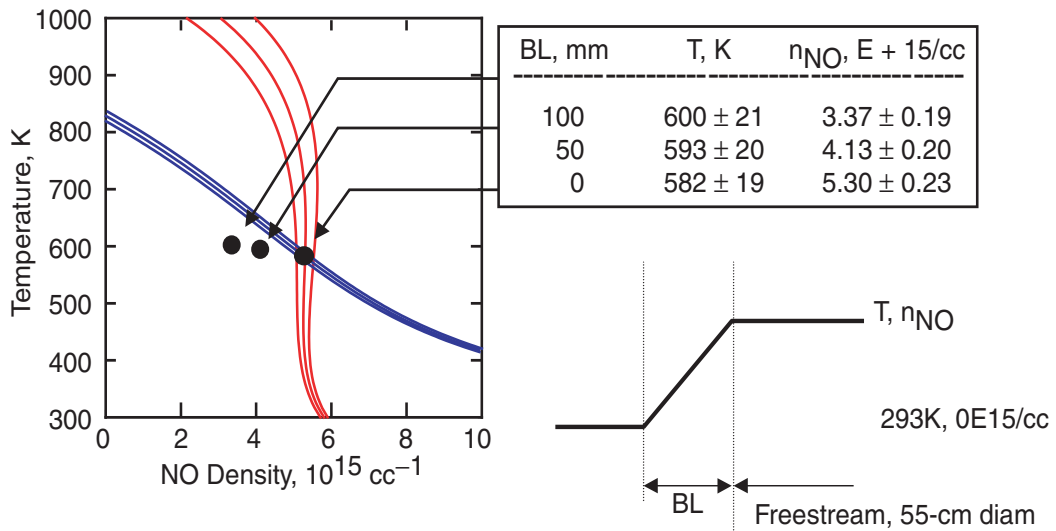
1. Replace three-line technique with two-line technique.
2. Retain use of PLIF signal ratio, e.g., $R_{31} = 0.938 \pm 0.008$ (Run 454).
3. Supplement use of effective absorption coefficient, e.g., $\beta_1 = 6.04 \pm 0.31/m$, $\beta_3 = 5.56 \pm 0.27m$ (Run 454, derived from experimental data).
4. Perform consistency check: Have three constraints (R_{31} , β_1 , β_3) with only two unknowns: T and n_{NO} .



Conclusion:

- Consistent results for Run 454 (common intersection of three sets of curves);
- No consistent results for Runs 455, 456;
- Extended theory warrants further study for future work.

Figure 104. Extension of Reference 30 Theory



Assumptions:

1. Uniform freestream flow, 55-cm diam
2. Linear variation of T and η_{NO} in BL

Conclusions:

- Presence of NO in BL has small effect on inferred NO temperature
- Larger effect on NO density

Figure 105. Effect of NO in Boundary Layer on Inferred Freestream Parameters

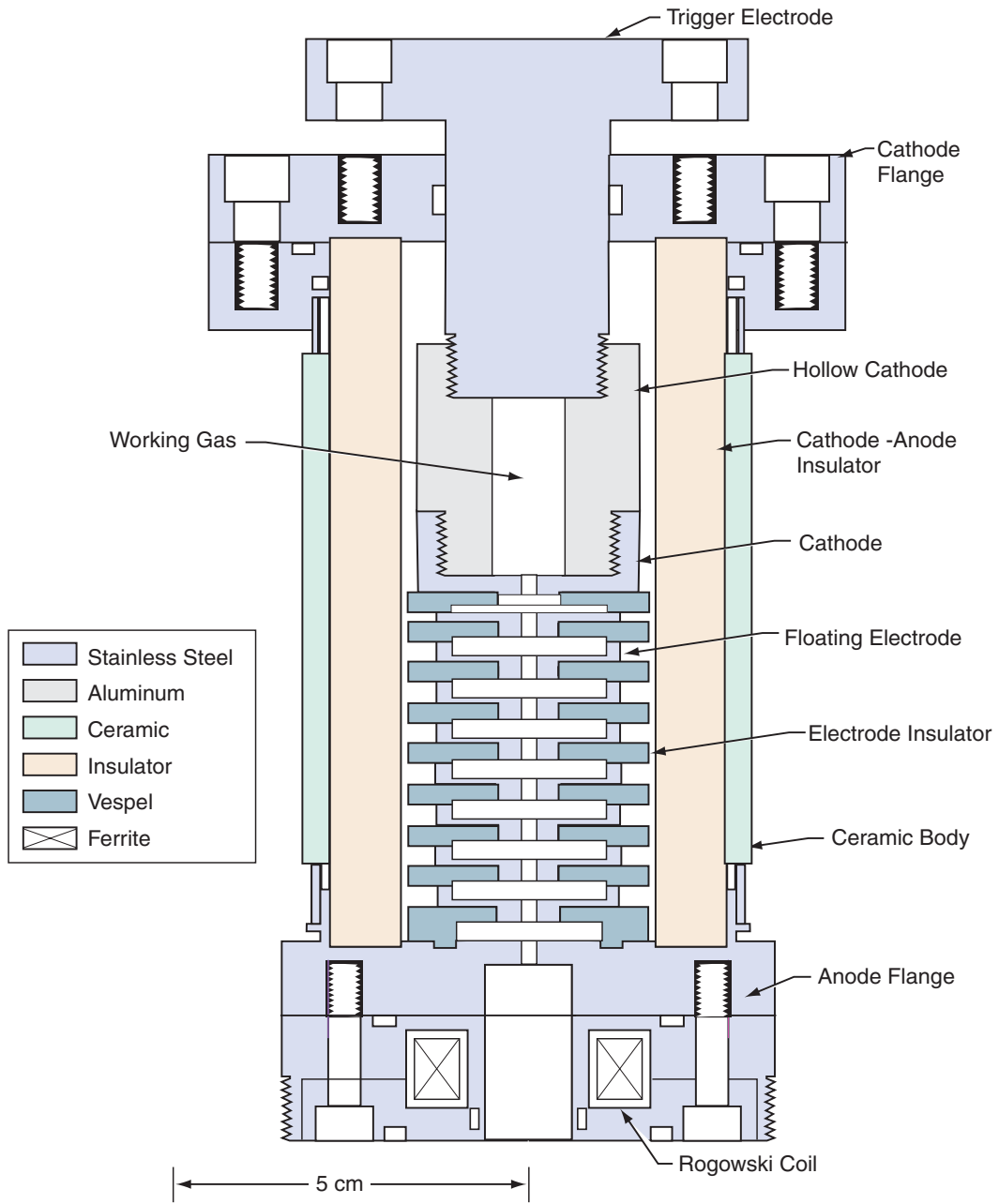


Figure 106. Sectional Drawing of the Pulsed Electron Gun

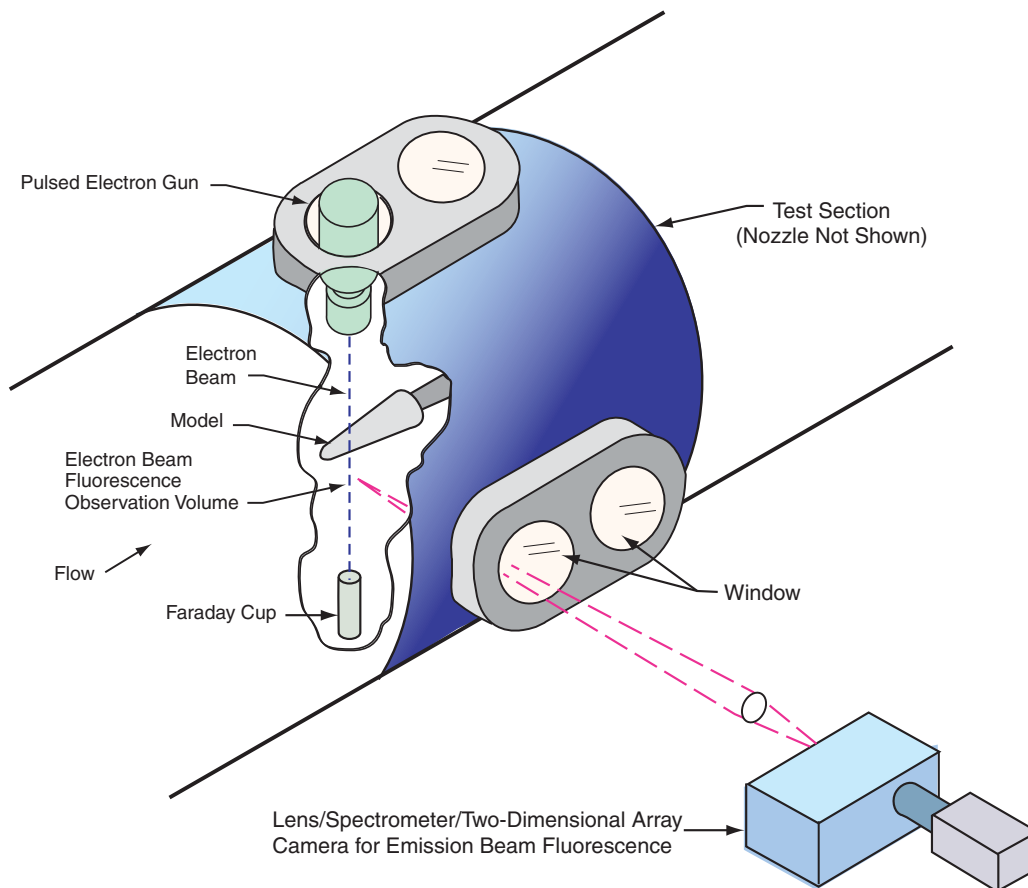


Figure 107. Conceived PEG Application at the FPST

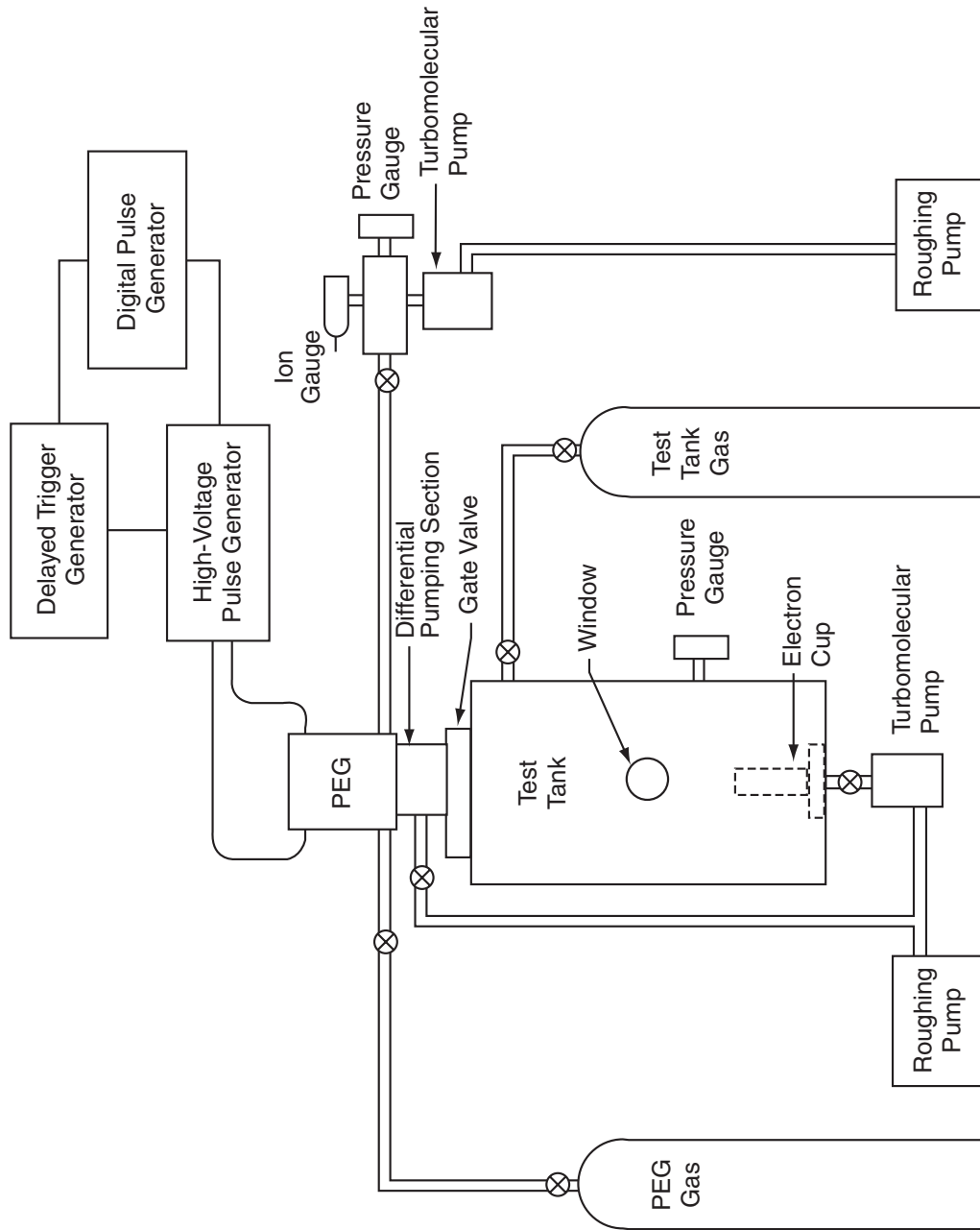


Figure 108. Laboratory PEG System

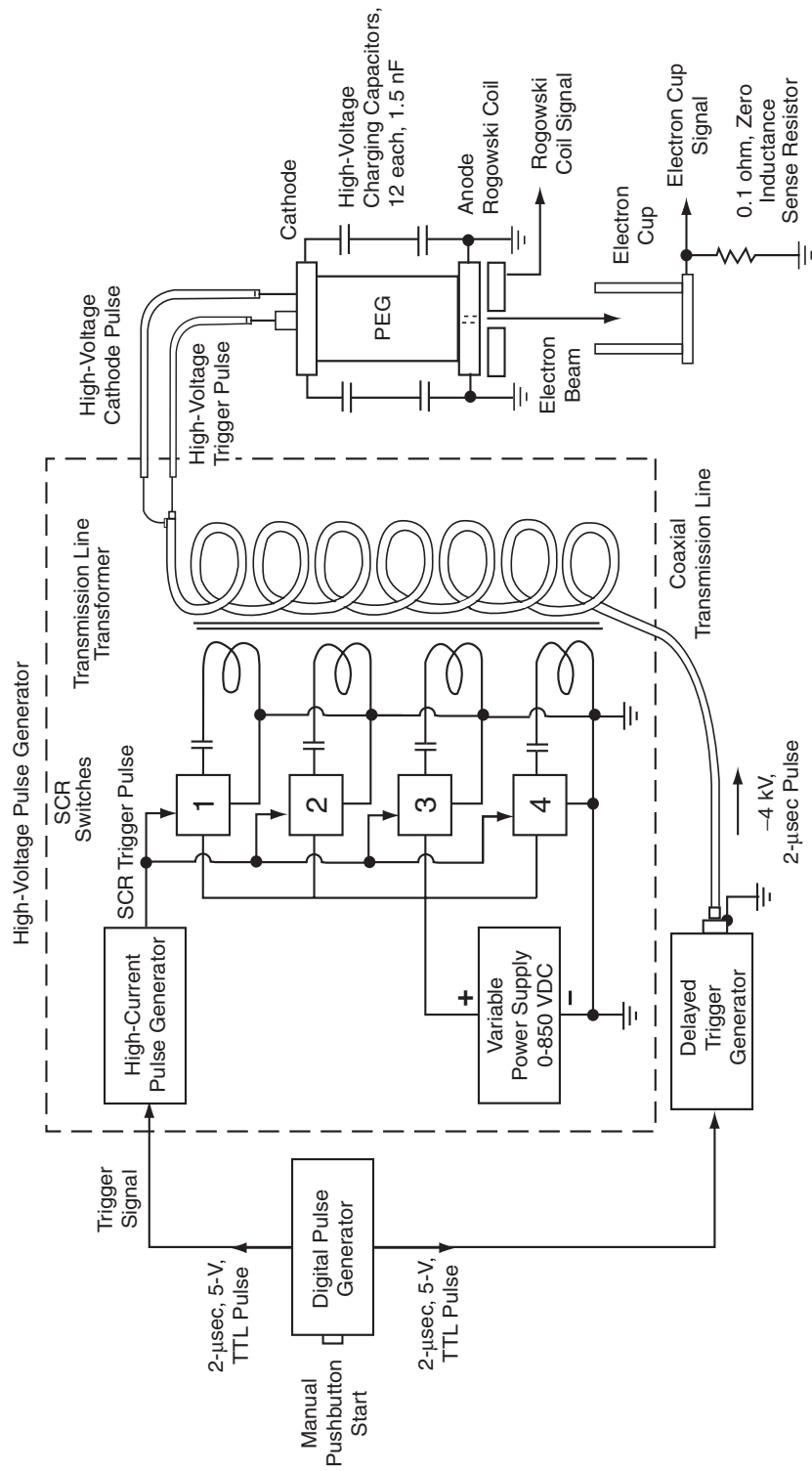


Figure 109. High-Voltage Pulsed Electronics for the PEG

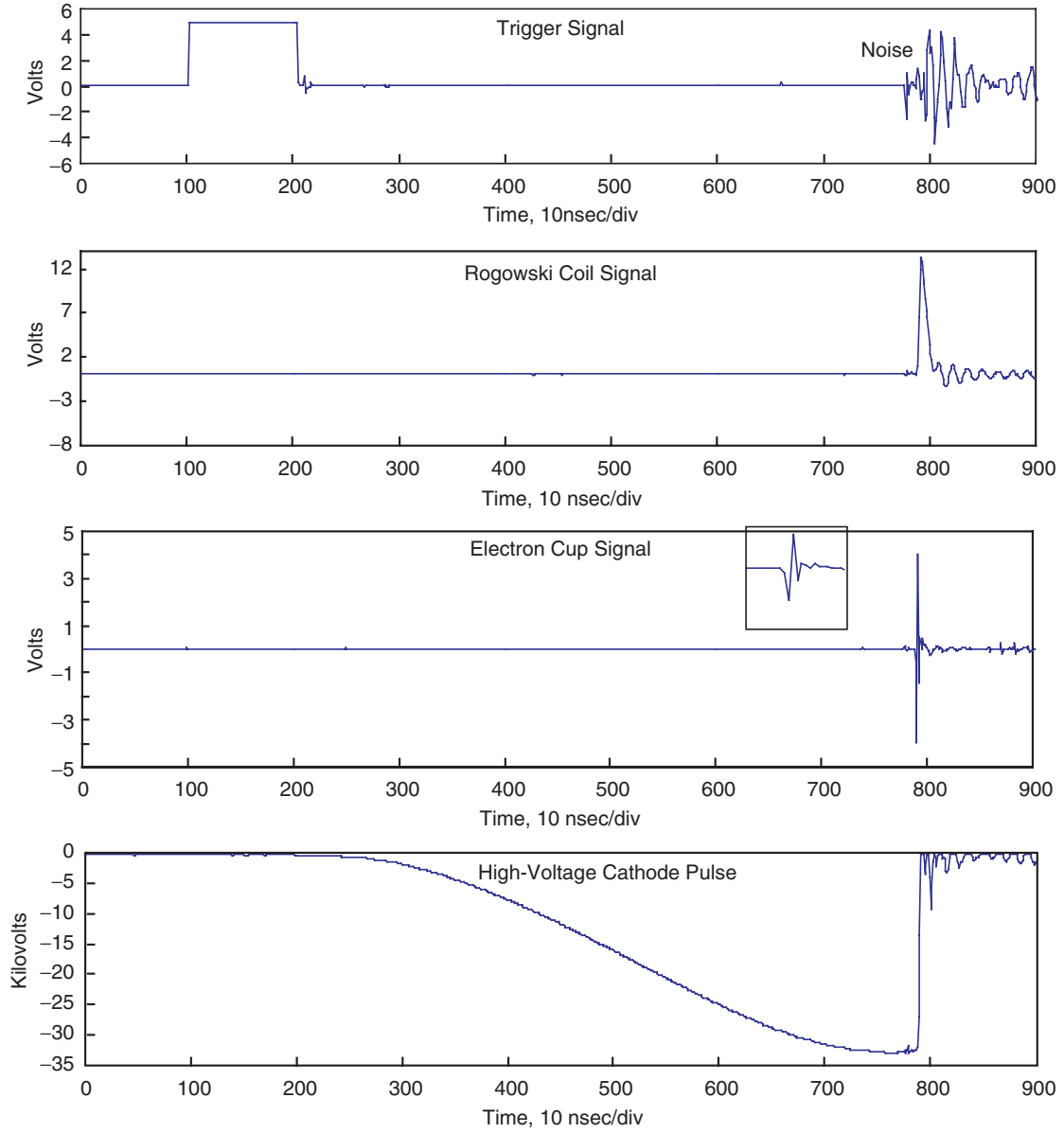


Figure 110. PEG Electronic Control and Instrumentation

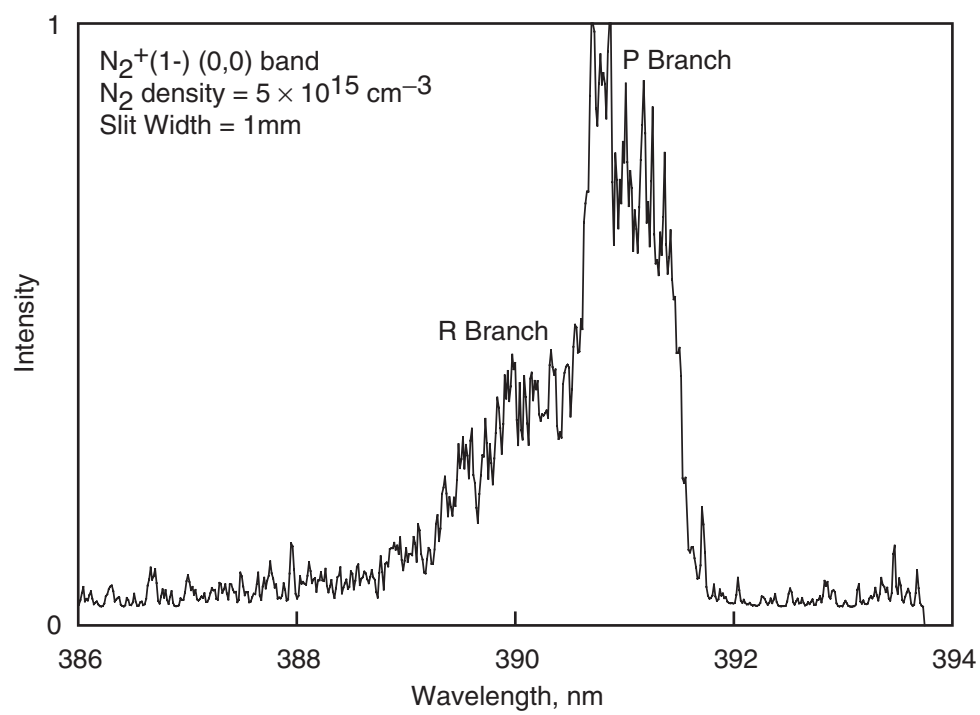


Figure 111. Nitrogen PEBF Spectrum

Table 1. AEDC FPST Conditions

Parameter	P₀, atm	H₀, MJ/kg	Model
Run Number			
26	419	10.3	Rake
27	392	10.8	Rake
28	419	11.2	Rake
29	1023	14.3	Rake
30	661	12.1	70% Electre
31	921	12.8	70% Electre
32	434	10.1	70% Electre
33	379	8.9	70% Electre
34	365	13.6	70% Electre
35	691	11.9	70% Electre
HEG Cond. III	462	12.9	Electre

Table 2. Size Comparison of DLR and AEDC Free-Piston Shock Tubes

Components	DLR HEG	AEDC FPST
Overall length, m	60	50
Diaphragm	8- to 10-mm Stainless Steel	Thickness Function of Pressure
Piston Driver	5 MPa Air Reservoir	Powder Charge
Compression Tube Length, m	33	27.5
Shock-Driven Tube Length, m	17	10.7
Piston, kg	280	
Piston Speed, m/sec	278	240-500
Nozzle	Converging/Diverging - Conical	Converging/Diverging - Conical
Length, m	3.75	1.63
Throat Diameter, cm	2.2	1.91
Exit Diameter, cm	88	45.72
Area Ratio, A/A*	1600	576
Half Angle, deg	6.5	8
Maximum Reservoir Conditions	90 MPa (888.5 atm) 8100K	2000 atm (202.6 MPa) 10,000K

Table 3. HEG Operating Conditions, Conical Nozzle, Air As Test Gas

Condition	I	II	III	IV
p_0 , MPa	35	85	44	90
t_0 , K	9100	9900	7000	8100
h_0 , MJ/kg	22	23	12	15
p_∞ , Pa	660	1800	790	1680
T_∞ , K	1140	1450	800	1060
ρ_∞ , g/m ³	1.7	3.5	3.3	5.3
M_∞	8.2	7.8	7.8	7.9
u_∞ , km/sec	5.9	6.2	602	5.2
Re_m	200,000	420,000	390,000	670,000

Table 4. Test Matrix for Double Ramp Experiments

Data for AEDC Campaign 1999			Ramp		Tunnel			
Run ID	Condition	SP, msec	Angle 1	Angle 2	SR, msec	TI, msec	P₀, MPa	pt2, kPa
448	III	0.2600	15	50	3.982	0.725	51.35	74.91
451	III	0.4000	15	45	4.671	0.819	44.41	80.23
452	III	1.3560	15	40	3.684	0.780	45.13	74.19
453	III	1.5250	15	35	3.511	0.785	44.87	69.92
454	III	1.5780	15	30	3.455	0.764	44.54	66.33
455	III	0.8190	15	25	3.424	0.751	45.16	64.46
456	I	---	15	25	2.541	0.647	38.81	55.34
457	I	0.6230	15	35	2.542	0.704	38.62	54.28
458	III	0.3893	20	35	3.415	0.765	45.91	72.00
460	III	0.7220	20	40	3.463	0.773	43.29	67.54
		Mean						
		Condition III				0.770	45.58	71.20
		Condition I				0.676	38.72	54.81

Table 5. HEG Freestream Conditions During AEDC Tests

HEG Condition I						
Variable	Units	(1)	(2)	(3)	(4)	(5)
H ₀	MJ/kg	21.06				
P ₀	Bar	386				
T ₀	K	9150				
P _{exit}	kPa		0.43		0.443	
Rho _{exit}	Kg/m ³	0.00219	0.00164	0.001717	0.001326	
T _{tr_exit}	K	797	790	1144	1011	1176
T _{v_exit}	K					3400
T _{v_N₂}	K	3818				
T _{v_O₂}	K	2146				
M _{exit}			9.7	8.17	8.57	
U _{exit}	M/sec		5919	5938	5937	
N ₂	Mass fract	0.743	0.749	0.745	0.752	0.7364
O ₂		0.0513	0.036	0.0469	0.0378	0.133
NO		0.036	0.0334	0.0293	0.0294	0.055
N		5e-07	8.7e-07	4.6e-9	8e-8	2.7e-5
O		0.165	0.181	0.178	0.18	0.075
NO ⁺			3.289e-07		6.55e-7	
HEG Condition III						
Variable	Units	(1)	(2)	(3)	(4)	(5)
H ₀	MJ/kg		13.19			
P ₀	bar		449.7			
T ₀	K		7279			
P _{exit}	kPa		0.47		0.517	
Rho _{exit}	Kg/m ³		0.00283	0.0033	0.002345	
T _{tr_exit}	K		553	806	744	
T _{v_exit}	K					
T _{v_N₂}	K					
T _{v_O₂}	K					
M _{exit}			9.98	8.14	8.04	
U _{exit}	M/sec		4813	4659	4778	
N ₂	Mass fract		0.732	0.731	0.738	
O ₂			0.1444	0.171	0.147	
NO			0.069	0.059	0.058	
N			3e-7	1.3e-10	2.1e-10	
O			0.054	0.038	0.0573	
NO ⁺			7.3e-8		1.3e-7	

(1) DLR calculation with NSHYP, 2-T (for Electre model)

(2) Standard HEG conditions, AIAA-98-2770, from calculations + experiment

(3) DLR calculation with thermal equilibrium (1-T); represents current DLR thinking

(4) AEDC calculation with TUFF (1-T)

(5) AEDC calculation with GASP (2-T)

Table 6. AEDC FPST Freestream Conditions

AEDC FPST Runs 16 and 30				
Variable	Units	TUFF	NEDANA	GASP
H ₀	MJ/kg			
P ₀	bar			
T ₀	K			
P _{exit}	atm	0.0245	0.01966	
Rho _{exit}	Kg/m ³	0.008	0.00836	
T _{tr-exit}	K	957	800	708
T _{v-exit}	K		2250	2858
T _{v-N₂}	K			
T _{v-O₂}	K			
M _{exit}		7.56		
U _{exit}	M/sec	4530	4504	
N ₂	Mass fract	0.735	0.744	
O ₂		0.163	0.173	
NO		0.0647	0.054	
N		1.08e-10	2.77e-8	
O		0.0373	0.0289	
NO ⁺		1.11e-7		

**Table 7. Stagnation Point Heating (W/cm²)
Fire II Configuration (1634 sec into flight)**

	GIANTS /NOVAR	LAURA /LORAN	GASP	Experiment
Convective	105	110	137	
Radiative	25	55	NEQAIR (uncoupled)	
Total	130	165	156	175

Table 8. PLIF-NO Measurements of T_{tr}

AEDC Run No.	T_{tr}, K Isentropic Est.	T_{tr}, K (T_v = T_{tr})	T_{tr}, K (T_v = 3000K)	T_{tr}, K (GASP, T_v = 2900K)
21	1382	350	750	661
23	1356	400	575	608
24	1923	340	700	641

Table 9. AEDC Nonintrusive Diagnostics in the Impulse Facility

NID Method	Molecule/Band	Excitation	Detection	Measurements
Filtered Rayleigh Scattering (FILRAY)	All	Cu-vapor laser; $\lambda_L = 510.6$ nm, 578.2 nm; 50 kHz max. pulse rate	Photomultiplier tube (PMT) with temperature-controlled iodine cell filter	He arrival
Planar Mie Scattering (PMIE)	All, but particle scattering dominates	Same as for FRS, but with special beam-shaping optics and single-shot operation.	Intensified detector array (ICCD) with temperature-controlled iodine cell filter	Particulate distribution visualization
Laser Beam Transmission (LBT)	Nonabsorptive laser wavelength; particle scattering dominates transmission loss	He-Ne or laser diode; $\lambda_L = 639$ nm or 690 nm	Quadrant detector	Particle concentration $\{n(p)\}$
Emission Spectra (ES)	Radiation from contaminants in flow	Flow processes at tips of test article.	Small spectrometer with an ICCD	Contamination species identification
High-Speed Flow Visualization (HSFV)	All	Same as for FILRAY	Cordin high-speed camera or spinning holographic storage disk	Shadowgraph, schlieren, holography
Planar Laser-Induced Fluorescence (PLIF)	NO/Gamma	Nd:YAG/2v/WEX(2), $\lambda_L \cong 226$ nm	ICCD(2) with filters	Nitric oxide number density $\{n(NO)\}$, rotational temperature (T_r)
Pulsed Electron Beam Fluorescence (PEBF)	N ₂ : (0-1) & (1-2) of 1 st Negative System He: NO: Gamma O ₂ :	40 kV, 200-A electron beam	Small spectrometer with an ICCD	$n(N_2, NO, He, O_2)$, T_r , T_v
Laser Diode Absorption (LDA)	Rb seeding in form of RbNO ₂	Scanning laser diode; 15-kHz scan rate; $\lambda_L \cong 780.2$ nm	Photodiode	He arrival, v

Table 10. AEDC Nonintrusive Diagnostics in the HEG

NID Method	Molecule/Band	Excitation	Detection	Measurements
Planar Mie Scattering (PMIE)	All, but particle scattering dominates	Cu-vapor laser; $\lambda_L = 510.6 \text{ nm}$, 578.2 nm; special beam-shaping optics single-shot operation	Intensified detector array (ICCD) with temperature-controlled iodine cell filter	Particulate distribution visualization
High-Speed Flow Visualization (HSFV)	All	Cu-vapor laser; $\lambda_L = 510.6 \text{ nm}$, 578.2 nm; 30-kHz pulse rate	Cordin high-speed camera	Shadowgraph, schlieren
Planar Laser-Induced Fluorescence (PLIF)	NO/Gamma	Nd:YAG/2v/WEX(2), $\lambda_L \approx 226 \text{ nm}$	ICCD(2) with filters	Nitric oxide number density $\{n(\text{NO})\}$, rotational temperature (T_r)
Laser Beam Transmission (LBT)	Nonabsorptive laser wavelength; particle scattering dominates transmission loss	He-Ne or laser diode; $\lambda_L = 639 \text{ nm}$ or 690 nm	Quadrant detector	Particle concentration $\{n(p)\}$

Table 11. Information Potentially Provided by NID About the Impulse Facility Flow Fields

- Run time defined (three independent methods)
- $n(\text{NO})$, T_r spatial map
- Shock position, curvature
- Identification of contaminant material
- Spatial distribution of contaminant particulates
- Correlation of $n(p)$ with reservoir parameters
- Temporal evolution of flow over test article
- v temporal evolution path integrated
- $n(\text{N}_2)$, $n(\text{O}_2)$, $n(\text{NO})$, $n(\text{He})$, $n(\text{O})$, T_v at a single spatial point on centerline
- $T_v \neq T_r$ evaluated

Table 12. Impluse Facility Nonintrusive Diagnostics Data Log

RUN	TUNNEL CONDITIONS	LBT	ES	HSV	WP	FILRAY	PMIE	LDA	HSFV	PLIF	NID REMARKS
*	P_0 (atm, MPa); T_0 (K); H_0 (MJ/kg)										
**	p_∞ (torr, Pa); t_{co} (K); t_v (K); n_∞ (cm^{-3})										
26	419, 42.5; 6245; 10.33 13.8, 1834; 594; 2729; 2.24e+17 Calibration Rake	Yes U	780 nm 1.6 msec U	Yes U	Two U	Yes U	Yes U	No	No	No	Order II Fe, Al lines interfering at Rb wavelength
27	392, 39.7; 6428; 10.83 12.7, 1702; 543; 2753; 2.26e+17 Calibration Rake	Yes U	780 nm U	Yes U	Two U	Yes U	Yes U	No	No	No	
28	419, 42.5; 6611; 11.25 11.2, 1500; 562; 2780; 1.93e+17 Calibration Rake	Yes U	780 nm 3.6 msec U	Yes U	One U	Yes U	Yes U	No	No	No	1mg Rb seed; strong Rb emission
29	1023,104; 793; 14.3 36.3, 4833; 914; 3022; 3.84e+17 Calibration Rake	Yes U	780 nm 2.6 msec U	Yes U	One U	Yes N	Yes No	No	No	No	LBT near zero; heavy ablation products; LBT, HSFV only good optical meas. 2 mg Rb seed
30	661, 66.9; 7061; 12.14 22.3, 2979; 708; 2858; 3.04e+17 70% scale cone model	Yes U	780 nm 2.6 msec U	Yes U	One U	Yes N	No	Yes U	Yes U	Yes U?	FILRAY not synchronized correctly 0.071 mg Rb seed; weak Rb emission PLIF strong only within shock; HSFV not at nose of test article
31	921, 93.3; 7394; 12.79 32.5, 4326; 846; 2924; 3.71e+17 70% scale cone model	Yes U	780 nm 2.6 msec U	Yes U	One U	Yes U	No	Yes U	Yes U	Yes U	Weak or no Rb emission; 0.426-mg Rb seed
32	434, 43.9; 6178; 10.15 14.1, 1884; 549; 2718; 2.48e+17 70% scale cone model	Yes U	780 nm 2.6 msec U	Yes U	One U	Yes N	No	Yes U	Yes U	Yes U	Rb emission 2-mg Rb seed
33	70% scale cone model	Yes	780 nm	Yes	One	Yes	No	Yes	Yes	Yes	Strong Rb emission
34	70% scale cone model	Yes	780 nm	Yes	One	Yes	No	Yes	Yes	Yes	Strong Rb emission
35	70% scale cone model	Yes	780 nm	Yes	One	Yes	No	Yes	Yes	Yes	Strong Rb emission

* Isentropic ** GASP U - Useful Data N - Not Useful Data

Table 13. LBT Measurements at the Impulse Facility

Run No.	P ₀ , atm; H ₀ , Btu/lb _m	Peak Transmission, %	Delta Time (Peak LBT-ST6), msec	Average Transmission % During the Estimated Good Run Time	Delta Time (Nozzle Length/Avg. Nozzle Flow Speed), msec
23*	483; 5185			91	
25*	1701; 7445			1	
26	419; 4434	87.5	0.4	98.5	0.56
27	392; 4650	82	0.45	95	0.55
28	419; 4829	70	0.43	98	0.54
29	1023; 6142		0.42	1.5	0.48
30	661; 5212	70	0.55	94	0.52
31	921; 5491	67	0.60	91	0.51
32	434; 4355	85	0.55	97	0.57
33	379; 3840	85	0.42	98	0.60
34	365; 5838	87	0.45	98	0.49
35	691; 5128	77	0.60	93	0.52

* Data from runs prior to ICR&W project.

Table 14. Tabulation of Facility Run Time Information

Run No.	P ₀ , atm; H ₀ , Btu/lb _m	LDA Earliest Detection, msec	LDA Peak Absorption Time, msec	FILRAY Rollover Time, msec	HSFV Detection of Effect on Bow Shock, msec
30	661; 5212	1.0	2.5		
31	921; 5491	1.0	2.1		
32	434; 4355	1.8	2.5	2.8	
33	379; 3840	1.8	2.8	2.4	
34	365; 5838	1.9	3.0	2.0	
35	691; 5128	1.0	2.0	2.6	3.0

Table 15. HEG Nonintrusive Diagnostics Data Log

HEG Shot	Condition	Model Angles	PLIF Beams	Camera 1, nm	Camera 1 Result	Camera 2, nm	Camera 2 Result	HSFV	LBT	REMARKS
446	III	dbl wedge 0 - 0	Yes, N Sheet	225.716	Image	225.134	No image	Yes, U		No "pulse-in-gate" measurement.
447	III	dbl wedge 15 - 50	Yes, N Sheet	225.716	Image	225.134	No image	No		Pulses in gates. Failed tunnel sensor led to low-energy laser pulses and no HSFV trigger.
448	III	dbl wedge 15 - 50	Yes, N Sheet	225.716	Image	225.134	No image	Yes		Pulses in gates.
449	IV	dbl wedge 15 - 50	Yes, N Sheet	225.716	No image	225.473	No image	No		Narrower sheets. Failed tunnel sensor led to mistrigger. Heavy window deposits.
450	IV	dbl wedge 15 - 50	Yes, N Sheet	225.716	No image	225.473	No image	No		Heavy window deposits - flow optically thick; thought to be impenetrable.
451	III	dbl wedge 15 - 45	Yes, N Sheet	225.716	Image	225.473	No image	Yes, U		Pulses in gates.
452	III	dbl wedge 15 - 40	Yes, N Pencil	225.473	Image	225.716	No image	Yes		Pulses in gates. Failed Camera 1 temperature controller led to high back-ground.
453	III	dbl wedge 15 - 35	Yes, N Pencil	225.716 and 225.473	Images	225.716 and 225.473	No images	Yes, U	Yes, U	Pulses in gates. Camera 2 not cooled.
454	III	dbl wedge 15 - 30	Yes, U Pencil	225.716 and 225.473	Images	225.716 and 225.473	Images	Yes, U	No	Pulses in gates. LBT not set up correctly.
455	III	dbl wedge 15 - 25	Yes, U Pencil	225.716 and 225.134	Images	225.716 and 225.134	Images	Yes, U	Yes, U	Pulses in gates.
456	I	dbl wedge 15 - 25	Yes, U Pencil	225.716 and 225.134	Images	Cu yellow 578	Saturation	Yes, U	Yes, (poor)	Pulses in gates. Particle imaging picture saturated.
457	I	dbl wedge 15 - 35	Yes, N Pencil	225.716 and 225.134	Image	Cu yellow 578	No image	Yes, U	No	Image of 225.134 nm beam only; 225.726 nm beam out of gate. LPT gain setting too high. No Mie scattering beam image seen.

APPENDIX 1
PROJECT AGREEMENT

DEPARTMENT OF THE AIR FORCE
WASHINGTON DC 20330-1000

fr2
MAY
1997

OFFICE OF THE UNDER SECRETARY

MEMORANDUM FOR DISTRIBUTION

FROM: SAF/IAQ

1745 Jefferson Davis Highway
Crystal Square 4, Suite 302
Arlington, VA 22202-3402

SUBJ: Memorandum of Transmittal for the Free Piston Shock Tunnel/High Enthalpy Göttingen (FPST) Project Arrangement (PA) to the Research and Technology Projects (RTP) Memorandum of Understanding between the United States and Germany

The attached international agreement and certification are transmitted in accordance with DoD Directive 5530.3 and AFI 51-701.

- a. Type of Agreement: Bilateral.
- b. Countries Involved: Germany and the United States.
- c. Responsible Organizations: German Federal Ministry of Defense and the United States Air Force.
- d. Full Title of Agreement: Project Agreement No. RTP-US-GE-A-F-96-0007 Between The Secretary of Defense on Behalf of the Department of Defense of the United States of America and the Federal Minister of Defense of the Federal Republic of Germany for the Free Piston Shock Tunnel/High Enthalpy Göttingen Project.
- e. Subject Matter: Under the FPST program, the USAF will combine efforts with the German MOD to accelerate and improve the development cycle of their respective state-of-the-art computational fluid dynamics (CFD) facilities. Two of the higher performance facilities of this type are the High Enthalpy Göttingen (HEG) Facility, operated by the Institute for Experimental Fluid Mechanics at the German Aerospace Establishment (DLR), Göttingen, Germany, and under contract with the German MOD, and the FPST Facility at Arnold Engineering Development Center (AEDC), Arnold Air Force Base, Tennessee. The HEG is the largest such facility in the world and the FPST facility will operate at the world's highest pressures and densities. Cooperation under this PA will allow expedited initial

operations with increased capability and data accuracy. These objectives will be accomplished by carrying out tests at both the FPST and HEG. The two facilities complement each other by exploiting their differences; very high velocity and pressure capabilities at the FPST and the large size and mass flow rate capability at the HEG. The PA was signed in Berlin, GE.

f. Legal Authority: Title 10, U.S.C. Section 2350a, Cooperative Research and Development Projects Allied Countries.

g. Date of Entry into Force: 28 April 1997.

h. Date of Termination: 28 April 2002.

i. All Signing Officials, Title/Offices Represented, and Countries:

(1) Herr Rolf Schreiber, Chief of the Air Armaments Division, Directorate General of Armament.

(2) Major General Clinton V. Horn, Principal Assistant Deputy Under Secretary of the Air Force (International Affairs).

j. Full Title and Date of Basic Agreement: Memorandum of Understanding between the Secretary of Defense on behalf of the Department of Defense of the United States of America and the Federal Minister of Defense of the Federal Republic of Germany for Research and Technology Projects, 17 March 1995.

k. Dates of Signature: 28 April 1997.

l. Conditions for Entry into Force: N/A.

m. Organizational Element Responsible for Maintaining Negotiating History: Armaments Cooperation Division (SAF/IAQ), Office of the Deputy Under Secretary of the Air Force (International Affairs), United States Air Force.

DAVID W. ABATI, Col, USAF Chief,
Armaments Cooperation Division Deputy
Under Secretary of the Air Force
(International Affairs)

PROJECT AGREEMENT NO. RTP-US-GE-AF-96-0007
BETWEEN
THE SECRETARY OF DEFENSE
ON BEHALF OF THE DEPARTMENT OF DEFENSE
OF THE
UNITED STATES OF AMERICA
AND THE
FEDERAL MINISTER OF DEFENSE
OF THE
FEDERAL REPUBLIC OF GERMANY
FOR
THE FREE PISTON SHOCK TUNNEL/HIGH ENTHALPY
GÖTTINGEN
PROJECT

28 APRIL 1997

TABLE OF CONTENTS

<u>Sections</u>		<u>Page</u>
Section 1	INTRODUCTION	183
Section 2	DEFINITION OF TERMS AND ABBREVIATIONS	183
Section 3	OBJECTIVES	184
Section 4	SCOPE OF WORK	184
Section 5	SHARING AND BREAKDOWN OF WORK	185
Section 6	SCHEDULE OF WORK	185
Section 7	MANAGEMENT	186
Section 8	FINANCIAL AGREEMENTS	186
Section 9	CLASSIFICATION	187
Section 10	PRINCIPAL ORGANIZATIONS INVOLVED	187
Section 11	LOAN OF MATERIALS, SUPPLIES AND EQUIPMENT	187
Section 12	ENTRY INTO FORCE, DURATION AND TERMINATION	189
Appendix A	WORK SCHEDULE CHART	190

SECTION ONE: INTRODUCTION

This Project Agreement (PA) hereby establishes the Free Piston Shock Tunnel (FPST) and the High Enthalpy Göttingen (HEG) cooperation as a project in accordance with the Memorandum of Understanding between the Secretary of Defense on behalf of the Department of Defense of the United States of America and the Federal Minister of Defense of the Federal Republic of Germany for Research and Technology Projects of 17 March, 1995.

Design of future hypersonic flight systems will rely heavily on computational fluid dynamics (CFD). A critical step is the acquisition of experimental data for validation of these codes. One advanced facility concept which is expected to provide much of the critical information about the flow fields around hypersonic vehicles is the free piston shock tunnel.

Two of the higher performance facilities of this type are the HEG, operated by the Institute for Experimental Fluid Mechanics at the German Aerospace Establishment (DLR), Göttingen, Germany, and under contract with the German MOD, and the FPST Facility at Arnold Engineering Development Center (AEDC), Arnold Air Force Base, Tennessee. The HEG is the largest such facility in the world and the FPST facility will operate at the world's highest pressures and densities.

SECTION TWO: DEFINITION OF TERMS AND ABBREVIATIONS

- AEDC - Arnold Engineering Development Center, located at Arnold Air Force Base in Tennessee
- DLR - Deutsche Forschungsanstalt für Luft- und Raumfahrt, located in Göttingen, Germany
- DoD - Department of Defense of the United States of America
- FPST - Free Piston Shock Tunnel, at AEDC, is a device used to generate very high speed and high pressure air flows for aerodynamic and real gas studies. AEDC's FPST is driven by a gunpowder charge.
- HEG - High Enthalpy Göttingen, free piston shock tunnel at DLR, differs from AEDC's FPST in that it is much larger in size and is driven by compressed air.
- CFD - Computational Fluid Dynamics, is the computer modeling of the movement of a fluid medium about an object.
- CFI - Computational Flow Imaging, is the computer model imaging of the movement of a fluid medium about an object.
- LIF - Laser Induced Fluorescence, is a wind tunnel diagnostic technique in which a constituent in the flow field is illuminated with a laser light source and recorded to yield an image of the flow pattern about an object.
- MOD - Federal Ministry of Defense of the Federal Republic of Germany

PLIF - Planar Laser Induced Florescence, is like LIF but yields an image field across a plane or a sheet, as opposed to the single line in LIF.

RTP/EA - Research Technology, Projects/Executive Agent

SECTION THREE: OBJECTIVES

The objectives of this PA are for the DoD to combine efforts with the MOD to accelerate and improve the development cycle of their respective state-of-the-art facilities through expedited initial operations with increased capability and data accuracy. These objectives will be accomplished by carrying out tests at both the FPST and HEG. These facilities complement each other by exploiting their differences; FPST's very high velocity and pressure capabilities and HEG's large size and mass flow rate capability. Testing will use corresponding configurations and flow conditions to:

- a. provide data for CFD code validations;
- b. improve capability via sharing different diagnostic techniques and equipment;
- c. understand flow and instrumentation anomalies;
- d. ascertain flow quality; and
- e. explore the applicability of binary scaling.

SECTION FOUR: SCOPE OF WORK

The following work will be undertaken under this PA:

- a) The participants will agree on a test plan that will include: standardized test conditions for test runs in the FPST and HEG; the models to be used; the instrumentation hardware, and diagnostic techniques.
- b) Data from the tests at both the FPST and the HEG will be fully shared and jointly analyzed.
- c) The work shall include both participants supporting the testing in the FPST and IMG through a comparison of the test data and both participants' CFD modeling. These results will then be shared.
- d) The participants will jointly prepare a final report to document the activities and findings for the duration of this project.

SECTION FIVE: SHARING AND BREAKDOWN OF WORK

The sharing of work will be as follows with the DoD and MOD participating in the tests at the partner's facility as required and agreed upon, availability permitting:

- a. DoD will, in accordance with the test plan:
 1. execute a test series for facility calibration;
 2. execute a test series using the DLR Blunt Cone model;
 3. fabricate two models (designed to AEDC specifications);
 4. execute a test series using two models (designed to AEDC specifications); and
 5. provide consultation on CFI techniques.

- b. MOD will, in accordance with the test plan:
 1. execute a test series using the Aero-braking model;
 2. execute a test series using the Blunt Cone model;
 3. execute a test series using the Shock Interaction model; and
 4. provide consultation on diagnostic techniques to include;
 - static cell design
 - holographic interferometry techniques
 - LIF analysis methods for temperature determination
 - PLIF collection optics laser diode absorption

- c. DoD and MOD will jointly perform in accordance with the test plan;
 1. the defining of standard conditions for tests;
 2. the selection of test articles;
 3. the selection of instrumentation and diagnostics to be exercised;
 4. data analysis of test runs at both the FPST and HEG facilities;
 5. authoring of individual test series technical reports;
 6. co-author a final report of the test activities and findings; and
 7. perform independent computational efforts based on shared test conditions.

SECTION SIX: SCHEDULE OF WORK

The project will proceed according to the schedule in Appendix A hereof, which is an integral part of this PA.

The final report shall be transmitted to the RTPs/EAs six months before the termination date for the PA.

SECTION SEVEN: MANAGEMENT

1. Project Officers:

US PO:	Ron Bishel
Title/Position:	Technology Project Manager
Organization:	AEDC Directorate of Technology
Address:	Arnold AFB, TN 37389-9011
Phone:	615-454-7734 DSN 340-7734 Fax -3559

US PO (alt):	Dave Stallings
Title/Position:	Engineering Specialist
Organization:	Sverdrup Technology, Inc.
Address:	Arnold AFB, TN 37389
Phone:	615-454-3314 DSN 340-3314 Fax -3644
Email:	dave.stallings@arnold.af.mil

German PO:	Georg Eitelberg
Title/Position:	Head Aerothermal Branch
Organization:	DLR Institute for Flow Mechanics
Address:	Bunsenstrasse 10 D-37073 Göttingen, Germany
Phone:	49-551-709-2339 Fax -2800

German PO:	Matthias Erich Funk
Title/Position:	Missile Aerodynamics
Organization:	Bundesamt für Wehrtechnik und Beschaffung (BWB) WF I 6
Address:	Postfach 7360 D-56057 Koblenz, Germany
Phone:	49-261-400-7306 Fax -7429

SECTION EIGHT: FINANCIAL ARRANGEMENTS

The Parties estimate that the total cost of performance of the work under this PA shall not exceed 4.48 million US dollars or 6.72 million German marks based on an exchange rate of \$1 equals 1.5 German marks. The work shall be shared approximately equally over the life of the project.

The DoD share of the work shall not cost more than \$2.24 million. The FMOD share of the work shall not cost more than 3.16 million German marks. Cooperative efforts of the Parties over and above the jointly agreed work set forth in the SCOPE OF WORK and SHARING OF WORK and FINANCIAL ARRANGEMENTS sections shall be subject to amendment to this PA or signature of a new PA.

SECTION NINE: CLASSIFICATION

No classified information will be exchanged under this PA.

SECTION TEN: PRINCIPAL ORGANIZATIONS INVOLVED

Arnold Engineering Development Center (AEDC)
 Directorate of Technology (DOT)
 1099 Avenue C
 Arnold Air Force Base, TN 37389-9011
 USA

Deutsche Forschungsanstalt für Luft-und Raumfahrt (DLR)
 10 Bunsenstrasse
 D-37073 - Göttingen
 Germany

SECTION ELEVEN: LOAN OF MATERIALS, SUPPLIES AND EQUIPMENT

One of the objectives of the project is to improve nonintrusive diagnostic capabilities by sharing different techniques and equipment.

To accomplish this, the DoD will loan instrumentation and diagnostic equipment to participate in the German tests at the BEG as required. This equipment is required to obtain data in the HEG to evaluate the effectiveness of the diagnostic hardware and techniques under different facility operating conditions. The MOD will also loan the instrumented "DLR BluntCone" model. This item is required to obtain comparative test data on one test article in the two different facilities. The following items (hereinafter referred to as the 'Property') will be loaned:

The DoD may provide the following listed Property to the MOD, as required and appropriate to meet the objectives of the cooperative program. Depending on the results of the experiments during the course of this agreement, some or all of this equipment may be required. Decisions as to which systems are ultimately used will be jointly agreed to by the DoD and MOD Project Officers.

QuantityDescription

1

A filtered Rayleigh scattering system which consists of a copper-vapor laser, laser focusing optics, scattered light collection/imaging optics, a temperature-controlled iodine cell for optical filtering, a cooled photomultiplier tube detector, and a personal computer for system control, data acquisition, and data reduction.

- 1 A mass spectroscopy probe which consists of a skimmer nozzle, a time-of-flight mass spectrometer, vacuum pumps, and a personal computer for system control, data acquisition, and data reduction.
- 1 A high speed flow visualization system which consists of a copper-vapor laser, laser sheet forming optics, scattered light collection/imaging optics, optical filters, a high speed framing camera, and a personal computer for system control, data acquisition, and data reduction.

None of this Property will be expended in the course of the RTP/PA. A typical loan period is expected to be approximately two to three months. The loan of the Property will be coordinated with the test schedules of the FPST and the HEG, as agreed to by the DoD and MOD Project Officers.

The US is responsible for all costs and preparation of transportation of Property. The US will deliver the Property at a point determined by the MOD and DoD Project Officers.

The Federal Republic of Germany will be responsible for properly maintaining the Property and will return the Property to the US at a point determined by the DoD and MOD Project Officers upon expiration of the agreed loan period in as good condition as when received, reasonable wear and tear excepted, or pay the cost of any damage.

The MoD will provide the following Property to the DoD. As with the US diagnostic equipment, the use of the laser diode absorption system will be as deemed appropriate and necessary, as agreed between the DoD and MOD Project Officers.

<u>Quantity</u>	<u>Description</u>
1	<p>DLR Blunt-Cone as built for testing in the HEG. This model is a spherically blunt cone with a 4.66-deg half angle, a 108.15 mm base diameter, and 29.17 mm nose radius.</p> <p>A laser diode beam transmission system will be supplied to monitor the particulate contamination level during facility runs. This system consists of the laser diode, power supply, wavelength control electronics, beam shaping optics, collection optics, photodiode transmission detector, and a PC for system control, data acquisition, and data reduction.</p>

This Property will not be expended in the course of the RTP/PA. The loan period is expected to be approximately two to three months. The loan of the Property will be coordinated with the test schedules of the FPST and the HEG, as agreed to by the DoD and MOD Project Officers.

The Federal Republic of Germany is responsible for all costs of preparation and transportation of Property. The MOD will deliver the Property at a point determined by the DoD and MOD Project Officers.

The US will be responsible for properly maintaining the Property and will return the Property to the Federal Republic of Germany at a point determined by the MOD and DoD Project Officers upon expiration of the agreed loan period in as good condition as when received, reasonable wear and tear excepted, or pay the cost of any damage.'

SECTION TWELVE: ENTRY INTO FORCE, DURATION AND TERMINATION

This FPST/HEG PA, a Project under the RTP MOU between the Secretary of Defense on behalf of the Department of Defense of the United States of America and the Federal Minister of Defense of the Federal Republic of Germany, shall enter into force upon signature by the RTP MOU Executive Agents, and shall remain in force for five years unless terminated by either Party. It may be extended by written agreement by the RTP MOU Executive Agents.

The US RTP/EA

Signature

Signature

Clinton V. Hom, Maj Gen. USAF
Name

Rolf Schreiber
Name

Principal Assistant Deputy Under Secretary
of the Air Force (International A
Title

Chief of the Air Armaments Division
Directorate General of Armament
Title

28 April 1997
Date

28 April 1997
Date

Berlin, Germany
Location

Berlin, Germany
Location

Appendix A: FPST/HEG
 WORK SCHEDULE (in months)

MONTHS	1-3	4-6	7-9	10-12	13-15	16-18	19-21	22-24
SPECIFICATIONS								
Standardized Conditions	X---X							
Test articles		X---X						
Instr & Diagnostics		X---X						
TESTS								
DLR								
Aero Braking		X---X						
Blunt Cone		X---X						
Shock Interaction						X---X		
AEDC								
Facility calibration	X---	---X						
Model fabrication		X---X						
Model #1				X---X				
DLR Blunt cone					X---X			
Model #2						X---X		
COMPUTATIONS								
Code validation	X---	---	---	---	---	---	---	---X
CONSULTATION								
AEDC								
CFI	X---	---	---	---X				
DLR								
Static cell, Holographic interferometry, LIF, PLIF, Laser diode absorption	X---	---	---	---X				
EQUIP EXCHANGE								
DLR Supplied								
DLR Blunt cone				X---	---X			
Laser diode absorption							X---X	
AEDC Supplied								
Mass spec probe			X---	---X				
Rayleigh scatter			X---	---X				
High Speed flow visual							X---	---X
REPORTING								
Progress	X	X	X	X	X	X	X	X
Test Series	X---	X---	X---	X---	X---	X---	X---	X---
Final								

APPENDIX 2
LDA DATA REDUCTION SOFTWARE

To measure gas properties, such as temperature, velocity, and species concentration, a laser diode absorption (LDA) spectroscopy system using rubidium (Rb) as the probe species was employed. Since the gas does not naturally contain this probe species, an aqueous Rb salt solution was applied to the driver gas diaphragm. The salt was dissociated into atomic Rb by the shock-heated gas. To detect the Rb, the D_2 ground state transition ($5S_{1/2} \rightarrow 5P_{3/2}$) at 780.2 nm was probed by an InGaAlAs single frequency mode diode laser beam passing through the test section. The laser drive current and temperature determine the wavelength emitted. To scan the laser frequency across the Rb transition, the laser temperature was held constant while the injection current was varied. In this application, the injection current was modulated by a 15 KHz symmetric triangle function. In addition to tuning the laser wavelength across the Rb transition, the current modulation also produced modulation in the laser power. Figure 1 is an example of a raw transmission signal obtained during laboratory testing, where the driver gas was seeded with 428 μg of Rb. The inset shown in Fig. 1 is a detail of this signal illustrating the unwanted amplitude modulation in laser power caused by the current tuning.

The goal of this effort was to determine driver gas arrival time with the LDA system. In order to achieve this goal, a data reduction program was needed to eliminate the laser power amplitude modulation, thus leaving the absorption spectra. In Figure 1, the driver gas arrival at 4 ms is clear from the large drop in laser transmission (the absorption between the firing of the shock tunnel at 0 ms and 1 ms is due to residual Rb present in the test gas flow), however this is not normally so. In order to make measurements based

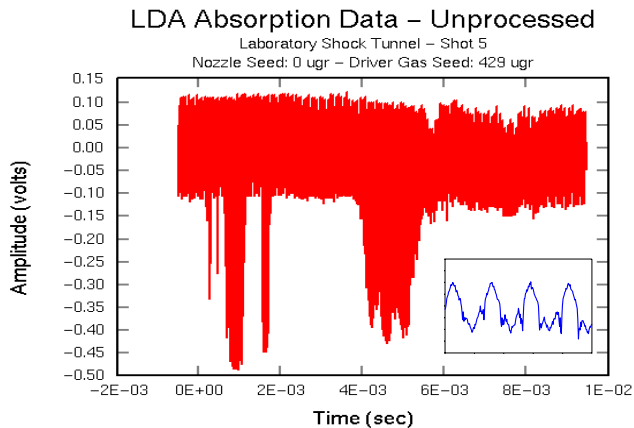


Figure 1: Raw photodiode signal obtained during a laboratory shock tunnel test. The inset is a detail of the signal showing the laser power modulation and the Rb absorption.

upon the Rb absorption, it is necessary to eliminate the modulation in the laser power. Unfortunately, a reference signal of the null laser power, that is to say the laser signal without the Rb absorption, was not taken. Therefore, a program to numerically eliminate the amplitude modulation from the data signals was developed. Also, for the data signals obtained in the Impulse Facility, the removal of noise spikes generated by a copper vapor laser (CuVL) was included in the data reduction program. The CuVL was used for filtered Rayleigh scattering and in the high-speed flow visualization system.

GeRiLA (shortened from generalized rubidium laser diode absorption algorithm) is the FORTRAN program developed to obtain the absorption spectra from the raw photodiode signals. The photodiode signals were acquired with a LeCroy digital oscilloscope that stores the signal in an ASCII formatted file with 50002 amplitude and time pairs. The sampling rate of the scope depends upon the time duration of the signal that is captured. The GeRiLA program manipulates this data file to get the desired results.

After declaring the needed parameters, arrays, and variables, a subroutine is called to read the input file where specific variables needed to reduce a file are stored. The input file contains the following variables:

1. the name of the data file to be reduced,
2. whether or not the CuVL noise is to be removed,
3. the number of points used in a smoothing filter,
4. the approximate number of points in the signal before the initial shock,
5. the offset needed to ensure the amplitude has a value greater than zero,
6. the upper and lower threshold of the pre-shock signal,
7. the amplitude value of the mid-point of the laser signal,
8. how many points to use for line fitting and the number of points to move in from the endpoints of the sweep,
9. which data to output,
10. the standardized frequency dimension,
11. whether to output the results in transmission or absorption form.

The program then reads the data points in the selected file into two different arrays: one for time (xin) and the other for amplitude (yin). The offset value is then added to the amplitude information stored in the yin array.

If the variable for the CuVL removal is set to 1 (as it would be for impulse facility data), the GeRiLA program finds the noise spikes via a two-point derivative marker, and uses the points around the noise spike to replace it with a linear fit between the points around the noise spike. The signal is then smoothed using a boxcar filter, and stored in a separate array from the actual data signal. This smoothed data set is only for finding the extrema of the signal for sweep separation, while the actual signal is used for the data reduction.

Using the approximate number of points before the shock and the upper and lower threshold values from the input file, the program segments the pre-shock signal into separate sweeps (both up and down) and analyzes the number of points in each sweep. This information is then used to find the actual extrema by taking this number as an estimate for the number of points in the next sweep and searching for the actual extremum around that point. The process is repeated until the end of the signal is reached. The time value for the maximum and minimum of each sweep are stored in the start and stop point arrays.

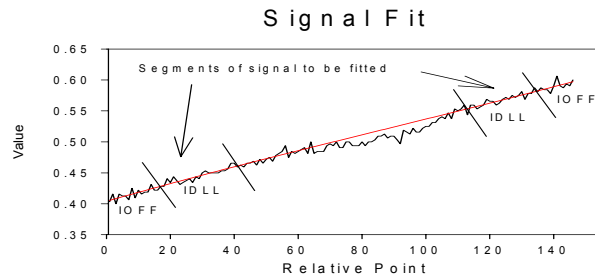


Figure 2: Graph depicting original sweep, the segments used to generate a fit, and the actual polynomial fit produced.

Offsetting from each start and stop point (determined by the input value IOFF) and counting a set number of points (input value IDLL), a linear and polynomial least squares function are fit to this sweep using the Numerical Recipes subroutines FIT and LFIT¹, and stored in the fit arrays. Figure 2 illustrates

1. W. H. Press, S. A. Teukolsky, W. T. Vetterling, B. P. Flannery, *Numerical Recipes in FORTRAN: The Art of Scientific Computing*, 2nd ed., New York: Cambridge University Press, 1992.

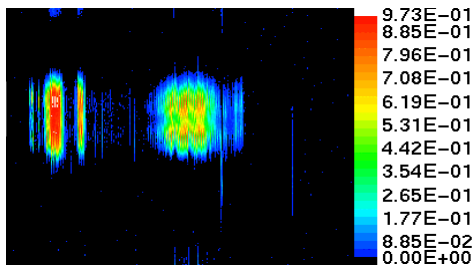


Figure 3: Image of all scan profiles. The first peak is test gas absorption. The second peak is driver gas absorption.

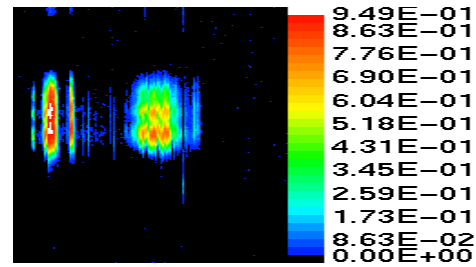


Figure 4: Image of even scan profiles. Note that the peak absorption is near the bottom of the image.

this process. If needed, these fit arrays are then written to files datoutxxx.asc and fitoutxxx.asc (where xxx represent the specific sweep number) for later analysis. Because it usually follows the signal more closely, the polynomial fit is subtracted from the signal leaving the pure absorption profile, which is stored in the absorption array. Since the absorption arrays have unequal dimensions (due to the variation in the number of points in each sweep), an interpolation routine LAGINT is used to map each array to a standard size, given by NF from the input file. The value used throughout this application was 256. The profile is next integrated and the value stored in the SUM array according to scan number. This process is repeated for each scan, typically 300 scans for this application.

The absorption profiles are each written to two image files: all profiles are written to COMPILE_BOTH.saf, the odd scans are written to COMPILE_ODD.saf, and the even scans are written to

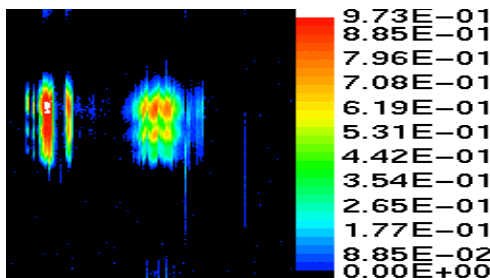


Figure 5: Image of odd scan profiles. Note the changes in direction of the profiles from the even scan image; the peak absorption is now near the top of the image.

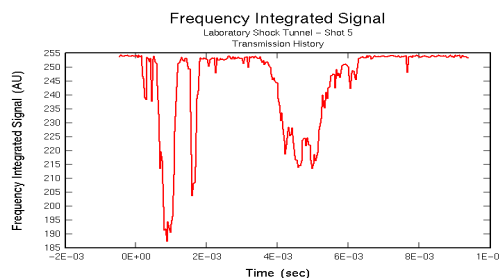


Figure 6: Frequency integrated signal showing laser beam transmission history. The drop in transmission around 4 msec is due to driver gas arrival.

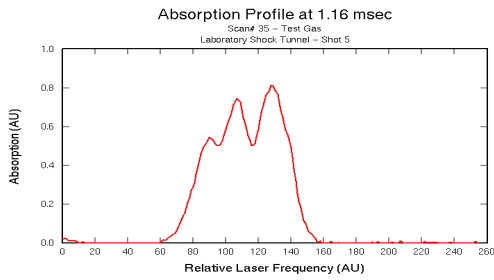


Figure 7: Absorption profile, generated by the GeRiLA program, showing rubidium absorption in the test gas.

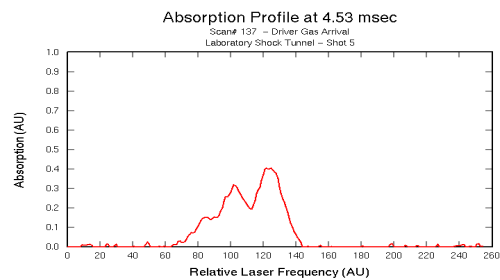


Figure 8: Profile showing rubidium absorption in the driver gas, also generated by the GeRiLA program.

COMPILE_EVEN.saf. The x-axis of the image file is the scan number, the y-axis is the relative laser frequency, and the color depth is the amplitude information of the absorption profiles. A sample combined image file from a laboratory shock tunnel test is shown in Fig. 3. Figures 4 and 5 are sample even and odd scan image profiles from a laboratory shock tunnel test; note that in Fig. 4 (even scans) the peak absorption (largest feature) is near the bottom of the image, and in Fig. 5 (odd scans) the peak absorption is near the top of the image. This effect, which is due to the laser scanning technique used, was later corrected by reversing the points in the odd scans. Finally, the SUM array is written to the file FIS.pod. When plotted, this file shows the time history of laser beam transmission or of Rb absorption, whichever is selected in the input file. Figure 6 is a sample transmission history plot from a laboratory shock tunnel test. Figures 7 and 8 are absorption profiles generated by the GeRiLA program from test gas absorption and driver gas absorption, respectively.

APPENDIX 3
SHEARING AND CONVENTIONAL INTERFEROMETRY
FROM HOLOGRAPHIC CINEMATOGRAPHY
AEDC IMPULSE FACILITY
RUNS 33 AND 35

**Shearing and Conventional
Interferometry from
Holographic Cinematography
AEDC Impulse Facility
Runs 33 and 35**

Purchase Order #T00-64

29JUN01

**North Dancer Labs, Inc.
4740 Shelburne Road
P. O. Box 99
Shelburne, VT 05482-0099
ndl@sover.net**

1 Introduction

This final report details the methods and results of work performed by North Dancer Labs (NDL), Inc., Shelburne, VT, under contract with AEDC/Sverdrup, Inc. (PO# T00-64.) The goal of this contract was to obtain 2D gas density data from holograms recorded by NDL at the AEDC Impulse Facility during Runs 33 and 35, on June 9-12, 1998. Specifically, NDL has, through optical and computer post-processing, performed both shearing and conventional holographic interferometry to obtain this data from the wavefronts recorded in the holograms. Deliverables for the contract include this report and the 2D number density data on CD in both tabulated text format compatible with Microsoft Excel and in Windows bitmap format. In addition, NDL has included the source code used to perform the computer processing.

With the holograms recorded on film, 70 and 75 time frames for Runs 33 and 35, both shearing and conventional interferometers were assembled. Each time frame was digitized using custom software with four phase-shifted images each. The sheared interferograms were digitized with shear in both the x and y axes. Post-processing with Interactive Data Language (IDL) 5.4 yielded phase maps. In the case of the sheared interferograms, the overall phase was reconstructed from the sheared phase, which is a finite-difference approximation of the gradient. Then all the resulting phase maps were converted to differential 2D density measurements. The results allow comparison of the relative merits of shearing and conventional interferometry for flow diagnostics.

2 Optical Methods

2.1 Holographic Recording

Figure 1 below illustrates the overall optical layout used to record holographic cinematography of Runs 33 and 35 at the AEDC Impulse Facility. The light source was an Oxford Lasers' LS series copper vapor laser with an off-axis unstable resonator cavity. The laser produced 20 W average power with roughly 30 ns pulses at 511 and 578 nm. First, the green and yellow lines were separated with a dichroic splitter and only the green line, which accounts for about 2/3 the power in the beam, was used. Then a standard spatial filter, consisting of a focusing lens, a pinhole and a recollimating lens, was used to improve the transverse mode of the laser.

The copper vapor laser beam was split into object and reference beams with about 50% going to each. The object beam was expanded to roughly 300 mm in diameter using a simple lens, a flat fold mirror and a concave mirror. This collimated object beam passed through the tube via windows on either side at which point an identical concave mirror and fold mirror focused the image into the holographic recorder (see Figure 1). The reference beam was directed, using various fold mirrors, under the tube and up into the holographic recorder. The path lengths of the object and reference beams from the splitter to the film plane were matched to within 1 cm. A slow ($f = 1$ m) lens was used to focus the

reference beam to the film plane in order to match the size and transverse mode of the object beam.

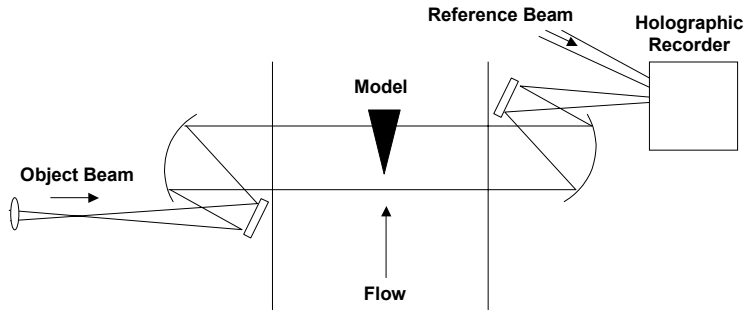


Figure 1: Holographic recording layout at the AEDC Impulse Facility

The holographic recorder was placed in the object beam as shown in Figure 2. The focal point of the concave mirror was after the film. The collimated portion of the beam focused at this point. The image, however, of the test model was a virtual image because the model was inside the focal length of the mirror. This arrangement, while not ideal for holographic recording, was used to minimize impact on the Cordin camera, which recorded the object beam after it passed through the holographic recorder.

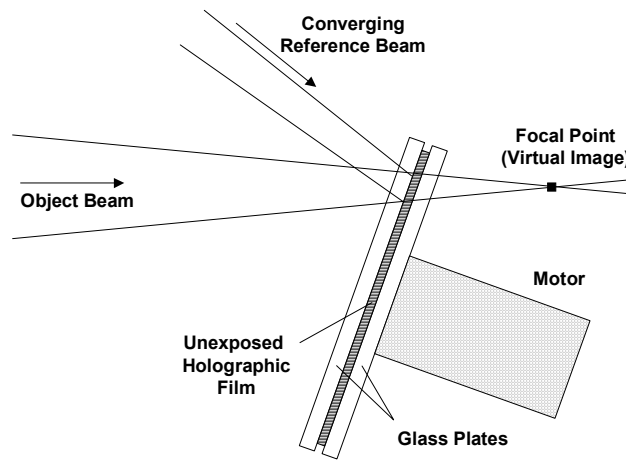


Figure 2: Holographic recorder

The motor of the disk transport spins the 115-mm diameter film disk at 6000 rpm (100 rps). The hologram is recorded at radius of 48 mm on the film giving a linear velocity of $2\pi(51 \text{ mm})(100 \text{ rps}) = 3.2 \times 10^4 \text{ mm/s}$. With the approximately 4 mm diameter of the hologram, a maximum recording rate of $(3.2 \times 10^4 \text{ mm/s})/(4 \text{ mm}) = 8.0 \text{ kHz}$ with the ability to record up to $2\pi(51 \text{ mm})/(4 \text{ mm}) = 80$ holograms for this particular configuration. Only about 75 holograms were actually recorded to prevent overlap of the first and last images.

The holograms of Runs 33 and 35 were both recorded at 8 kHz on Agfa 8E75 green-sensitive holographic film. Timing of the laser was accomplished with an Oxford Lasers' 'n'-shot controller. It accepted a TTL timing signal from a transducer built into the shock tube facility and shuttered and fired the copper vapor for approximately 75 pulses. The film was processed using a pyrogallol developer and bleached, not fixed, to produce phase holograms.

2.2 Holographic Reconstruction and Interferometry

The immediate goal of the shearing interferometer is to interfere the reconstructed wavefront with a copy of itself at a slight lateral displacement, or shear (see Figure 3). Shearing interferometry is an alternative to conventional interferometry where the wavefront is interfered with a plane wave or a "no-flow" wavefront. Conventional interferometry measures refractive index, which can then be related to other quantities, typically density. In the limit of small shear distances, shearing interferometry measures a finite-difference approximation of the partial derivative of the refractive index in the direction of the shear. The gradient itself may be interesting or it can be inverted in some cases to give the refractive index.

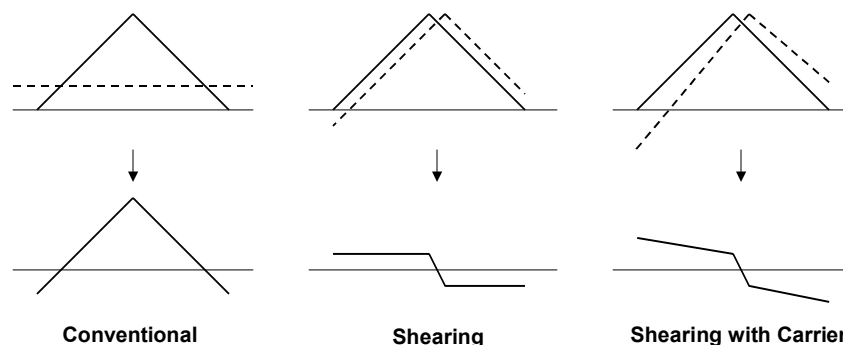


Figure 3: One-dimensional illustration of the difference between conventional and shearing interferometry. The top images show the phase of the two wavefronts being subtracted. The bottom images show the results of the subtraction. Note that in the actual interferogram the phase is represented by the fringe number.

In practice, a linear component is often added to the shear by introducing a slight tilt in one leg of the interferometer. This produces a finite fringe interferogram, i.e., an interferogram with straight carrier fringes. This was done for several reasons. Primarily, the carrier fringes allow visualization and calculation of the phase shift, ψ , when calibrating the piezoelectric stage. Second, introducing carrier fringes tends to reduce the susceptibility of the interferometer to digitization errors resulting from external vibrations. In addition, it is simply easier to purposely introduce a linear carrier and subtract it than it is to perfectly nullify the fringes.

Figure 4 shows the optical layout used to reconstruct the holograms and perform shearing interferometry on the resulting wavefronts.

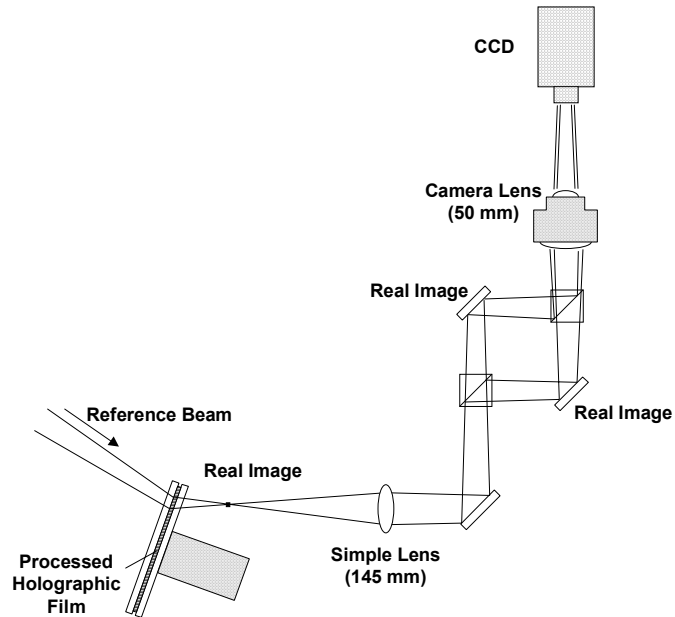


Figure 4: Shearing Interferometry

Ideally the holograms, recorded at 511 nm, would be reconstructed with either another copper vapor laser or with an air-cooled argon at 514.5 nm. In the absence of a green laser, a HeNe laser at 632.8 was used to reconstruct the holograms. Optically, the only compensation necessary to reconstruct in the red is to increase the reference beam angle so that $\lambda_{\text{red}} \sin \theta_{\text{green}} = \lambda_{\text{green}} \sin \theta_{\text{red}}$. Additionally, using the HeNe introduces a shift in focus and magnification such that the real image will be smaller and form in a shorter distance in the red. In reconstructing these holograms, the cone angle of the converging reference beam (a 1 m positive lens was used) was only approximately matched to that of the original green reference beam because the optics of the subsequent interferometer could compensate for moderate magnification changes.

The film is mounted on glass disks that can be rotated so that different time frames are illuminated. A simple lens relayed the real image formed by holographic reconstruction and formed real images on each mirror of the Mach-Zehnder interferometer (see Figure 5). The first beam splitter forms the two legs of the interferometer. The first leg passes straight through the second splitter via a fold mirror. The second leg is similar except that the fold mirror in this case is mounted on the piezoelectric translation stage to allow multiple phase-shifted interferograms to be recorded.

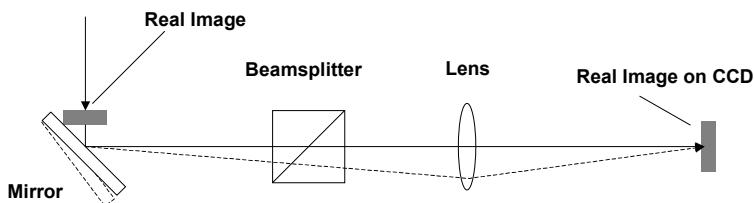


Figure 5: Illustration of the insensitivity of the image placement (and therefore the shear) to the tilt of the mirror for controlling carrier frequency. The first real image is shown slightly off the mirror for clarity.

The advantage of re-imaging onto the interferometer mirror is that it is now possible to adjust the carrier frequency (finite fringes) of the interferogram independently of the shear. This greatly simplifies alignment by allowing the shear to be set first followed by adjustment of the fringe frequency without affecting the shear.

The piezoelectric stage used to alter the path length in the second leg of the interferometer was a Burleigh model PZ-81 open-loop piezo with 2 μm full travel at 1 kV applied voltage. This particular model stage is actually an aligner/translator type stage incorporating three piezos at 120°. By driving all three crystals at the same voltage, each crystal translates equally and the device performs as a linear translation stage.

The stage was driven using a Bertan model 602C-30P high voltage power supply capable of 0-3 kV at 5 mA. The voltage is adjusted via an analog input where 0-5 V DC produces 0-3 kV DC. Either a simple potentiometer arrangement or a remote analog signal can be connected to this input to provide manual or automatic control, respectively.

The images were digitized using a Hitachi KP-F2A 640 x 480 x 8-bit CCD camera. No lens was necessary on the camera because a real image was formed by the lenses in the interferometer optics.

Alignment of the images consisted of setting the carrier frequency and the shear to the desired values – roughly 5 fringes and 5 pixels, respectively. The shear amount was chosen to give more sensitivity than just 1 pixel shear but low enough that the spatial bandwidth of the resulting phase maps would not be too limited (see Section Shear Removal (Shearing Interferometry Only)). The carrier fringe frequency was chosen to give good visualization of the phase shift but low enough that there would be no fringe aliasing. The shear could be set first by rotating or tilting the first beam splitter. Carrier frequency was adjusted by tilting the mirror of the interferometer leg without the piezo stage.

Conventional interferometry was also performed with holograms from Runs 33 and 35. The original plan had been to physically remove the first hologram from each disk and use them to optically subtract the no-flow phase. Instead NDL made a copy of the first holograms. Figure 6 shows the layout, a modified version of the shearing interferometer.

The phase-shifting leg and both beamsplitters of the Mach-Zehnder are removed. A holographic plate (Slavich PFG-01) is inserted in the reconstructed image just after the film disk. A second reference beam is directed to the plate via a mirror on the piezoelectric stage. A short, shuttered exposure followed by a pyrogallol developer and bleach results in a copy of the no-flow hologram. Reinserting the second hologram reconstructs a second copy of the wavefront. Adding a slight tilt in the desired axis generates carrier fringes. Applying voltage to the piezo stage imparts a phase shift on the second reference beam and, therefore, on the second wavefront.

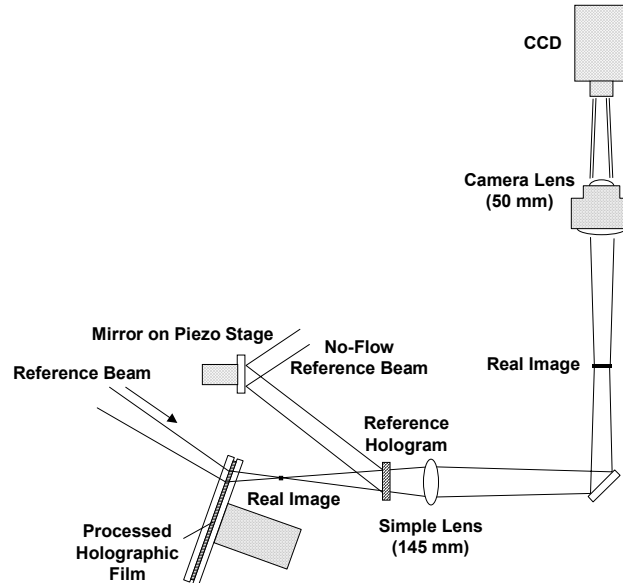


Figure 6: Conventional Interferometry

In the case of both the shearing and conventional interferometry, calibration of the phase shift was necessary because of the non-trivial geometry of the interferometers. The ideal phase shift is $\pi/4$ or $1/4$ fringe. Once the image was aligned with the proper shear and phase shift, the voltages for the phase shift were set to a best guess by visually checking that the fringes shifted by half a fringe from the first phase shift to the third phase shift. Then images of the first and third phase shifts were digitized. Line profiles in the appropriate direction - horizontal for x shear, vertical for y shear - were extracted from the images and the FFT's of each profile were examined. The peak corresponding to the carrier frequency was located and the phase was calculated from the complex value at that frequency in both profiles. The phase shift voltages were then adjusted by the ratio of that phase shift to the ideal phase shift between the first and third images of $\pi/2$.

2.2.1 Digitization Software

With four conventional and eight sheared interferograms needed for each hologram and, with a total of about 145 holograms on the Run 33 and 35 disks, over 1700 images were digitized. Because of this large volume of data, a simple Windows application was written

that automates several aspects of the digitization process. Figure 7 below shows a screen shot of the application.

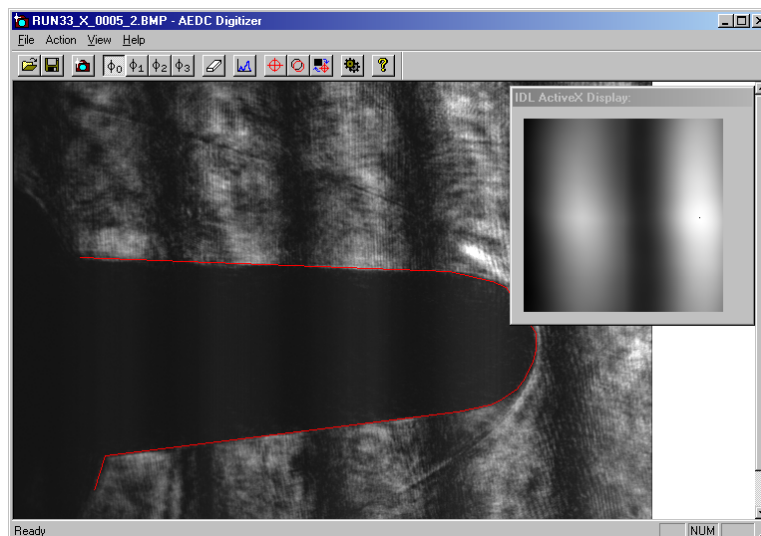


Figure 7: Digitization software used to acquire interferometry data.

The application allows software control of both the phase-shifting piezoelectric mirror translation stage and the Hitachi KP-F2A CCD camera. The piezo stage is controlled with a National Instruments PCI-MIO-16 analog and digital I/O board. Four toolbar buttons (and keyboard shortcuts), one for each of the four phase shifts, are provided. Clicking one of the buttons causes the I/O board to output a predetermined 0-5V DC analog voltage to the high voltage supply. The high voltage supply translates 0-5V DC to 0-3kV DC. The piezo then translates at 1 $\mu\text{m}/\text{kV}$. The four phase shift voltages are altered in a property settings window.

Control of the Hitachi CCD is accomplished with a Coreco Imaging PCVision 8-bit, 640 x 480 resolution framegrabber. The software development kit for the camera provides simple function calls that allow initializing the CCD, display of live video to the client area of a window, and acquisition of digitized frames into host computer memory. The application makes use of these functions by providing toolbar buttons (and keyboard shortcuts) to allow the user to start/stop live video and to grab an image. However, the most important enhanced feature for CCD control is the ability to snap multiple frames and average them. This effectively eliminates the effects of vibrations, providing that the amplitude of the vibrations is less than the fringe separation. In this case, irreversible smearing would occur.

In addition to providing simple control of the piezo and the CCD from one application, the application provides two other important features. First, it automatically names files to be saved to disk. The user provides a base file name such as "Run33_X_Sheared_", and when the user saves, the application automatically appends the frame number and the phase shift number to the filename in a format that the IDL image processing code can

recognize, e.g., "Run33_X_Sheared_0021_2.bmp". Significant efficiency is gained by not requiring the user to type a filename for each of the 1700 digitized images.

The final and perhaps most critical feature of the application is that it provides a means for alignment of the images to a reference image. The user can draw alignment marks directly over a live or grabbed image. The marks can be used to align the next image. This is particularly useful in aligning the disk rotation before digitizing each time frame. In addition to visually aligning the live image to the alignment overlay, the application can make a Remote Procedure Call to IDL via an ActiveX control. IDL then performs a cross-correlation between the current image and a reference image and relays the amount of misalignment (in pixels) back to the user.

The commented Visual C++ 6.0 source code for the digitization application is included on CD-ROM. Because the IDL ActiveX control requires a site license, IDL 5.4 must be installed with the proper hardware or software key on the computer platform in order for the cross-correlation alignment feature to function.

3 Computational Methods

With the phase-shifted interferograms digitized, the images were processed to extract number densities. This processing was carried out on a Dell Dimension desktop computer with a 350 MHz Pentium III processor with 64 MB RAM and a 6 GB hard drive. All of the software involved was implemented using Research System's Interactive Data Language (IDL) version 5.4. The commented source code is included on CD-ROM.

IDL 5.4 is high-level programming language similar to programs such as MATLAB. Included with IDL is an extensive library of routines oriented toward image processing, signal processing, statistical analysis, 3D visualization, etc.. In addition, IDL provides widget routines that encapsulate the Windows API and allow the creation of event-driven graphical user interfaces with controls such as buttons, scroll bars, pull-down menus, etc. NDJ used IDL to perform the post-processing and visualization of the digitized interferograms. The use of IDL greatly reduced the overhead involved with writing the code in Visual C++ or Visual Basic.

The overall processing scheme was implemented as follows:

1. Pre-process interferograms
2. Calculate phase shift
3. Extract phase modulo 2π
4. Unwrap phase
5. Remove linear phase
6. Remove no-flow phase
7. Convert phase to 2D gas density (or density gradient)
8. Invert density gradient to give density (sheared phase maps only)
9. Output data to files

Unless noted each step applies to both conventional and shearing interferometry. The only difference in processing the conventional and sheared interferograms is the addition of step 8 to integrate the density gradient to give the density.

3.1 Interferogram Pre-Processing

The only preprocessing performed on the interferograms prior calculation of the phase was the use of an IDL routine called “smooth” to filter out some of the high frequency noise. This low pass filtering was used for two reasons. First, it eliminated the high frequency noise that the Hitachi camera introduced. Second, it helped reduce the number of residues in the phase, thus improving the performance of the phase unwrapping. This routine performs a 2D boxcar average with the kernel size set by the user. The kernel is truncated at the edges of the image. A 3 pixel kernel was used in all the interferograms. Thus, each pixel was given a value equal to the average pixel value of the 3 x 3 block of pixels centered on itself. This routine was chosen over a standard low pass filter because it does not introduce “ringing” at sharp edges that might interfere with phase extraction.

3.2 Calculation of Phase Shift and Phase Modulo 2π

Recall that the first step in obtaining number densities from the interferograms is to calculate the phase, θ , of the wavefront. The phase will, in turn, yield the refractive index, which can be related to the density. An interferogram, $I(x,y)$, can be expressed as follows

$$I(x, y) = a(x, y)\{1 + m(x, y)\cos[\theta(x, y)]\}, \quad (3.1)$$

where $a(x,y)$ is referred to as the bias and the constant of proportionality, $a(x,y)m(x,y)$, for the cosine term is referred to as the modulation.

One of n phase-shifted images satisfies the following equation:

$$I_n(x, y) = a(x, y)\{1 + m(x, y)\cos[\theta(x, y) + n\Psi]\}, \quad (3.2)$$

where Ψ is the phase shift. The phase shift is assumed to be equal in each case.

Because of the potential for phase shift inaccuracies due both to the open-loop nature of the piezo stage and to the more complex geometry of the Mach-Zehnder interferometer used, the size of the phase shift, ψ , was considered to be unknown (see Section Holographic Reconstruction and Interferometry). The algorithm used to extract the phase from the interferograms was therefore chosen because of its ability to calculate ψ empirically from the four phase-shifted images without any *a priori* knowledge of the optical geometry or the performance of the piezo stage. The only assumption made about ψ is that the phase shifts are all equal.

Four images, each with equal phase shift, ψ , allow solving for the four unknowns: θ , ψ , modulation and bias. First, the following equation calculates the phase shift, $\psi(x,y)$, on a pixel by pixel basis from the four images:

$$\Psi = \cos^{-1} \left[\frac{(I_4 - I_1) - (I_3 - I_2)}{(I_3 - I_2)} \right]. \quad (3.3)$$

While this equation calculates $\psi(x,y)$ for each pixel, no real significance is attached to the individual values both because of the inherent noise in the measurement from the finite precision arithmetic and because no real variation is expected other than the equal phase shift in each pixel. Thus, the mean phase shift, $\bar{\Psi}$, is used as the measured value of ψ .

In implementing the calculation of this equation, two pitfalls must be avoided. First, it is possible and, in fact, almost guaranteed that the denominator in Eq. 3.3 will be zero leading to an illegal floating point operation and an indeterminate ψ at that pixel. Second, because of finite precision effects, it is again very likely that for some pixels, the operand of the inverse cosine in Eq. 3.3 will have an absolute value greater than one. This again leads to an indeterminate ψ . The solution for both of these cases is to check for values of $\psi(x,y)$ outside the interval $[-1,1]$ or special values such as $\pm\text{Inf}$ and $\pm\text{NaN}$, and not include them in the mean.

Once ψ is calculated, the phase, θ , can be calculated from the following:

$$\theta(x,y) = \tan^{-1} \left\{ \frac{(\cos \Psi - 1)[(2 \cos \Psi + 1)I_1 - (2 \cos \Psi + 2)I_2 + I_3]}{\sqrt{1 - \cos^2 \Psi} [(2 \cos \Psi - 1)I_1 - (2 \cos \Psi)I_2 + I_3]} \right\}. \quad (3.4)$$

In implementing this equation one must use an inverse tangent routine that accepts not one argument but two arguments in the form of the numerator and denominator of the operand. By checking the numerator prior to division, such functions prevent division by zero and allow proper calculation of, e.g., $\tan^{-1}(1/0)$, which should be $\pi/2$.

The modulation can then be calculated with

$$a(x,y)m(x,y) = \frac{I_2 - I_1}{(\cos \Psi - 1)\cos \theta - \sin \Psi \sin \theta}. \quad (3.5)$$

The bias, which is not currently used in any subsequent calculations, can be calculated with

$$a(x,y) = I_1 - a(x,y)m(x,y)\cos \theta. \quad (3.6)$$

Figure 8 below shows the user interface for the routine that was used to calculate the modulo 2π phase from the images. The user selects which time frames to process and the routine locates the pertinent image files and processes them with a visual status display showing the progress of the calculation.

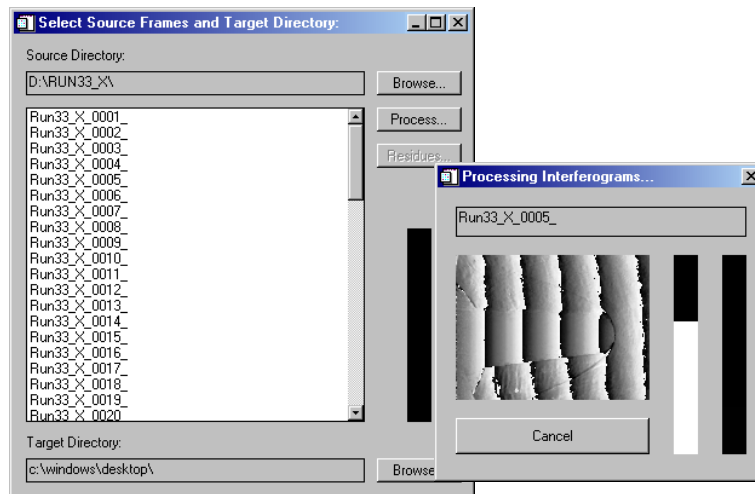


Figure 8: User interface for the calculation of the modulo 2π phase.

A typical phase map is shown below in Figure 9 and plot of the pixel values for row number 470 (tenth from the top) is shown in Figure 10. Note the characteristic sawtooth pattern of the carrier frequency.

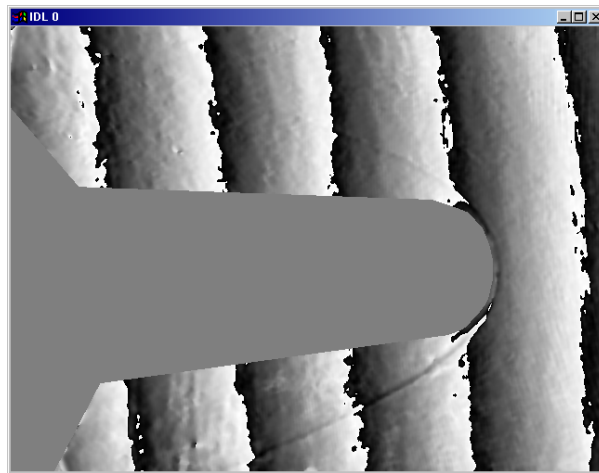


Figure 9: A typical modulo 2π phase map calculated from sheared interferograms.

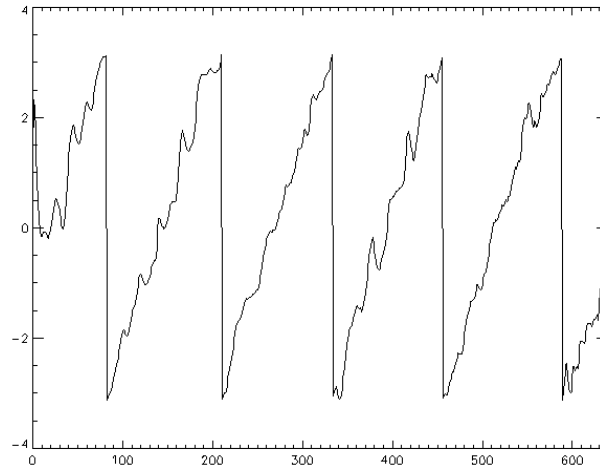


Figure 10: Profile of row 470 of the modulo 2π phase map in Figure 9.

3.3 Phase Unwrapping

As is always the case in interferometry, Eq. 3.4 only calculates θ modulo 2π . The phase must then be unwrapped to yield the principal phase. Figure 11 illustrates the basics of phase unwrapping.

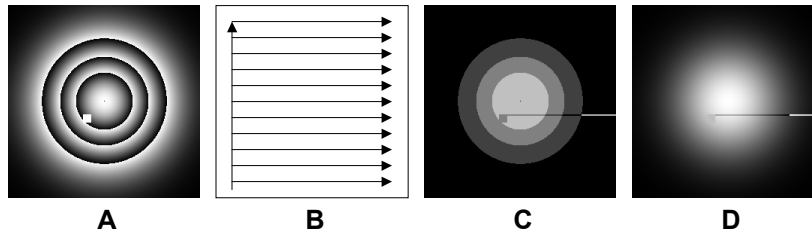


Figure 11: Illustration of phase unwrapping.

Figure 11A is the modulo 2π phase map with its characteristic sawtooth appearance. An anomalous region has been deliberately introduced. Figure 11B shows the path taken in unwrapping this particular image. Whenever a jump is detected, the bias image (Figure 11C) is incremented/decremented by 2π . When the path has been fully traversed, the bias image is added to the modulo 2π phase to produce the principal phase (Figure 11D).

Volumes have been dedicated to unwrapping noisy, i.e., real world, phase maps. It is non-trivial to produce both a robust and a fully automatic phase unwrapping algorithm. The difficulty lies in the fact that unwrapping the phase is a path-dependent operation. An arbitrary path can be used, but any error, such as missing a phase jump or including noise-induced phase jump, will propagate through the remainder of that branch of the unwrapping path as in Figure 11.

The optimum method for eliminating errors due to residues is to optically prevent them by making the interferograms as noise and artifact free as possible. Digitally, the general method for minimizing these phase unwrapping errors is to locate the regions of the image that will cause phase errors. Then a path is chosen that will either process these areas as late as possible or avoid them altogether.

Regions at or between “residues” can cause propagating phase errors. The term residue comes from the mathematical usage indicating a point about which a path integral does not equal zero, as it should in a conservative field. Figure 12 shows two magnified views of the residues in the lower left corner of Figure 9. In the context of digital phase unwrapping, a residue is a point where if a path is followed, e.g., clockwise, around it through its eight neighbors, the number of positive and negative phase discontinuities are not equal. The dotted paths in Figure 12 are examples. Each has only one discontinuity and therefore is a residue. Of course the numerical definition of discontinuity is subjective and depends on the threshold used to detect it. If the absolute value of the change in phase from one pixel to its neighbor exceeds the threshold, then the boundary between the two is considered a discontinuity.

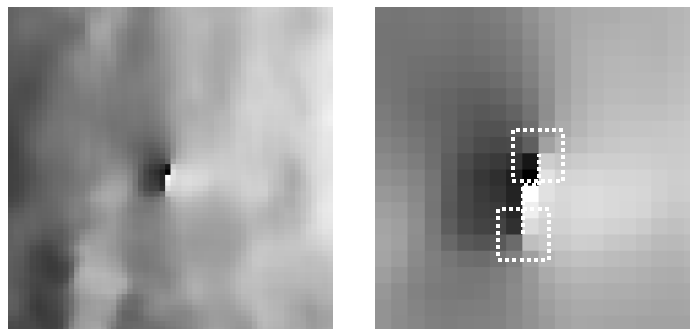


Figure 12: Magnified view of residue in lower left region of Figure 9.

Figure 13 shows the horizontal profile of the phase map passing through the residue. The residue is roughly at pixel 200. The eye can visually see that probably the spike at the residue is in violation of the general upward slope and probably should be ignored. It is, of course, not trivial to give the computer the same intuition. (Note that the region from pixel 0 to 60 corresponds to the test model and therefore will be masked out later in the processing.)

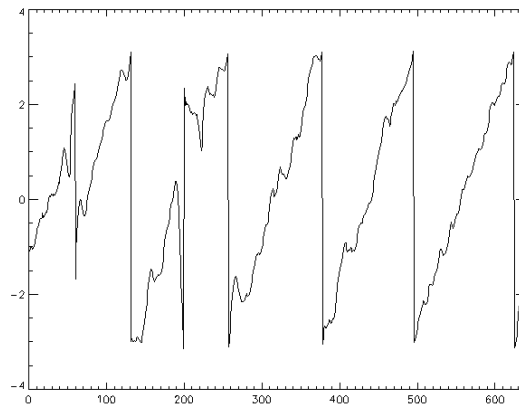


Figure 13: Horizontal profile of modulo 2π phase passing through the residue in Figure 12.

Development of fully automated unwrapping code capable locating residues and choosing an optimal path around them was beyond the scope of this effort. Instead the concentration was on simplicity of programming and minimal time in a low volume effort. Therefore, a semi-manual approach was taken. First the phase is unwrapped by the computer in the comb-shaped path shown in Figure 11B (except from right to left). The unwrapped version of the phase map in Figure 9 is shown in Figure 14 below. Note the artifact appearing as a streak that resulted from the residues shown in Figure 12.

Then the user corrects those residues that defy the basic algorithm. The manual user interface used to remove residue artifacts is shown below in Figure 14. The full phase map with an optional mask is shown in the large window. The mask is used to delineate object boundaries in the field.

The user clicks on a pixel in the full image and that area is displayed with 4X magnification in the small window at the upper right. As the cursor tracks over either window, the pixel index and phase in radians is displayed. The user clicks on the rightmost pixel in each horizontal line comprising the artifact. A left click will automatically increment by 2π that pixel and all pixels to its left on the same horizontal line. Conversely, right clicking will decrement by 2π the same pixels. Alternatively the user can drag either button in a vertical or diagonal line to automatically repair multiple adjacent horizontal lines.



Figure 14: User interface for the phase-unwrapping routine. The streak is a propagating error in the unwrapping. Clicking in the magnified view at the upper right allows correction of these anomalous regions.

Figure 15 and Figure 16 show profiles of rows without and with a residue, respectively. The overall linear slope of both is due to the carrier frequency introduced in the interferogram. Note that in Figure 16, the discontinuity is of magnitude 2π radians.

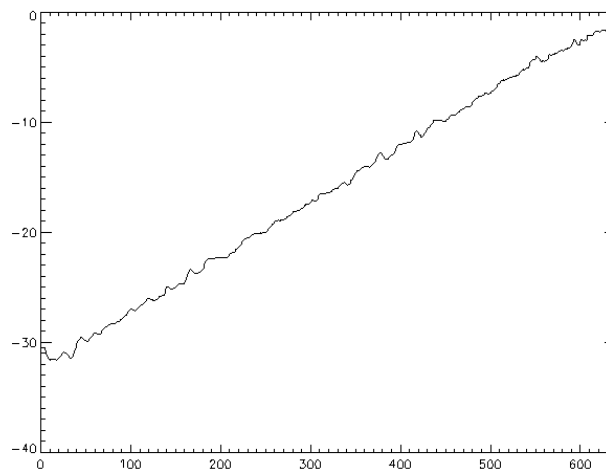


Figure 15: Horizontal profile of unwrapped phase at row 470, which has no residues. The linear slope comes from the carrier frequency.

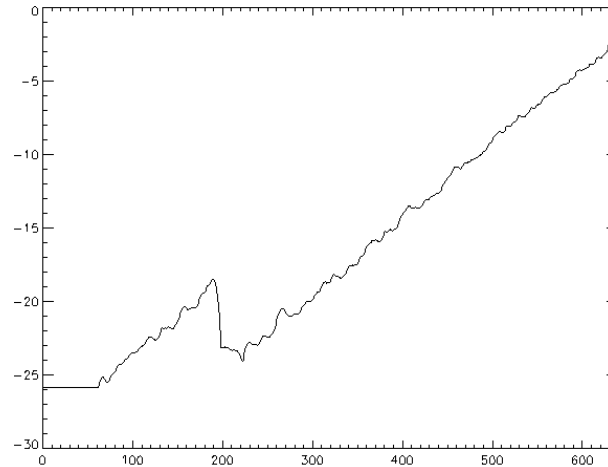


Figure 16: Horizontal profile of the unwrapped phase at the residue. Note that the slopes before and after the residue are the same but their intercepts differ by 2π .

3.4 Subtraction of Linear and No-Flow Phase

Before the density calculations can occur, the linear phase of the carrier frequency must be removed and the reference beam should be subtracted. In order to implement a simple and effective method, it was assumed that the phase in the free stream was on average flat with no linear phase. Thus, two profiles are extracted from the free stream of the images, one horizontal and one vertical. Least squares fits are made with the profiles giving slopes in the x and y axes. These slopes are then used to create a plane that is subtracted from the phase to eliminate the carrier. Figure 17 show a phase map with the carrier subtracted.

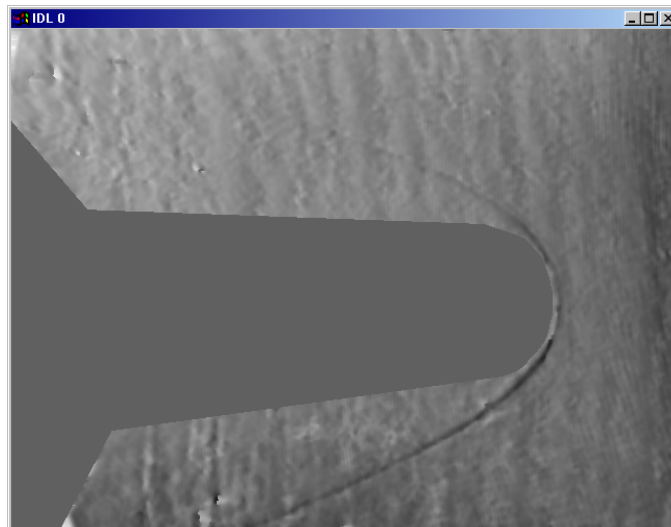


Figure 17: The result of removing the carrier phase from Figure14.

There is generally a constant value remaining, i.e., the mean of the image is nonzero. This constant offset is corrected later in the processing.

The final step in calculating the phase of the interferogram is to subtract the phase map of the first interferogram, which was recorded prior to the arrival of the shock front. This helps remove phase artifacts introduced by the optics of the recording system and the windows of the tube. Figure 18 shows the no-flow phase map corresponding to Figure 17 and Figure 19 shows the results of the subtraction.



Figure 18: No-flow image phase map.

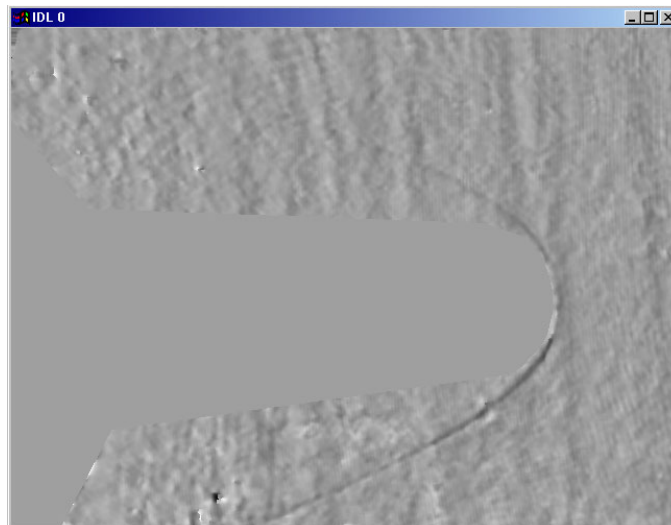


Figure 19: Phase from Figure 17 with reference phase subtracted.

3.5 Density Calculations

With the phase of the wavefront now known, further calculations yield information about the gas densities. The fringe number, N , is easily obtained from the phase data, θ , with Eq. 3.7

$$N = \frac{\theta(x, y)}{2\pi}. \quad (3.7)$$

In this case reconstruction is done in the red at $\lambda_r = 632.8$ nm so the path length difference, $\Delta\Phi(x, y)$, is

$$\Delta\Phi = N\lambda_r \quad (3.8)$$

The path length difference, in turn, is related to the refractive index by

$$\Delta\Phi(x, y) = \int [n(x, y, z) - n_0] dz = \int [\Delta n(x, y, z)] dz, \quad (3.9)$$

where $n(x, y, z)$ is the refractive index at a point in the flow, n_0 is the free stream refractive index in the flow, and $\Delta n(x, y, z)$ is the change in refractive index at a point in the flow measured relative to n_0 . As with all interferometric measurements, the direct measurements are of differential refractive index, $\Delta n(x, y, z)$. Absolute measurements require the knowledge that $n(x, y, z)$ at a particular point, $\{x_p, y_p, z_p\}$, is equal to n_0 . Then the absolute refractive index can be found as

$$n(x, y, z) = \Delta n(x, y, z) + [n_0 - n(x_p, y_p, z_p)], \quad (3.10)$$

Typically, $\{x_p, y_p, z_p\}$ is a free stream point.

If the flow is two-dimensional, i.e., the refractive index is not a function of z , the direction parallel to the object beam, then

$$\int [\Delta n(x, y)] dz = \Delta n(x, y) \int dz = \Delta n(x, y) z \Big|_0^L = \Delta n(x, y) L, \quad (3.11)$$

where L is the interaction length through the tube from window to window which in this case is 1205 mm. Thus, $\Delta n(x, y)$ and $n(x, y)$ are, respectively,

$$\Delta n(x, y) = \frac{\Delta\Phi(x, y)}{L} \quad \text{and} \quad n(x, y) = \frac{\Delta\Phi(x, y)}{L} + n_0. \quad (3.12) \text{ and } (3.13)$$

With a radially symmetric phase object such as the flow in Runs 33 and 35, the refractive index does depend on z . Therefore, Eqs. 3.12 and 3.13 must be interpreted as giving the mean refractive index in the z direction as a function of x and y . Notice that rearranging Eq. 3.11 slightly and making Δn a function of z also gives a form of the mean-value theorem

$$\Delta n(x, y) = \frac{\int [\Delta n(x, y, z)] dz}{L}, \quad (3.14)$$

where $\Delta n(x, y)$ is the mean refractive index which is a function of x and y only. This is the 2D mean refractive index calculation used in this project to calculate 2D density values.

While outside the scope of this contract, the knowledge that a flow is radially symmetric (about an axis perpendicular to z) makes it possible to invert the 2D path length, $\Delta\Phi(x, y)$, to calculate the 3D refractive index, $\Delta n(x, y, z)$ using a numerical inverse Abel transform.

From the refractive index, gas density is derived using the Gladstone-Dale equation

$$n(x, y, z) - 1 = K\rho(x, y, z) \quad (3.15)$$

where ρ is the gas density and K is the Gladstone-Dale constant, which for a particular gas is relatively insensitive to temperature and pressure variations and is a weak function of wavelength. Differential density can also be found

$$\Delta n(x, y, z) = K\Delta\rho(x, y, z) \quad (3.16)$$

For a mixture of gases, the Gladstone-Dale constant is a weighted average of the constants of the constituents

$$K = \sum_i a_i K_i \quad (3.17)$$

where K_i is the Gladstone-Dale constant for i^{th} constituent species with mass fraction a_i . Table 1 below shows the constituent species, Gladstone-Dale constants and mass fractions for Runs 33 and 35.

Table 1: Free stream composition of Runs 33 and 35

Species	K (m ³ /kg)	a_i , Run 33	a_i , Run 35
N ₂	$0.240 \times 10^{-3}\dagger$	0.733	0.735
O ₂	$0.191 \times 10^{-3}\dagger$	0.183	0.169
N	$0.305 \times 10^{-3}\ddagger$	3.03×10^{-11}	7.13×10^{-11}
O	$0.182 \times 10^{-3}\ddagger$	0.0151	0.0304
NO	N/A	.0695	.0654
NO+	N/A	5.02×10^{-8}	8.97×10^{-8}

† 514.5 nm (argon) ‡ 694.3 nm (ruby)

Unfortunately, at the time of this report and processing, Gladstone-Dale constants for NO and NO+ could not be located. Thus, the most valid assumption was to exclude those species and use the following formula:

$$K = \frac{\sum_i a_i K_i}{\sum_i a_i} \quad (3.18)$$

which essentially re-normalizes the sum of the mass fractions to unity. Note also that the Gladstone-Dale constants for N and O were measured at 694.3 nm. While this does introduce some error, it is less than the error introduced by not including NO. In fact, using three significant digits, the atomic nitrogen did not contribute to the calculated value with such a low concentration. The atomic oxygen did have a contribution in the least significant digit but the variation of K with wavelength over the range of 500-700 nm is generally in the third significant digit (0.002×10^{-3} for air from 509.7-703.4 nm.) The wavelength shift for O would only have affected the fifth or sixth significant digit of the aggregate K.

Using Table 1 and Eq. 3.18, Gladstone-Dale constants of 0.2294×10^{-3} and 0.2293×10^{-3} , respectively. By comparison, the Gladstone-Dale constant of air at 509.7 nm is 0.2274×10^{-3} . With only three significant digits the identical value of 0.229×10^{-3} was used for both runs.

Taking Eqs. 3.7-3.17 and the calculated Gladstone-Dale constant we have for the differential density and the absolute density

$$\Delta\rho(x, y) = \frac{\theta(x, y)\lambda_r}{2\pi L} \quad (3.19)$$

and

$$\rho(x, y) = \Delta\rho(x, y) + [\rho_0 - \Delta\rho(x_p, y_p)] \quad (3.20)$$

where $\rho(x, y)$ and $\Delta\rho(x, y)$ denote average density and differential density parallel to the z axis and where $\{x_p, y_p\}$ is a particular path in z where the average density is known. Eq. 3.19 was used to calculate the differential densities for Runs 33 and 35 in the deliverables.

3.6 Shear Removal (Shearing Interferometry Only)

This step in the processing is used in shearing interferometry only and then only if it is necessary to calculate the density from the density gradient.

Prior to removing the shear from the sheared density maps, it was necessary to divide by the shear distance to get a density gradient in kg/m^4 . The shear distances for each run and shear direction are given in Table 2 in both pixels and meters (in object space). Unfortunately, without a good distance calibration in the image, it was necessary to estimate the magnification of the images as (256 mm/640 pixels =) 0.4 mm/pixel.

Table 2: Shear distances

Shear Direction	Run 33		Run 35	
x shear	2 mm	5 pixels	3.6 mm	9 pixels
y shear	2.4 mm	6 pixels	3.2 mm	8 pixels

When shearing interferometry is used, the phase-shifted interferograms measure the phase difference between the original wavefront and a slightly translated copy of itself. In the limit of small translations, this phase difference amounts to a finite-difference approximation of the partial derivative with respect to an axis parallel to the shear. When using interferograms sheared by an arbitrary amount $\{\sigma_x, \sigma_y\}$, phase calculation and unwrapping from the interferograms is identical to conventional interferometry. However, the phase that is calculated is no longer equal to $\theta(x,y)$. As mentioned, the phase is

$$\Delta\theta(x,y) = \theta(x,y) - \theta(x + \sigma_x, y + \sigma_y) \quad (3.21)$$

where σ_x and σ_y are the shear distances for the x and y axes, respectively. In calculations described subsequently, σ_x and σ_y will be measure in units of pixels.

In conventional interferometry, the processing documented in previous sections results in a map of density relative to some unknown constant value which may be know via some other measurement. With sheared interferograms, the same processing results in a map of the differential density with respect to the density $\{\sigma_x, \sigma_y\}$ units away. There is no unknown constant in this finite difference, however, when the sheared density is integrated or inverted to give the absolute density, the unknown constant will again arise.

Two techniques for inverting the sheared density maps were investigated: direct integration and a convolution method. The term invert is used in this process because of the close relation to the mathematical process of inverting a gradient or vector field to give the potential function. Because both processes are linear, they can be performed either before or after the conversion of phase to density as described in Section 3.5. For this contract, density was calculated first in the sheared interferograms to give a map of the partial derivative of the density. The inversion of the shear was performed afterward.

As with the unwrapping of the modulo 2π phase, the major obstacle in trying to back out the shear is that the operation is path dependent. Therefore, errors will propagate through subsequent segments of the chosen path. This effect is immediately apparent in Figure 20, which shows the results of such a direct integration.



Figure 20: Results of direct integration of the sheared phase. Note the streaks propagating from right to left.

Unlike phase unwrapping, where the errors were always multiples of 2π , a simple manual solution is not possible. Thus, with the assumption of a noise-free sheared density map approximating the partial derivative, direct integration would provide a simple, effective means of removing the shear.

The convolution technique is based on an assumed linear impulse response representing the shearing process. The discrete impulse response should be 1 at $\{0,0\}$ and -1 at $\{\sigma_x, \sigma_y\}$ as shown in Figure 21. With the impulse response zero elsewhere, one sees that the convolution of the original wavefront with this kernel results in that wavefront minus itself shifted by $\{\sigma_x, \sigma_y\}$, i.e., the sheared wavefront.

0	0	0	0	0	0	0	0	0
0	0	0	0	0	0	-1	0	0
0	0	0	0	0	0	0	0	0
0	0	0	0	0	0	0	0	0
0	0	0	0	1	0	0	0	0
0	0	0	0	0	0	0	0	0
0	0	0	0	0	0	0	0	0
0	0	0	0	0	0	0	0	0
0	0	0	0	0	0	0	0	0
0	0	0	0	0	0	0	0	0

Figure 21: Impulse response of the shearing interferometer. In this example the shear, σ , is $\{2,3\}$ pixels.

From the impulse response, it is possible to find the impulse response of the inverse system that would accept the sheared phase as input and then output the phase of the original wavefront. This is accomplished most simply by transforming to the frequency domain

with the FFT where convolution is performed by multiplication and the inverse of a system is found by taking the reciprocal of its system response. Figure 22 shows the FFT of the system response for a system with a shear of $\{5,0\}$ pixels. Note that the shear must be expressed in units of pixels.

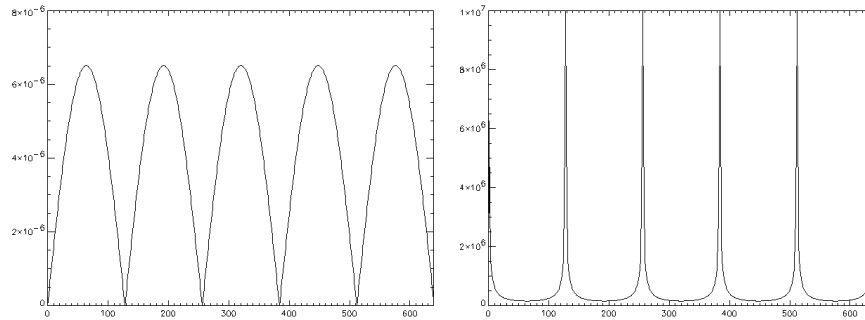


Figure 22: Left: Impulse response in the frequency domain. Right: Impulse response of the inverse system in the frequency domain. (A 1D plot of one line of the FFT is shown because the 2D FFT is independent of frequency in the y axis.)

Figure 22 also shows the reciprocal of this system. The key feature of these inverse systems, which arises from the existence of zero value at multiples of the shear fundamental frequency, is the appearance of indeterminate locations where the value approaches infinity. These indeterminate locations result from division by zero in the reciprocal.

More intuitively, they exist because a sinusoid whose frequency is a multiple of the shear fundamental frequency (which in Figure 22 is $640/5 = 128$ cycles) will exactly cancel itself in the interferometric subtraction and therefore not contribute to the sheared interferogram. Hence the zero values in the impulse response. Therefore, those spatial frequencies are meaningless and the reciprocal indicates this having indeterminate values at those frequencies.

Ideally, with the inverse frequency response, calculation of $\theta(x,y)$ follows

$$\theta(x,y) = FFT^{-1} \left\{ \Delta \theta(x,y) \frac{1}{h} \right\} \quad (3.22)$$

where FFT^{-1} denotes the inverse discrete Fourier transform and h is the impulse response.

As shown in Figure 22, the frequency response repeats itself over intervals of the shear fundamental frequency. This is again related to the inherent aliasing that results from the interferometric subtraction. This response must be bandlimited at that frequency to prevent aliasing during the convolution. The bandlimited frequency response of the inverse system, $1/h$, is shown in Figure 23.

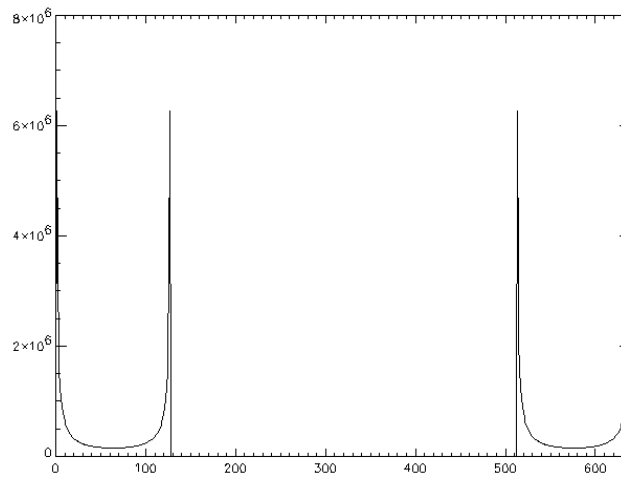


Figure 23: Bandlimited frequency response of the inverse shearing system.

The results of applying Eq. 3.22 to the sheared phase of Figure 19 are shown in Figure 24.

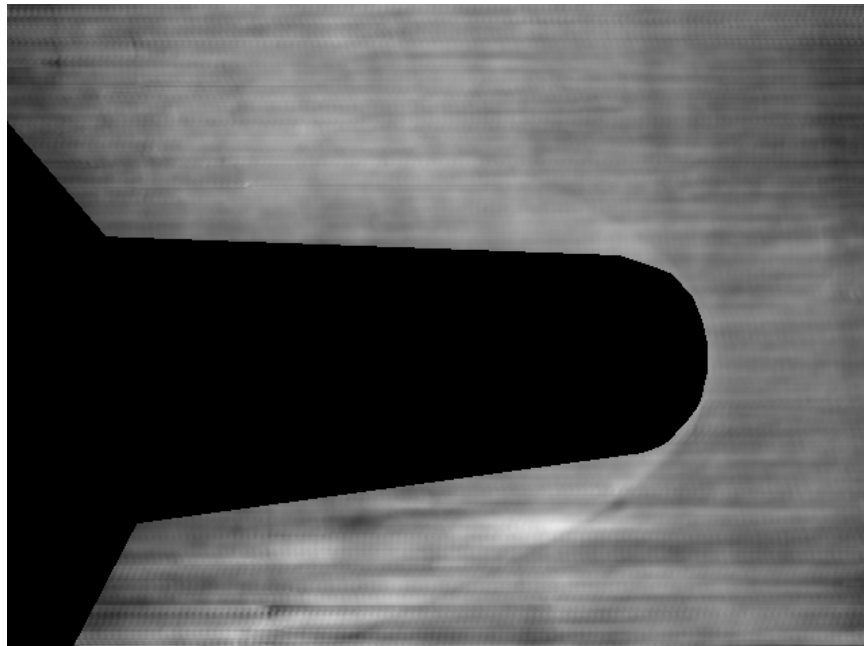


Figure 24: Results of using the frequency domain convolution with the inverse of the shearing interferometer response.

While this convolution-based method appears to be at least somewhat more resistant to noise in the phase, one of the limitations of the technique comes from the finite resolution of the Fourier transform. As Figure 25 shows, the singularity at $\omega = 0$ cannot be properly

represented. The result is that the subharmonic frequencies of the images are not reconstructed properly and very low (less than one cycle across the image) frequency errors can occur across the image. One potential fix for this would be to pad the sheared phase map with zeroes, e.g., to create a 2048×2048 image. The resolution of the FFT would then be 3-4 times higher. Then the misrepresented frequencies would be 3-4 times lower and they would approximate a linear error. The linear error could then be removed just as the carrier frequency linear phase was removed in Section 3.4.

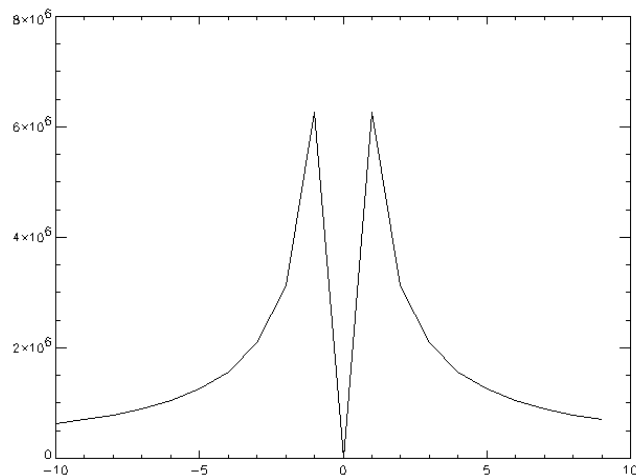


Figure 25: Magnified view of the low frequencies of the FFT of the inverse response.

3.7 Output

With the gas density and/or gas density gradient information calculated in the form of arrays of 640×480 floating point values, the data has been output to files for visualization and archival purposes.

To allow further processing later, possibly with Microsoft Excel, one output format is tabulated text. Each image is contained in a text file consisting of 640 tab-delineated columns and 480 rows. The first row in the text file is the top row in the image, i.e., the top to bottom order is reversed compared to many image formats where the first row of data in the image file is the bottom row of the image. Each value is ASCII text in the form of a floating-point mantissa with optional exponent of the form $[E\pm\#]$.

The second format for the output data is 24-bit Windows bitmap format. Both grayscale and color images are included. The images are scaled linearly between a maximum and minimum value noted in the readme file with each CD. In both the black & white and color images, a black pixel is less than or equal to the minimum and a white pixel is greater than or equal to the maximum.

The file “colormap.bmp” is included with the data on CD. It shows the color table used to produce the color bitmap images.

3.8 *Fourier Processing*

Fourier processing as a method for modulo 2π phase extraction was also investigated briefly as an alternative to the phase-shifting technique outlined in Section 3.1. Fourier processing, unlike phase shifting, requires a high carrier frequency in the fringes. This is sometimes referred to as fringe injection. This is a special case of finite fringe interferograms. An example interferogram is shown in Figure 26.

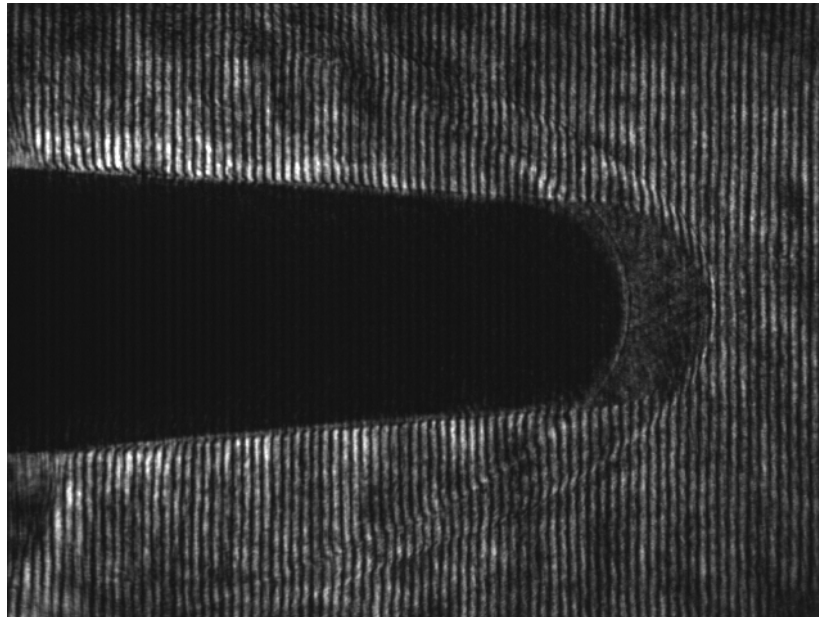


Figure 26: Example of an interferogram for Fourier processing. This particular interferogram has a very large shear to increase sensitivity.

The main advantage of this technique is that only a single interferogram is necessary for unambiguous phase measurements. This is because the carrier frequency, which is a linear phase term added to the phase of interest, is made high enough that the slope of the phase never changes sign.

Figure 27 shows the process for extracting the modulo 2π phase from such an interferogram. The central lobe of the FFT represents the amplitude data, i.e., the image of the test model. The two side lobes correspond to the carrier frequency modulated by the phase of the wavefront. The phase is recovered by shifting the FFT to remove the carrier and cropping out the amplitude data. The inverse FFT then yields a complex representation of the wavefront from which the phase is calculated using:

$$\theta = \tan^{-1} \left[\frac{\text{Im}\{\psi\}}{\text{Re}\{\psi\}} \right] = \text{Im}\{\ln \psi\} \quad (3.23)$$

where ψ represent the wavefront calculated from the FFT. (The wavefront, ψ , should not be confused with Ψ , the phase shift in phase-shifting interferometry.)

The result of applying Eq. 3.23 to Figure 26 is shown in Figure 28. Note that the phase map has not been unwrapped.

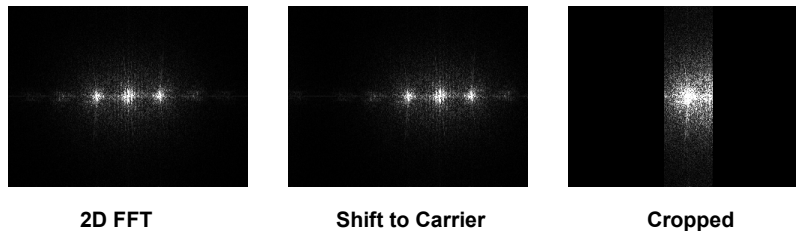


Figure 27: Processing used to extract phase from an interferogram using the 2D FFT. Note that the brightness in the cropped FFT is higher so it appears larger.

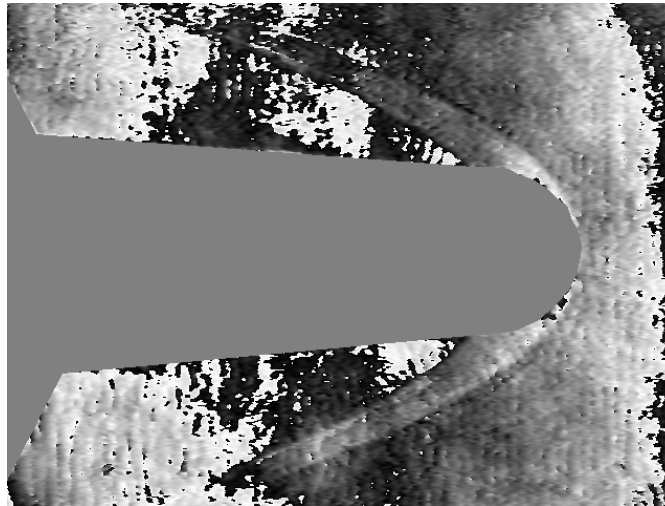


Figure 28: Modulo 2π phase calculated from the interferogram in Figure 26.

Two limitations must be considered in comparing Fourier processing with phase shifting. First, the spatial frequencies in the phase field being measured will be bandlimited by the carrier frequency. Otherwise, it will not be possible to crop out the amplitude data from the FFT without affecting the phase data modulating the carrier. Second, the phase sensitivity is decreased because the carrier frequency occupies a significant portion of the dynamic range leaving less for the signal of interest. Thus, if both of these limitations are

acceptable, Fourier processing could potentially be a much simpler method for digitization and phase extraction from the holograms.

4 Results

For each run, both conventional and shearing interferometry were performed for each time frame. The shearing interferometry was applied with both x axis and y axis shears, giving approximations of the x and y components of the density gradient. In addition, every sheared interferogram was integrated/inverted to give the density.

4.1 Conventional Interferometry

Figure 29 and Figure 30 show four time frames for Run 33 and 35, respectively. The numbering in the figures indicates from which time frame the images are taken. Frame #1 is the no-flow image and, therefore, is not a density map but a phase map of the optical system. This frame is subtracted in the phase post-processing detailed in Section 3.4. The remaining phase maps are density maps. Frame #2 shows the arrival of the shock front. Frame #6 shows the density at $(6/8 \text{ kHz} =) 750 \mu\text{s}$ and Frame #45 shows the density at $(45/8 \text{ kHz} =) 5.6 \text{ ms}$.

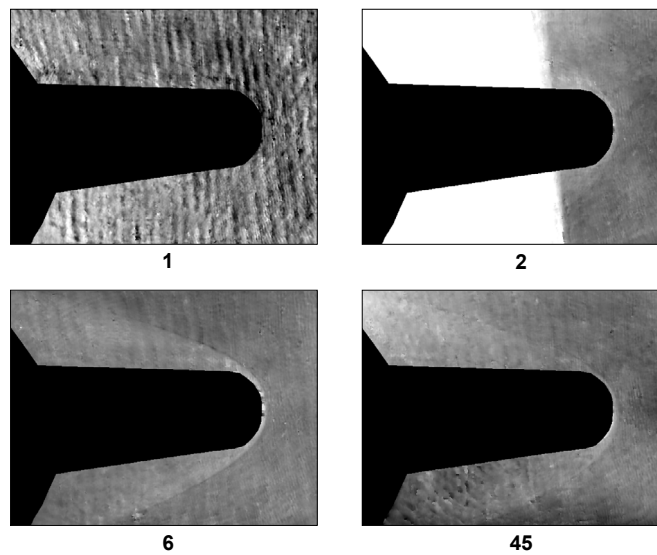


Figure 29: Conventional - Run 33

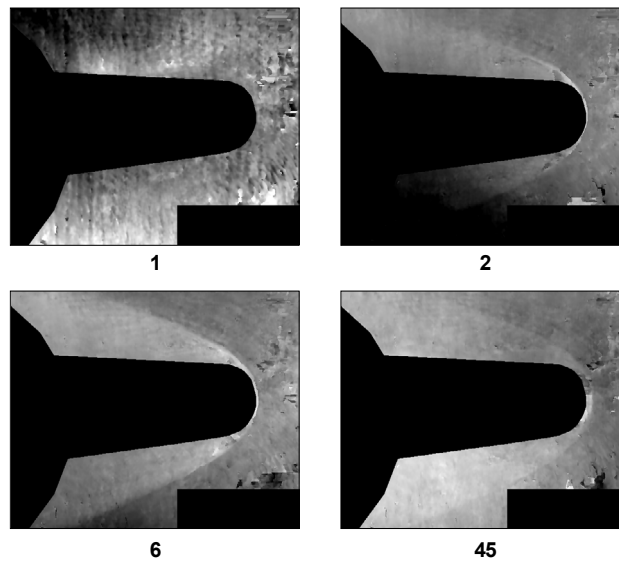


Figure 30: Conventional - Run 35

A few interesting aspects of these images are apparent:

The phase map of the no-flow shows that the system optics were somewhat less than ideal. The primary defect is the low-horizontal-frequency fringes across the image. It has been verified that the defects were not present in the playback system but were recorded in the holograms. The most probable culprits therefore are the windows through which the object beam illuminated the flow.

The shock front in Frame #2 shows the opposite of the expected behavior, i.e., the density to the left of the shock is higher. It is believed that this is because in this case the refractive index gradient is so high at the shock that aliasing occurs. The resolution of the digitized images is insufficient to properly sample the fringes in the area of the shock. This is a standard issue with interferometry, which has high sensitivity.

Frames #6 and #45 highlight two related points. Subtraction of the no-flow did not completely remove the defects from the system optics. In addition, a misalignment of the density map in Frame #45 compared to the other can be seen. (The mask is in an identical location in all four images.) This misalignment is probably due to difficulty in exactly aligning the processed film on the transport during playback. More specifically, it is related to runout from too much clearance between the center hole of the film disk and the spindle on which it is mounted.

4.2 Shearing Interferometry

Figure 31 through Figure 34 show the density gradient maps from shearing interferometry for both runs with shear in both the x and y axes.

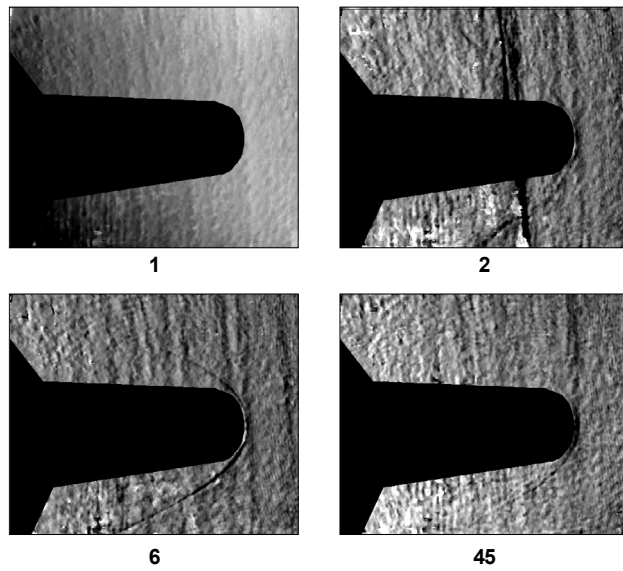


Figure 31: Shearing - Run 33, x component of density gradient.

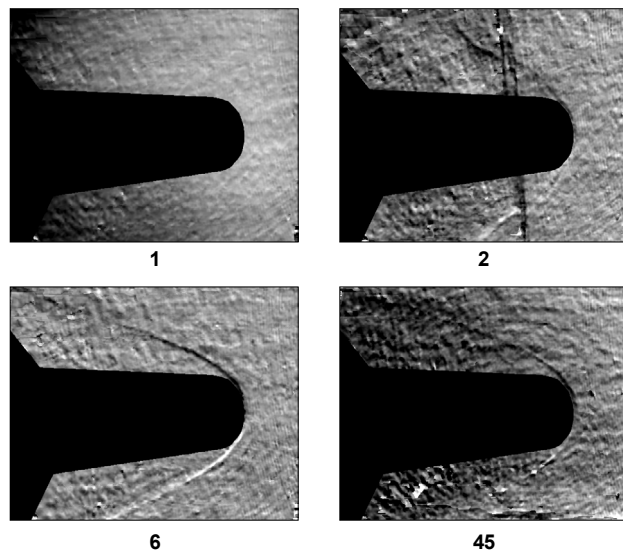


Figure 32: Shearing - Run 33, y component of density gradient.

The x and y axes start at the lower left corner of the images. Therefore, a negative (black) gradient in the x-sheared images indicates a decrease from left to right.

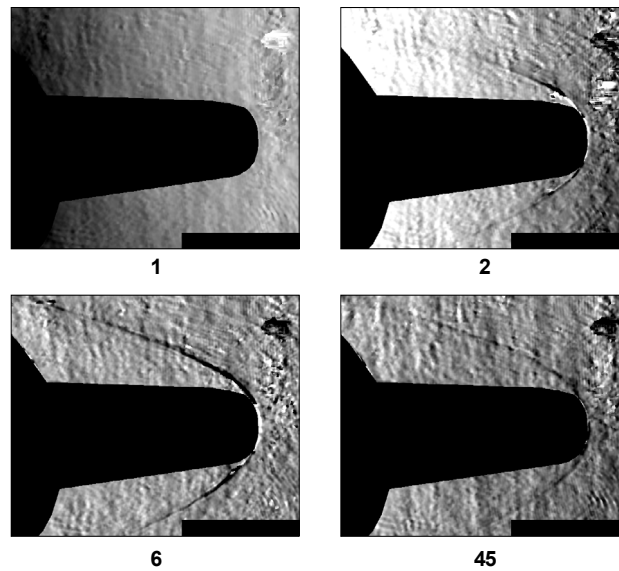


Figure 33: Shearing - Run 35, x component of density gradient.

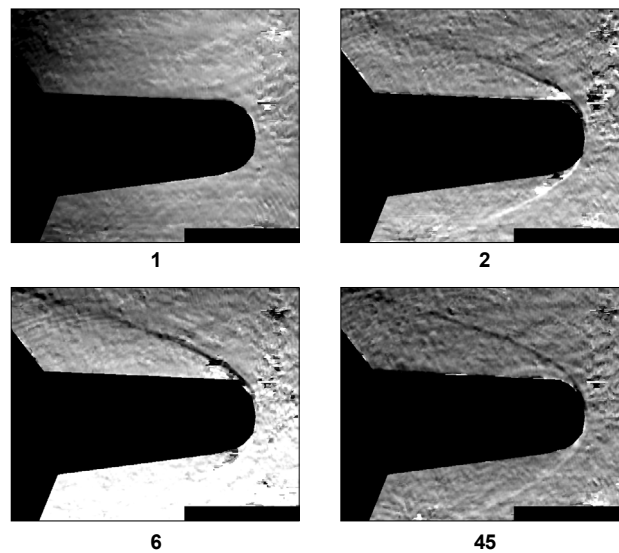


Figure 34: Shearing - Run 35, y component of density gradient.

Note that in some of the images, e.g., Figure 34, Frame #6, the carrier frequency was not properly removed. Because that part of the processing was carried out automatically for all time frames, the most likely explanation is that the noise in the right corner gave a poor least-squares fit for the y axis.

Figure 33, Frames #2 and #6, further illustrates the previously mentioned issue of sensitivity and dynamic range. Aliasing has occurred in these two frames at the tip of the model where the density gradient is particularly high. The gradient at the bow shock should be

negative (density increases from right to left). In these two frames the gradient was so high that from one pixel to the next the phase jumped by more than the threshold for a modulo 2π discontinuity. Thus, during unwrapping, the software mistook the high gradient for a phase discontinuity and tried to unwrap it when it should not have done so.

Sensitivity in interferometry is primarily related to the species being measured, the interaction length, and the wavelength of light used. Dynamic range is determined by the resolution of the imaging system and is somewhat analogous to slew rate in an electronic amplifier. If the gradient of the measured field is too high, the fringe density will be beyond the resolution of the system and aliasing will occur. This sort of behavior is typical with interferometry.

In conventional interferometry this would be overcome by magnifying the problem area until the fringes are resolvable, essentially increasing the sampling frequency in the region. Shearing interferometry offers an alternative method whereby the interferometer is desensitized by reducing the shearing distance. As the shearing distance approaches zero so does the phase. Thus, a large gradient at a boundary layer can be measured by desensitizing the interferometer. Unfortunately, in the testing performed under this contract, this issue did not become apparent until the interferograms were processed and time restrictions did not permit re-digitizing the interferograms.

4.3 Inverted Shearing Interferometry

Figure 35 through Figure 38 show the results of inverting the sheared density gradient maps of Figure 31 through Figure 34 using the convolution method discussed in Section Shear Removal (Shearing Interferometry Only).

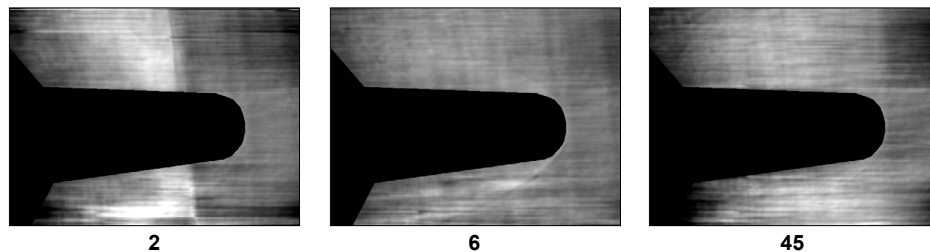


Figure 35: Shearing - Run 33, Density calculated from x axis shear.

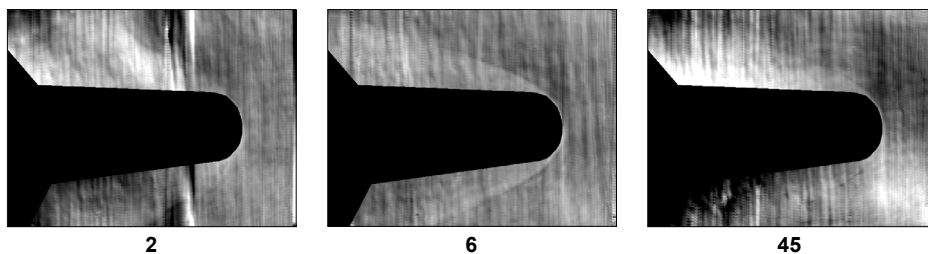


Figure 36: Shearing - Run 33, Density calculated from y axis shear.

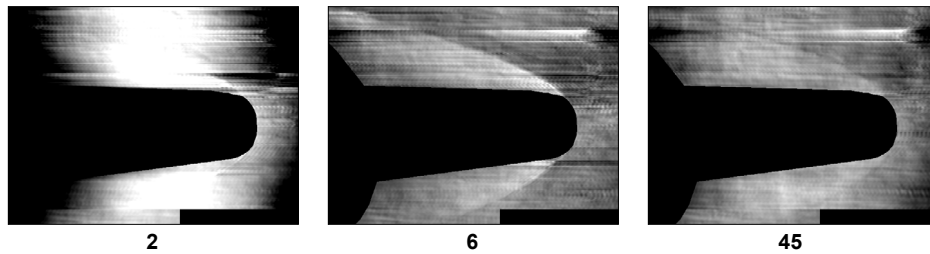


Figure 37: Shearing - Run 35, Density calculated from x axis shear.

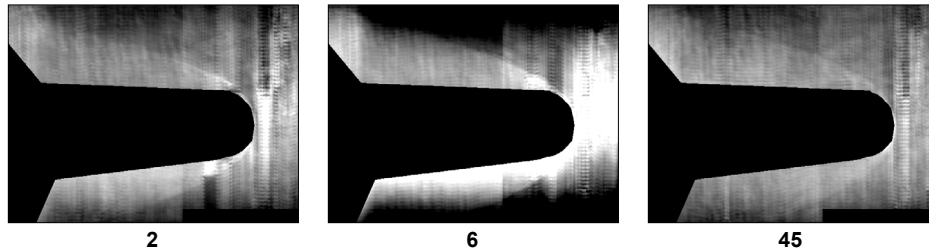


Figure 38: Shearing - Run 35, Density calculated from y axis shear.

Figure 37, Frame #2, is a good illustration of the effects of limited resolution in the FFT. The entire image has a significant component at a frequency of 1/2 cycle resulting in the obvious inverted "U" shape profile in the x axis. Figure 38, Frame #6, also illustrates the effects of limited resolution in the FFT but in this case the effect is seen in the y axis because of the y axis shear.

The calculated values in the shear-removed density maps are quantitatively incorrect in that the density values are nonsensical. There appears to be some unknown factor in the calculation that is causing the values to be unusually large. The errors are introduced by the Fourier convolution. Further investigation is necessary to pinpoint the cause and incorporate a solution.

5 Conclusions

The work performed under this contract has accomplished several important goals. The ability to extract density data from holograms recorded by NDL's holographic recorder has been proven and the versatility of the hologram in performing multiple interferometric analyses from a single test run has been demonstrated. From each hologram/time-frame, 12 interferograms were digitized with complete freedom in choosing fringe frequencies and shear distances. This is clearly beyond the ability of a CCD camera. Because one camera is needed for each image, four CCD's would be needed just to record a single series phase shifted interferogram for one time frame of a high-speed event. Furthermore, to achieve 8 kHz with a CCD, camera makers must typically limit resolution to about 256 in one axis. Thus, holographic recorder compares favorably with a CCD camera for performing interferometric measurements.

In addition to proving the versatility of the holographic recorder, this work has provided a valuable comparison between the capabilities of conventional and shearing interferometry. Optically, shearing interferometry is simpler, not requiring the copying of the no-flow hologram. It is also more resistant to vibrations and to hologram alignment. Another significant advantage of shearing interferometry is the ability to desensitize to allow unaliased measurement of the density gradient near a boundary layer.

On the other hand, unless noise in the interferograms can be significantly reduced the ability to invert the shear and produce density maps from the density gradients is limited.

Conventional interferometry, while requiring a copy of the no-flow be made, was found to be easier and more effective than expected. The primary difficulty lies in alignment of the holograms with the no-flow and is related to the runout in the film disk.

Thus, conventional interferometry appears to be better suited to density measurements away from the boundary layers and shearing interferometry provides a means for measuring behavior in high gradient regions. The ability of this interferometric post-processing to perform both on a single hologram raises the possibility of combining the data from each. The data from the shearing interferometry could be used to fill gaps in the conventional interferometry at boundary layers.

From the experience gained in the undertaking of this contract, several recommended goals and areas for improvement can be suggested:

- Improve system optics/noise reduction
- Improve disk alignment techniques
- Improve dynamic range of holograms/digitization
- Integrate closed loop piezoelectric phase-shifting stage
- Reinvestigate Michelson interferometer
- Automate unwrapping technique

6 References

1. C. M. Vest, Holographic Interferometry, John Wiley & Sons, Inc., 1970.
2. Timothy D. Upton, "Experiments on Transient Natural Convection in Inclined Enclosures Using Calibrated Multichannel Electronic Interferometry and Digital Particle Image Velocimetry," doctoral dissertation, University of New Hampshire, 1995.
3. M. Takeda, H. Ina, and S. Kobayashi, "Fourier-transform method of fringe-pattern analysis for computer-based topography and interferometry," J. Opt. Soc. Am., **72**:1, January 1982, pp. 156-160.

APPENDIX 4
CONVERTING CORDIN CAMERA FILM TO .AVI DIGITAL MOVIES

1. Remove film from camera and process. Avoid fingerprints, scratches, and lint. **Warning!** Trimming film ends or use of drier hanging clamps can result in loss of or damage to the head/tail frames.
2. Locate first and last frames. Write frame numbers on film edge. (every 10th frame)
3. Cut film (between frames) into 5- to 8-inch lengths, depending on scanner capacity.
4. Make positive contact print of strips (optional). (arrange strips in order and ~parallel to paper edge)
5. Scan film OR contact print on flatbed scanner. (adapter required for transparencies)
 - place image material flat against glass and ~parallel to side/end of scanner bed
 - scan strips individually at high resolution (800 dpi or higher depending on memory available)
 - maintain identical resolution and brightness/contrast settings for all strips
 - create a work directory, e.g., *C:\AVTR260*
 - save raw images as 256 grayscale (black and white photo) e.g., *r460s1.bmp, r460s2.bmp, etc.*
6. Process raw filmstrip images. (software: Paint Shop Pro Version 5.00, © JASC Software)
 - re-orient raw filmstrip image as required (90 deg. rotate, mirror, flip, etc.)
 - select frame reference feature(s) (x- and y-refs may be different but must be visible in ALL frames)
 - calculate angular deviation of strip from horizontal (use extreme left and right frame x- and y-refs)
 - rotate strip as required to horizontal (Paint Shop Pro provides 0.01 degree precision)
 - adjust brightness/contrast, sharpen, enhance as desired (use identical values for ALL strips)
 - select dimension of “final cropped frame” (x * y pixels) and record on data table, e.g., *r460.txt*
 - determine offset from x- and y-refs to cropped frame upper left corner and record on data table
 - trim filmstrip image (optional). (remove excess borders, sprocket holes, etc. to reduce file size)
 - save rotated filmstrip images in work directory, e.g., *r460s1r.bmp, r460s2r.bmp, etc.*
 - repeat step 6 for each raw filmstrip image
7. Register individual frames. (software: Paint Shop Pro Version 5.00, © JASC Software)
 - locate x- and y-refs for every frame in each rotated filmstrip image
 - record x- and y-refs and rotated filmstrip image filename (omit .bmp extension) on data table
 - record cropped frame image destination filenames on data table, e.g., *f001, f002, etc.* (omit .bmp)
 - repeat step 7 for each rotated filmstrip image
8. Crop and save individual frames. (software: AEDC-generated Fortran program, W. Ruyten)
 - in the work directory, execute the frame cropping program (reads data table, e.g., *r460.txt*)
 - cropped frame images will be saved in work directory as *.bmp files, e.g., *f001.bmp, f002.bmp, etc.*
9. Create and save “title frame”.
 - re-open first cropped frame image, *f001.bmp*, and save in work directory as *f000.bmp* (title frame)
 - apply appropriate title text to *f000.bmp* and re-save in work directory
10. Assemble *.avi digital movie (software: AVI Constructor 32 bit Version 2.4, © Michael Caracena)
 - select “add images” and open appropriate work directory
 - highlight and add title frame, e.g., *f000.bmp*
 - highlight and add all appropriate cropped frame images in order, e.g., *f001, f002, etc.*
 - set title frame duration to 30 flips (default is 1 flip/frame for all other cropped frame images)
 - press “256” (color) button to create and save movie
 - open work directory and enter movie filename, e.g., *r260.avi*

Nomenclature

2v	Optical frequency doubler
A/A*	Test facility nozzle area ratio
AEDC	Arnold Engineering Development Center
Ca	Calcium
CFD	Computational fluid dynamics
Cl	Chlorine
Ch	Heat-transfer coefficient
Cp	Pressure coefficient
Cr	Chromium
Cu	Copper
DLR	German Research Center
DPG	Digital pulse generator
EBF	Electron beam fluorescence
ES	Emission spectroscopy
Fe	Iron
FPST	Free-Piston Shock Tunnel
FWHM	Spectral full width at half-maximum
H ₀	Reservoir enthalpy
He	Helium
HEG	German Free-Piston Shock Tube
He-Ne	Helium-neon laser
HI	Holographic interferometry
HSFV	High-speed flow visualization
HVPG	High-voltage pulse generator
IAP	Integrated Applied Physics, Inc.
ICCD	Intensified charge-coupled device
K	Potassium
kHz	Kilohertz
LBT	Laser beam transmission
LDA	Laser diode absorption

L_{sep}	Total length of separated region, Fig. 9
L_u	Separation length on first ramp, Fig. 9
M	Mach number
N	Atomic nitrogen
$n(p)$	Particulate number density, cm^{-3}
$n(x)$	Number density of gas species x, cm^{-3}
N_2	Molecular nitrogen
NATO	North Atlantic Treaty Organization
NDL	North Dancer Laboratories, Inc.
Ni	Nickel
NID	Nonintrusive Diagnostics
NO	Nitric oxide
No	Indicates that NID technique was not used
n_∞	Freestream number density
O	Atomic oxygen
O_2	Molecular oxygen
ONERA	French Research Center
P_0	Reservoir pressure, MPa or atm
P1	Initial shock tube pressure
P3	Model nose pressure
PEBF	Pulsed electron beam fluorescence
PEG	Pulsed electron gun
PLIF	Planar laser-induced fluorescence
PMIE	Planar Mie scattering
PMT	Photomultiplier tube
p_{t2}	Pitot pressure (total pressure behind shock)
P_∞	Freestream static pressure
qt00	Temperature signal from stagnation point heat-transfer gage
q_{t2}	Stagnation point heat transfer
Rb/RbNO ₃	Rubidium/Rubidium Nitrate
s	Distance along body surface

SCR	Silicon-controlled rectifier
SEM	Scanning electron microscope
Si	Silicon
ST6	Impulse Facility shock tube pressure gage 6
T_0	Reservoir temperature
T_1	Shock tube initial gas temperature
T_r	Rotational temperature
T_{tr}	Translational temperature
T_v	Vibrational temperature
T_∞	Freestream or static temperature
u	Velocity, m/sec
WEX	Wavelength extender
WP	Witness plate
x/r	Rectangular coordinate ratioed to model nose radius
y/r	Rectangular coordinate ratioed to model nose radius
Yes	Indicates that NID technique was used
ΔT	Time increment, msec
β_i	Absorption coefficient
λ_i	Wavelength
λ_L	Laser wavelength
ρ_0	Reservoir density
ρ/ρ_{cl}	Ratio of flow density to facility centerline flow density
ρL	Hypersonic similarity parameter
θ	Initial ramp angle
θ_w	Second ramp angle, measured w.r.t. the first, Fig. 9

CFD Codes

CEVCATS-N	3D, full Navier-Stokes solver with chemistry, Ref. 27
GASP	3D, finite volume flow solver, Ref. 18
GIANTS	CFD flow solver, Ref. 17
GPACT	3D flow solver with finite-rate chemistry, Ref. 21
LAURA	CFD flow solver, Ref. 17
LORAN	Simplified radiation solver, Ref. 17
NEDANA	3D, locally implicit Navier-Stokes solver, Ref. 19
NEQAIR	Nonequilibrium radiation solver, Ref. 16
NOVAR	Simplified radiation solver, Ref. 17
NSHYP	3D, thin-layer Navier-Stokes solver, Ref. 23
TUFF	3D, thin-layer Navier-Stokes code, Refs. 14 and 15